THE STRUCTURE OF SOME COMPOUNDS OF TRANSITION METALS WITH CARBON, NITROGEN AND OXYGEN

by

P. S. BELL

A dissertation submitted
to the University of Warwick for
admission to the degree of
Doctor of Philosophy

Department of Physics

July 1972

MEMORANDUM

This dissertation is submitted to the University of Warwick in support of my application for admission to the degree of Doctor of Philosophy. It contains an account of my own work performed at the Department of Physics of the University of Warwick in the period October 1968 to October 1971 under the general supervision of Dr. M.H.Lewis. No part of it has been used previously in a degree thesis submitted to this or any other University. The work described in this thesis is the result of my own independent research except where specifically acknowledged in the text.

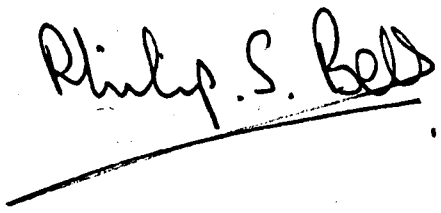

July 1972

P. S. Bell

ACKNOWLEDGEMENTS

I should like to thank Professor A.J.Forty for making available to me the facilities at the Department of Physics. I am extremely grateful to Dr. M.H.Lewis for his interest and advice during the course of this work, and especially in the preparation of this thesis.
My thanks are due to the Science Research Council for providing the financial support of a Research Studentship.
I would also like to thank Messrs. L.Bulmer and M.Davies of the University of Warwick Library for their helpful service.

Finally, I would like to thank my wife Sandra, for her patience and encouragement throughout the period of this work.

ABSTRACT

Many carbides, nitrides, and oxides of the Group IVa and Va transition metals show large deviations from stoichiometric compositions. These deviations are accomplished by the subtraction of the interstitial nonmetal atoms, or in some cases the metal atoms, from their lattice sites. The formation of superlattice structures resulting from the ordering of the remaining atoms and vacancies is then possible. The structures and modes of formation of these superlattices have been examined for a number of compounds using transmission electron microscopy and electron diffraction.

The nominally NaCl-type titanium and niobium monocarbides were examined within the composition limits $TiC_{0.45}$ to $TiC_{0.65}$ and $NbC_{0.70}$ to $NbC_{0.95}$ respectively. In the first system the cubic superlattice based on the composition Ti_2C was found, while niobium carbide showed similarities to vanadium carbide in the formation of ordered structures based on the composition Nb_6C_5. Three possible structures for Nb_6C_5, two with monoclinic and one with trigonal symmetry, are discussed in terms of periodic low energy planar faults within the carbon-atom sublattice.

Although the two hexagonal close-packed hemicarbides, V_2C and Nb_2C, show very small deviations from the stoichiometric composition, ordering is possible in the carbon-atom sublattice since this contains 50% vacancies. In both hemicarbides two ordered structures were found, stable at high and low temperatures. The high-temperature modifications of both V_2C and Nb_2C show similarities to

the ε-Fe_2N structure, though the exact nature of the ordered distribution could not be determined. The low-temperature modifications, although slightly different, both possess orthorhombic symmetry.

Titanium and vanadium mononitrides (NaCl-type) were examined within the ranges of composition $TiN_{0.50}$ to $TiN_{1.0}$ and $VN_{0.72}$ to $VN_{0.95}$. In neither case was the presence of long-range order detected. However the hcp heminitride, V_2N, exhibited nitrogen-atom order giving an ε-Fe_2N-type structure.

The NaCl-type monoxides of titanium and vanadium were examined within the ranges of composition $TiO_{0.7}$ to $TiO_{1.25}$ and $VO_{0.70}$ to $VO_{1.35}$. In vanadium monoxide a tetragonal superlattice based on the unit cell composition $V_{244}O_{320}$ was found. The complex structure of this superlattice, which results from vanadium-atom order, contains vanadium atoms in interstitial (tetrahedrally coordinated) positions, surrounded by four vanadium vacancies, as well as helices of vanadium vacancies. Isothermal heat-treatments enabled a partial phase diagram to be constructed showing the conditions for the formation of the $V_{244}O_{320}$ superlattice. Electrical resistivity measurements showed that vanadium monoxide was semiconducting down to liquid-nitrogen temperature.

In titanium monoxide the structures of the two superlattices with compositions $TiO_{1.0}$ and $TiO_{1.25}$ were confirmed. Examination of quenched specimens in the region $TiO_{0.7}$ to $TiO_{0.9}$ showed a metastable ordered domain structure formed by the segregation of oxygen vacancies onto every third (110) plane of the cubic matrix. Specimens with compositions near $TiO_{1.20}$ contained a

small fraction of an orthorhombic superlattice formed by titanium vacancy segregation onto every third (110) plane.

Two further investigations were made which were not directly concerned with superlattice structure. Examination of vanadium and niobium carbides within the nominal hemicarbide and monocarbide two-phase region showed the occurrence of compounds with unit cells based on long repeat sequences in the stacking of close-packed metal-atom planes. In both carbides the ζ-phase, containing twelve planes, and also in niobium carbide the ε-phase, containing nine planes, were found. The accommodation of carbon atoms in the ζ- and ε-phases resulting in possible ordered structures are discussed. Also, the modes of transformation between structures with different stacking sequences are critically examined.

The second investigation was an in situ study in the electron microscope of the effect of electron irradiation on the superlattice $V_{244}O_{320}$. Disordering was observed, resulting from atomic displacements caused by collisions with electrons. The disordering process was found to proceed in two stages. Certain displacements in the $V_{244}O_{320}$ superlattice led to the formation of another superlattice with a smaller unit cell, $V_{52}O_{64}$, but with a structure closely related to that of $V_{244}O_{320}$. Further irradiation then causes the destruction of all long-range order. A value of 7.8ev was found for the vanadium-atom displacement energy, and numerical calculations based on a theoretical model for the disordering process gave good agreement with the observed time for disordering.

Finally, the factors that control the formation of the observed superlattices are discussed. The various structures adopted by the different superlattices are explained in terms of the type of atomic bonding and the electronic structure in these transition-metal compounds.

PUBLICATIONS

Certain parts of the work reported in this thesis have been published in scientific journals, as follows;

(1). "Non-Stoichiometric Vacancy Order in Vanadium Monoxide", P.S.Bell and M.H.Lewis, Phys. Stat. Sol. (a), 7, 431 (1971).

(2). "The Ordered Distribution of Carbon Atoms in Titanium Carbide", P.S.Bell and M.H.Lewis, Phil. Mag., 24, 1249 (1971).

(3). "A Superlattice with Monoclinic Symmetry Based on the Compound V_6C_5", J.Billingham, P.S.Bell and M.H.Lewis, Phil. Mag., 25, 661 (1972).

(4). "Vacancy Short-Range Order in Substoichiometric Transition-Metal Carbides and Nitrides", Part 1, "Electron Diffraction Studies of Short-Range Ordered Compounds", J.Billingham, P.S.Bell and M.H.Lewis, Acta Cryst., Accepted For Publication (1973). (Part 2, "Numerical Calculation of Vacancy Arrangement", M.Sauvage and E.Parthé)

(5). "Non-Stoichiometry in Ceramic Compounds", M.H.Lewis, J.Billingham and P.S.Bell in "Electron Microscopy and Structure of Materials", ed. G.Thomas (University of California Press, Berkeley, 1972). (Proc. 5th. Int. Mater. Symp. University of California, Berkeley, Sept. 1972).

(6). "The Crystal Growth of Transition-Metal Interstitial Compounds by a Floating Zone Technique", J.Billingham, P.S.Bell and M.H.Lewis, J. Cryst. Growth, 13/14, 693 (1972). (Proc. 3rd. Int. Conf. on Crystal Growth, Marseille, July 1971).

CONTENTS

CHAPTER ONE

INTRODUCTION

1.1 Interstitial Compounds

Compounds of transition metals with the elements hydrogen, boron, carbon, nitrogen and oxygen are referred to as interstitial compounds because the small nonmetal atoms are usually situated in the interstices of the metal-atom sublattice. Interest in these compounds arises from their unusual combination of metallic and ceramic properties, viz. good electrical conductivity, hardness and mechanical strength, high melting point and chemical stability.

The factors determining the crystal structures of transition-metal interstitial compounds were originally examined by Hägg (1). An empirical rule governing the structure of these compounds is found from the atomic radius ratio of the metal and nonmetal atoms, r_X/r_M. Simple structures are found when this ratio is less than 0.59, and complex ones for larger values. This critical value in radius ratio does not produce a sharp division in structure types, since atomic radii vary according to coordination and bonding type, but represents the upper limit in a region of overlap.

Interstitial compounds present a wide variety of crystal structures. The research described in this thesis is limited to compounds which fulfil the conditions for a Hägg phase (or which at least show close structural similarities to Hägg phases). These compounds have metal-atom structures which may be described in terms of the sequential stacking of close-packed planes using the familiar notation, ...ABCABC... for face-centred cubic, ...ABABA... for hexagonal close-packed, ...AAA... for

simple hexagonal etc. The interlayer interstices are denoted by the Greek letters α, β, and γ. Thus the octahedral interstices between an A and B layer are γ positions, and the tetrahedral interstices α and β positions. The projections of the A, B and C positions onto the close-packed planes are coincident with the α, β and γ positions respectively.

In fig. 1.1.1 the structures of some common types of Hägg compounds are shown. Complexities may arise from the following:

(1) Periodic combinations of the simple metal-atom stacking sequences may result in structures related to polytypes.

(2) Incomplete occupancy of the interstices in the metal-atom structure provides the possibility for various distributions (either ordered or disordered) of the interstitial atoms.

The research described in this thesis is concerned mainly with a study of these structural variations for a range of Hägg compounds based on the transition-metal elements, titanium, vanadium and niobium. In the following sections a number of important topics are introduced which are relevant to the structural analyses described in the subsequent Chapters. Of particular importance are the structural variations that accompany gross deviations from the stoichiometric ratio of metal and nonmetal atoms. The subject of nonstoichiometry will therefore be introduced in the following section.

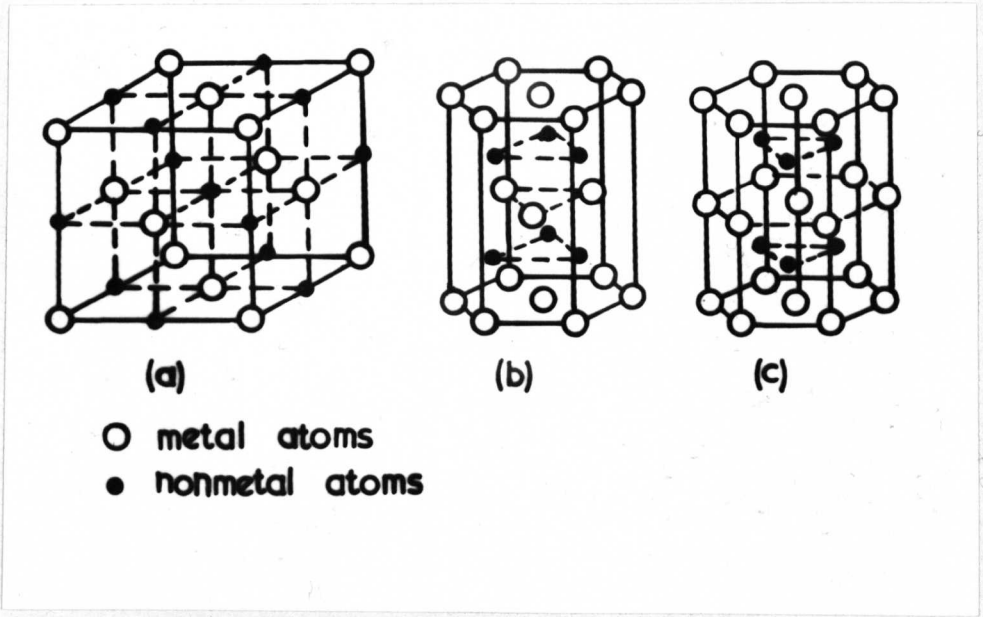

Fig. 1.1.1 Some of the common structure types for interstitial compounds. (a) fcc NaCl-type ...AγBaCβA... (b) hcp NiAs-type ...AγBγAγB... (c) simple hexagonal WC-type ...AγAγA...

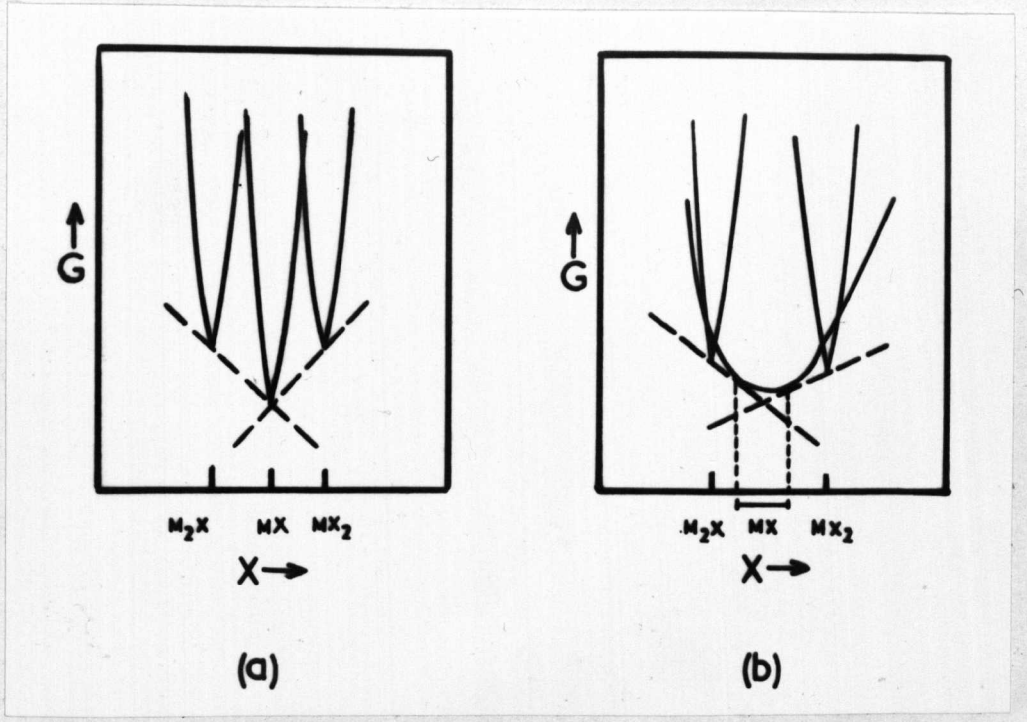

Fig. 1.2.1 Free energy - composition (G - X) curves for (a) stoichiometric and (b) nonstoichiometric MX phase.

1.2 Nonstoichiometry

1.2.1 General principles

The concept of nonstoichiometry provided one of the great philosophic arguments in the history of chemical thought. On the one hand, Dalton's laws of constant and multiple proportions based on the study of simple substances, stated that different species of atoms combined in simple and fixed proportions, while on the other hand, Berthollet suggested that compounds could exist where these rules did not apply. The former argument found favour due mainly to the lack of examples showing deviation from Dalton's laws. However Kurnikow, in his work on metallic compounds, found several phases that existed over a range of composition (nonstoichiometric) which he called 'Berthollides', as opposed to those of fixed composition (stoichiometric) which were called 'Daltonides'.

The work of Schottky and Wagner (2) on the statistical thermodynamics of solid phases showed that the occurrence of a Daltonide was a limiting case, and that all compounds contained a small number of defects at finite temperatures. Although the number of these defects may vary considerably with temperature, a distinction is generally made between compounds where even at high temperatures the concentration of defects is very small (less than 0.1%), and those which show gross variable departures from a stoichiometric ratio. Borderline cases will occur, and furthermore a given compound showing considerable nonstoichiometry at high temperatures may well have a very narrow homogeneity range at low temperatures.

The free energy - composition (G - X) curve for the stoichiometric compound is sharply pointed, and rises very steeply on either side of the integral composition.

The small number of defects present may be of several types, e.g. Schottky (vacancy), Frenkel (vacancy interstitial pair). Their detection is made by special techniques such as electrical resistivity, and optical absorption (for colour centres). The G - X relationship for a nonstoichiometric compound presents a broad shallow curve which may well be asymmetric about the stoichiometric composition (3,4). It follows that the width of the homogeneity range depends on the shape of the G - X curve, since the compositions of coexisting phases are given by the common tangent points for adjacent G - X curves as shown in fig. 1.2.1.

An important factor that determines the extent of nonstoichiometry is the endothermicity of the defects. For a compound which exhibits nonstoichiometry, the energy needed to create defects will be low, and the gain in energy from the extra configurational entropy will be high. For a stoichiometric compound, the energy needed for defect production cannot be counterbalanced.

Above a low concentration the defects present in a solid may no longer be considered to form an ideal solution, and the interaction between defects must be taken into account. The interaction may be attractive, leading to clustering, or repulsive, leading to superstructure ordering. At thermodynamic equilibrium the structure of a solid compound is that which has the lowest free energy. This free energy is determined by two competing processes, minimization of internal energy with a state of perfect order, and maximization of entropy via random order. The first process will dominate at low temperatures, the second at high temperatures. Thus a phase which at high temperatures has a broad homogeneity range with a random arrangement of defects, should at low temperatures form

a series of ordered phases with narrow homogeneity limits. This presupposes the attainment of equilibrium, which in the case of a major rearrangement of defects will be controlled by atomic diffusion. Thus depending on the contribution to the free energy that results from ordering, the high temperature random state may be retained in a metastable condition at low temperatures.

1.2.2 Structural Accommodation of Nonstoichiometry in Crystals

Although Berthollide phases were first found in intermetallic compounds, a large number of nonstoichiometric phases has been found in the compounds of transition metals. These include, hydrides, borides, carbides, nitrides, silicides, phosphides and chalcogenides. Many binary and ternary nonstoichiometric oxides exist. These often have extremely complex structures which can only be satisfactorily visualized as chains, layers, cages, etc. of coordination polyhedra. Nonstoichiometry can be achieved in the following five general ways for a compound MX;

(1) Substitution. An excess number of M atoms can occupy vacated X sites or vice versa.

(2) Interpolation. Sites which are normally vacant are occupied by excess M or X atoms, or by the addition of a third element.

(3) Subtraction. Atoms of M or X (or both in unequal proportions) may be missing from sites normally occupied.

(4) Shear Structures. Vacant sites of M, but more usually X, form planar arrays which collapse by shear, resulting in modified coordination for one type of atom.

(5) Intergrowth. Different overall compositions achieved by a mixture of two related compounds having a coherent interface plane.

1.2.3 Binary interstitial compounds with the NaCl-type structure

Of the five ways in which nonstoichiometry can be introduced into a crystalline solid, that of subtraction is the most important for the compounds of the type described in this thesis.

With a few exceptions the mono- carbides, nitrides and oxides of the Group IVa and Va metals exhibit large homogeneity ranges within the nominal NaCl-type structure. For example, the stoichiometry range of vanadium carbide from $VC_{0.72}$ to $VC_{0.88}$ (5) is achieved by the subtraction of carbon atoms while the vanadium sublattice remains completely occupied. Termination of the phase field before the stoichiometric ($VC_{1.0}$) composition is quite common for these carbides, and vacancies in the metal sublattice do not occur. For the nitrides there is often a limited extension of the homogeneity range above the stoichiometric composition, as well as large substoichiometric deviations. Thus for titanium nitride the homogeneity range is from $TiN_{0.6}$ to $TiN_{1.16}$ (6). Nitrogen excess is achieved by metal-atom vacancies, and even the stoichiometric composition contains a small number of vacant sites on both sublattices (7).

For oxides, compounds in which the metal exhibits its theoretical maximum valency are normally found. This is reflected in monoxides which show large deviations on either side of the stoichiometric composition. In an early investigation by Ehrlich (8), the titanium monoxide phase field was found to extend from $TiO_{0.7}$ to $TiO_{1.25}$. At the metal-rich end the titanium sublattice is fully occupied, while the oxygen sublattice is fully occupied at the oxygen-rich end. At intermediate compositions vacancies

occur in both sublattices, and the stoichiometric composition is better represented by the formula $Ti_{0.85}O_{0.85}$, than by $TiO_{1.0}$.

For a number of the carbides, nitrides and oxides of transition metals, ordered arrangements of nonstoichiometric vacancies have been detected. The major part of the work described in this thesis is concerned with the structure of these ordered distributions. The following section contains a description of order - disorder transformations, and of the physical techniques for the analysis of ordered structures. Particular emphasis is placed on the use of diffraction methods which have been extensively used in this research.

1.3 Order - Disorder Transformations

Development in the theories of order - disorder transformations has been a consequence of the observation of superlattices in metallic alloys. However, most of the principles involved in these theories are applicable to the systems forming the subject of the present investigation. Although in the past diffraction effects have been closely linked with X-ray analysis, the methods developed are general to other diffraction techniques.

1.3.1 Long-range order (LRO)

The occurrence of LRO can be established when there is a difference in the occupancy of two equivalent sublattices of the crystal. It should be pointed out in this respect that Hägg phases consist of metal and nonmetal atoms which are restricted to their own sublattices up to the melting point. Thus all the lattice points of, for example, the NaCl-type structure form a simple cubic lattice, which is subdivided into two equivalent fcc sublattices containing the metal and nonmetal atoms. However, this

process of lattice subdivision may be continued indefinitely, and thus LRO in the present instance will involve a rearrangement of one species of atoms and vacancies on a primary fcc sublattice. Although there are three components, metal and nonmetal atoms, and vacancies, the system may be regarded as binary since the atoms on the fully occupied primary sublattice (usually the metal atoms) play a passive rôle in the ordering process.

The possible degree of LRO depends on composition and temperature. For a binary alloy with atomic (or vacancy and atomic) fractions x_A and x_B, the Bragg - Williams (9) LRO parameter is given by,

$$S = (x_{A\alpha} - x_{A\beta}) = (x_{B\beta} - x_{B\alpha})$$

where $x_{A\alpha}$ etc. is the number of A atoms on correct (α) sites. When the atomic fractions correspond to the stoichiometric composition of the superlattice, S has a maximum value of unity for perfect order, and is zero for random order. For off-stoichiometric fractions, S must always be less than unity. In the original Bragg - Williams theory the energy needed to accomplish the interchange $A\alpha \rightarrow A\beta$ (disordering energy per atom) was assumed to be directly proportional to S, and thence the degree of LRO was found to decrease continuously at an accelerating rate with increasing temperature, reaching a value of zero at the critical temperature T_c.

There are several techniques for detecting LRO such as changes in specific heat, electrical conductivity, and differential thermal analysis. However the structure determination of a superlattice is invariably made by one of three methods, X-ray, neutron, or electron diffraction. The extra lattice periodicities introduced into a crystal

as the result of LRO give rise to extra (superlattice) reflections besides those already present (fundamental) characteristic of the disordered state. The structure factor for a reflection hkl can be written in the general form,

$$F_{(hkl)} = \sum f_{(\theta)} \exp 2\pi i(hu + kv + lw)$$

where the summation is taken over all atoms in the unit cell with coordinates u,v,w. $f_{(\theta)}$ is the scattering power of each atom for the particular type of incident radiation. The intensity of fundamental reflections is not usually influenced by ordering, while the superlattice reflection intensities will depend on the degree of order such that,

$$I \propto (FS)^2$$

An arbitrary degree of LRO may be determined by diffraction measurements only for a binary alloy. The number of order parameters not accessible by diffraction alone is given by $(n-2)(c-1)$, where n is the number of atomic species, and c the number of sublattices describing the structure. For higher-order systems it may be possible that for some fortuitous combination of scattering factors and degree of order, no superlattice reflections are observed despite the presence of LRO.

1.3.2 Short-range order (SRO)

While LRO is defined in terms of sublattice occupation, SRO considers an atom and its neighbours with regard to the formation of energetically favourable and unfavourable pairs. This idea, originally proposed by Bethe (10), considered only nearest-neighbour pairs, but has since been extended to longer range interactions.

The most convenient description of the state of SRO is given by the set of Warren SRO coefficients a_{lmn} (11), thus,

$$a_{lmn} = \frac{P^{AB}_{lim} - P^{AB}_{lmn}}{x_B}$$

The integers l,m,n define a particular lattice site according to the relation,

$$R_{lmn} = l\frac{a_1}{2} + m\frac{a_2}{2} + n\frac{a_3}{2}$$

where a_1, a_2 and a_3 are the translation vectors of the (cubic) unit cell. P^{AB}_{lmn} is the probability of finding a B atom as an (lmn) neighbour of an A atom. P^{AB}_{lim} is the limiting value of the probability for large R, and can usually be taken as equal to x_B. Only for a binary alloy is there one independent set of atom position probabilities. For a state of perfect LRO, the SRO coefficients attain maximum positive or negative values. However when there is no overall LRO, the degree of SRO may be quite high, but will decrease as the temperature is raised above T_c.

An alternative viewpoint considers the SRO state to be achieved by a successive division of the LRO state by antiphase boundaries. When the ordered domains are sufficiently small, the sharp LRO diffraction peaks can be broadened such that the resulting intensity has a diffuse appearance (characteristic of SRO), although the total intensity of the diffuse scattering will be the same as for the LRO superlattice reflections, since the amount of disorder introduced at the antiphase boundaries is very small. This model implies fluctuations in the degree of SRO between neighbouring domains, while in the statistical Warren approach an average degree of SRO extending over the

whole crystal is implied.

The detection of SRO is more difficult than LRO. While nuclear magnetic resonance (NMR) techniques (12) may give some additional information on the atomic configurations, diffraction methods have proved most useful. SRO is one of several phenomena that produce diffuse scattering. Others, such as atomic-size effects, clustering, particle-size and antiphase boundary broadening, are relevant to order - disorder transformations in alloys, and in any quantitative study the intensity produced by these different effects must be separated. For a binary alloy AB the SRO intensity is directly related to the coefficients a_{lmn} in,

$$I_{SRO} = Nx_A x_B (f_A - f_B)^2 \sum_{l,m,n} a_{lmn} \exp 2\pi i (2h_1 l + 2h_2 m + 2h_3 n)$$

N is the number of atoms irradiated, and f_A and f_B are the atomic scattering factors. The h's are continuous coordinates in reciprocal space equal to one-half the usual Miller indices at the reciprocal lattice points. The term before the summation is the Laue monotonic scattering which is present even when there is complete disorder. The a_{lmn}'s usually converge to zero after about the 10^{th} coordination shell. It is often found that the SRO intensity is centred about the positions where the LRO superlattice reflections would exist, suggesting that the preferred SRO configuration is similar to that in the LRO state.

For SRO a_{100} is negative. However, the theory is equally applicable to the clustering of similar atoms, where a_{100} is positive. Both effects give similar diffuse scattering, and a distinction between these two possibilities is not always easy due to the presence of size-effect diffuse scattering. This latter scattering is caused by static displacements from the exact lattice positions when the component atoms have different sizes.

1.3.3 Nucleation and propagation of LRO

Order-disorder transformations are usually first- or second-order reactions. The first-order reaction is characterized by a discontinuous jump in the degree of LRO to zero at the critical temperature T_c. There will also be a two-phase region where ordered and disordered parts with different compositions will coexist. For a second-order reaction there is no two-phase region, and the ordered structure may show a considerable range of composition. Raising the temperature of the ordered phase results in a continuous decrease in the degree of LRO to zero at T_c.

There are two general processes for the formation of the ordered structure from the disordered matrix.

(1) Nucleation and growth is the typical mechanism for a first-order reaction. Discrete ordered domains may nucleate either homogeneously in the disordered matrix, or heterogeneously at crystal imperfections such as grain boundaries or dislocations. Further growth of the ordered regions is controlled by long-range diffusion if the ordered phase has a different composition from the matrix, or by advancement of the domain - matrix interface when the two phases have the same composition. When adjacent domains impinge, various types of boundary may result. If the unit cell axes of the ordered structure in the adjacent domains are similarly directed, then an antiphase boundary will result when the ordering of each domain was initiated on a different sublattice. In other instances various types of twin-related boundary may form. In these latter examples there is a displacement of the atom positions across the boundary, compared to the pure translation characteristic of domains in antiphase-relation.

(2) Continuous ordering, typical of a second-order reaction, may be described as the homogeneous development of order throughout the matrix, where no discrete nucleation site can be identified. As the transformation proceeds, the increase in the overall degree of long-range order will eventually lead to the formation of ordered domains separated by antiphase boundaries.

1.4 Aims Of The Present Work

On account of their unusual physical properties, the carbides, nitrides and oxides of transition metals are potentially useful materials. Although these compounds are based on simple crystal structures, the explanation of these properties in terms of fundamental physical concepts is incompletely understood. A particular feature of these compounds is the tendency to show large variations in composition, and yet to retain the same structure. The introduction of nonstoichiometry via the subtraction of atoms from lattice sites should, however, lead to the formation of ordered phases at sufficiently low temperatures.

The main objectives of the present work are therefore to examine the structures of these ordered phases and the factors that control their formation. There are two reasons which have prevented the previous observation of these ordered phases. The first lay in the inability to prepare suitable specimens. This was a matter of obtaining the pure components, followed by solid-state reaction at high temperatures, or melting under an inert atmosphere. The second factor lay in the techniques that were available for structure analysis. Detection of the superlattice reflections by X-ray diffraction was not usually possible for an ordered structure that resulted from a rearrangement of weakly scattering light atoms.

Apart from the obvious facility of direct observation of the ordering process, the greater scattering power of light atoms for electrons than X-rays, makes the use of electron microscopy combined with selected area diffraction invaluable for the study of these materials. The techniques used for the preparation of crystalline specimens and the methods of structure analysis by electron microscopy and diffraction are described in Chapter 2.

In the specific field of vacancy order in non-stoichiometric refractory compounds, there have been several reports of ordered phase formation, and where relevant, these have been reviewed at the beginning of each Chapter. Carbides based on fcc (TiC, NbC), hcp (V_2C, Nb_2C), and mixed sequences of fcc and hcp metal-atom stacking (VC, NbC) are examined in Chapters 3, 4 and 5 respectively. Chapter 6 describes the work on nitrides (VN, TiN), while the two oxides, VO and TiO, are studied in Chapter 7. A further study on vanadium oxide, involving radiation damage in the electron microscope, is presented in Chapter 8. In Chapter 9 the factors which influence the formation of the various vacancy distributions are discussed collectively.

REFERENCES

1. G.Hägg, Z. Phys. Chem., B6, 221 (1930); B12, 33 (1931).
2. W.Schottky and C.Wagner, Z. Phys. Chem., B11, 163(1930).
3. R.F.Brebrick in "Progress in Solid State Chemistry", Vol. 3, ed. H.Reiss (Pergamon, New York, 1967).
4. F.A.Kröger, Phys. Chem. Solids, 29, 1889 (1968).
5. E.Rudy, St.Windisch and C.E.Brukl, Planseeber. Pulvermet., 16, 3 (1968).
6. A.Brager, Acta Physiochim. URSS., 11, 617 (1939).
7. P.Ehrlich, Z. Anorg. Allg. Chem., 259, 1 (1949).
8. P.Ehrlich, Z. Anorg. Allg. Chem., 247, 53 (1941).
9. W.L.Bragg and E.J.Williams, Proc. Roy. Soc., A145, 699 (1934).
10. H.A.Bethe, Proc. Roy. Soc., A150, 552 (1935).
11. J.M.Cowley, Phys. Rev., 77, 699 (1950); J. Appl. Phys., 21, 24 (1950).
12. C.Froidevaux and D.Rossier, Phys. Chem. Solids, 28, 1197 (1967).

CHAPTER TWO

EXPERIMENTAL METHODS

2.1 Crystal Preparation

The various stages of crystalline perfection towards the homogeneous, defect- and strain-free single crystal are attained with increasing degrees of difficulty, and a compromise is usually made to suit the requirements of the particular investigation. For transmission electron microscopy an electron transparent area of crystal is required. The type of specimen from which such a thin area is to be obtained will often be determined by some other requirement, e.g. from a post-mechanical test specimen, and also on the methods of thinning available and the desired size of the thin area. For a study of crystal structure by electron microscopy using the fragmentation method for specimen preparation (described in section 2.2.1), the initial material need only have a low degree of perfection.

The most important factors that restrict the method of crystal growth for a material are, reactivity towards container and atmosphere, and stability towards thermal decomposition. The form of the available starting material, and the desire for close control over composition may also influence the method used. In the following sections the potential methods that may be used for crystal growth are listed, and those methods selected for the present study are noted.

2.1.1 Possible methods of crystal growth

(i) Growth from the vapour

In chemical transport crystals are produced by the thermal decomposition of a volatile compound onto a substrate. The number of compounds that may be grown by this method is limited by the availability of a suitable carrier gas. However a large number of vanadium oxides with compositions between V_2O_3 and VO_2 have been grown using $TeCl_4$ (1,2), and titanium carbide has been grown using $TiCl_4$, methane and hydrogen (3). Usually the rate of growth is low, and only small single crystals can be obtained.

Direct vaporization of elemental constituents under vacuum onto a substrate to produce thin crystalline films has been used for niobium carbide (4). However, considerable caution must be used to avoid contamination by residual gases in the vacuum system.

(ii) Growth from solution

In solution growth crystals are precipitated (at temperatures below their melting points) from a supersaturated solution, produced by slow cooling or flux evaporation. The use of this method is restricted by the availability of fluxes with a very low solid-solubility in the precipitated crystals. There is also very little control over the composition of nonstoichiometric materials.

(iii) Growth from the solid

Large grain-sized rods, and in some cases single crystals of transition-metal carbides, have been produced by the high temperature strain annealing method developed by Fleischer and Tobin (5). It is claimed that this method can give crystals free from macroscopic defects (cracks, pores, etc.), and virtually free from microscopic defects (dislocations etc.). Its wider application is limited to materials where suitable rods for initial straining can be produced.

Another method of growth from the solid is by sintering in powder form component elements (or suitable compounds of the elements) at high temperatures. Although the resulting material is often porous and polycrystalline, this method is rapid and may be applied to any material which has reasonable stability below its melting point, and where component powders may be obtained in a finely divided and pure form. This method has been used for a number of compounds in the present work, and is described in greater detail in section 2.1.5.

(iv) Growth from the melt

This is the most widely used method for growing large single crystals, and a number of techniques have been devised for different materials. These may be subdivided according to, the method of containing the molten material, the heat source, and the environmental conditions during growth. The floating zone technique is a crucible-free method, and is used where high purity single crystals are required. Several transition-metal borides and carbides have been grown by this method using high frequency (HF) induction heating and a high pressure of inert gas to reduce vaporization (6-8).

There is also a number of possible methods for crystal growth where the molten material is contained in a crucible, such as the Bridgeman and Czochralski techniques. Of particular interest are cold crucible methods where the material is held, without contamination, on a water cooled hearth usually made from copper. A cold crucible Czochralski method employing arc melting has been used for obtaining single crystals of several high melting point compounds (9).

The Verneuil or flame fusion process is suitable for non-reactive compounds such as Al_2O_3, but control over

composition is difficult for nonstoichiometric compounds. However, some transition-metal carbides have been grown by this method (10).

Since suitable refractory crucibles for containing these particular types of high melting point compounds are unavailable, the floating zone technique, and melting in a water-cooled copper boat have presently been used.

2.1.2 Starting materials

Details of the powders used for the preparation of specimens are given in Table 2.1. The purest commercially available powders were used. High purity vanadium metal is particularly difficult to obtain, and unless sealed in an airtight container the powder is rapidly contaminated.

A particular feature during sintering was the large amount of degassing from loose powders, and thus in those samples prepared from pressed rods, gas adsorbed on the surface or trapped between the powder particles may not be completely removed. However, during high temperature preparation, volatile impurities will be removed, and the refining effect of the floating zone method may in some cases result in improved purity.

TABLE 2.1

Starting Materials

element or compound	powder size μm	purity percent	source
Ti	100	99.5	(a)
V	<10	99.2	(b)
Nb	<30	99.9	(a)
C		99.999	(a)
VC	<100	99.8	(b)
TiN	<80	99.9	(c)
VN	<80	99.1	(c)
TiO_2	1	99.5	(a)
V_2O_5		99.99	(b)

(a) Koch Light

(b) New Metals and Chemicals

(c) Materials Research Corporation

2.1.3 Vertical floating zone technique

This method was used for the growth of vanadium monoxide and the vanadium heminitride (V_2N) - vanadium mononitride eutectic, as well as the attempted growth of titanium nitride. Although the objective of this method to produce single crystals was unsuccessful, polycrystalline specimens of the vanadium compounds were produced.

Sintered rods of the three compounds having different X/M ratios were prepared from powder mixtures of the respective metal with, vanadium sesquioxide (V_2O_3, prepared by reducing V_2O_5 in hydrogen at 500°C), vanadium nitride ($VN_{1.0}$), and titanium nitride ($TiN_{1.0}$). The blended powders were packed into rubber tubes (10-15mm diameter, approximately 150mm length) and sealed with a rubber cap. Room temperature hydrostatic pressing to 50 tons psi was carried out at the BSA Group Research Centre, Birmingham. Since only straight rods would be of use, additional rigidity was given to the rubber tubes by wire-mesh cages.

For the two nitrides the addition of 2 wt. % of paraffin wax binder was necessary in order to facilitate pressing. For vanadium monoxide, good pressing was obtained without the use of a binder, due to the more granular nature of the V_2O_3 after reduction.

The nitrides were dewaxed and sintered in vacuum at 500°C and 1500°C respectively. For the growth of vanadium monoxide it was found that the formation of a molten zone could only be achieved if the starting rod had a high density. This required prolonged sintering (about 50h) at 1500°C in an alumina-tube vacuum furnace. Higher temperatures obtainable with an HF induction furnace could not be used, since the rods were very sensitive to thermal shock, which occurred with this method. Even when the pressed

vanadium monoxide rods were slowly heated and cooled in the alumina tube furnace, they were often badly bent and frequently broken, thus considerably reducing the number of suitable rods obtained from a given amount of the initial starting powders.

The crystal growth apparatus has been previously described by Billingham et al. (11), and is shown schematically in fig. 2.1.1. The main feature is the provision for the growth of crystals in ambient gas pressures of up to 20 atmospheres. The top of the specimen is attached to a graphite holder by a tantalum pin, and the graphite holder is attached to a stainless steel holder by another pin, this latter holder being screwed into the upper pull-rod. The bottom of the specimen rests without pinning in a similar series of holders. Several designs of HF heating coil were tried, and finally a three-turn coplanar arrangement was found to give best results for all materials.

(i) Vanadium monoxide

The occurrence of cracked and low density starting rods made the formation of an initial molten zone difficult. As the rod was heated, the centre shrank inwards leaving a cracked outer skin which was considerably cooler than the inner region. Increasing the power caused melting of the inner region which would then suddenly overrun through a crack in the outer skin. This problem was more serious for the high oxygen-content samples, since these contained a relatively greater amount of the low density V_2O_3. However, after initial melting of the centre portion, the power was held constant and a complete molten zone formed after about thirty minutes.

The crystals were grown by passing the zone in an upwards direction at 10mm/h under 15 atmospheres of helium. Crystal compositions were varied from $VO_{0.70}$ to $VO_{1.35}$ in steps of 0.05 in the O/V ratio, although in some

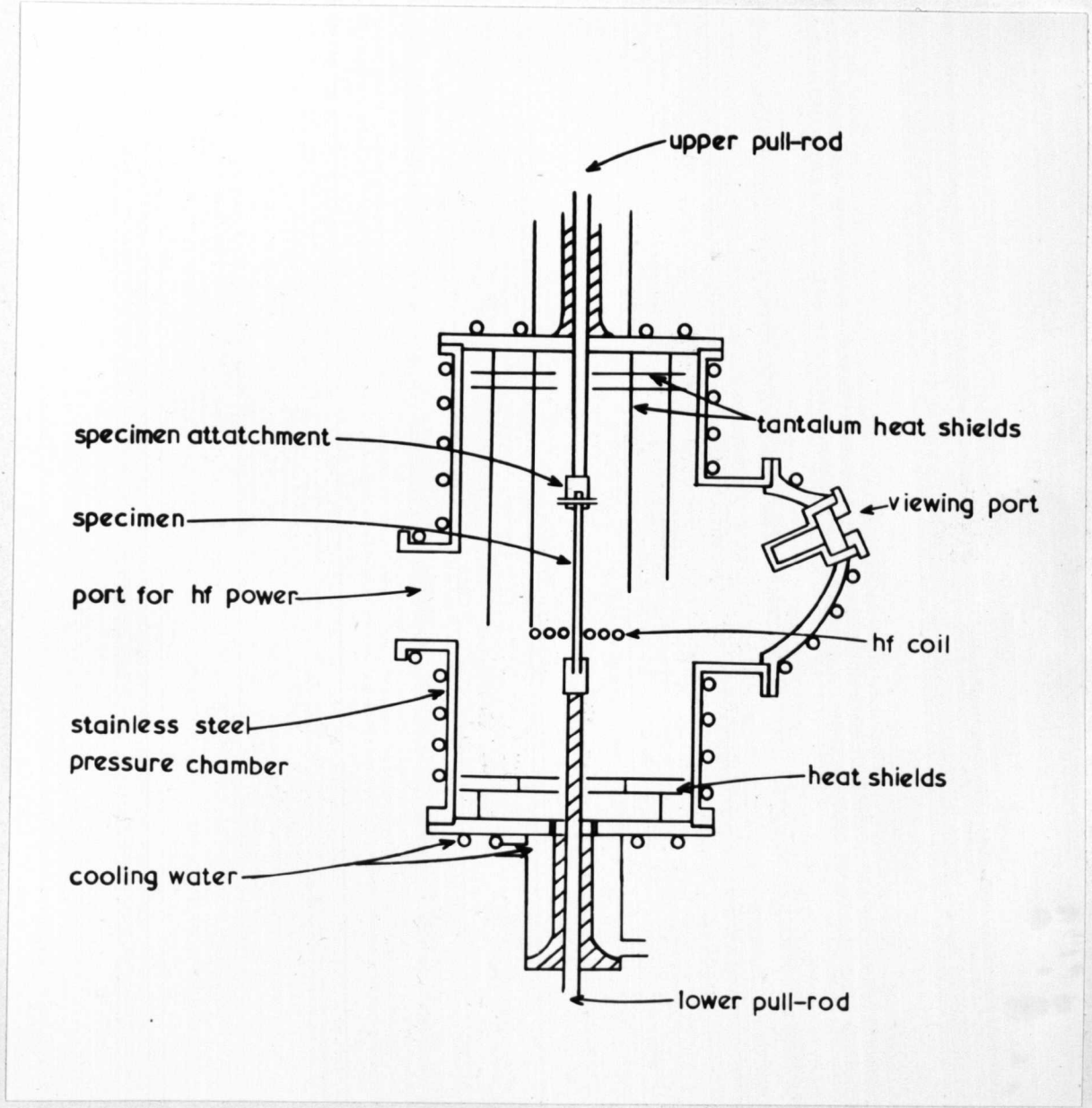

Fig. 2.1.1 Schematic diagram of the vertical floating zone crystal growth apparatus.

cases only short lengths of crystal were traversed before a terminating overrun occurred. The grain-size was found to increase with the O/V ratio, however those crystals with compositions above the oxygen-rich phase boundary were slightly cracked.

(ii) Vanadium nitride

Although the growth of vanadium nitride had not been attempted prior to this present work, the available thermodynamic data (12,13) suggested that there would be a large equilibrium nitrogen pressure. Since the melting temperature increases with the N/V ratio, it was expected that the equilibrium nitrogen pressure would increase extremely rapidly at the melting points of the higher nitrogen-content specimens.

The crystals were grown under the same conditions as vanadium monoxide, except that mixtures of helium and nitrogen, totalling 15 atmospheres, were used. The maximum nitrogen partial pressure was limited to 10 atmospheres. Above this pressure there was severe arcing between the coil and specimen, and excessive heating of the chamber walls. The final composition of the crystals depended on the nitrogen pressure, and was independent of the initial rod composition (within the range $VN_{0.6}$ to $VN_{1.0}$). For 0-2 atmospheres of nitrogen, the crystals consisted of the hexagonal V_2N-phase with a large fraction of needle-shaped precipitates of the primary vanadium - nitrogen solid solution (fig. 2.1.2). For 2-10 atmospheres of nitrogen, coarse-grained crystals of a eutectic between V_2N and cubic vanadium nitride were obtained (see fig. 6.3.1 and section 6.3.1 for further discussion of the V_2N/VN eutectic). In this latter case a rim of the single-phase mononitride formed on the surface due to further reaction with the nitrogen atmosphere as the sample slowly cooled behind the

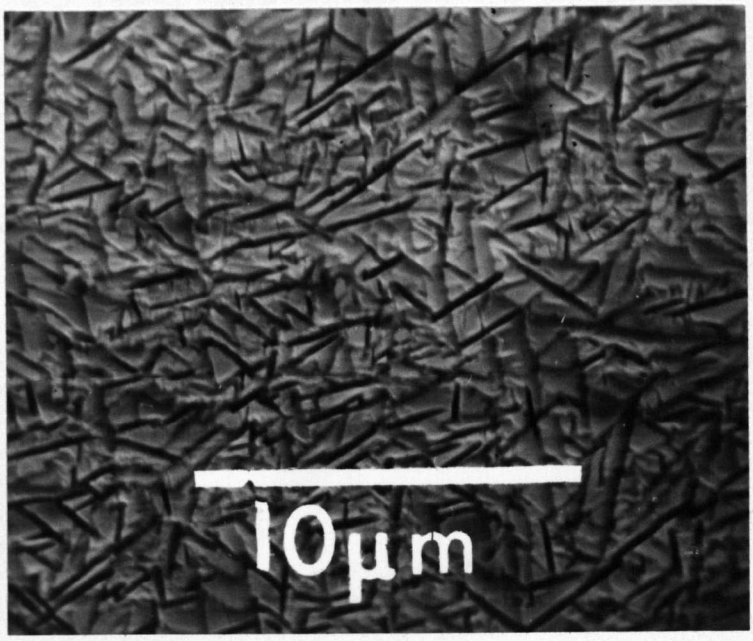

Fig. 2.1.2 Two-phase microstructure consisting of precipitates of the primary vanadium - nitrogen solid solution in a matrix of vanadium heminitride (V_2N). (Scanning electron micrograph)

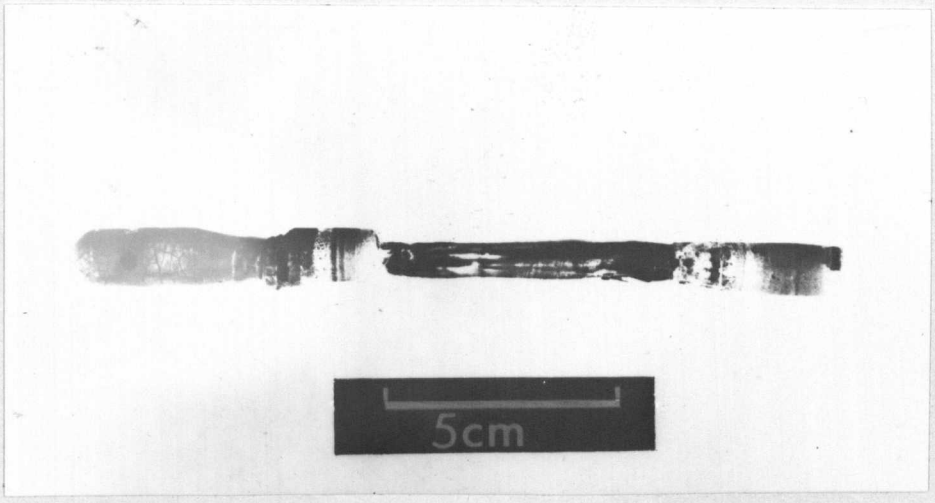

Fig. 2.1.3 Eutectic (V_2N/VN) crystal grown by the vertical floating zone technique.

molten zone. One such crystal is shown in fig. 2.1.3.

(iii) Titanium nitride

The reported arc melting of titanium nitride (of uncertain composition) under 3 atmospheres of nitrogen (14), served as an approximate guide to the nitrogen partial pressures that would be required to produce the cubic mononitride (in this case considerably less than for vanadium mononitride). However, when the rods were heated near their melting point they expanded considerably and became porous, and then could not be melted due to the resultant loss of power-coupling with the HF coil. After attempted melting the specimens contained many small cube-shaped crystallites. Local changes in composition were also observed as regions of different colour, i.e. silvery white, low nitrogen, to golden yellow, high nitrogen. None of the sample rods with N/Ti ratios from 0.4 to 1.0 could be melted by this method.

2.1.4 Horizontal Zone Technique

A water-cooled copper boat was used for preparing titanium nitride, and additional samples of vanadium monoxide. This method of melting was developed by Stirling (15). Both the high frequency primary current in the work coil, and the secondary induced current in the boat, induce currents in the same direction in the specimen. Although the exact nature of the melt - boat interface is uncertain, it is probable that a few points of the specimen remain solid and in contact with the boat, while the rest of the specimen is levitated a small distance off the surface of the boat. Titanium (3), and niobium (16) carbides have been melted by this method at 3020°C and 3600°C respectively. Powder mixtures could not be melted in the boat, and the starting materials consisted of pieces of pressed and sintered rod.

Two sizes of boat were made. The first larger boat was used for vanadium monoxide, while the second boat with a smaller HF coil-to-sample separation (giving a greater heating effect) was used for titanium nitride. The boats were constructed from standard 1" and 3/4" Yorkshire copper tube. A depression to hold the specimens was made by pressing a cylindrical steel tool, of approximately the same size as the specimen to be melted, onto the surface of the tube to a depth such that the axis of the tool coincided with that of the tube. Fig. 2.1.4 is a schematic diagram showing the complete assembly. A closely fitting silica tube surrounds the boat and fits into "O" ring seals in the brass end-caps, which have further seals onto the copper tube. The boat is attached to a sliding carriage which can be traversed by means of a lead screw driven by a variable-speed motor. A small overpressure of helium was used for vanadium monoxide, while titanium nitride was heated in mixtures of helium and nitrogen.

(i) Vanadium monoxide

When the whole sample was melted simultaneously a small hole running down the centre of the ingot was left, due to solidification proceeding inwards from the surface. Traversing the sample with a horizontal molten zone overcame this problem as the solidification front was then nearly vertical. There was a pinch effect on the melt which caused it to be pushed away from the centre of the coil, thus increasing the cross-section of the solidified portion.

Small adjustments to the final composition could be made by using pieces of starting material with different compositions. The samples were homogenized by melting four times. After each melt the ingot was broken up and the pieces redistributed in the boat before remelting. The resulting material was always polycrystalline, although

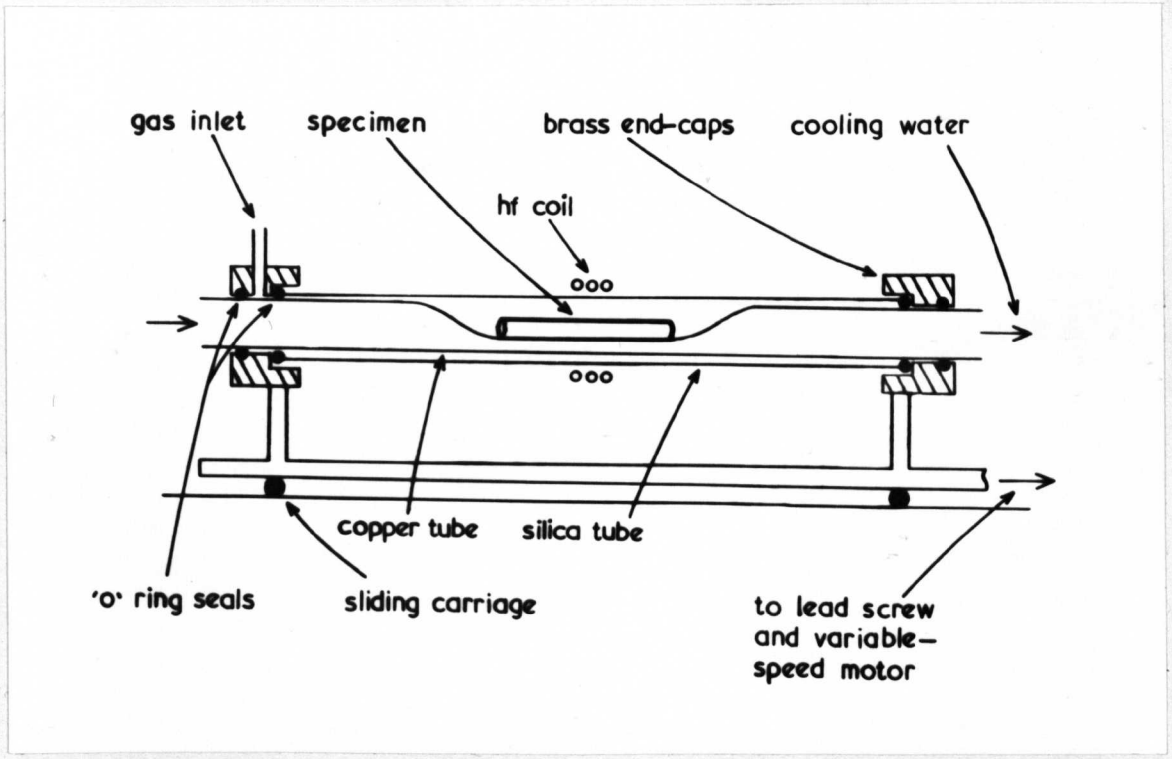

Fig. 2.1.4 Schematic diagram of the horizontal zone melting copper boat apparatus.

the oxygen-rich specimens contained grains several millimetres in dimension. The zone was traversed rapidly (20cm/h) in order to reduce vaporization, since slower speeds gave no increase in the grain-size.

(ii) Titanium nitride

One advantadge of the horizontal boat technique is that the run can be continued even if the specimen cracks due to thermal shock during initial heating. By switching-on to full power from the HF generator, heating rates of up to 500°C/s could be obtained. It was thought that by using this facility the problems associated with the growth of titanium nitride by the vertical zone method might be over-come. However, only melting at the centre of the rods occurred, and usually a large number of small crystallites formed on the surface of the rods, probably from material which vaporized inside the rod and condensed on the slightly cooler surface.

2.1.5 Solid State Sintering

Titanium and vanadium carbides, and titanium monoxide could be satisfactorily prepared by sintering in a thoria crucible. For niobium carbide, an initial sintering in a thoria crucible was followed by reaction at over 3000°C under 15 atmospheres of helium.

Appropriate mixtures of the powders were packed into thoria crucibles 15mm high and 10mm wide. The thoria crucible was contained inside a graphite susceptor positioned at the centre of the HF heating coil. The susceptor fitted onto a larger graphite block (below the HF coil) which then rested on a water-cooled copper collar. The vacuum chamber, enclosed by a water-cooled baseplate and jacket, was evacua-ted by a liquid-nitrogen-trapped oil diffusion pump backed by a rotary pump.

The samples were initially heated very slowly to ensure complete degassing. This usually required holding at a few hundred degrees for up to three hours. The temperature could then be rapidly raised, and when the sintering was complete, quenching was effected by switching-off the HF power.

Up to 2000°C there was a negligible weight-loss from the sample and thoria crucible. The samples shrank away from the crucible walls, and thus contamination was low. During high temperature operation the pressure furthest from the pumping source was always less than $2X10^{-5}$ torr.

Above 2400°C considerable evaporation of the thoria crucible occurred, and since temperatures in excess of 2500°C were known to be required for the hot-press sintering of niobium carbide (17), a slightly different procedure was adopted for this material. An initial sintering at 1200°C in the thoria crucible provided a plug which was sufficiently strong to be self-supporting. This plug was transferred onto a graphite pedestal inside the high pressure crystal growth chamber, and sintered at a temperature in excess of 3200°C (as evidenced by the partial melting of the specimen with composition $NbC_{0.5}$). A pressure of 15 atmospheres of helium was used, which had been previously gettered by titanium powder at 1000°C.

2.2 Electron Microscopy and Diffraction

All micrographs and diffraction patterns shown in the succeeding Chapters were obtained using a JEM 200 electron microscope, operating at 200kev. Use was also made of the lower accelerating voltages (from 100kev in 25kev steps) for the electron irradiation studies on vanadium monoxide. Thin specimens were mounted in a $\pm 30^{\circ}$ tilting stage. 8μm objective apertures were needed to select closely spaced diffraction spots for dark-field microscopy, and 10μm size selected-area apertures to record diffraction patterns from small regions of crystal.

2.2.1 Specimen Preparation

Prior to obtaining thin sections for electron misroscopy, the crystals were given various heat-treatments. For those microscope specimens prepared by electrochemical thinning (vanadium monoxide and vanadium nitride), 3mm X 0.5mm discs were obtained. Vanadium monoxide was sliced using an annular diamond saw, while for the harder vanadium nitride, slices were prepared by spark erosion. Discs were spark-cut from these slices and heat-treated in a silica-tube vacuum furnace. A small amount of the powdered parent metal was also included in the furnace tube to reduce contamination by gettering residual furnace gases.

The large surface area of the specimens prepared by sintering made them very susceptible to contamination. These were heat-treated in evacuated and sealed silica tubes. Again a small amount of metal powder was added and, after sealing, this was heated in a flame to remove any residual gas.

Thin sections of vanadium monoxide and vanadium nitride were prepared by electrochemical thinning using a standard PTFE holder arrangement. The electrolyte used was a 10 vol.% solution of perchloric acid in methanol, cooled

with liquid nitrogen. The cell was operated at about 13 volts.

The fragmentation technique for producing thin areas was found to be particularly simple for the brittle compounds studied in this work. A brief account of this method will be given. A small crystallite, about 1mm in size, was gently ground in a mortar by a rolling action of the pestle. The residue was tapped-out in a stream onto a glass microscope slide. A 100 mesh copper grid, which had been previously coated in a solution of 'sellotape' adhesive dissolved in chloroform, was pressed onto the finest fragments. The grid was inverted and placed in the microscope specimen holder. The grid squares were then systematically examined, and the position of those containing thin areas noted for subsequent investigation.

2.2.2 Electron Diffraction

When a beam of high energy electrons with wavelength λ interacts with a thin foil of crystalline material, part of this beam is directly transmitted, and, if the foil is suitably orientated, a number of diffracted beams are produced. The observation of the diffracted beams may be explained by the Ewald sphere construction (fig. 2.2.1). One point on the circumference of this sphere (radius $1/\lambda$, 39.87Å^{-1} for 200kev electrons), is fixed to the origin of the reciprocal lattice, and represents the position of the transmitted beam. Diffracted beams are then observed when this sphere intersects reciprocal lattice points. As the latter are elongated in a direction perpendicular to the specimen plane, and as the radius of the Ewald sphere is very large compared with the distance between the reciprocal lattice points, the observed diffraction pattern will then approximate to a planar section through the reciprocal lattice. Different reciprocal lattice sections

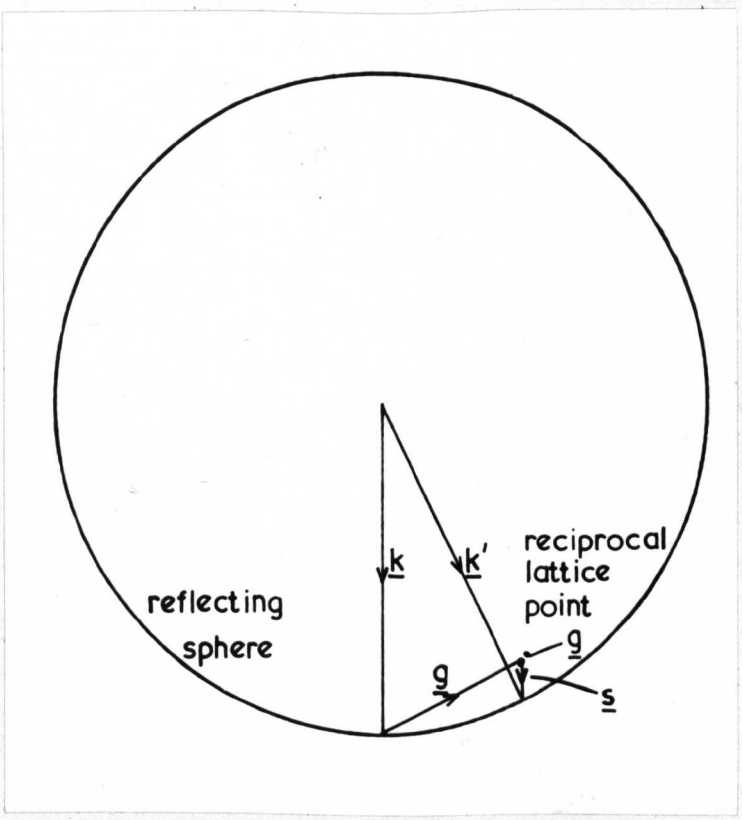

Fig. 2.2.1 The Ewald sphere construction, showing the relationship between the direct beam with wave vector $\underline{k}$, and the diffracted beam with wave vector $\underline{k}' = \underline{k} + \underline{g} + \underline{s}$.

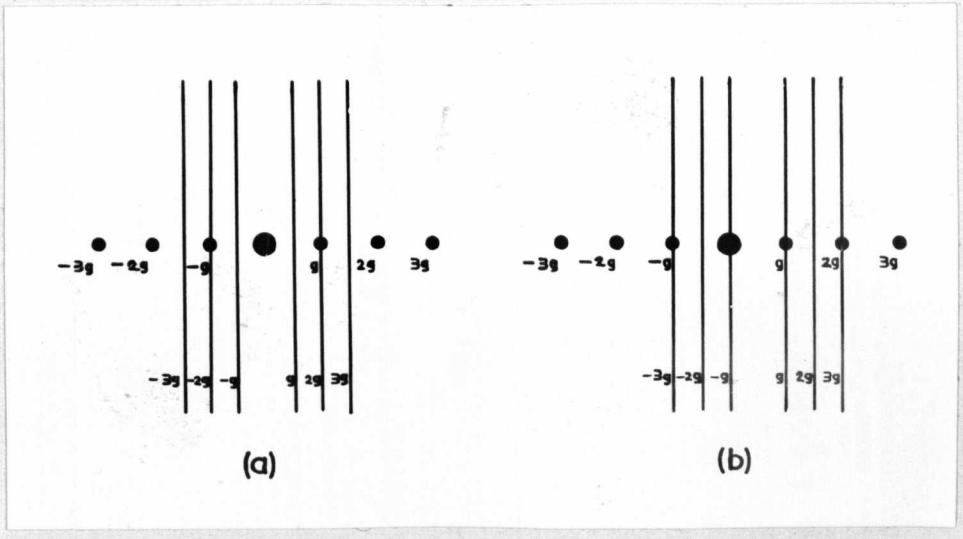

Fig. 2.2.2 The relationship between diffraction spots and Kikuchi lines. In (a) at the symmetric position the value of s for the +g and -g reflections is $-|g|^2\lambda/2$. In (b) the value of s for +g reflection is zero. By convention the sign of s is positive when the reciprocal lattice point lies inside the reflecting sphere.

may be obtained by tilting the specimen, thus enabling a three-dimensional model of the reciprocal lattice to be constructed.

A particularly important technique used in this research work is that of selected area diffraction. Within a single crystal of the disordered structure it is often found that ordered domains may form in a number of equivalent orientations. Using conventional X-ray techniques reflections contributed from all orientations will be recorded, while by selected area diffraction, the reflections from a single orientation may be obtained down to domain sizes of about $1\mu m^2$.

2.2.3 Image Formation in the Electron Microscope

Although the theoretical details of image formation in the electron microscope are outside the scope of this present work, a brief resumé is necessary since most of the results presented in the following Chapters have been obtained by the exclusive use of this technique. This account will also serve as a useful means of introducing the notations used in electron diffraction.

The two-beam dynamical theory developed by Howie and Whelan (18) is the starting point for most discussions of contrast effects. The amplitudes ϕ_o and ϕ_g of the transmitted and diffracted waves associated with reciprocal lattice vector g at a depth z in the crystal are given by,

$$\frac{d\phi_o}{dz} = \frac{\pi i}{\xi_o}\phi_o + \frac{\pi i}{\xi_g}\phi_g \exp(2\pi i s z)$$

$$\frac{d\phi_g}{dz} = \frac{\pi i}{\xi_o}\phi_g + \frac{\pi i}{\xi_g}\phi_o \exp(-2\pi i s z)$$

These amplitudes result from a continuous series of scattering events between the incident wave, with wave vector k, and the

diffracted wave, with wave vector $\mathbf{k} + \mathbf{g} + \mathbf{s}$, where $\mathbf{s}$ is a small vector representing the deviation from the exact Bragg reflecting position. The quantities ξ_o and ξ_g are known as the extinction distances for scattering in the foreward and diffracted directions respectively, and are given by,

$$\xi_o = \frac{\pi V_c \cos\theta}{\lambda F_o} \qquad \text{and} \qquad \xi_g = \frac{\pi V_c \cos\theta}{\lambda F_g}$$

where θ is the Bragg angle and V_c the unit cell volume. F_o is the structure factor for foreward scattering, and depends on the electron scattering power of the atoms in the unit cell at zero angle, f_o. F_g is the structure factor for scattering through the Bragg angle, and depends on the position as well as the type of atom in the unit cell, and their electron scattering power, f_θ.

It is found that two independent solutions exist for both ϕ_o and ϕ_g in terms of two Bloch waves. Contrast effects arise from the beating between these waves as they have slightly different wavelengths, because one wave (by convention Bloch wave (1)) is excited between the atom positions, while wave (2) is excited near the atom positions. Different positions for the maxima of the two waves in the crystal lead to the anomalous absorption effect, where wave (2) is more strongly scattered outside the objective aperture than wave (1). In the phenomenological treatment, this greater attenuation of wave (2) is taken into account by making a simple modification to the extinction distances, i.e. $1/\xi_o$ and $1/\xi_g$ are replaced by,

$$\frac{1}{\xi_o} + \frac{i}{\xi'_o}, \quad \text{and} \quad \frac{1}{\xi_g} + \frac{i}{\xi'_g}, \quad \text{where} \quad \frac{\xi'_o}{\xi_o} \approx \frac{\xi'_g}{\xi_g}$$

The values of this ratio for the real to complex parts of the extinction distances (the absorption length) vary from about 8 to 100 depending on the scattering material.

2.2.4 Interface Analysis

On the basis of the equations for two-beam dynamical diffraction, excellent agreement has been found between the observed and calculated contrast for many microstructural features. This is particularly true for crystal interfaces, where Amelinckx and coworkers (19) have made a detailed examination of many types of interface. In the work to be described there are a frequent number of observations of interfaces between long-range-ordered domains. The observation of image contrast at these interfaces provides valuable information which supplements the data from selected area diffraction.

There are two general types of interface which are distinguished by their associated atomic displacements. In the α-interface there is a discontinuous displacement across one plane of atoms which results in a phase-change in the electron waves given by, $\alpha = 2\pi g.R$, where R is the vector representing the displacement. The δ-interface is characterized by a continuous displacement field across the interface which results in a small difference in diffracting conditions between the two crystal parts given by, $\delta = s_1\xi_{g_1} - s_2\xi_{g_2}$ In this latter case, contrast is due either to the difference in the extinction distances, or the deviation from the reflecting condition of the two crystal parts. In addition to pure α- and δ-interfaces, mixed $(\alpha - \delta)$-interfaces exist. These show a type of contrast in proportion to the relative magnitudes of the α and δ components. Stacking faults and antiphase boundaries are representative of α-interfaces, while certain types of twin and coherent precipitate interfaces are δ-type.

By observing the fringe contrast at an interface for various g, s, and z, it is possible to determine the nature

of the interface from simple qualitative rules derived from the theoretical equations.

2.2.5 Transmission Modes

In the present work extensive use has been made of the dark-field imaging technique. The dark-field images shown in this thesis were obtained by making a particular diffracted beam pass along the optic-axis of the image-forming lenses, by tilting the illuminating beam above the specimen plane. This method gives higher resolution than that obtained with the displaced aperture technique. In the dark-field mode only those parts of the specimen which give rise to the selected reflection will appear in bright contrast, and a correlation can then be made between these areas and the particular diffracted beam. The dark-field mode is also useful for the study of defects within ordered domains. Often the structure factors for the superlattice reflections are so weak that when one of these reflections is used in bright-field illumination under two-beam conditions, the fundamental reflection, i.e. the n(hkl) reflection where hkl is the superlattice reflection, is also strongly excited. Thus effects due to the superlattice reflection will be partly obscured. However, if the superlattice reflection is used to form the image in dark-field, the full contrast effect may be recorded.

Bright-field micrographs were usually made with a positive deviation from the Bragg condition on the diffraction pattern, a small final adjustment being made when viewing the image to give optimum contrast. Similarly for dark-field work, small negative deviations give good intensity, although there is still good intensity at the Bragg position. When necessary the deviation, s, (for a first-order reflection) could be measured from the relative positions of the 3g-Kikuchi line and the 2g-diffraction

spot (fig. 2.2.2). At the Bragg position for the reflection with vector g these two positions will coincide on the diffraction pattern.

2.2.6 Multiple Diffraction

The appearance of diffraction spots which are kinematically non-allowed, due to zero structure factor, may be explained by the phenomonen of multiple diffraction, where a strongly excited allowed reflection acts as a source for further diffraction. The indices of possible multiple diffraction spots are given by the combination of the indices of two allowed reflections. Thus if $h_1k_1l_1$ and $h_2k_2l_2$ are allowed reflections, then spots of the form h_1+h_2, k_1+k_2, l_1+l_2 may be present by multiple diffraction. Most of the previously observed examples of multiple diffraction are satisfactorily explained by considering combinations of allowed reflections within the two-dimensional section of the reciprocal lattice forming the diffraction pattern. It has been pointed out by Gjønnes and Moodie (20) that interactions involving higher layers of the reciprocal lattice may occur, especially when the beam direction coincides with a long axis of the unit cell.

The presence of multiple diffraction spots may lead to uncertainties in a later structure determination. However, if the specimen is tilted about the axis of the multiple diffraction spot vector, then one of the contributing allowed reflections will no longer be excited, and the multiple diffraction spot will disappear.

2.3 Crystal Structure Determination

The following sequence has been suggested (21) as showing the important steps in a crystal structure determination;

(1) Symmetry class

(2) Unit cell, space lattice and dimensions

(3) Space group

(4) Number of atoms in the unit cell

(5) Sets of equivalent positions

(6) Determination of atom positions

(7) Refinement of atom positions

With X-ray diffraction the initial steps 1 to 3 are often the most difficult. However, once the approximate atom positions are known, precise atom positions and lattice dimensions may be found from the measured positions and intensities of the reflections. For electron diffraction this situation is reversed. From a few single crystal selected area diffraction patterns the allowed reflections in reciprocal space may be readily determined. This will then provide immediate information on the symmetry, space group, and unit cell dimensions. However, it is often impossible to find the exact atom positions, since the observed intensities are not easily related to the calculated structure factors, due to dynamical scattering effects. Ideally then, a combination of X-ray and electron diffraction could provide the quickest route to the structure. In some instances it is not possible to prepare electron microscope specimens, while in the present work the superlattice reflections that arise from the ordering of light interstitial elements may not be detected by X-ray diffraction, because the difference in the scattering power of the two types of atom (metal and interstitial) is much greater than for electron diffraction. Furthermore, due to dynamical interactions in electron diffraction, weak reflections tend to be intensified at the expense of stronger reflections.

For the ordering of vacancies and atoms, steps 6 and 7 above may not be necessary. All that is required is to know which of the available positions in a particular sublattice are occupied. There will usually be some

small distortions of the lattice due to ordering, but in general this will be of secondary importance. Only one example was found where such displacements resulted in extra reflections over those produced by the geometric distribution of atoms and vacancies on sites with the same coordinates as in the disordered state. This does not mean that there were no displacements in other examples, only that in these cases there was a modification in the spot intensities which could not be detected by electron diffraction. Information on the crystalline distortion can however be obtained from the analysis of δ-interfaces outlined above.

2.3.1 Computational Method

A trial-and-error computer programme* has been written which will compare a theoretical reciprocal lattice, associated with a computer generated distribution of atoms and vacancies, with the reciprocal lattice found from electron diffraction patterns. In the previous section it was noted that usually there will be no loss of information with regard to the observed superlattice reflections if it is assumed that the possible coordinates of atom positions in the ordered structure are the same as those in the disordered structure. Thus the information required from the computer programme is which arrangement of atoms and vacancies will produce superlattice reflections consistent with those observed in the diffraction patterns.

From the indexed reciprocal lattice and the specimen composition, the number of vacancies in the super-

* Details of all the computer programmes mentioned throughout the thesis may be obtained on request from the author.

lattice unit cell are determined. If there is a total of m sites, of which n may be occupied, there will be n!/(n-m)!m! possible arrangements of these atoms (or vacancies). Many of these arrangements will be crystallographically equivalent, with only relative translations between unit cell axes. Since the observed intensities were of no quantitative use, a small arbitrary value for the structure factor was chosen as a minimum in deciding whether a calculated reflection for a generated arrangement of atoms and vacancies may be taken as an allowed reflection. When the first reflection is found that was not observed in the diffraction patterns, that particular arrangement is rejected and a new one tried. By choosing trial reflections of the type h00, 0k0, and 00l for the first three, rapid rejection of incorrect arrangements is possible.

The total number of arrangements given by the above expression puts a practical limit on the number of atoms and vacancies in the unit cell for which the programme may be run in a reasonable amount of computer time. If some of the atom positions are already known, the way in which successive arrangements are generated will leave these atoms unmoved until all other possibilities have been tried. For a simple case of three atoms which can occupy five positions labelled 1,2,..5, then successive combinations of allowed positions will be,

123, 124, 125, 134, . . etc.

Thus all combinations of positions above a given position will be tried first. About ten reflections are tested before a generated arrangement is considered a possibility.

2.3.2 Crystallographic Notations

Several conventions will be used throughout this work when discussing the use of electron microscopy for the study of superlattice structures. Thus although it is correct to refer to the beam - specimen orientation relation in terms of the electron beam being parallel to a certain crystallographic direction, a diffraction pattern will be referred to as an (hkl) section, and the corresponding micrograph will be from a specimen in an (hkl) orientation. For cubic structures, where planes are perpendicular to directions with the same indices, the beam direction will also be [hkl]. For close-packed hexagonal structures this latter relation is not usually true. However it does hold for the (0001), $(1\bar{1}00)$ and $(11\bar{2}0)$ orientations which have been frequently used.

Another useful convention is the retention of the indices for sections and orientations derived from the disordered structure, and not the superlattice structure. This allows easy comparisons to be made as the respective superlattice indices may not be readily related to the orientation of the matrix in which the ordering has taken place. As ordering gives rise to increased periodicities in the matrix structure planes, the reciprocal lattice vectors for the superlattice reflections are simple fractions of the fundamental reflections, and will often be written as m/n(hkl), where hkl refers to the fundamental reflection, and m and n are integers. Of course, correctly indexed superlattice reflections are necessary for the structure determination. When the indices for reflections, planes, directions etc. are quoted without a subscript, it is understood that these refer to the parent metal lattice.

In particular instances subscripts will be used, these are, c - cubic, h - hexagonal, r - rhombohedral, t - tetragonal, o - orthorhombic, and m - monoclinic.

REFERENCES

1. Y.Bando, K.Nagasawa, Y.Kato and T.Takada, Japanese J. Appl. Phys., 8, 633 (1969).
2. K.Nagasawa, Y.Bando and T.Takada, Japanese J. Appl. Phys., 8, 1262 (1969); 8, 1267 (1969); 9, 407 (1970).
3. J.-L.Chermant, Rev. Int. Hautes Temp. et Réfract., 6, 299 (1969).
4. N.Terao, Japanese J. Appl. Phys., 3, 104 (1964).
5. L.R.Fleischer and J.M.Tobin, J. Cryst. Growth, 8, 235 (1971); 8, 243 (1971).
6. W.Precht and G.E.Hollox, J. Cryst. Growth, 3, 818 (1968).
7. J.F.Wenkus, J.S.Haggerty and D.W.Lee, AFML Tech. Rept., No. TR-68-228 (Sept. 1968).
8. J.S.Haggerty, J.L.O'Brien and J.F.Wenkus, J. Cryst. Growth, 3, 291 (1968).
9. T.B.Reed, Proc. 3rd. Int. Symp. on High Temperature Technology (Butterworths, London, 1969).
10. R.W.Bartlett, F.A.Halden and J.W.Fowler, Rev. Sci. Instr., 38, 291 (1967).
11. J.Billingham, P.S.Bell and M.H.Lewis, J. Cryst. Growth, 13/14, 693 (1972).
12. G.Brauer and W.D.Schnell, J. Less-Commom Metals, 6, 326 (1964).
13. A.D.Mah, U.S. Bur. Mines, Rept. RI-6177 (1963).
14. F.ThUmmler, H.Wedemeyer and C.Politis, Kernforschungszentrum Karlruhe, Tech. Rept., KFK 1023 (Aug. 1969).
15. H.F.Sterling and R.W.Warren, Metallurgia, 67, 301 (1963).
16. C.A.Brookes and M.E.Packer, Special Ceramics, 4, 15 (1967).
17. G.V.Samsonov, R.Ya.Petrykina and V.Ya.Naumenko, Izv. Acad. Nauk. SSSR Neorg. Mater., 6, 2123 (1970).

18. A.Howie and M.J.Whelan in "Electron Microscopy of Thin Crystals", P.B.Hirsch, A.Howie, R.B.Nicholson D.W.Pashley and M.J.Whelan (Butterworths, London, 1965).
19. S.Amelinckx in "Modern Imaging and Diffraction Techniques in Materials Science", eds. S.Amelinckx, R.Gevers, G.Remaut and J.Van Landuyt (North-Holland, Amsterdam,1970).
20. J.Gjønnes and A.F.Moodie, Acta Cryst., 19, 65 (1965).
21. C.S.Barrett and T.B.Massalski, "Structure of Metals", (McGraw-Hill, New York, 1966).

CHAPTER THREE

CARBIDES WITH AN FCC METAL-ATOM STRUCTURE

3.1 Titanium Carbide

3.1.1 Introduction

Part of the titanium - carbon phase diagram is shown in fig. 3.1.1. The phase-relationships in this system are well established. The NaCl-type monocarbide phase extends from $TiC_{1.0}$ to about $TiC_{0.5}$ with carbon deficiency only. At lower carbon concentrations, the cubic phase coexists with the primary titanium - carbon solid solution which is hcp below 920°C (α-Ti), and bcc above this temperature (β-Ti).

Previous work (2,3) has shown that in the monocarbide phase at the higher carbon concentrations, the vacancies are randomly arranged. In a neutron diffraction study of specimens near $TiC_{0.5}$, Goretzki (4) observed extra reflections which he attributed to carbon-atom ordering, and assigned the structure to the cubic Fd3m space group. In a recent electron diffraction investigation of the precipitation of α-Ti from $TiC_{0.45}$, Chermant et al. (5) noted diffuse extra reflections at 1/2(111) positions, but did not observe an ordered-domain structure in the carbide matrix.

Parthé and Yvon (6) have shown that X-ray and neutron powder diffraction techniques do not enable a distinction to be made between two possible types of superstructure, with space groups Fd3m (cubic) and $R\bar{3}m$ (trigonal), formed by the ordering of carbon atoms in compounds with composition M_2C, and with nominally fcc metal-atom stacking. In the cubic form all ⟨111⟩ directions are equivalent, while the trigonal form possesses a unique c-axis (parallel to a particular $[111]_c$ direction) with the carbon-atom planes

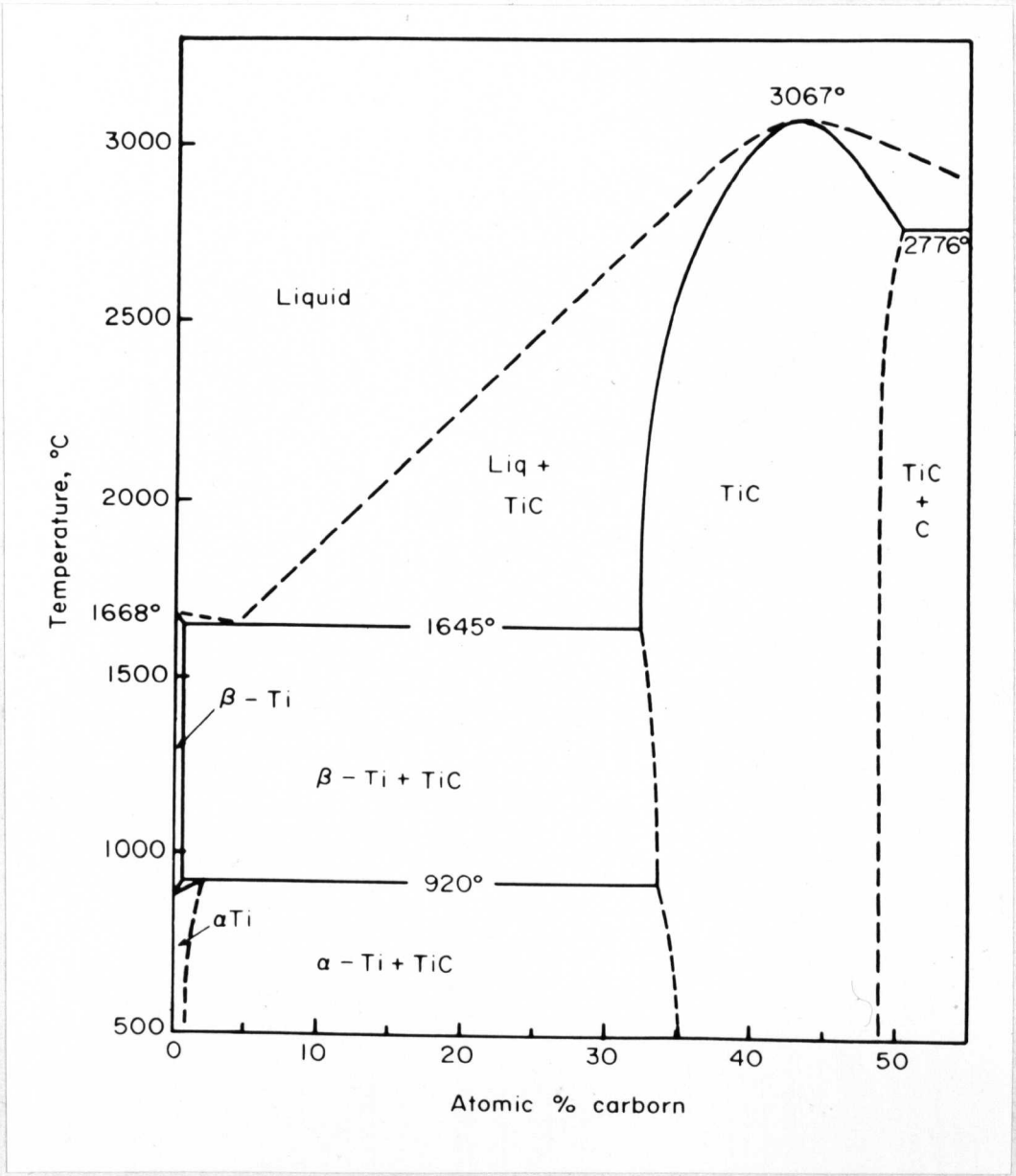

Fig. 3.1.1 Phase diagram for the titanium - carbon system, after Storms (1).

perpendicular to this direction being alternately full and empty. For these two structures it is found that the positions and intensities of both fundamental (NaCl) and superstructure reflections are identical. If there is a small rhombohedral distortion associated with the trigonal form, then measurement of the separation of the superlattice reflections may enable a distinction to be made. However it is found that X-ray reflections are too weak, and neutron reflections too broad to permit this. It should be possible to make a distinction between these two possibilities by selected area electron diffraction from single domains, and dark-field imaging from superlattice reflections.

3.1.2 The Ordered Compound Ti_2C

(i) Electron microscopy and diffraction

In the as-grown (rapidly cooled) condition crystals within the composition range $TiC_{0.45}$ to $TiC_{0.60}$ showed, apart from the fundamental reflections, a diffuse type of electron scattering similar to that found for several other compounds investigated. A more detailed discussion of this scattering will be given later, but it may be considered to arise from short-range order existing in the carbon-atom sublattice. Fig. 3.1.2(a) shows a diffraction pattern from a crystal after annealing for 90h at 900°C. Although the diffuse scattering is still present, extra reflections are observed at 1/2(111) and 1/2(311) positions. At this stage there is no positive identification of domains, although the corresponding micrographs have a mottled appearance. After annealing at lower temperatures the fine distribution of domains shown in fig. 3.1.2(c) is produced. Fig. 3.1.3 shows the larger domains formed by prolonged annealing at 650°C.

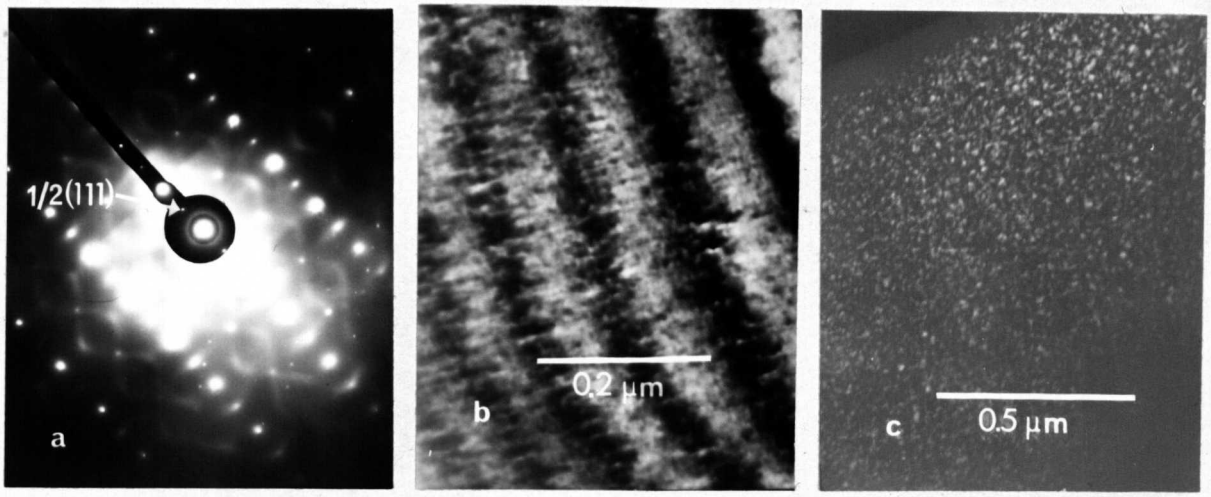

Fig. 3.1.2 Initial stages in the formation of ordered Ti_2C. (a) (211) section and (b) DF from indicated reflection, (90h at 900°C). (c) DF from 1/2(111), (50h at 650°C)

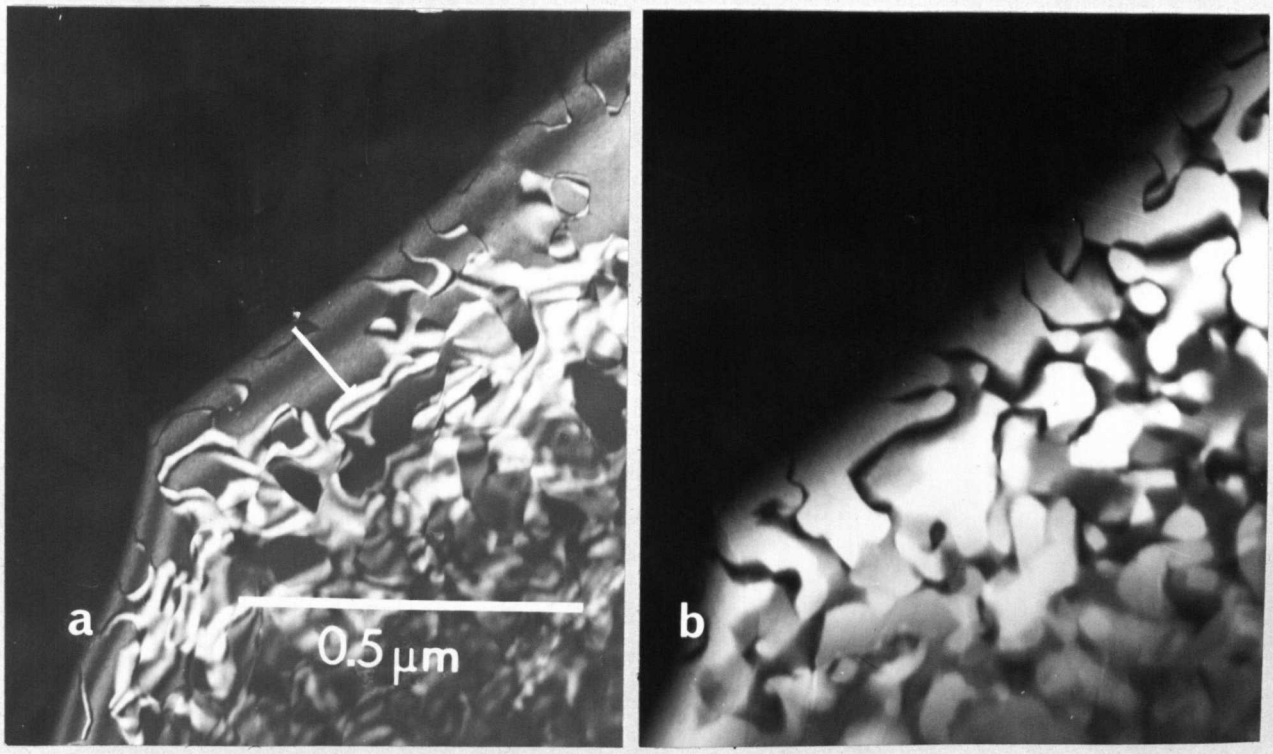

Fig. 3.1.3 APB foam structure formed after 770h at 650°C. (a) DF 1/2(111), (b) DF 1/2(311), (211) orientation. Reversal in the visibility of some boundaries occurs from (a) to (b).

The diffraction patterns now contain sharp superlattice reflections (fig. 3.1.4). For $TiC_{0.45}$ to $TiC_{0.50}$ the critical temperature for maximum domain growth-rates was near 650°C, and ordering was just detected up to $TiC_{0.60}$.

(ii) Structure of the ordered compound Ti_2C

Although the domain sizes obtained were too small to allow diffraction patterns from single domains to be recorded, it was possible to make an unambiguous structure determination aided by the observed domain and antiphase boundary contrast. Consider first the type of (110) section diffraction pattern that would be obtained from the trigonal $R\bar{3}m$ structure. If the c-axis of a domain were perpendicular to the electron beam, then the sequence of full and empty carbon-atom planes would result in just one row-direction of 1/2(111) reflections parallel to the direction of the c-axis. Those domains with c-axes not perpendicular to the beam would not show any superlattice reflections, since the carbon-atom planes now parallel to the beam would all have the same composition, i.e. they would all appear to be half-full. Forming a dark-field image from one of the 1/2(111) reflections would show only one quarter of the domains in bright contrast. The dark-field images of fig. 3.1.3 show that all the domains have bright contrast, and thus the cubic structure is inferred.

Some of the superlattice reflections in fig. 3.1.4(a) are caused by multiple diffraction. When the sample is tilted slightly from this orientation these reflections disappear. Fig. 3.1.4(c) shows a (110) section pattern from domains having a low degree of long-range order. Only the allowed reflections of 1/2(111) and 1/2(311) type

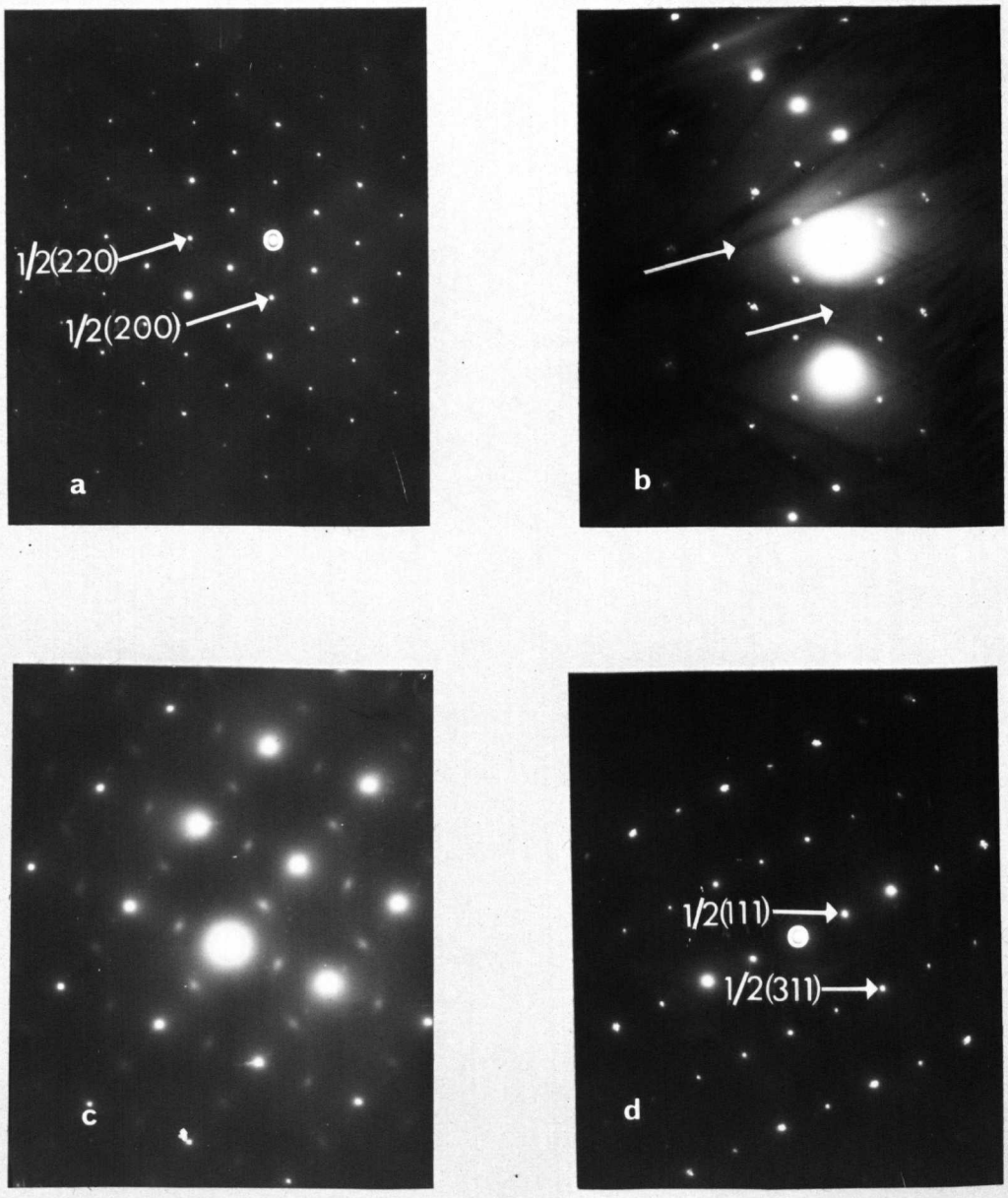

Fig. 3.1.4 Superlattice reflections from Ti_2C. (a) exact, and (b) slightly deviated (110) sections showing extinction of nonallowed 1/2(200) and 1/2(220) reflections. (c) (110) section from partially ordered specimen showing only allowed reflections. (d) (211) section, fully ordered.

are present, because they are too weak to act as primary beams for the formation of reflections by multiple diffraction.

The allowed reflections were fitted to the computer programme and the resulting vacancy positions were found to be identical with those proposed by Goretzki (4), although from his information the structure could equally well have been the undistorted trigonal form. The structure, shown in fig. 3.1.5, may be briefly described as having {111} carbon-atom planes alternately 1/4- and 3/4-occupied. In projection onto any {111} plane the carbon atoms in a 1/4-full layer lie at the centre of the triangles formed by the projection of the vacant positions in the 3/4-full layers directly above and below.

The morphology and visibility criteria of the APB's may be interpreted in terms of the cubic structure. The multiplicity of possible antiphase vectors for this structure exceeds four, and hence provides the condition for the formation of a stable three-dimensional 'foam' structure of APB's (7), separating crystal parts which are translated relatively by a partial vector of the cubic superlattice of magnitude $a/4\langle 110\rangle$ (the superlattice parameters are parallel to, and twice the length of those of the NaCl cell). There is a total of six vectors of this type parallel to the edges of a tetrahedron formed by $\{111\}_c$ planes. For the two imaging reflections of fig. 3.1.3 half of the possible types of APB should be visible, and only one type of boundary should be visible in both. In (a) the value of $2\pi\mathbf{g}.\mathbf{R}$ is either 0 or $\pm\pi$, and the marked boundary shows contrast similar to that for a π-boundary (8), i.e. symmetric fringes with a dark central fringe in dark-field. Fringes are not observed in (b) as the

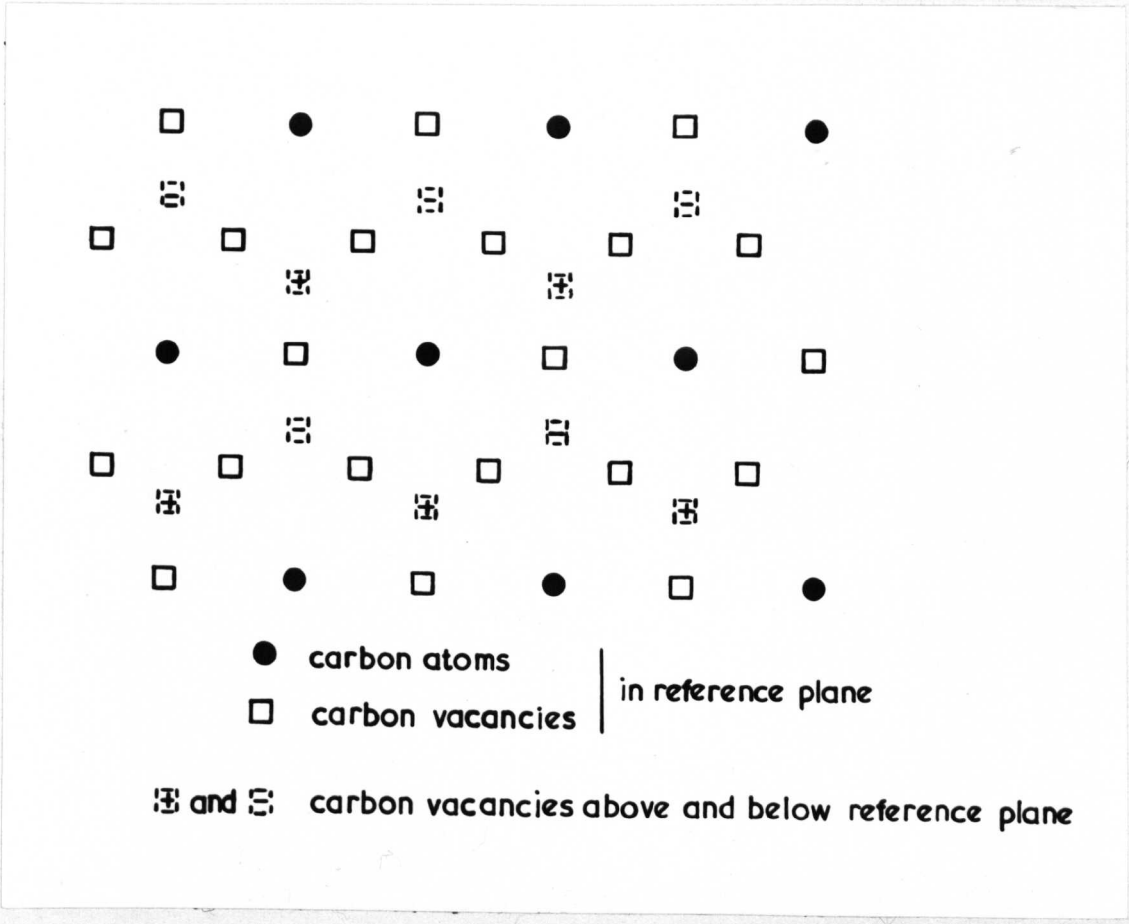

Fig. 3.1.5 The carbon-atom positions in the Ti_2C superlattice shown in projection onto a (111) plane.

extinction distance for the 1/2(311) reflection is much greater than for the 1/2(111), and thus the boundaries appear as a single band.

The slow increase in domain size with annealing time may be explained by the initial formation of domains with incomplete order, and the possibility that the composition of the phase in equilibrium with a-Ti at the low annealing temperatures is greater than the ideal $TiC_{0.50}$. This will result in a lowering of the APB energy, and when coupled with the slow rate of carbon diffusion at these temperatures, will account for the low domain-growth and coarsening rates.

3.1.3 Precipitation of a-Ti

For specimens with composition $TiC_{0.45}$, precipitates of a-Ti were observed in the form of thin plates. Figs. 3.1.6(a) and (b) show two different areas both with (110) orientation. The longest edge of the plates is parallel to the traces of {111} planes. The matrix dislocations observed in these micrographs are undissociated. This is an exceptional case, since it has been found that in the other carbides and nitrides with the NaCl-type structure, dislocation dissociation occurs for compositions near the nonmetal-deficient phase boundary.

The diffraction patterns of figs. 3.1.6(c) and (d) show the relationship between the hcp a-Ti and the fcc matrix. The orientation relation of the precipitates is,

$$(111)\text{TiC} \parallel (0001)\text{a-Ti}$$
$$\langle 110\rangle\text{TiC} \parallel \langle 11\bar{2}0\rangle\text{a-Ti}$$

This result is in agreement with the findings of Chermant et al. (5), who showed that the mismatch of the (220)-TiC and $(11\bar{2}0)$-a-Ti interplanar spacings perpendicular to the

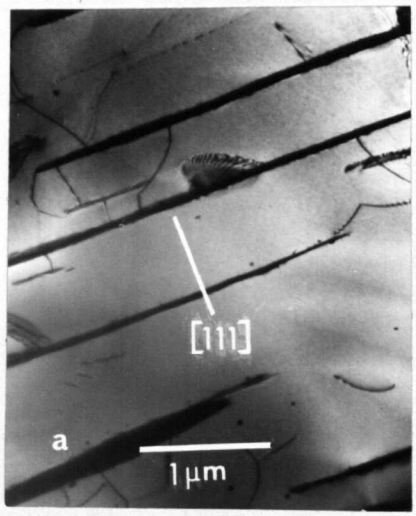

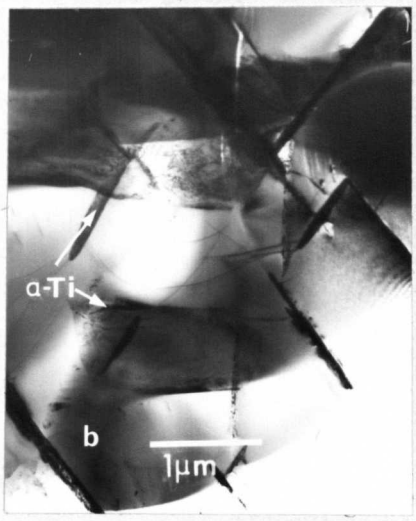

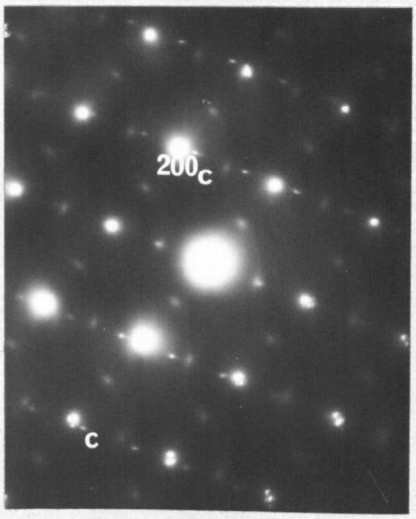

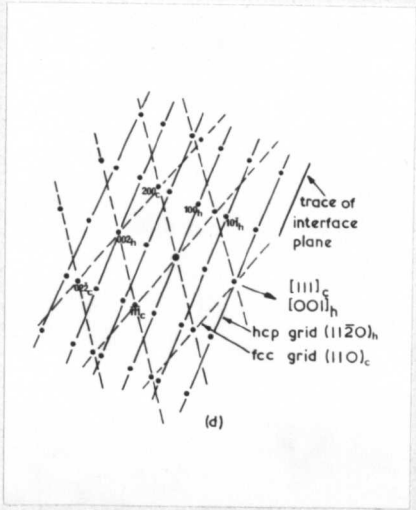

Fig. 3.1.6 Precipitation of α-Ti from cubic $TiC_{0.45}$. (a) one orientation (edge-on) and (b) three orientations of plate precipitates lying in (111) planes. (c) diffraction pattern showing superposition of hexagonal α-Ti and fcc-TiC reflections (weak Ti_2C superlattice reflections are also visible). (d) schematic diffraction pattern showing orientation relation between precipitate and fcc matrix.

interface was about 3%, and that the spacing of the (111)-TiC and (0001)-α-Ti planes parallel to the interface differed by only 4%.

3.2 Niobium Carbide

3.2.1 Introduction

Phase equilibria in the niobium - carbon system are less well established than for the titanium - carbon system. In the two phase diagrams shown in fig. 3.2.1, the major difference is the relationship of the hexagonal Nb_2C-phase with the monocarbide and liquid phases at high temperatures. The present work tends to support the more recent diagram of Storms (10), in that as-grown specimens with low carbon concentrations consisted mainly of the cubic phase which, after annealing at low temperatures, was converted into the hexagonal phase. Below 1500°C the two diagrams are in agreement. The monocarbide phase extends from just below the stoichiometric composition to about $NbC_{0.72}$ by the subtraction of carbon atoms.

Prior to the present work there has been no detailed investigation of this phase. Terao (11) did not observe any superstructure ordering using transmission electron microscopy from vapour deposited films. Theoretical work by Zubkov et al. (12) has predicted that near the composition Nb_4C_3 the interaction of the remaining carbon atoms would lead to the formation of an ordered phase, where the carbon atoms and vacancies on their primary fcc sublattice would occupy respectively the equivalent positions of copper and gold atoms in the Cu_3Au superlattice. Previous work on the vanadium - carbon system has shown the occurrence of, two closely related

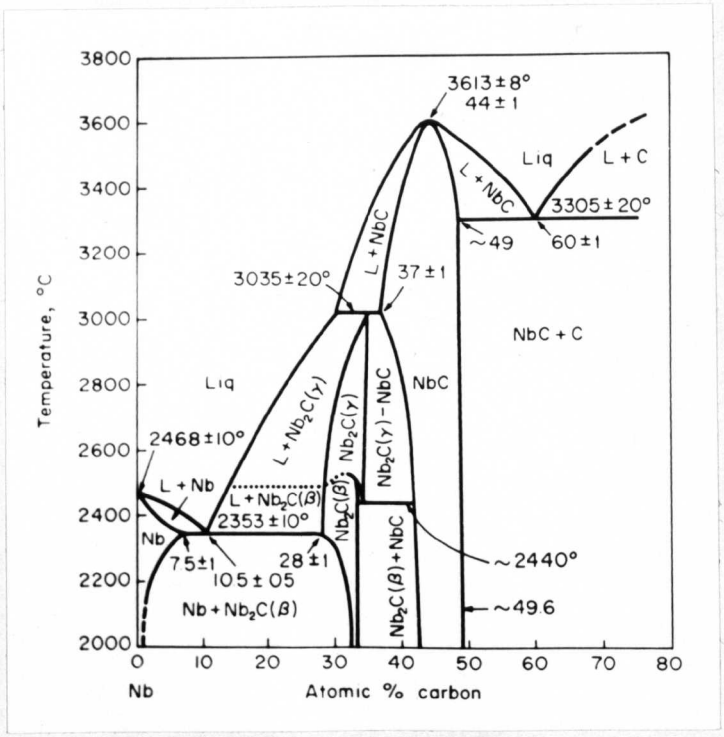

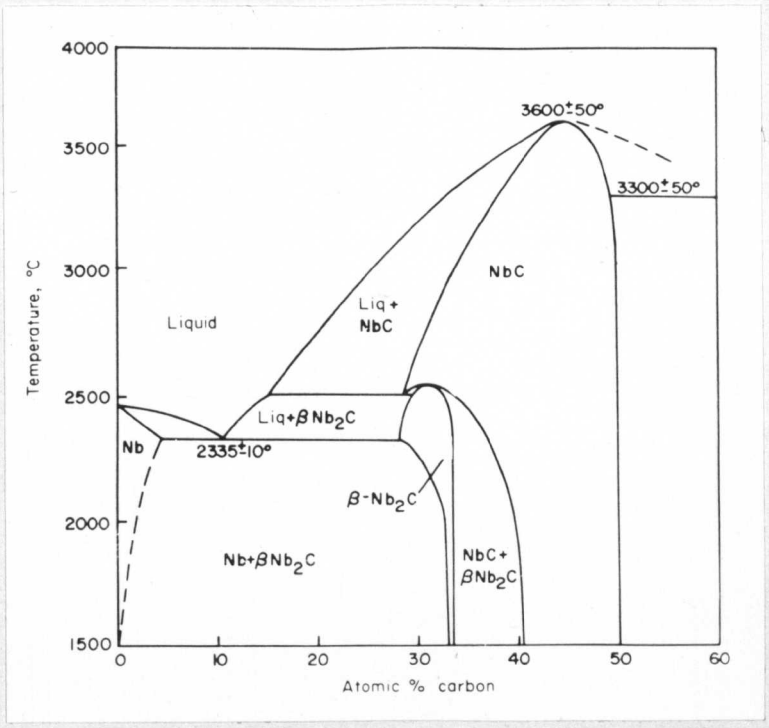

Fig. 3.2.1 Possible phase diagrams for the niobium - carbon system. Top, after Rudy et al. (9), bottom, after Storms et al. (10).

superlattices based on the composition V_6C_5 with trigonal (13) and monoclinic (14) symmetry, and a cubic superlattice V_8C_7 (15-18)

3.2.2 Electron Microscopy and Diffraction

An ordered phase showing superalttice reflections simialr to those of V_6C_5 was observed (as a single phase or coexisting with the cubic carbide matrix) within the approximate range $NbC_{0.78}$ to $NbC_{0.95}$ at low temperatures, and with a maximum in the order - disorder transformation temperature at 1040°C for the composition $NbC_{0.83}$ (Nb_6C_5). In the vanadium - carbon system, for compositions higher than about $VC_{0.80}$, the disordered state cannot be retained by readily available quenching techniques, since the maximum in the order - disorder transformation temperature occurs at $0.55T_m$, as opposed to $0.35T_m$ for niobium carbide. Thus it was possible to examine compositions from $NbC_{0.5}$ (quenched-in cubic phase) to $NbC_{0.95}$ in the disordered state. The familiar type of diffuse scattering was observed for all these compositions, the diffraction patterns of fig. 3.2.2 being typical examples. Although it is particularly difficult to judge the relative intensity of the diffuse scattering for specimens of different composition, since it depends markedly on the thickness and uniformity of the thin-foil specimen, it appeared to remain constant over the whole composition range.

A further consequence of the lower order - disorder transformation temperatures in niobium carbide is that the domain-sizes were always very small (<1μm), even after prolonged heat-treatments on specimens which were slowly cooled and then maintained just below the transformation

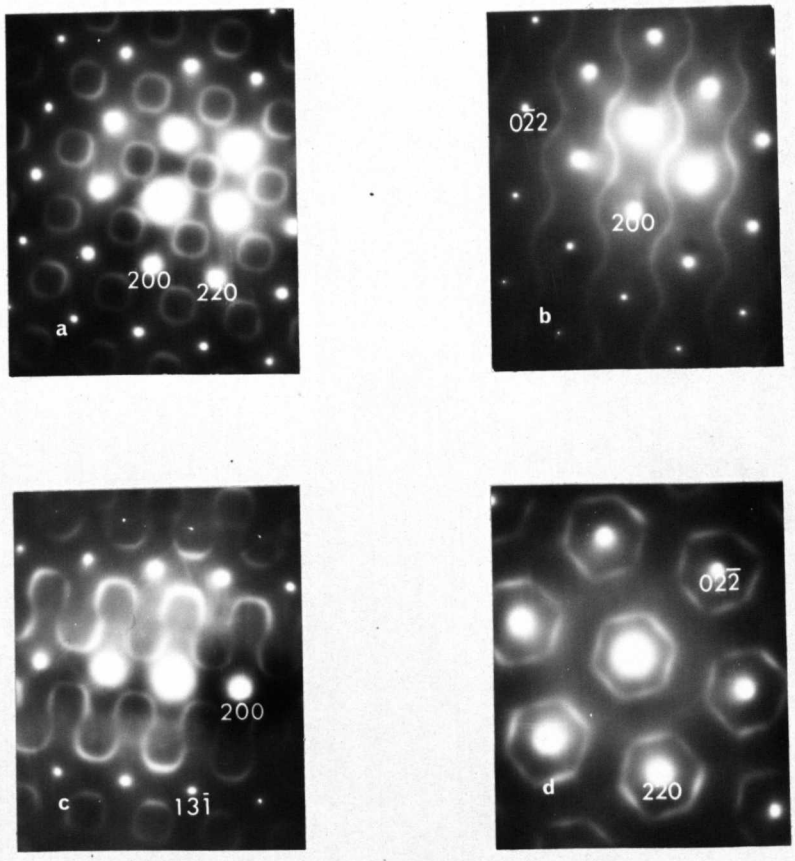

Fig. 3.2.2 Diffuse electron scattering in $NbC_{0.75}$. (a) (100), (b) (110), (c) (310), and (d) (111) sections.

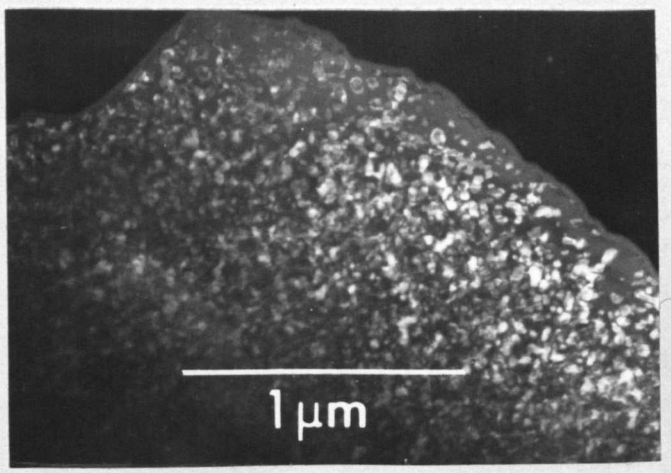

Fig. 3.2.3 Small ordered domains in $NbC_{0.83}$, 72h 800°C 1/2(111) DF.

temperature. Fig. 3.2.3 is a dark-field micrograph showing a fine distribution of ordered domains. Although the diffraction patterns from single domains could not be recorded, a very close similarity exists between the patterns shown in fig. 3.2.4 and those obtained under the same conditions from vanadium carbide, for which single domain diffraction patterns could be obtained from suitably annealed specimens (14). The observed superlattice reflections are of the type, 1/3(220) in (100), (111), and (110) sections, and 1/2(111) in (110) sections. (211) sections (fig. 3.2.5) showed, apart from sharp reflections, rows of weaker diffuse spots which in some instances formed continuous lines of intensity. Fig. 3.2.6 shows the dark-field images obtained using the various superlattice reflections in a (211) section. The 1/2(111) reflection, (b), shows one orientation of domains in bright contrast. The image recorded from one of the reflections comprising the rows of spots (in this case at 1/3(311), (c)) shows within the same orientation of domains as in (a), a substructure in the form of alternate light and dark bands. The position of these bands in the domains changed as different reflections from the rows were chosen for the image formation. The selection of a 1/2(311) reflection, (d), shows domains containing a small number of wavy antiphase boundaries.

There was no evidence for the proposed Nb_4C_3 superlattice, or for a superlattice equivalent to V_8C_7.

3.2.3 Structure of the Ordered Compound Nb_6C_5

Because of the similarity in the diffraction patterns observed for niobium and vanadium carbides for the ordered phase found near the 6/5 metal-to-carbon ratio,

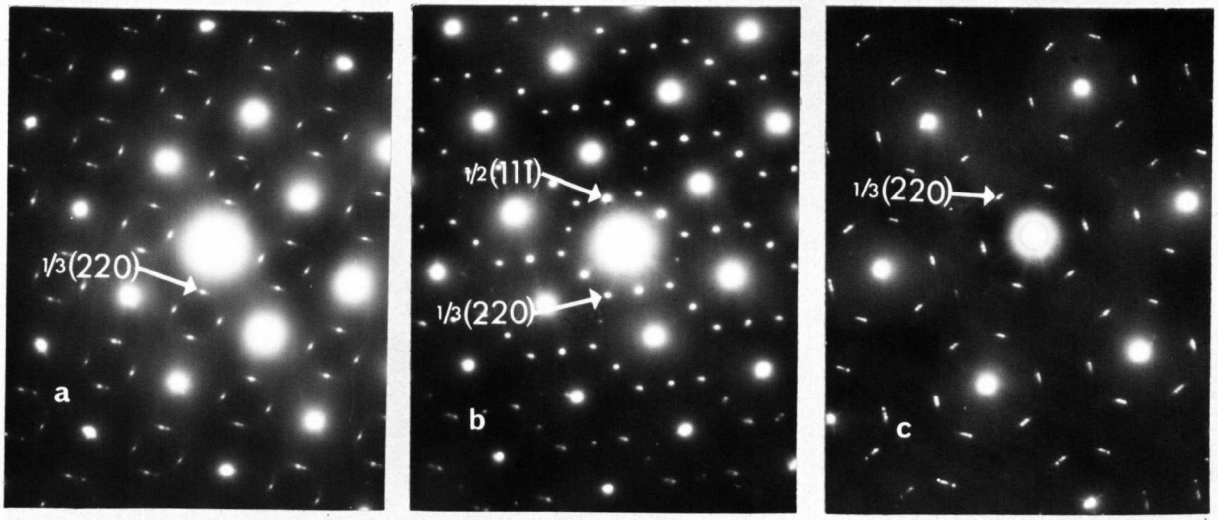

Fig. 3.2.4 $NbC_{0.83}$ 170h 900°C, superlattice reflections. (a) (100), (b) (110), (c) (111) sections.

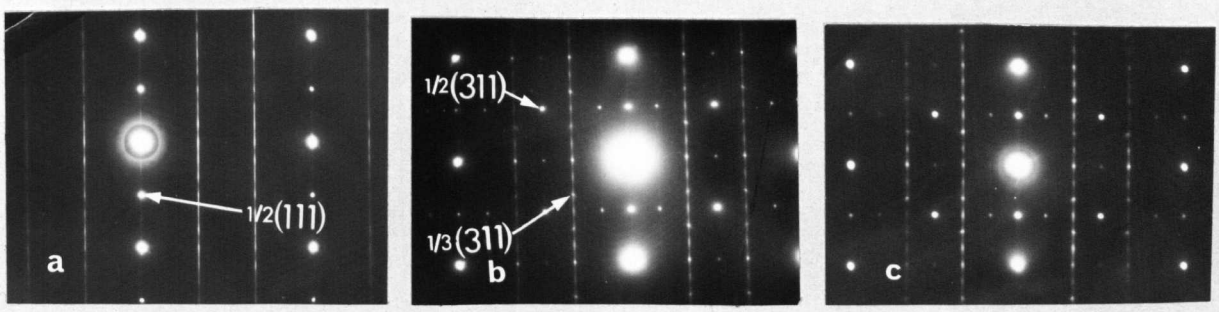

Fig. 3.2.5 (211) sections. (a) and (b) show the development of superlattice reflections. (c) taken from a vanadium carbide specimen containing small ordered domains of V_6C_5.

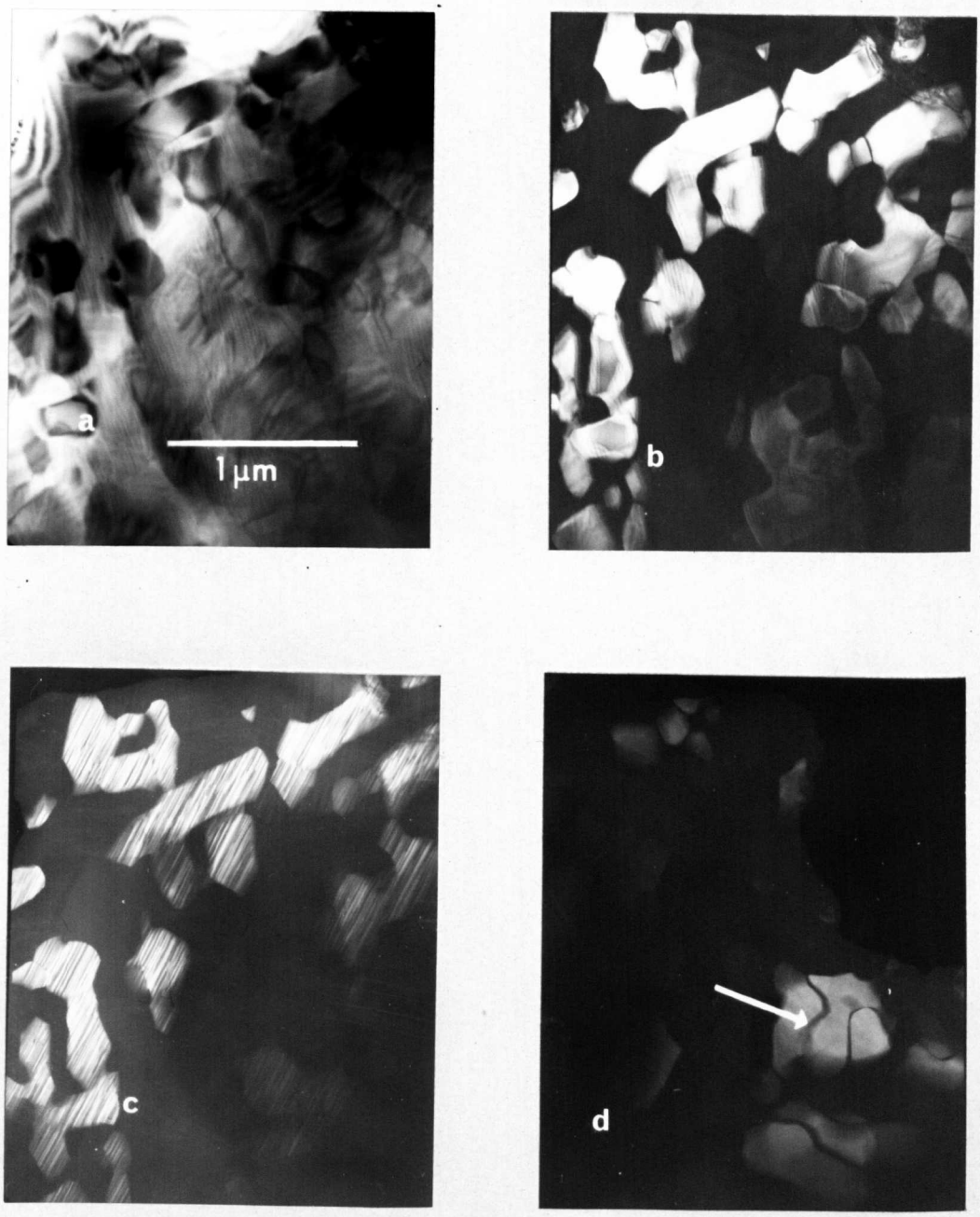

Fig. 3.2.6 Ordered domains in $NbC_{0.87}$, 360h 920°C.
(211) orientation, (a) BF, (b) 1/2(111) DF,
(c) 1/3(311) DF, (d) 1/2(311) DF (different area).

the structures previously proposed for V_6C_5 are highly relevant to the present work on niobium carbide. For the purposes of discussion it is necessary to refer to those single domain diffraction patterns obtained by Billingham (14) for V_6C_5. The structure analysis using the data obtained from these patterns in combination with the computer method is thus applicable to both V_6C_5 and Nb_6C_5.

(i) The trigonal $P3_1$ modification

Venables et al. (13) assigned the V_6C_5-phase to the trigonal space group $P3_1$ (and its enantiomorph $P3_2$), using electron diffraction patterns from single domains, with additional information about the vanadium nearest- and next-nearest-neighbour carbon atom/vacancy configurations, found from a study of the V^{51} NMR spectrum. This latter work showed that there were two types of configuration, such that all the vanadium atoms were surrounded by one nearest-neighbour carbon vacancy with either one or two next-nearest-neighbour carbon vacancies. The ratio of the number of these configurations was found to be 2:1 respectively. The presence of the 1/2(111) reflections, and the observation of a three-fold symmetric (111) pattern for a particular domain orientation led to the choice of the trigonal structure shown in fig. 3.2.7(a). In this structure the orientation of a domain with respect to the cubic matrix is determined by the direction of the trigonal c-axis which defines the normal to the (hexagonal) basal plane. This direction may lie along any one of the four cubic ⟨111⟩ directions. The carbon-atom planes perpendicular to the c-axis are alternately two-thirds and fully occupied, and when viewed in projection onto the basal plane the vacancies lie on helices parallel to the

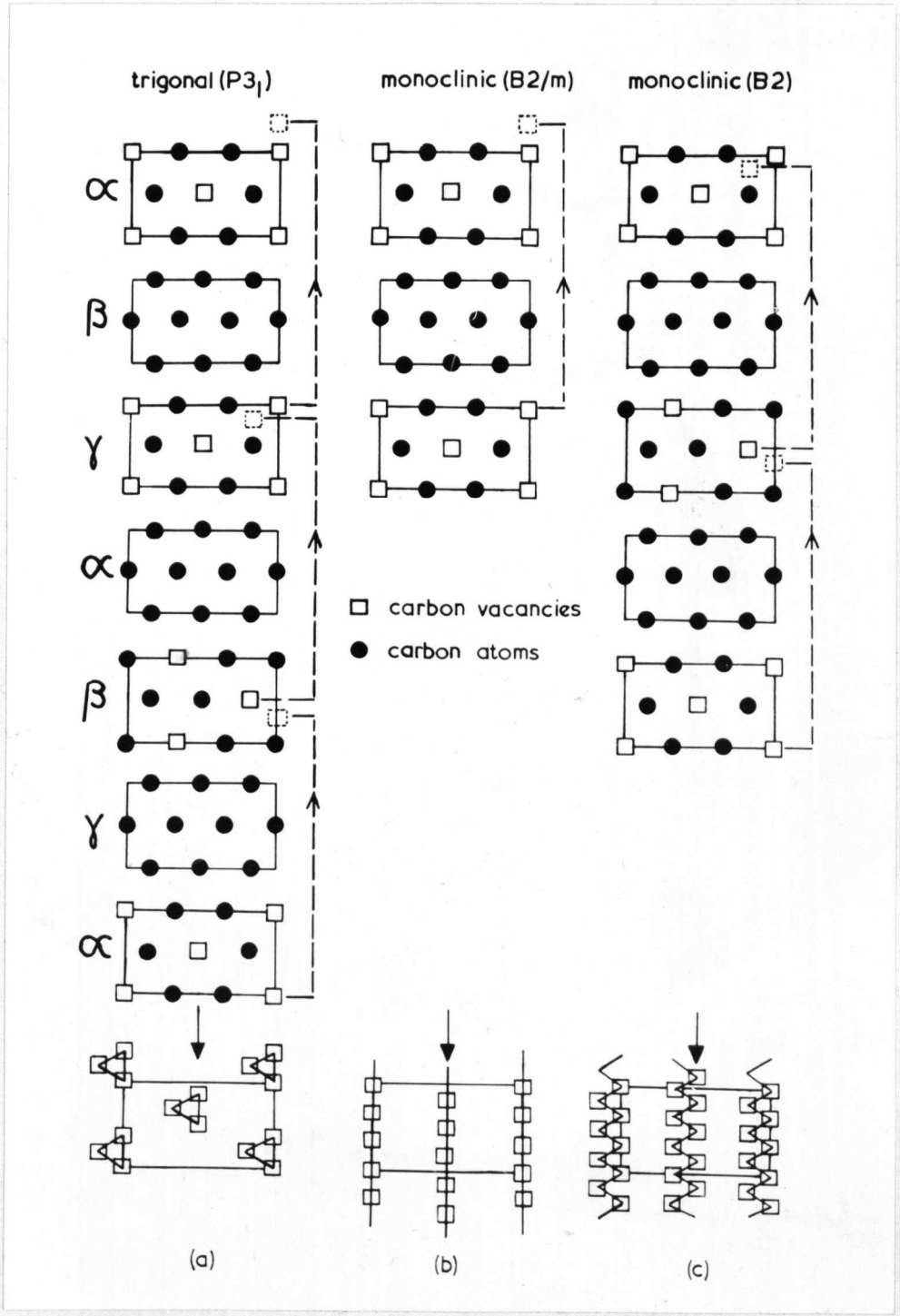

Fig. 3.2.7 Carbon-atom positions in successive close-packed planes, and the projection of these positions onto the base plane (bottom) for the three possible ordered structures based on the composition M_6C_5. Dotted lines indicate the stacking positions of successive part-filled layers. For convenience of comparison the trigonal form (a) has been drawn with reference to the monoclinic base plane.

c-axis. The unit cell c-parameter is six-times the carbon - carbon {111} plane spacing of the disordered structure.

(ii) The monoclinic B2/m modification

In an extensive study of the cubic vanadium carbide phase made by Billingham (14), prolonged annealing removed most of the banded substructure within the ordered domains of V_6C_5. At the same time the domain-size increased, enabling diffraction patterns from single domains to be recorded. Two features of the diffraction patterns were found to be inconsistent with the trigonal structure. Firstly, for certain (110) and (211) sections no superlattice reflections were detected despite the presence of long-range order, and secondly, for particular (211) sections extra superlattice reflections were observed which could not be accounted for by the trigonal form or by multiple diffraction (fig. 3.2.8). A monoclinic structure, shown in fig. 3.2.7(b), with space group B2/m was proposed. The distribution of carbon atoms within the 2/3-occupied monoclinic base plane layers is the same as in the basal plane of the trigonal form, the difference in structure arising from the relative positions of the vacancies when subsequently projected onto this plane. The vacant positions lie on straight lines at 19.28° to the base-plane normal. Computed structure factors did show (110) and (211) sections with no superlattice reflections, although the structure did not give the extra reflections seen in particular (211) sections. In fact no reflections inconsistent with the trigonal form were found. Thus the monoclinic (B2/m) structure could not be positively identified, although its existence could not be ruled out.

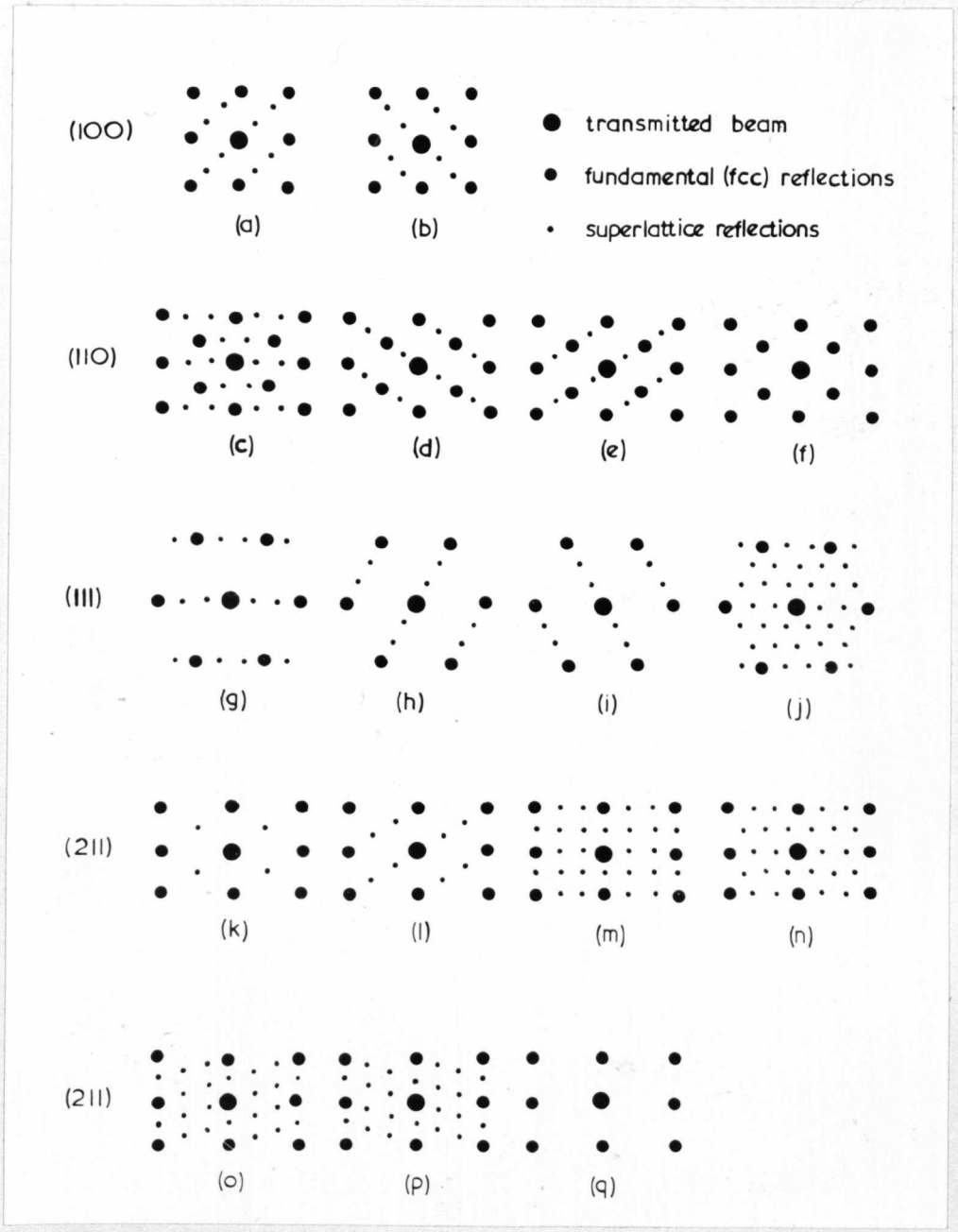

Fig. 3.2.8 Diffraction patterns obtained from single domains of the ordered structures based on the composition V_6C_5, after Billingham (14).

(iii) The monoclinic B2 modification

It appeared likely that the correct structure would retain the stacking sequence of alternate filled and part-filled carbon-atom planes, and the hexagonal symmetry of carbon atoms and vacancies within the partially full layers. It was therefore necessary to determine the correct sequence of lateral displacements of successive part-filled carbon-atom layers. These possible displacements may be identified with antiphase boundaries whose plane and displacement vector lie in the basal plane, as shown in fig. 3.2.9(a). The presence of a high density of these antiphase boundaries gives rise to the banded substructure in the domains.

The diffraction patterns were indexed in terms of a monoclinic unit cell belonging to the space group B2, and containing two part-filled carbon-atom layers. The vacancy distribution in these layers obtained from the computer programme is shown in fig. 3.2.7(c).

The vacancy positions on proceeding through successive part-filled layers lie on a zigzag path. The unique c_m-axis (first setting of the International Tables for Crystallography) and the a_m-axis lie in the base plane. If this base plane is chosen as (111), then the c_m-axis may adopt three equivalent orientations, i.e., $[01\bar{1}]$, $[\bar{1}01]$ and $[1\bar{1}0]$, making a total of twelve orientations with respect to the matrix (fig. 3.2.10). The b_m-axis lies in a second {111} plane and is orthogonal to c_m. For the chosen (111) base plane, then with c_m in the $[1\bar{1}0]$ direction, the zigzag of vacant sites will lie in the $(\bar{1}\bar{1}3)$ plane and [332] direction. The orient-

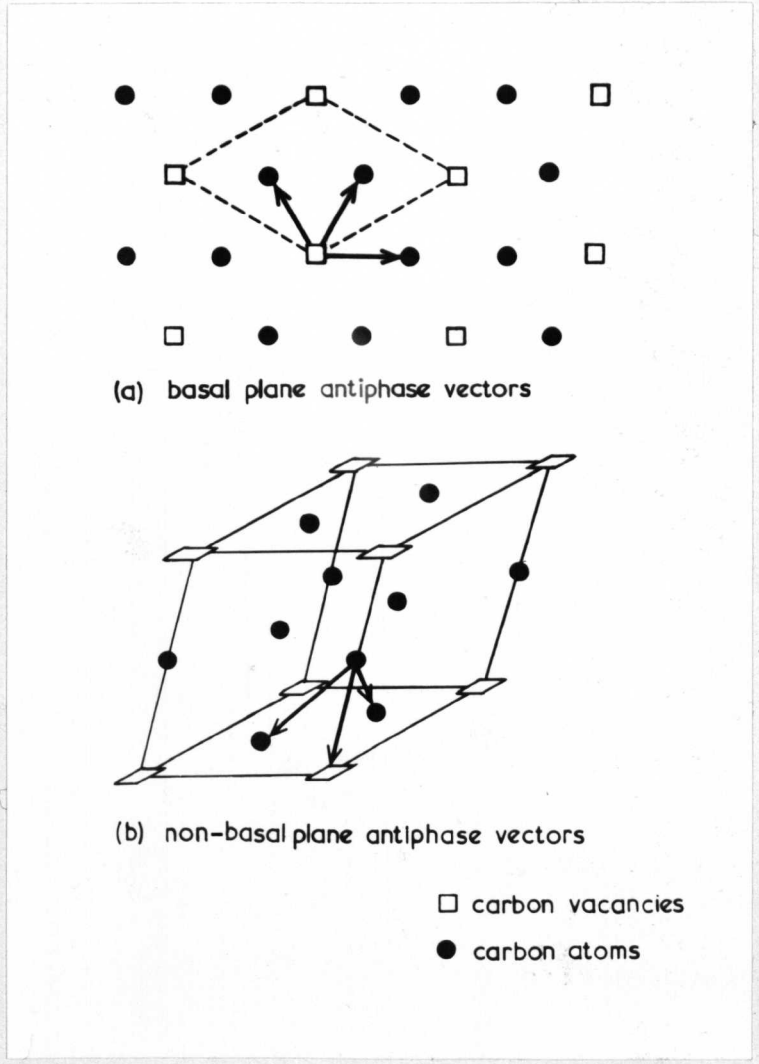

Fig. 3.2.9 Possible antiphase displacement vectors in the ordered carbon sublattice.

ation relation between the cubic matrix and the superlattice may be specified as,

$$(111)\text{-matrix} \parallel (010)\text{-superlattice}$$
$$(1\bar{1}0)\text{-matrix} \parallel (001)\text{-superlattice}$$

The absence of a mirror plane in the space group for this structure implies the existence of enantiomorphic forms. These are represented by the two senses of zigzag for each monoclinic orientation shown in fig. 3.2.10. These enantiomorphs may not be distinguished by electron diffraction, and for the beam direction indicated in this figure, the domain orientations (1), (2), and (3), will give rise to the diffraction patterns (m), (o), and (p), in fig. 3.2.8 respectively, for both senses of zigzag.

3.2.4 Discussion of the Proposed Ordered Structures.

The following conclusions regarding the possible occurrence of the three proposed ordered distributions may be drawn from the available electron diffraction data. The monoclinic form having the B2 space group may be positively identified from the two (211) sections (fig. 3.2.8 (o) and (p)) and its existence is undoubted. Similarly the trigonal form could be identified from the (111) section which shows superlattice reflections with six-fold rotation symmetry (fig. 3.2.8(j)). However, the parallel streaks in the (211) sections, such as in fig. 3.2.5, will intersect the (111) section at the positions of the 1/3(220) reflections to give a pattern with apparent six-fold symmetry. Thus well annealed specimens with a low fault density must be used when searching for this diffraction pattern characteristic of the trigonal form. This has not been possible

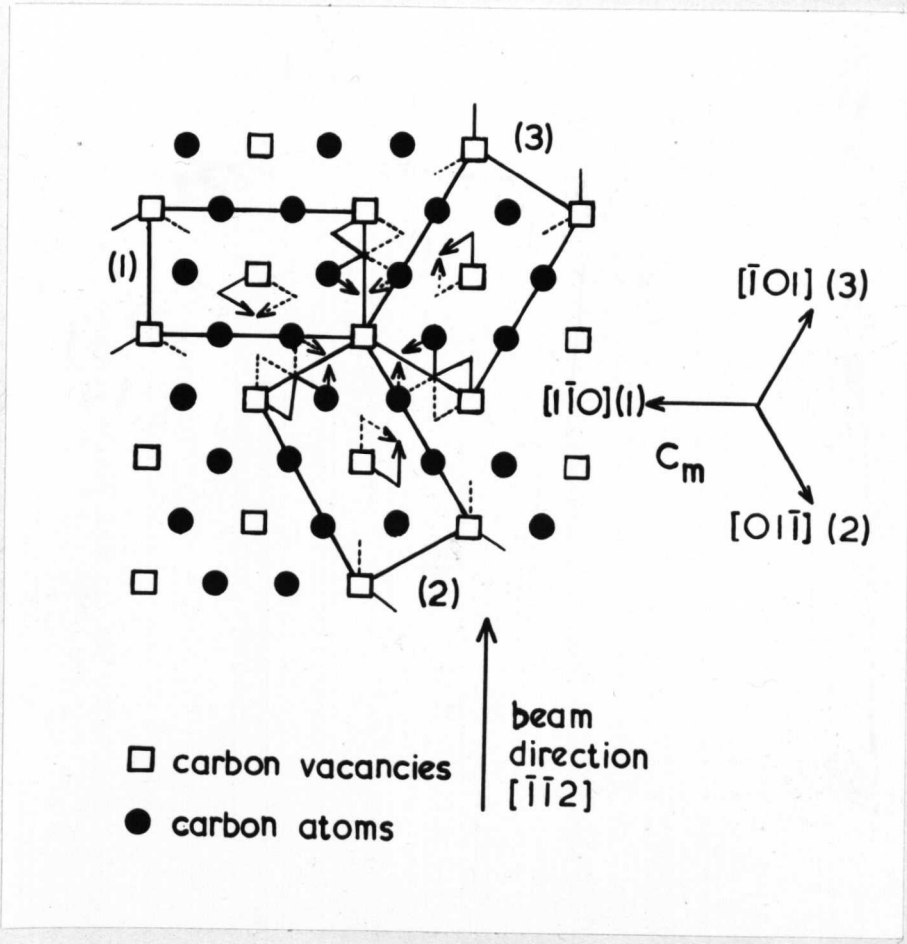

Fig. 3.2.10 The three possible c_m-axis directions within one monoclinic base plane. Full and dotted lines represent the projection of enantiomorphic vacancy zigzags.

for niobium carbide due to the stability of the faulted substructure, while for vanadium carbide the identification of domains showing this pattern has not been made with certainty, because even in annealed specimens the density of faults was usually sufficient to cause some streaking.

Fig. 3.2.9 shows how the different structure types may be derived one from another by introducing basal plane antiphase boundaries at regular intervals. In this way any number of hypothetical structures may be devised where the description of the unit cells will require increasing numbers of vacancy-containing layers*.

A sequence of ordered structures analogous to those in vanadium and niobium carbides has been observed in the compound Fe_7Se_8 (19). The selenium atoms form an hcp sublattice with the iron atoms occupying the octahedral interstices. Due to the small iron deficiency from the NiAs-type structure, ordering of the remaining iron atoms is found. Only alternate layer-planes contain vacancies, and the distribution within a partially full layer is always the same, except the partially full layers may be arranged with different stacking sequences. Ordered compounds with c_h-axes two-, three-, and four-times that of the parent disordered cell are found within limited temperature ranges, with the shorter c_h-axis forms stable in the higher temperature ranges (these also have higher symmetry).

The banded substructure within the domains is consistent with the various types of ordered structure

* All of these possibilities will have the same V^{51} NMR spectrum as observed for the trigonal form, since the introduction of APB's will not alter the vanadium nearest- and next-nearest-neighbour carbon atom/vacancy configurations.

dicusssed above. The high density of antiphase boundaries associated with this substructure, indicates that there are only small differences in energy between the various possible stacking positions of successive part-filled layers.
The second type of antiphase vector, shown in fig. 3.2.9(b), contains a component displacement out of the basal plane. These vectors will introduce displacements that disrupt the stacking sequence of filled and part-filled carbon-atom planes. This is a relatively high energy configuration, since there is a low number of these antiphase boundaries (one example is shown in fig. 3.2.6(d)).

While the trigonal form has the highest symmetry, it also includes the greatest number of layer-planes, and thus might be expected to be more stable at lower temperatures. Although no sharp delineation in temperature stability has been observed, there is some evidence in vanadium carbide (14) that the monoclinic B2 form is stable at lower temperatures, and thus it is possible that the trigonal and monoclinic B2 forms coexist in a metastable state in highly faulted domains.

REFERENCES

1. E.K.Storms, "The Refractory Carbides", (Academic Press, New York, 1967).
2. N.S.Gorbunov, N.A.Shishakov and C.G.Saidkov, Izv. Acad. Nauk. SSSR, 11, 2093 (1961).
3. G.E.Hollox, Private Communication.
4. H.Goretzki, Phys. Stat. Sol., 20, K141 (1967).
5. J.-L.Chermant, P.Delavignette and A.Deschanvres, J. Less-Common Metals, 21, 89 (1970).
6. E.Parthé and K.Yvon, Acta Cryst., B26, 153 (1970).
7. H.Lipson in Prog. Met. Phys., 2, ed. B.Chalmers (Interscience, New York, 1950).
8. J.Van Landuyt, R.Gevers and S.Amelinckx, Phys. Stat. Sol., 7, 519 (1964).
9. E.Rudy, St.Windisch and C.E.Brukl, Planseeber. Pulvermet., 16, 3 (1968).
10. E.K.Storms, B.Calken and A.Yencha in "Transition Metal Carbides and Nitrides", L.E.Toth (Academic Press, New York, 1971).
11. N.Terao, Japanese J. Appl. Phys., 3, 104 (1964).
12. V.G.Zubkov, L.Dubrovskaya, P.V.Gel'd, Y.A.Iskhai and Y.A.Dorafeer, Dokl. Acad. Nauk. SSSR, 184, 874 (1969).
13. J.D.Venables, D.Kahn and R.G.Lye, Phil. Mag., 18, 177 (1968).
14. J.Billingham, PhD Thesis, University of Warwick (1971).
15. C.H.de Novion, R.Lorenzelli and P.Costa, Compt. Rend. Acad. Sci. Paris, 263, 775 (1966).
16. D.Kordes, Phys. Stat. Sol., 26, K103 (1968).
17. S.I.Alyamovskii, G.P.Shveikin, P.V.Gel'd and E.M.Shchetnikov, Russ. J. Inorg. Chem., 13, 472 (1968).

18. J.Billingham and M.H.Lewis, Proc. 7th. Int. Congress on Electron Microscopy, Grenoble (1970).

19. A.Okazaki, J. Phys. Soc. Japan, 14, 112 (1959); 16, 1162 (1961).

CHAPTER FOUR

CARBIDES WITH AN HCP METAL-ATOM STRUCTURE

4.1 Introduction

This Chapter is concerned with carbon-atom ordering in vanadium and niobium hemicarbides which have hexagonal close-packed metal-atom stacking, and are based on the composition M_2C. These compounds are separated from the carbides with the NaCl-type structure by a region of composition that contains structures with mixed cubic and hexagonal metal-atom stacking. These latter structures will be examined in detail in the following Chapter.

The position of the M_2C phase in the vanadium - carbon phase diagram is shown in fig. 4.1.1, and in the niobium - carbon phase diagram in fig. 3.2.1. Both hemicarbides show very small nonstoichiometric deviations (less than 1 at.% carbon) from the M_2C composition below 1500°C. An ordered carbon-atom arrangement will therefore involve a distribution of atoms over half of the available octahedral interstices, which form a simple hexagonal sublattice. The number of possible distributions is expected to be reduced following an experimentally observed rule (2), which states that for two octahedral interstices, where one is located directly above the other along the hexagonal c-axis, only one may be occupied by a nonmetal atom. Some of the possible ordered arrangements are shown in fig. 4.1.2.

The results of previous diffraction studies on vanadium and niobium hemicarbides are summarized in Table 4.1. Although conflicting observations have been made, it is generally found that two ordered forms exist for both compounds,

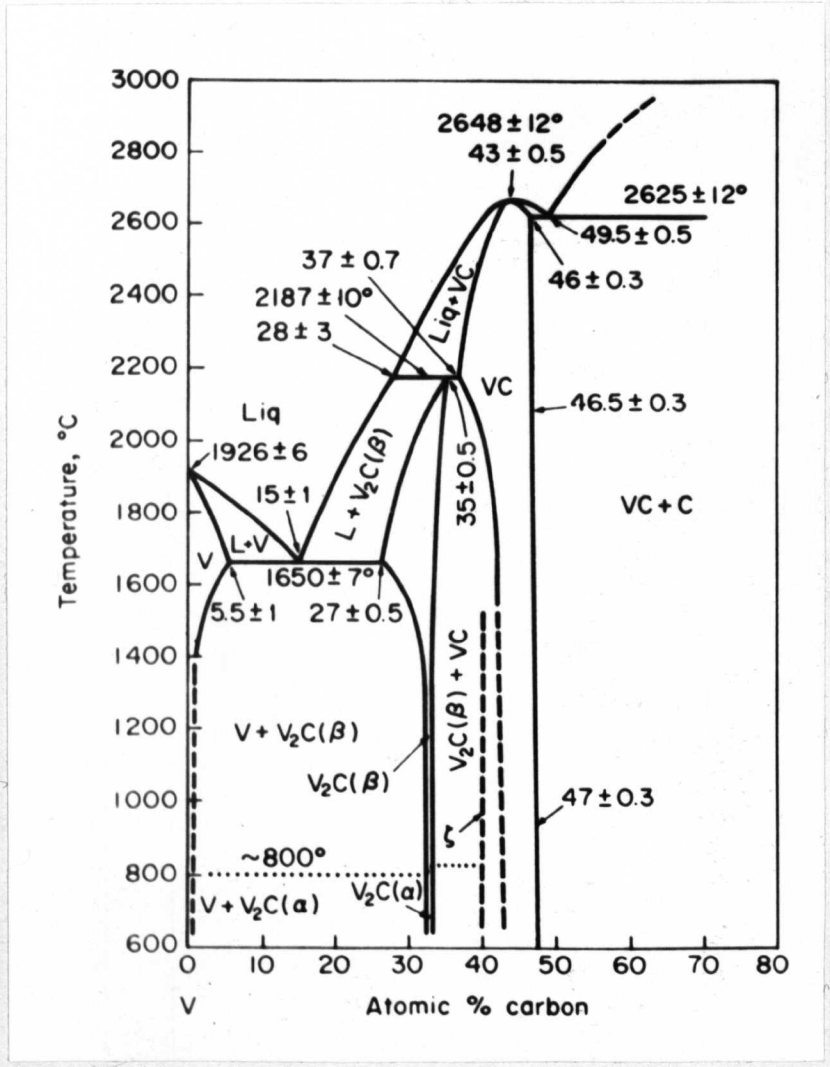

Fig.4.1.1 Phase diagram for the vanadium - carbon system, after Rudy et al. (1).

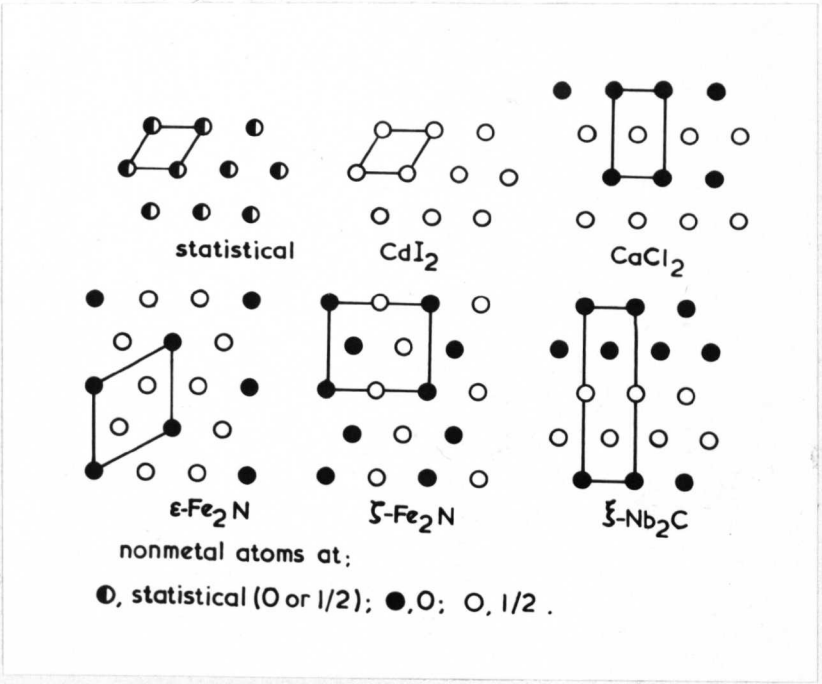

Fig. 4.1.2 Some possible ordered arrangements of nonmetal atoms in hexagonal close-packed M_2X compounds. (only nonmetal atoms are shown)

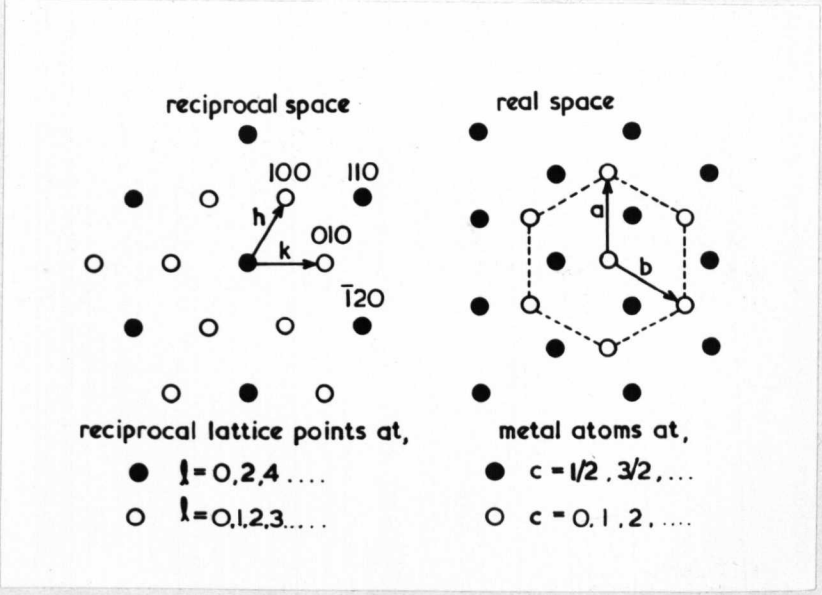

Fig. 4.1.3 Relationship between reciprocal and real space lattices for the three-axis hexagonal notation.

TABLE 4.1

Reference*	Phase	Structure	Stability range °C	Unit cell	Method
3	Nb_2C	L'3	>2500	hex. prim.	X-ray
4	V_2C	L'3	>800	hex. prim.	X-ray
5	Nb_2C	ε-Fe_2N	?	$a=\sqrt{3}a_h$ $c=c_h$	Electron
6	V_2C	L'3	1400	hex. prim.	neutron X-ray
7	V_2C	ζ-Fe_2N	<800	$a=c_h$ $b=2a_h$ $c=\sqrt{3}a_h$	X-ray
8	Nb_2C	ξ-Nb_2C	<1230	$a=2\sqrt{3}a_h$ $b=c_h$ $c=a_h$	neutron
	Nb_2C	ε-Fe_2N	>1230	$a=\sqrt{3}a_h$ $c=c_h$	"
	V_2C	ε-Fe_2N	>800	"	"
9	Nb_2C	ζ-Fe_2N	<1230	$a=4a_h$ $b=2\sqrt{3}a_h$ $c=c_h$	X-ray
	V_2C	ζ-Fe_2N	<800	"	"
	Nb_2C	ε-Fe_2N	>1230	$a=\sqrt{3}a_h$ $c=c_h$	"
	V_2C	ε-Fe_2N	>800	"	"

* In chronological order

stable at high and low temperatures, and that below the melting point for the compound the carbon atoms assume a random distribution. No previous single crystal diffraction measurements have been made, powder X-ray and neutron methods, and electron diffraction from polycrystalline films having been used.

The present analysis of hexagonal structures requires a brief explanation of the crystallographic notations that have been used. The four-index Miller-Bravais notation reflects the symmetry of crystallographically equivalent planes, but confusion can arise when indexing the reciprocal lattice in this notation. Since the present work involves analysis from diffraction patterns, the three-index hexagonal notation will be used, although the Miller-Bravais system will be retained for certain important crystallographic orientations and their corresponding reciprocal lattice sections. Two types of three-figure indexing are in common use, three-axis hexagonal and orthohexagonal. The relationship between real and reciprocal space axes for the three-axis hexagonal system is shown in fig. 4.1.3. The orthohexagonal system is useful for indexing the diffraction patterns from ordered carbon-atom structures, where the resulting symmetry may no longer remain hexagonal.

4.2 Vanadium Hemicarbide (V_2C)

4.2.1 High-Temperature Structure in V_2C

(i) Electron microscopy and diffraction

This form was found to be stable between the temperature limits of approximately 1050°C to 1500°C. Specimens quenched from below 1460°C contained wavy antiphase boundaries

separating regions of crystal that initially appeared to be homogeneous (fig. 4.2.1). On quenching from 1500°C (the highest temperature used), the microstructure showed irregular contrast (fig. 4.2.2), indicating that either the degree of long-range order in equilibrium at this temperature is low, or, the carbon-atom sublattice is disordered at the annealing temperature and some ordering takes place during the quench. Whichever of these possibilities may be correct, the temperature for the transition to the disordered state is close to 1500°C. The diffraction pattern from the specimen with more complete long-range order shows several extra superlattice reflections compared to the partially ordered specimen, where the reflections are quite diffuse. $(11\bar{2}0)$ sections (fig. 4.2.3) show diffuse streaks which are sometimes resolved into spots. These streaks also appear in $(1\bar{1}00)$ sections, but were always less intense than those in $(11\bar{2}0)$ sections, and were never resolved into discrete spots. The degree to which the streaking peaked into spots was not completely reproducible, and may have depended on the effectiveness of the quench. However, there was a tendency for more pronounced peaking at higher annealing temperatures. Extra reflections were seen in (0001) sections as shown in fig. 4.2.4, although only six of these have significant intensity.

Several of the superlattice reflections described above are attributable to multiple diffraction effects. Particular difficulty is found for hexagonal structures when attempting to eliminate possible multiple diffraction reflections when the specimen tilting procedure involves rotation about the hexagonal c-axis. Reference to fig. 4.1.3 shows that the reciprocal lattice of the hcp matrix may

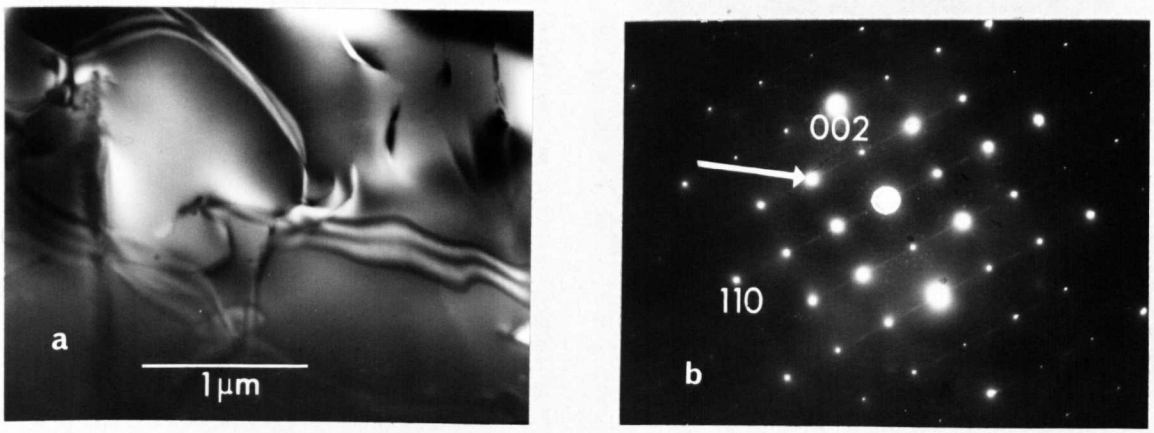

Fig. 4.2.1 Antiphase domain structure in V_2C, 5h at 1460°C. (a) DF from indicated superlattice reflection showing whole crystal diffracting with uniform contrast, (b) $(1\bar{1}00)$ section.

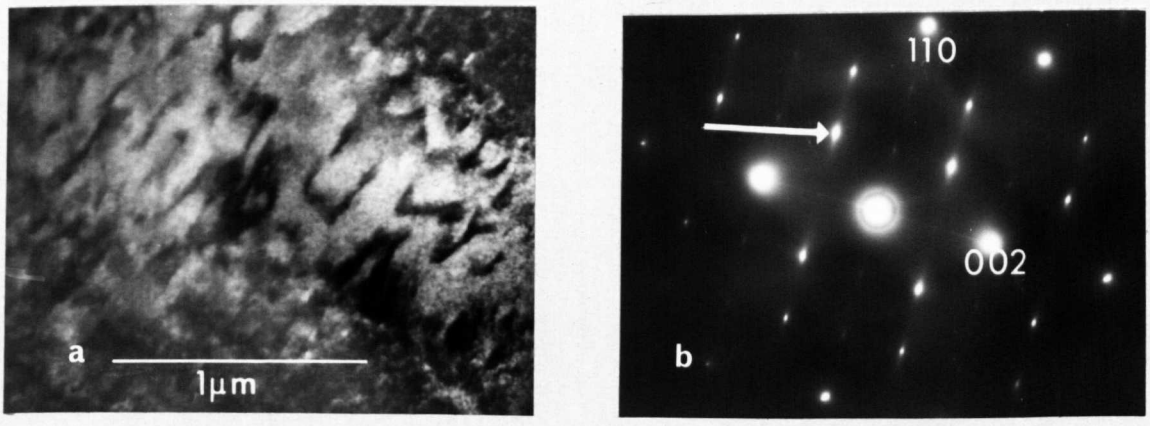

Fig. 4.2.2 V_2C annealed for 5h at 1500°C. (a) DF from indicated reflection showing irregular contrast, (b) $(1\bar{1}00)$ section with fewer reflections than in (b) above.

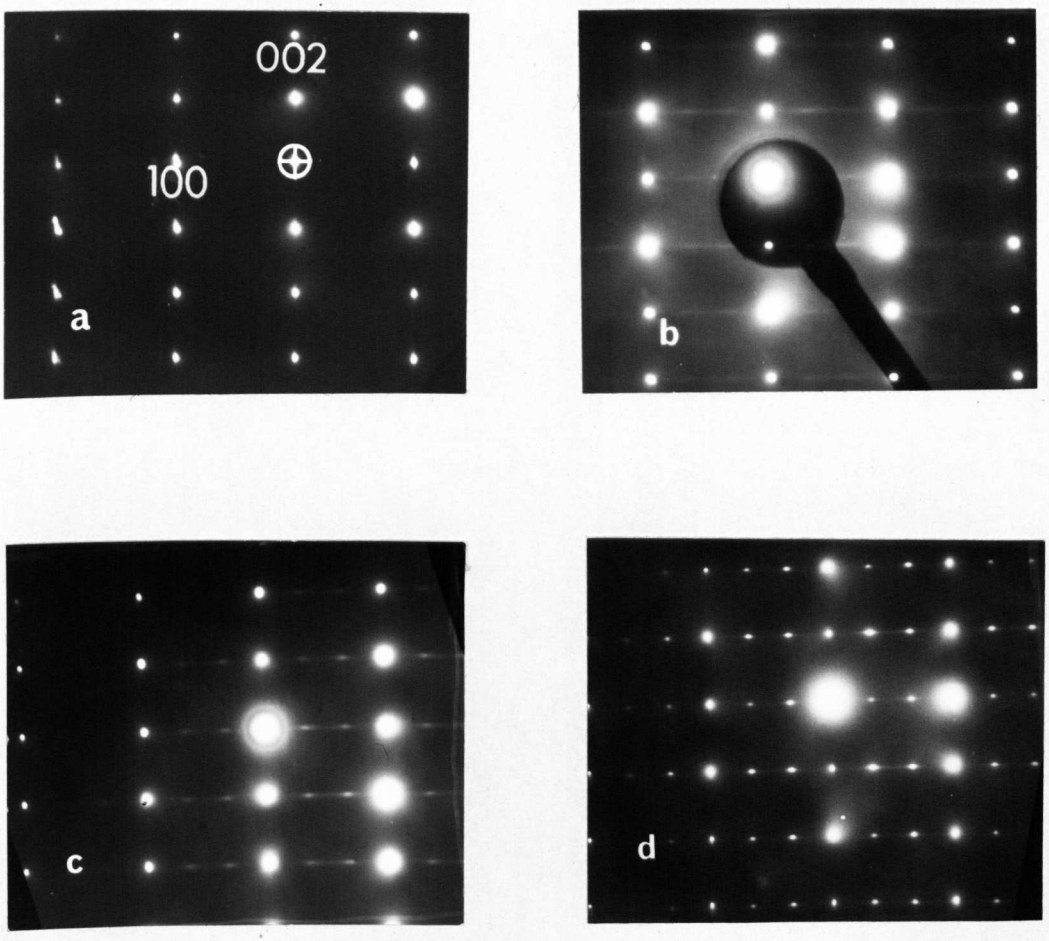

Fig. 4.2.3 $(11\bar{2}0)$ section diffraction patterns showing development of superlattice reflections and diffuse streaking.

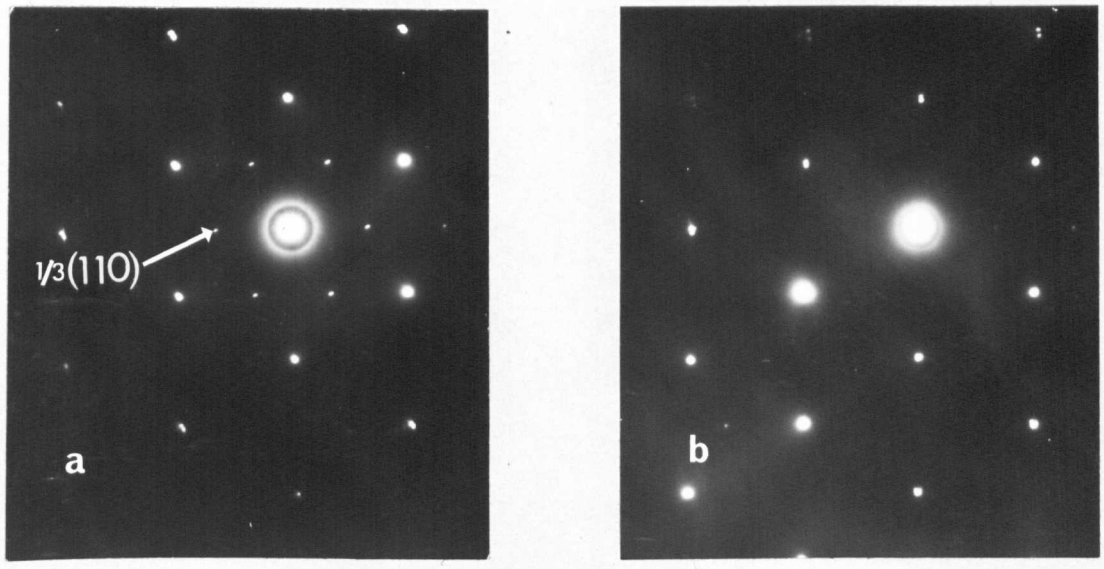

Fig. 4.2.4 (0001) section diffraction patterns showing, (a) extra reflections at 1/3(110) positions for exact orientation and (b) disappearance of these reflections after tilting the specimen.

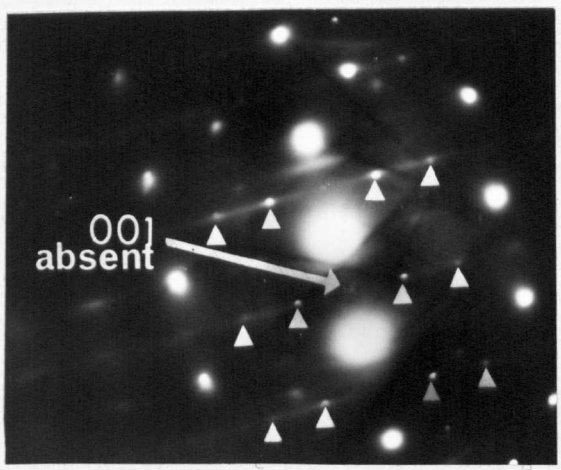

Fig. 4.2.5 $(1\bar{1}00)$ section after a small rotation about the hexagonal c-axis (allowed reflections indicated).

be considered as parallel rows of points running in the l-direction, two-thirds of which have allowed reflections at l = 0,1,2,3... , and one-third at l = 0,2,4,6... . Thus for $(1\bar{1}00)$ sections, an Ewald sphere of infinite radius would only intersect rows with allowed reflections for even values of l, and thus nonallowed reflections such as 001 would not appear.

In the present case the occurrence of an 001 superlattice reflection is of critical importance in the analysis of the ordered structure, since this would indicate differences in the occupancy of adjacent close-packed carbon-atom planes. The $(1\bar{1}00)$ section in fig. 4.2.1(b) does show such an 001 reflection, this could be either an allowed superlattice reflection, or formed by multiple diffraction from a combination of other superlattice reflections. It is thus necessary to rotate the specimen about the hexagonal c-axis to supress sufficiently the remaining superlattice reflections, but not to excite a row of fundamental reflections with odd values of l. In the rotated diffraction pattern of fig. 4.2.5 the 001 and 1/3(110) reflections have zero intensity, and the remaining reflections should be compared with those from the partially ordered structure (fig. 4.2.2(b))*

The reflections at 1/3(110) positions in the (0001) section (fig. 4.2.4(a)) are due to multiple diffraction from the first-order Laue zone. A very small

* A close analogy is seen here to the diffraction patterns from Ti_2C, where in the partially ordered condition only the allowed reflections are seen, whereas in the fully ordered condition multiple diffraction effects give rise to nonallowed reflections.

displacement from this exact orientation causes the excitation of a different group of six similar reflections around one of the fundamental reflections. For slightly larger displacements the reflections disappear altogether. For the $(11\bar{2}0)$ sections, rotation about the hexagonal c-axis causes extinction of alternate rows of superlattice reflections and streaks. Forming the image with one of the allowed superlattice reflections in this orientation reveals the substructure shown in fig. 4.2.6. Any one of these reflections from the particular $(11\bar{2}0)$ section produces dark-field images in which the same small regions are in bright contrast. This indicates that the reflections in each of the three possible $(11\bar{2}0)$-type sections originate from one particular orientation of the small bright regions seen in fig. 4.2.6.

(ii) Structure of the high-temperature ordered phase

As the distribution of superlattice reflections for the high-temperature forms of Nb_2C (section 4.3.1) and V_2C were found to be very similar, the possible types of carbon-atom ordering will be discussed together.

Reference to Table 4.1 shows that the carbon-atom arrangement in this form was most often found to be similar to the nitrogen-atom distribution in ε-Fe_2N (see fig. 4.1.2). The close-packed nitrogen-atom planes in this structure are alternately 1/3- and 2/3-occupied. This arrangement results in an 001 superlattice reflection, and the hexagonal six-fold rotation axis is retained on ordering. In (8) the neutron diffractogram of V_2C shows the 001 reflection as a very small peak, while this reflection is not marked on the X-ray powder photograph of (9).

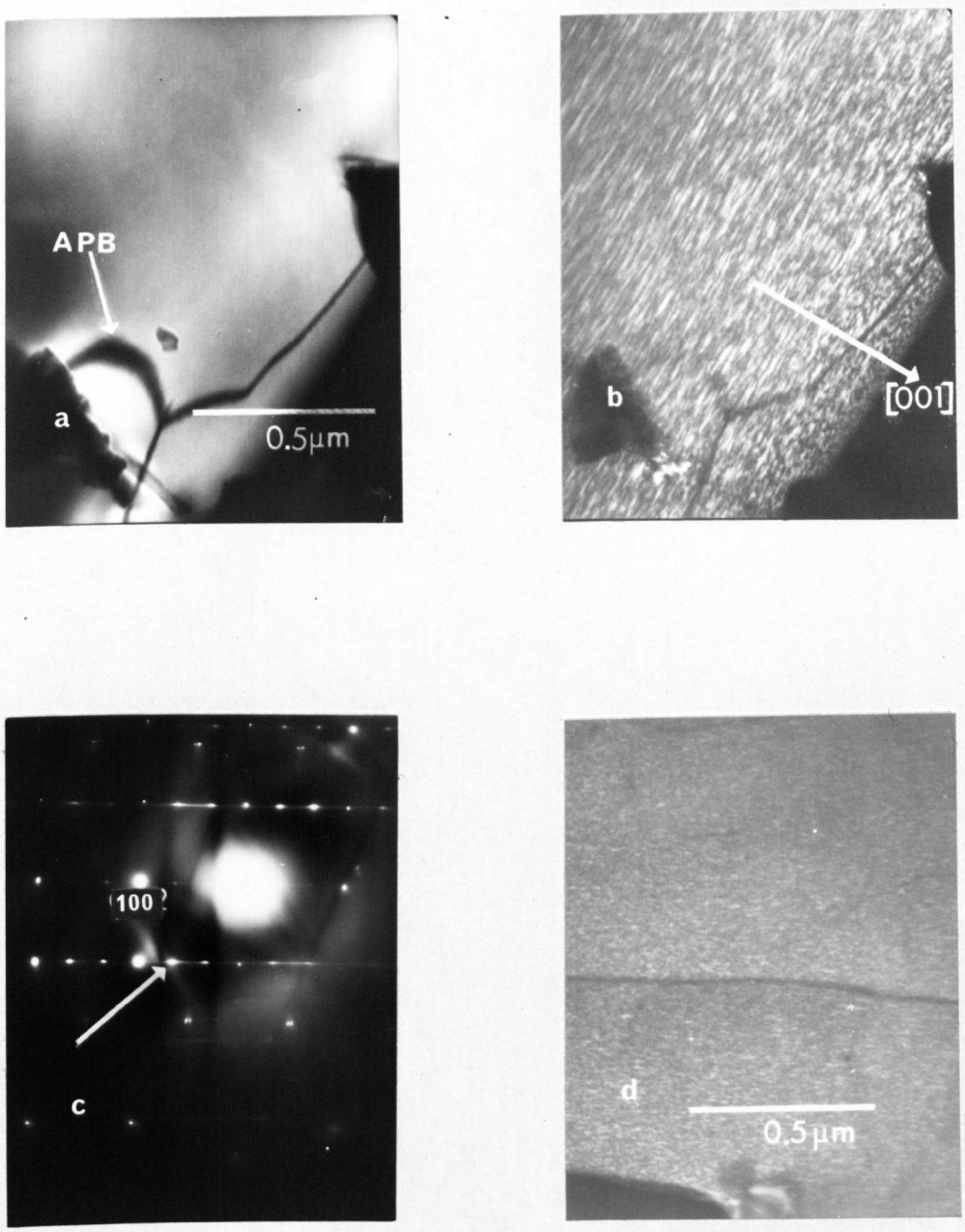

Fig. 4.2.6 Substructure in the high-temperature form of V_2C. (a) DF from superlattice reflection in $(1\bar{1}00)$ section, (b) same area as (a), DF from indicated reflection in (c) $(11\bar{2}0)$ section, (d) similar to (b) but with finer substructure.

In (5) neither the 001 nor 003 reflections are visible on the electron diffraction ring pattern of Nb_2C. However, in all these studies the remaining superlattice reflections were consistent with an ε-Fe_2N-type structure, and this was then the assigned structure. The absence of the 001 reflection from partially ordered specimens, and its formation by multiple diffraction in fully ordered specimens in the present work, indicates that the choice of the ε-Fe_2N type of structure is incorrect, since the calculated electron diffraction intensities of the 001 reflection and other strong superlattice reflections for an ε-Fe_2N-type structure are similar.

The structural information obtained from the electron micrographs is that the set of occupied carbon-atom positions that gives rise to the superlattice reflections in $(1\bar{1}00)$ sections has hexagonal symmetry, since the whole crystal is diffracting with uniform contrast when these reflections are used to form dark-field images. Thus these carbon-atom positions have only one orientation with respect to the hexagonal matrix. The weaker reflections in $(11\bar{2}0)$ sections are associated with atom positions having non-hexagonal symmetry. Thus the small regions giving bright contrast in fig. 4.2.6 have one of several possible orientations with respect to the matrix.

A reciprocal lattice was tentatively constructed including the superlattice reflections in the $(1\bar{1}00)$ sections, and those in one $(11\bar{2}0)$ section. All the reflections were indexed with respect to a monoclinic unit cell containing eighteen octahedral interstices. However, a space group could not be assigned to the unit cell, and the trial-and-error computer programme did not

give any possible ordered arrangements using this diffraction data.

The interstitial atom positions found in Ni_3N, consisting of 1/3-filled (0001) plane layers, is the only hexagonal arrangement which will maintain equal occupancy of the basal plane layers, since it is impossible to have a 1/2-filled layer possessing hexagonal symmetry. However, an Ni_3N-type structure will give rise to reflections which are not presently observed, i.e. at 1/3(110). Various other arrangements were tried without success, and the nature of the ordered carbon-atom distribution appears intractable.

A small level of impurity atoms may influence the kinetics of ordering or the particular type of structure adopted, but will not be included in the point positions of the unit cell. Thus for one impurity atom (for example oxygen) to be included in the proposed unit cell, a concentration of at least 3 at.% would be required. Another possibility is that incipient precipitation of the low-temperature modification in a metastable form takes place during quenching. This could result in a redistribution of the carbon atoms between the layer planes from the 1/3- and 2/3-occupied sequence of the ε-Fe_2N-type structure to the 1/2-full sequence of the low-temperature modification, thus eliminating the superlattice reflection at 001.

4.2.2 Low-Temperature Structure in V_2C

(i) Electron microscopy and diffraction

Specimens annealed below 1000°C showed a different type of ordered-domain microstructure from that described above. The superlattice reflections for the low-temperature form are associated with specific domain orientations.

The micrographs in fig. 4.2.7 show the (0001) section diffraction pattern where each 1/2(110) superlattice reflection is formed from one of the three possible orientations of domains revealed in the dark-field images. Fig. 4.2.7(f) was obtained from a specimen of the V/V_2C eutectic, where the hemicarbide phase is most carbon-deficient. Although the maximum temperature for the transformation to the low-temperature modification showed no appreciable variation with composition on the carbon-deficient side of $VC_{0.5}$, the domains formed sluggishly from the high-temperature phase and were much smaller than those for stoichiometric compositions. Planar antiphase boundaries are observed within the individual domains, and in the (0001) orientation of the specimen shown in fig. 4.2.7 the domain-domain boundaries are parallel to the electron beam and lie in $\{1\bar{1}00\}$ planes. In fig. 4.2.8 both types of boundary are inclined to the beam. Two other reciprocal lattice sections from single domain orientations are shown in fig. 4.2.9.

(ii) Structure of the low-temperature ordered phase

The ζ-Fe_2N-type structure (see fig. 4.1.2) assigned to this modification of V_2C by Yvon et al. (7) is found to be correct, apart from a minor alteration in the carbon-atom positions. The indexed reciprocal lattice is shown in fig. 4.2.10(a), and the orthorhombic unit cell dimensions are related to the parent cell by,

$$a_o = c_h$$
$$b_o = 2a_h$$
$$c_o = \sqrt{3}a_h$$

Eight vanadium atoms occupy the 8(d) positions, and four carbon atoms the 4(c) positions, in the space group Pbcn.

Fig. 4.2.7 Three orientations of orthorhombic domains in V_2C annealed for 120h at 850°C. (a) BF, (b), (c), and (d) DF from 1/2(110) reflections indicated in (e) (0001) section, (f) hemicarbide phase in V/V_2C eutectic specimen showing APB's within one orientation of domains in bright contrast.

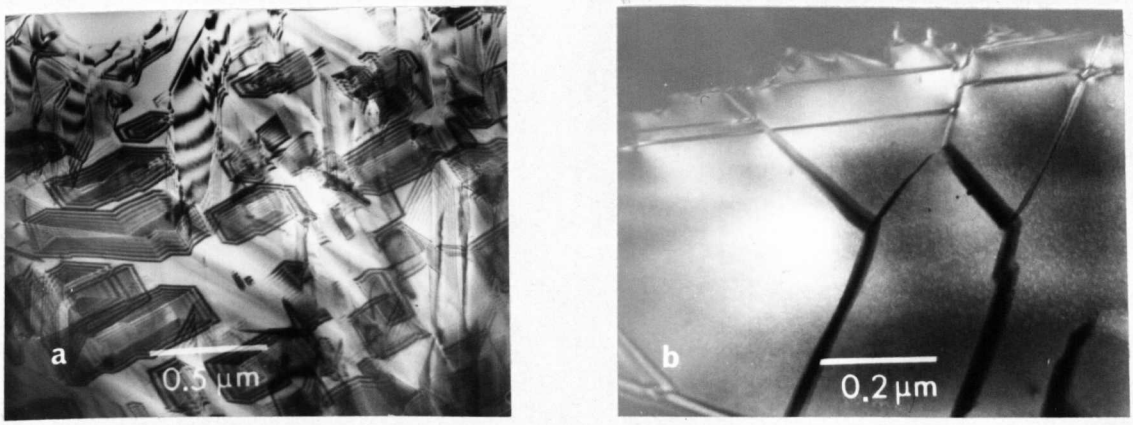

Fig. 4.2.8 (a) BF domain/domain boundaries inclined to beam showing δ-fringe contrast, (b) DF showing inclined APB's within one domain orientation.

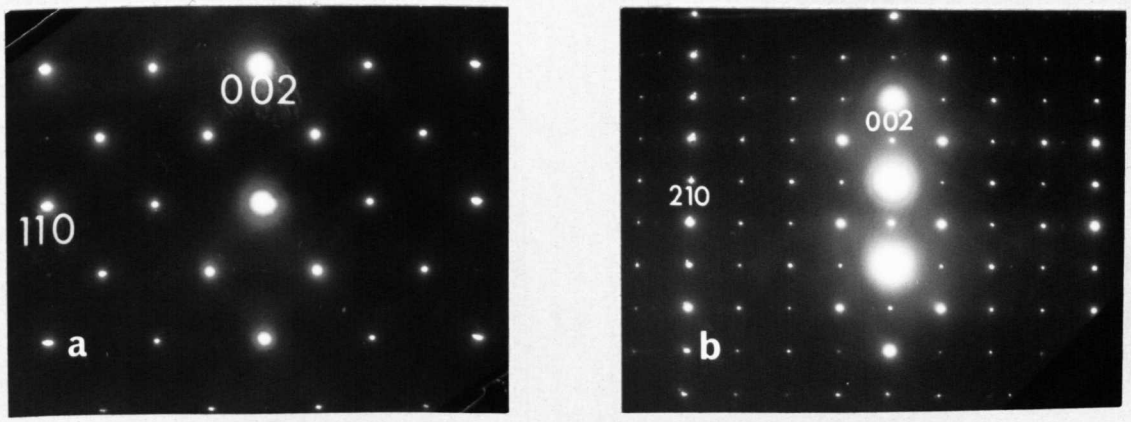

Fig. 4.2.9 (a) $(1\bar{1}00)$ section and (b) $(31\bar{4}0)$ section diffraction patterns from single orthorhombic domain orientations

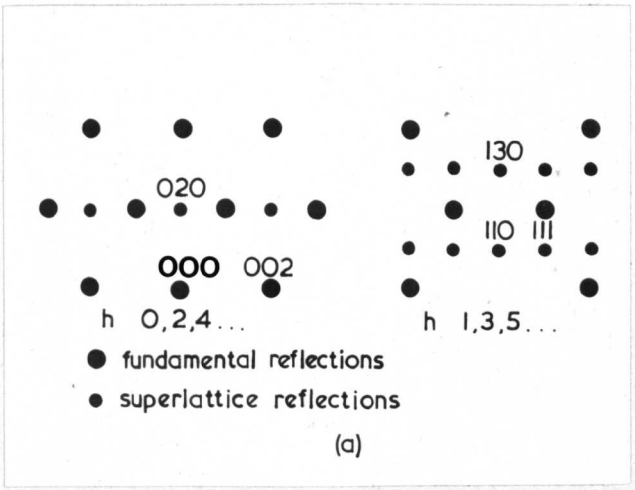

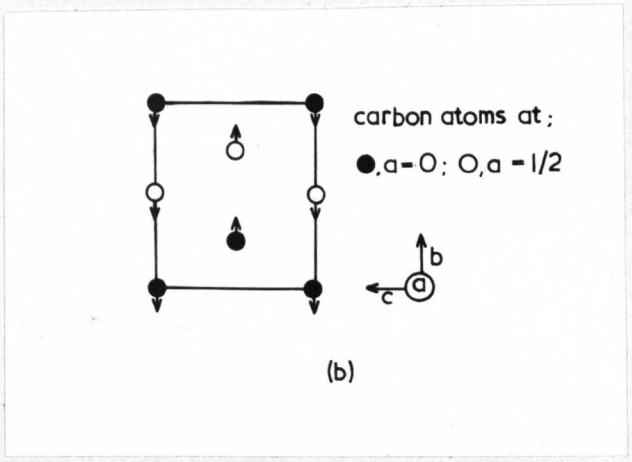

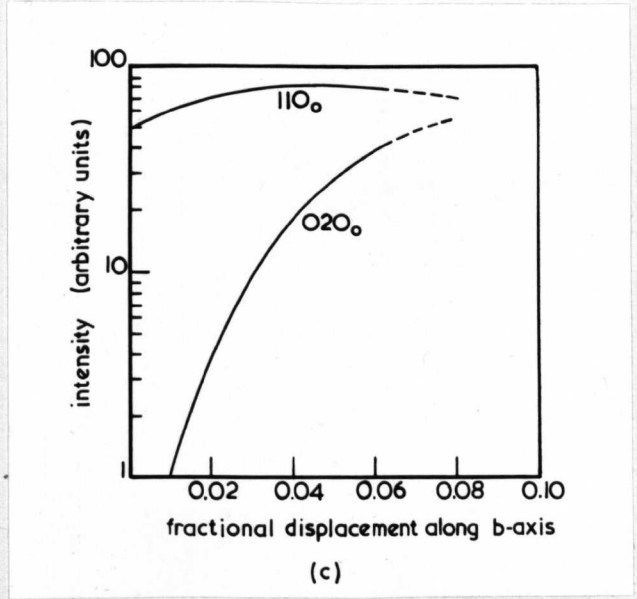

Fig. 4.2.10 Low-temperature modification of V_2C.
(a) indexed reciprocal lattice,
(b) unit cell showing only the carbon atom positions and the direction of displacement,
(c) intensities of the 110_o and 020_o superlattice reflections as a function of fractional displacement along the b-axis.

The observed reflections are the same as those found in (7), apart from the presence of weak reflections at 1/2(110) positions, i.e. 020_o. The low intensity of these reflections indicates that there is a slight displacement of the carbon atoms along the b-axis, as shown in fig. 4.2.10(b). This may be interpreted as a repulsion between carbon atoms on the same close-packed plane. The magnitude of the displacement may not be accurately determined, since this would require correct values for the relative intensities of the superlattice reflections. However, from fig. 4.2.10(c), where the computed intensities of the 020_o and 110_o (strong superlattice reflection) reflections are plotted against the displacement of the carbon atoms along the b-axis, the value of this displacement is probably less than 0.02b, or about 0.1Å.

4.2.3 Specimens Containing Two Ordered Phases

At only one annealing temperature (1030°C) were both ordered forms observed in equilibrium. The $(1\bar{1}00)$ section in fig. 4.2.11 shows reflections characteristic of both superlattices as well as a number of weaker reflections caused by multiple diffraction from combinations of the two different sets of allowed reflections. The dark-field images show alternate bands of the two ordered phases in this $(1\bar{1}00)$ orientation.

4.3 Niobium Hemicarbide Nb_2C

4.3.1 High-Temperature Structure in Nb_2C

(i) Electron microscopy and diffraction

This ordered structure, which gave diffraction patterns similar to those of the high-temperature ordered phase in V_2C, was observed in Nb_2C above 1020°C. The diffraction pattern from a $(1\bar{1}00)$ section is shown in fig. 4.3.1, together with a dark-field micrograph in which

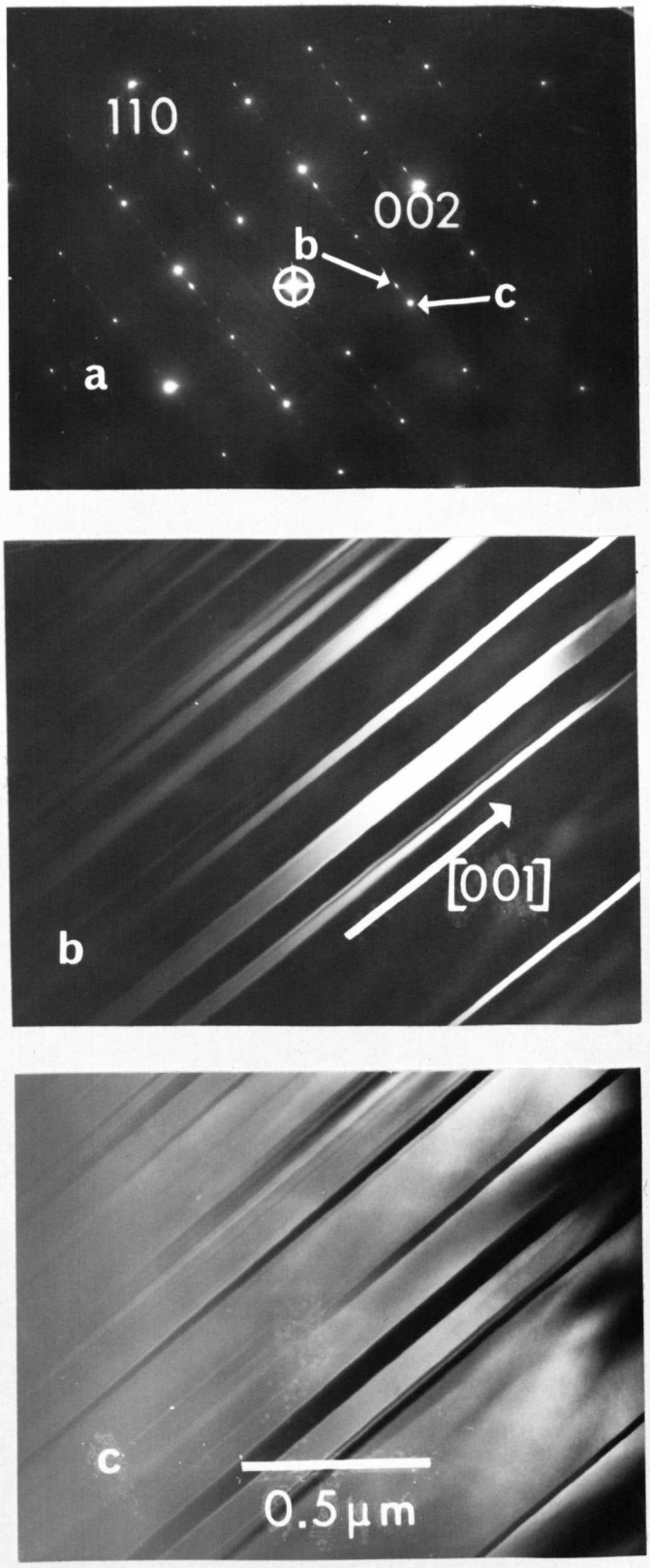

Fig. 4.2.11 Two ordered phases in V_2C, 65h at 1030°C. (a) $(1\bar{1}00)$ section showing superlattice reflections from both phases, and weak multiple diffraction reflections, (b) DF low-temperature and (c) DF high-temperature modifications.

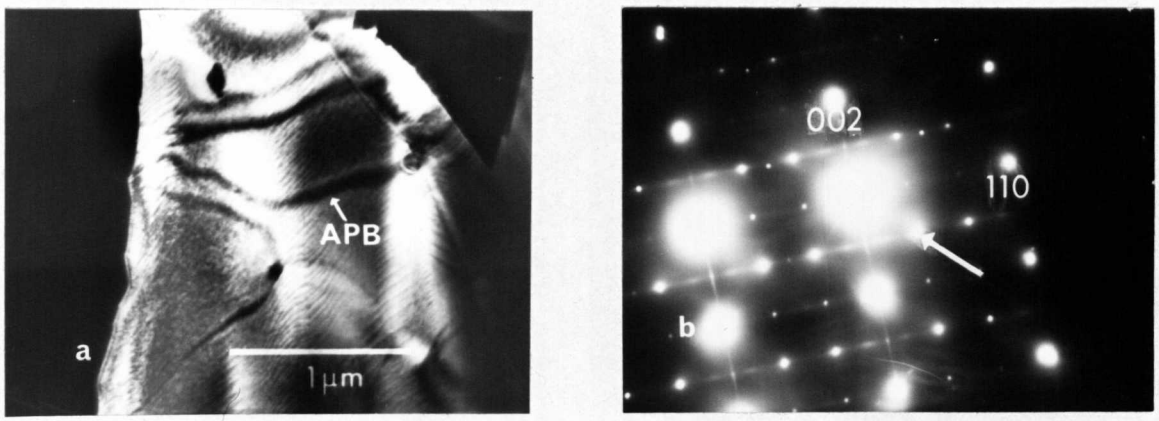

Fig. 4.3.1 High-temperature modification of Nb_2C. (a) DF showing antiphase domain structure (striations are a cleavage effect), (b) $(1\bar{1}00)$ section similar to V_2C (fig. 4.2.1(b)).

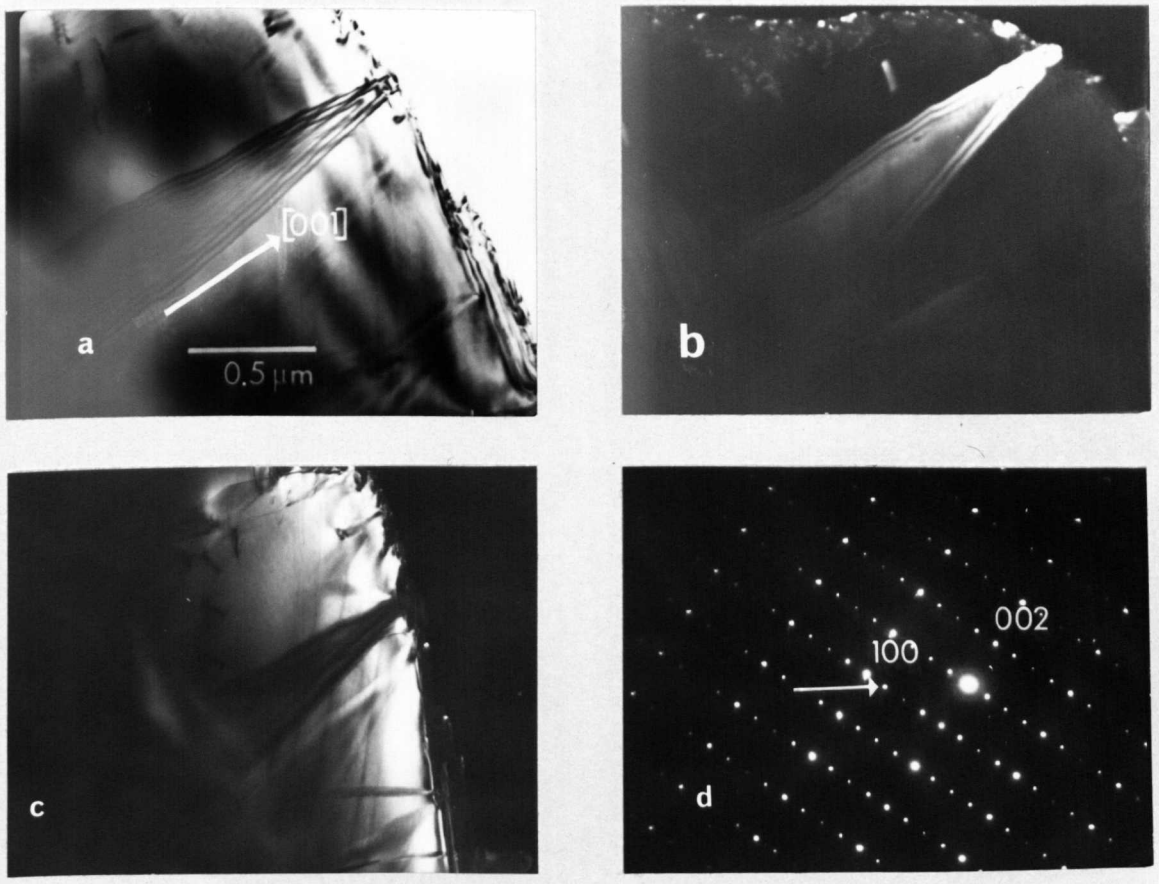

Fig. 4.3.2 Low-temperature orthorhombic modification of Nb_2C. (a) BF, (b) DF from superlattice reflection indicated in (d) $(11\bar{2}0)$ section, (c) DF from second domain orientation.

several antiphase boundaries are visible. The pronounced streaking observed in $(11\bar{2}0)$ sections of V_2C is very much weaker in Nb_2C, with no evidence for modulation of the streaks into distinct reflections. Thus it was impossible to reveal any fine substructure (as observed for V_2C) by dark-field imaging.

The possible form of the carbon-atom ordering in the high-temperature modification of Nb_2C has been dealt with in section 4.2.1(ii) in conjunction with vanadium hemicarbide, and no further discussion is necessary.

4.3.2 Low-Temperature Structure in Nb_2C

(i) Electron microscopy and diffraction

The series of micrographs and diffraction patterns in fig. 4.3.2 show two of the three possible orientations of orthorhombic domains characteristic of the low-temperature ξ-phase modification of Nb_2C. In the dark field micrograph taken from the indicated reflection in the $(11\bar{2}0)$ section, one domain orientation is in bright contrast, while the other orientations give no superlattice reflections in this reciprocal lattice section. However, after rotating the specimen, superlattice reflections of the second orientation are intersected, as shown by the dark-field micrograph in fig. 4.3.2(c). No superlattice reflections are observed in (0001) or $(1\bar{1}00)$ sections.

(ii) Structure of the low-temperature ordered phase

The present investigation shows that the structure of the low-temperature modification is similar to that determined by Yvon et al. (8). The reciprocal lattice constructed from the diffraction data described above may be indexed for an orthorhombic unit cell (see fig. 4.1.2)

which is related to the parent lattice by,

$$a_o = 2\sqrt{3}a_h$$
$$b_o = c_h$$
$$c_o = a_h$$

The observed reflections are consistent with the space group $Pna2_1$, although several reflections allowed for the occupied positions in this space group have zero intensity. In particular the 200_o reflection, which would be observed in the basal plane section, is absent. This implies that the carbon atoms are equally spaced along the a-direction, in contrast to the small distortion found in the low-temperature modification of V_2C.

REFERENCES

1. E.Rudy, St.Windisch and C.E.Brukl, Planseeber Pulvermet., 16, 3 (1968).
2. E.Parthé and K.Yvon, Acta Cryst., B26, 153 (1970).
3. E.K.Storms and N.H.Krikorian, J. Phys. Chem., 66, 1471 (1960).
4. E.K.Storms and R.J.McNeal, J. Phys. Chem., 66, 1401 (1962).
5. N.Terao, Japanese J. Appl. Phys., 3, 104 (1964).
6. A.L.Bowman, T.C.Wallace, J.L.Yarnell, R.G.Wenzel and E.K.Storms, Acta Cryst., 19, 6 (1965).
7. K.Yvon, W.Rieger and H.Nowotny, Monatsh. Chem., 97, 689 (1967).
8. K.Yvon, H.Nowotny and R.Kieffer, Monatsh. Chem., 98, 34 (1967).
9. E.Rudy and C.E.Brukl, J. Amer. Ceram. Soc., 50, 265 (1967).

CHAPTER FIVE

DEVIATIONS FROM FCC AND HCP METAL-ATOM STACKING

5.1 Introduction

The two most common close-packed structures are based on ...ABCABC... (fcc), and ...ABABA... (hcp) stacking sequences. However, it is possible to devise an infinite number of structures which have different periodic repeat sequences of similar A, B, and C planes. These structures are known as polytypes when stacking variations occur in a compound of fixed overall chemical composition. In the present case, each metal-atom stacking sequence is usually associated with a particular concentration of nonmetal atoms. Since these compounds contain elements of fcc- and hcp-type stacking, they are often known as structures with 'mixed' metal-atom stacking.

(i) Stacking sequence notations

It is often sufficient to describe the structure of a polytype in terms of the A,B,C sequence of the close-packed planes. While the ...ABC... notation is adequate for the description of polytypes with a small periodic repeat sequence in the layer stacking, there are several other notations which give a compact and more descriptive picture of the stacking sequence. Frank (1) suggested the operator symbols Δ and ∇ for the cyclic sequence $A \rightarrow B \rightarrow C \rightarrow A$, and the anticyclic sequence $A \rightarrow C \rightarrow B \rightarrow A$ respectively. In the Zhdanov notation (2,3) the numbers of successive Frank operators of each type are summed in sequence, while Jagodzinski (4) has suggested the symbols (c), cubic, for $\nabla\nabla$ or $\Delta\Delta$, and (h), hexagonal, for $\Delta\nabla$ or $\nabla\Delta$.

The relation between these notations is given below for one of the polytypes of silicon carbide.

...ABCACBABC... SiC six layer planes in unit cell

Frank △△△▽▽▽

Zhdanov 3(△)3(▽) = 33

Jagodzinski (cchcch) = $(cch)_2$

(ii) Stacking faults in fcc and hcp structures

Since a large part of this Chapter is concerned with the observation of stacking faults in various carbides and nitrides, some preliminary background will be given on this subject. The following description of stacking faults is however limited to those that can form in an fcc or hcp metal by partial dislocation motion. The part played by the nonmetal atoms in the formation of stacking faults in these compounds will be examined later in discussion.

Three types of fault may be distinguished in the fcc structure, intrinsic, extrinsic, and twin. The intrinsic fault is formed by the passage of a single Shockley partial dislocation on a glide plane, causing displacement of all the atoms above (or below) the fault plane by $a/6\langle 211\rangle$, thus,

...ABCABCABC...

...ABC<u>B</u>CABCA...

where the dash indicates the plane where partial shear has taken place. An extrinsic fault can then be formed from an intrinsic fault by a similar displacement of all the atoms below (or above) the fault plane, thus,

...ABCABC<u>B</u>CABC...

...CABC<u>A</u>C<u>B</u>CABC...

An fcc twin is produced by partial shear on every plane above the fault plane, thus,

...ABCABCABC...

...ABCA<u>CBACB</u>...

where the arrow indicates shear on every successive plane.

In the hcp structure the basal planes are the most frequently observed glide planes. Three types of fault configuration may be distinguished. Reference to fig. 5.2.2 shows that a perfect dislocation in the basal plane with Burgers vector a [100] may dissociate into two partials, thus,

$$a\,[100] \longrightarrow a/3\,[1\bar{1}0] + a/3\,[210]$$

The passage of one of these partials will produce an intrinsic fault,

...ABABABAB...

...ABAB<u>C</u>ACA...

A second fault, also intrinsic in type, is produced by successive shear above the fault plane, thus,

...ABABABAB...

...ABA<u>CACAC</u>...

An extrinsic fault can be formed from single shear followed by repeated shear, thus,

...ABABABAB...

...ABA<u>CBABA</u>...

The fault configurations described by repeated displacements are unlikely to be formed by precisely these mechanisms. In fcc crystals twins may form from deformation or growth accidents. Even the extrinsic fault is found to

be relatively rare. In the hcp structure the repeated shear configurations are likely to be produced by the removal of a close-packed plane by vacancy condensation, or the insertion of a close-packed plane by interstitial condensation, followed by single shear.

(iii) Structures with mixed metal-atom stacking

Five different stacking variations of the transition-metal atoms have been distinguished for the close-packed carbides and nitrides. Apart from the fcc and hcp end-members, there are also sequences corresponding to $(hcc)_2$, $(hhc)_3$, and $(hhcc)_3$. The nine- and twelve-layer structures are conventionally known as ε- and ζ-phases respectively. All the various structures may be described by hexagonal cells, and are shown in fig. 5.1.1 as sections through the $(11\bar{2}0)$ plane. This plane intersects all three possible stacking positions. In (h)-stacking layers the octahedral interstices are situated directly over each other, and the ratio of the distances between nearest octahedral interstices in successive layers for (h) and (c)-stacking is 2:3. The 'ideal' compositions shown in fig. 5.1.1 may be found by restricting the number of occupied interstices such that only one nonmetal atom is associated with each pair of interstices directly above one another (as found in the compounds with pure hcp metal-atom stacking).

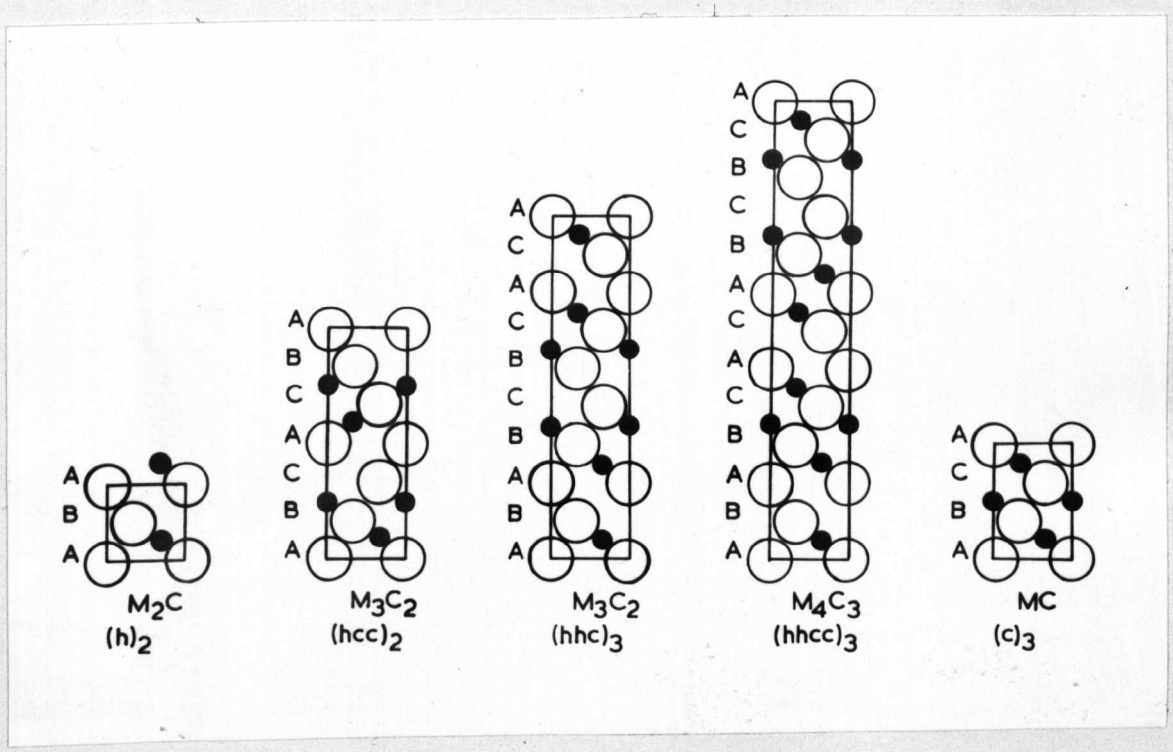

Fig. 5.1.1 Stacking variations of close-packed carbides and nitrides, shown as sections through the $(11\bar{2}0)$ plane. Large open circles, metal atoms; small filled circles, nonmetal atoms.

5.2 Compounds Containing Stacking Faults

5.2.1 Electron Microscope Contrast

(i) Stacking faults

The theory of electron microscope contrast for stacking faults is well established (5-8). Analysis is readily accomplished from micrographs recorded under two-beam conditions, with due regard to specimen thickness and deviation from the Bragg position. For extrinsic and intrinsic faults in the fcc structure, fringe contrast is observed when the phase-change on traversing the fault plane, given by $\alpha = 2\pi \mathbf{g}.\mathbf{R}$, has the values $\pm 2\pi/3$, $4\pi/3$ etc. For positive or negative α the outermost fringe contrast relative to the perfect crystal background is reversed. In dark-field images the outer-fringe contrast at the upper surface is the same as in bright-field, whereas at the lower surface the fringe contrast is reversed. The upper and lower surfaces of the fault may be distinguished by the overall contrast in dark-field with w (a dimensionless parameter relating to the deviation from the Bragg position given by $s\xi_g$) negative or positive (9).

During examination of the stacking faults in the various compounds, it was found that in dark-field images reversal from the 'correct' outer-fringe contrast occured for small deviations in one direction only from the position w = 0. Since it was thought that this effect might be peculiar to the transition-metal compounds, it was decided to make a theoretical and experimental investigation of the fringe contrast from metal-alloy specimens, and then to compare these results with the present observations.

In a theoretical study of the rule proposed by

Hashimoto et al. (5) giving the contrast of outer fringes of a stacking fault, Head (10) found the validity of the rule in dark-field for varying thickness of specimen was symmetrical about $w = 0$, up to $w = \pm 0.5$. In order to check this rule, stacking fault intensity profiles were computed for different deviation, thickness, absorption length etc., making use of the equations for two-beam dynamical scattering quoted by Woods (11), which are based on the original work of Van Landuyt et al. (12).

Reversal in the outer-fringe contrast was found in the plotted profiles for only one sense of deviation from the Bragg position (up to $w = \pm 0.6$). These profiles were then compared with those found from the examination of a Cu- 8wt.% Al alloy which contained both intrinsic and a small number of extrinsic stacking faults. The contrast reversal in the profiles from the metal alloy occurred to the same extent as in the transition-metal compounds, though in both instances for slightly smaller values of w than found theoretically. These results may be summarized in that reversal from the 'correct' outer-fringe contrast occurs for those dark-field images when, (a), $w>0.3$ with an operating reflection that gives bright outer fringes in bright-field, and (b), $w<-0.3$ with an operating reflection that gives dark outer fringes in bright-field. Care must be taken especially for (b), where it is often necessary to record dark-field images with w negative to obtain good diffracted intensity.

(ii) Partial dislocations

Bounding Shockley partial dislocations are invisible for $\mathbf{g}.\mathbf{b} = \pm 1/3$ (13), and for $\mathbf{g}.\mathbf{b} = -2/3$ with

large w, and visible for g.b = $\pm 2/3$ (14) (with w<0.4 for g.b = -2/3)*. A Frank partial dislocation bounding a fault may be distinguished from a Shockley by comparing a number of micrographs recorded using various two-beam reflections, or from the residual contrast when g.b = 0. Since the Frank dislocation is edge-type, there will be a displacement perpendicular to the Burgers vector (a/3[111]) and the dislocation line. This displacement gives a characteristic black and white dot contrast at one surface of the thin foil for non-zero values of $\mathbf{g.b} \wedge \mathbf{u}$, where **u** is the unit vector along the positive direction of the dislocation line.

It should be noted that in the following sections describing the observations made on stacking faults and partial dislocations, that the sets of g-vectors used at any one time, while being self-consistent, are arbitrary with respect to the choice of foil normal from the form {hkl}.

5.2.2 Observation of Stacking Faults

(i) Niobium carbide

In $NbC_{0.5}$, quenched from the reaction sintering temperature, the observed fringe contrast was associated with the precipitation of niobium hemicarbide from the fcc monocarbide matrix. The orientation relation between these phases is,

$$(111)NbC \parallel (0001)Nb_2C$$
$$\langle 110\rangle NbC \parallel \langle 11\bar{2}0\rangle Nb_2C$$

* Although these conditions for g.b = $\pm 2/3$ are generally true, Clarebrough (15) has shown that the visibility criterion for this g.b product depends in a complicated way on w, specimen thickness, and g-vector.

In fig. 5.2.1(a) two types of fringe contrast are seen. There is δ-fringe contrast at the interface between the monocarbide and thick region of Nb_2C, while the other fringe contrast, although not of one definite type, does show some similarity to stacking fault contrast.
The regions giving this second type of contrast are believed to be thin lamellae of Nb_2C. It has been shown (16) that for a series of overlying faults, the observed contrast will be given to a first approximation by the sum of the phase-changes at each fault. The observed contrast should then be the same as that for a single intrinsic or extrinsic fault, or zero when the total phase-change is an integral multiple of 2π. Humble (17) showed this would be correct only in the limiting case for all the faults lying on one plane. Even when the faults lie on adjacent planes the phase-change at each fault will alter the way in which the electron waves propagate in the region between the faults. While the difference in contrast between two adjacent intrinsic faults and one extrinsic fault is very small, weak fringes are observed for three similar faults where none would have been previously predicted. It would be expected that the fringe profile will show a greater deviation from that for a single fault as the number of overlying faults is increased. As yet no calculations have been made for the contrast expected for a large number of closely spaced faults. For a thick lamella of Nb_2C, which may be considered to consist of faults spaced on alternate planes with respect to the fcc matrix, δ-fringe contrast will be observed since the electron beam has effectively traversed an interphase boundary, i.e. fcc → hcp.

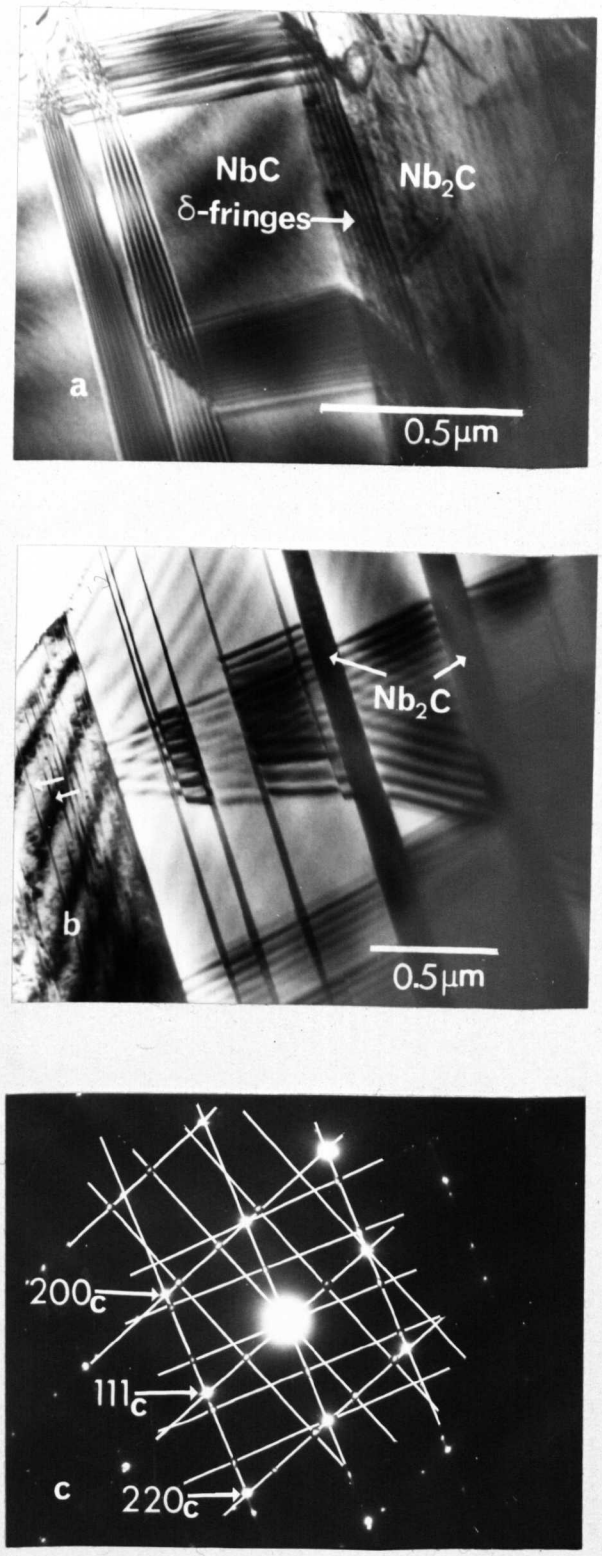

Fig. 5.2.1 Precipitation of hcp-Nb_2C lamellae from a matrix of fcc-NbC. (a) δ-fringe contrast at hcp/fcc interface, and pseudo-stacking fault contrast at thin plates of Nb_2C, (b) stacking faults in Nb_2C (arrowed), (c) (110)-fcc/$(11\bar{2}0)$-hcp section showing orientation relation between the two phases (hexagonal $(11\bar{2}0)$ grids outlined).

As there was a whole range of Nb_2C lamella sizes, no fault analysis was made even where the fringes appeared similar to those for single faults, since these fringes may have been caused by a small number of overlying faults.

Stacking fault type of contrast is seen in the large region of Nb_2C in fig. 5.2.1(b), where the fault plane lies in the basal plane. The formation of the Nb_2C lamellae is a possible example of the 'stacking fault reflection' mechanism. This is discussed in greater detail in section 5.3.4(iii).

(ii) Vanadium hemicarbide

Stacking faults were observed in V_2C specimens which were quenched from 1500°C. It is expected that these faults will arise from the splitting of perfect dislocations lying in the basal plane, into two partial dislocations separated by an area of intrinsic stacking fault. This corresponds to the first type of stacking fault in the hcp structure described in section 5.1(ii). The mode of dissociation will differ according to whether the dislocation lies in an A or B plane. Fig. 5.2.2 shows that if a perfect dislocation ab on an A plane dissociates as ab = ac + cb, the same dislocation will then dissociate as ab = cb + ac on a B plane. There are six (including negatives) perfect dislocation Burgers vectors in the basal plane, and thus twelve types of dissociation reaction.

For the purposes of electron microscope contrast only three partial dislocation Burgers vectors, $a/3[2\bar{1}0]$, $a/3[\bar{1}20]$ and $a/3[1\bar{1}0]$ need be considered. The two micrographs shown in fig. 5.2.3 were taken under two-beam conditions with (a), $g = 110$ and (b), $g = 1\bar{1}\bar{1}$. Table 5.1

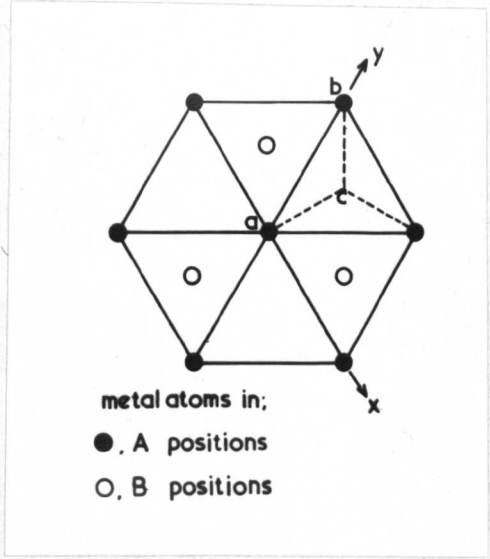

Fig. 5.2.2 Burgers vectors of perfect and partial dislocations in the hcp basal plane, (see text for details).

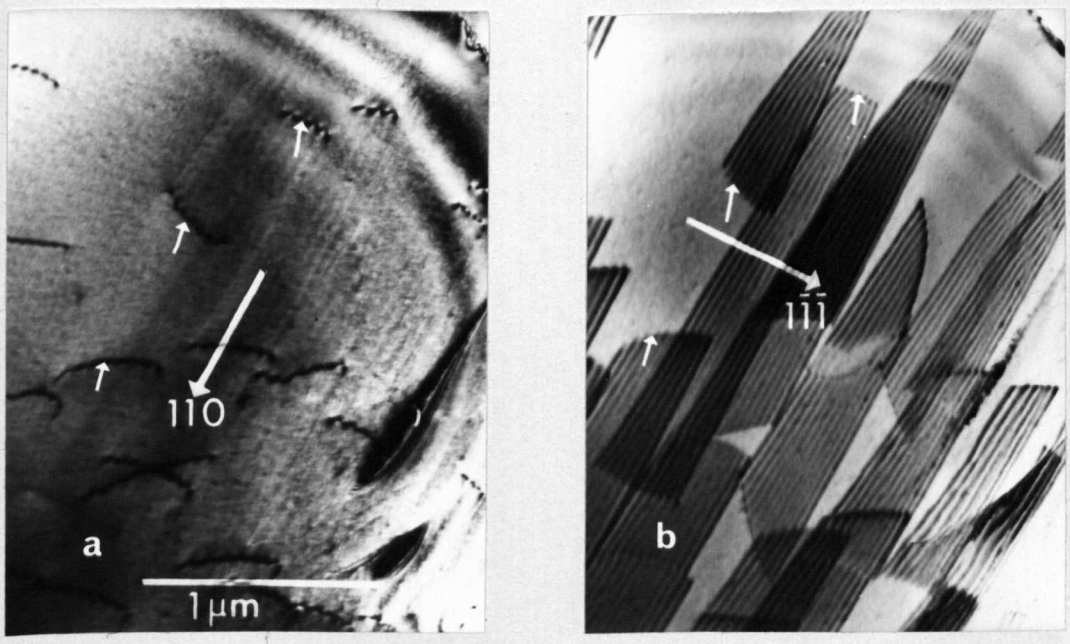

Fig. 5.2.3 Stacking fault and partial dislocation contrast in hcp vanadium hemicarbide. All the partial dislocations show reversal in visibility from (a) to (b).

shows the values of g.b for the three types of partial dislocation.

TABLE 5.1

g \ b	1/3 [120]	1/3 [210]	1/3 [110]
110	+1	+1	0
$1\bar{1}\bar{1}$	-1/3	+1/3	+2/3

The stacking fault introduced by the partial dislocation displacement gives no contrast for g = 110, since $\alpha = 0, 2\pi$, etc., while for g = $1\bar{1}\bar{1}$, α has the values $\pm 2\pi/3$ etc., and fringe contrast is observed. A particular feature of the predicted dislocation contrast is that a partial visible in one reflection, will be invisible in the other. This visibility criterion is evident from a comparison of the two micrographs.

(iii) Vanadium nitride

The cubic mononitride phase in the VN/V_2N eutectic contained the highest stacking fault density observed in all these compounds, and a typical example is shown in fig. 5.2.4. The (110) section diffraction pattern shows considerable streaking, and many faults are seen to terminate at the coherent interface with the V_2N-phase. This latter phase contains a high density of grown-in dislocations, some of which show evidence for slight dissociation. When specimens of the eutectic were annealed in vacuum the stacking fault density decreased, enabling analysis of isolated faults. This decrease is surprising, since the loss in nitrogen

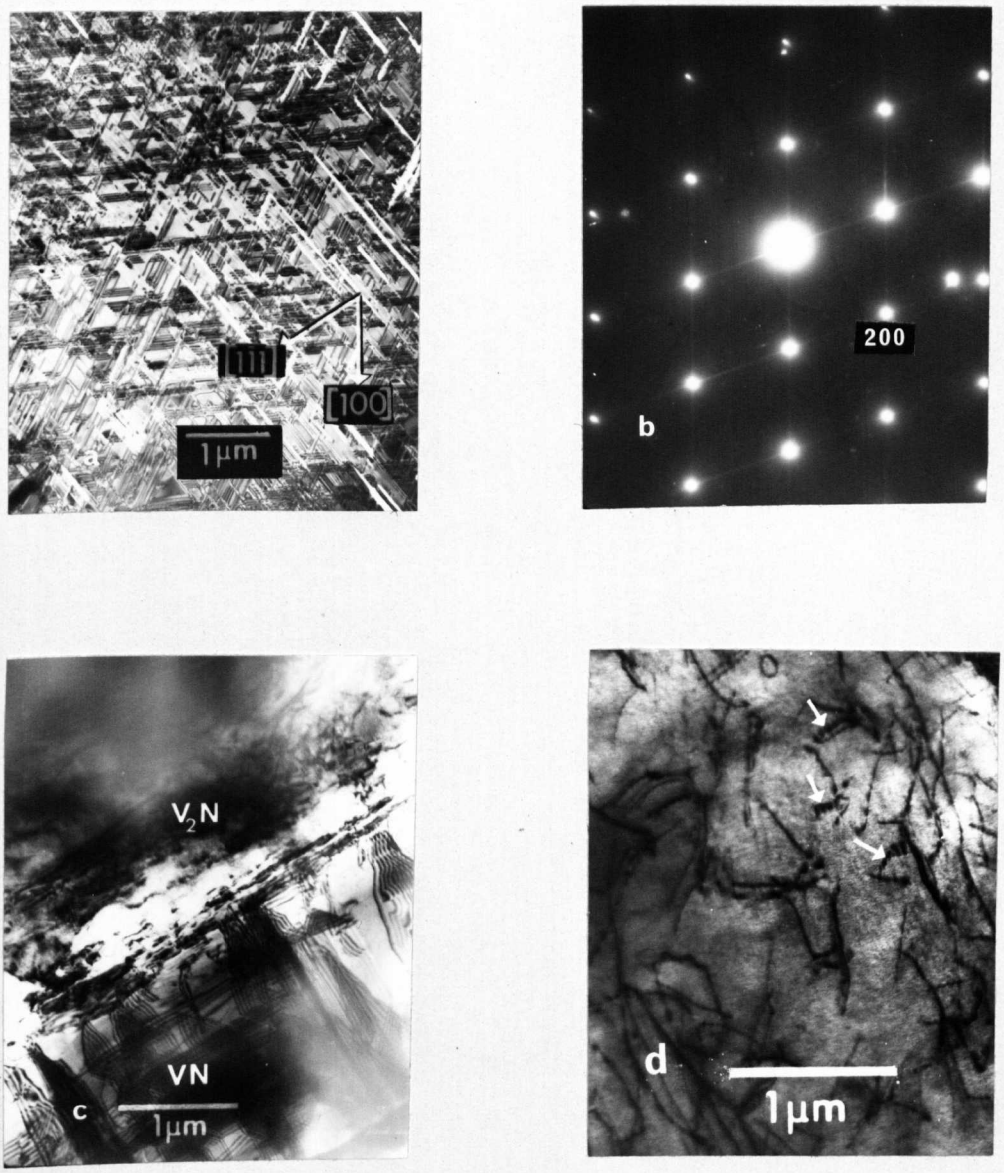

Fig. 5.2.4 Stacking faults in as-grown VN/V_2N eutectic. (a) VN-phase, (b) (110) section showing streaks through (111)-type reflections, (c) faults originating at interface with V_2N, (d) V_2N-phase with some dislocations showing a small amount of dissociation.

during annealing should tend to stabilize the hexagonal V_2N-phase which might then be expected to precipitate at the stacking faults.

The sequence of stacking fault images in fig. 5.2.5, obtained from a (110) orientation, were recorded with $g = 200$ and $\bar{2}00$ in bright-field with $w = 0$, and in dark-field with $w = 0$, $+0.3$, and -0.3. The reversal in the contrast of the outermost fringes in dark-field predicted from the theoretical profiles is clearly seen. From the direction of the indicated g-vectors, and outer fringe contrast, the faults are found to be intrinsic.

The partial dislocations bounding the faults were analysed from the set of micrographs shown in fig. 5.2.6, recorded from an (011) section, (a) to (g), and the neighbouring (121) section, (h). The set of inclined faults in this figure then lie on the (111) plane. The products of the operating reflections, and the Shockley and Frank partial dislocation Burgers vectors on this plane are given in Table 5.2. The four possible partial dislocations may be distinguished by the criterion, $\mathbf{g}.\mathbf{b} = \pm 1, \pm 2/3$, and $\mathbf{g}.\mathbf{b} = 0, \pm 1/3$ for in- and out-of contrast respectively. The observed contrast is consistent with Shockley dislocations with Burgers vectors $a/6[2\bar{1}\bar{1}]$ and $a/6[\bar{1}2\bar{1}]$, and with a fault vector $a/3[11\bar{1}]$. The trace at the intersection of the fault plane with the foil surface is an artefact probably introduced by chemical thinning.

(iv) Titanium nitride

Single stacking faults were observed in specimens of titanium nitride with compositions below about $TiN_{0.70}$. In all the specimens examined these faults were found to

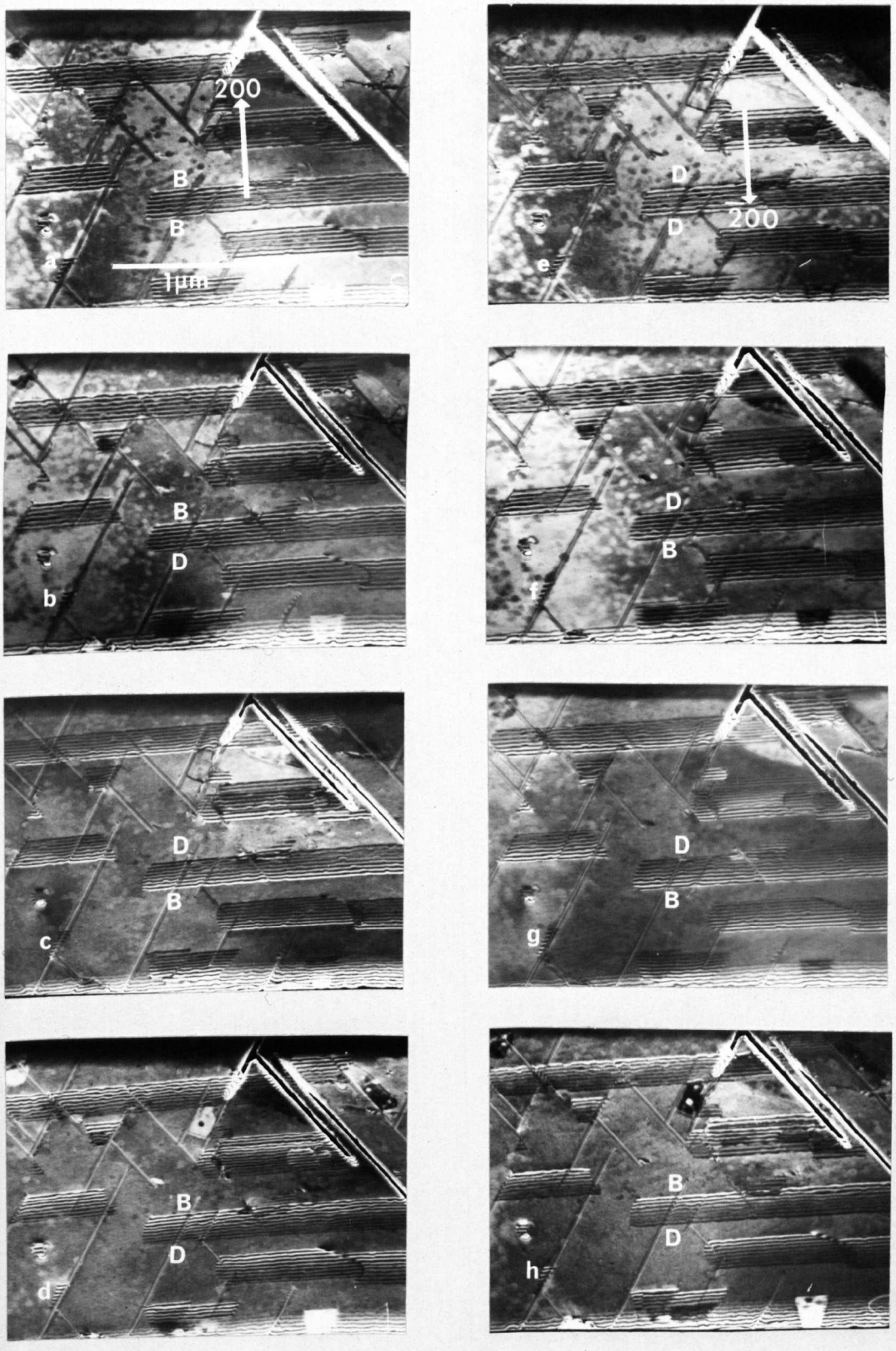

Fig. 5.2.5 Stacking faults in $VN_{0.72}$ showing reversal in the contrast of the outermost fringes for certain dark-field images. (a) to (d) $g = 200$, (e) to (h) $g = \bar{2}00$, (a) and (e) BF, (b) and (f) DF $w = 0$, (c) and (g) DF $w = +0.3$, (d) and (h) DF $w = -0.3$. Reversal from the correct contrast occurs in (c) and (h). B and D, bright and dark outer fringes respectively.

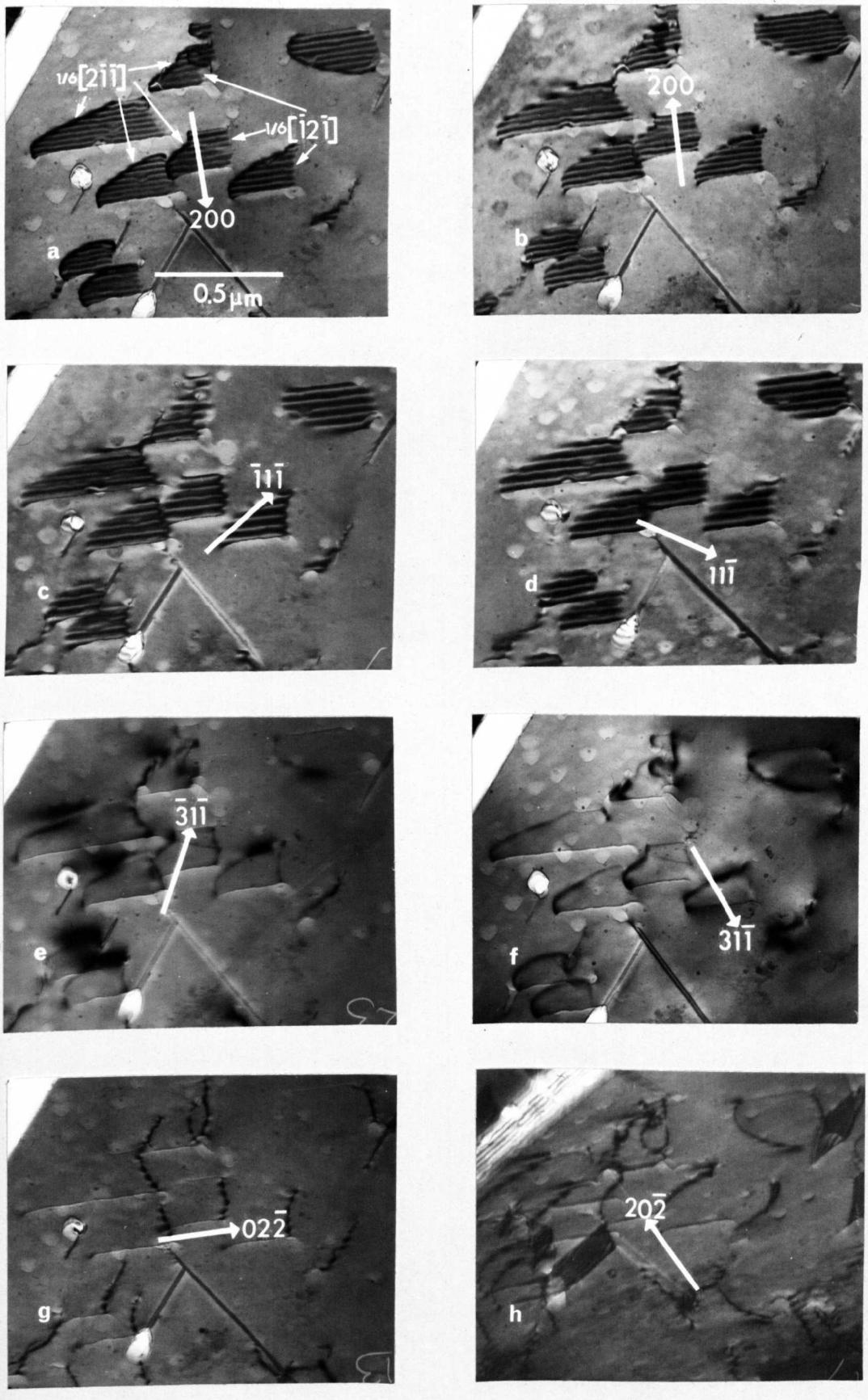

Fig. 5.2.6 Partial dislocation analysis in $VN_{0.72}$. BF images, (a) to (g) (011) orientation, (h) (121) orientation.

TABLE 5.2

g \ b	1/6 [$\bar{1}2\bar{1}$]	1/6 [$\bar{1}\bar{1}2$]	1/6 [$2\bar{1}\bar{1}$]	1/3 [$\bar{1}11$]
200	-1/3	-1/3	+2/3	+2/3
$\bar{2}00$	+1/3	+1/3	-2/3	-2/3
$\bar{1}\bar{1}1$	+2/3	-1/3	-1/3	-1/3
$11\bar{1}$	+1/3	-2/3	+1/3	+1/3
$\bar{3}1\bar{1}$	+1	0	-1	-1
$31\bar{1}$	0	-1	+1	+1
$02\bar{2}$	+1	-1	0	0
$\bar{2}02$	0	+1	-1	0

be intrinsic and bounded by Shockley partial dislocations. For specimens with compositions down to $TiN_{0.50}$ there was no evidence for the precipitation of either ε-Ti_2N, or the α-titanium - nitrogen solid solution. In fig. 5.2.7, (a) to (f) were recorded from a (211) orientation, and (g) and (h) from the neighbouring (111) orientation. Micrographs (d) and (e) have g-vectors reversed to establish the outer-fringe contrast, and the dark-field image (f) was used to confirm the intrinsic nature of the faults. In Table 5.3 the values of g.b for the relevant Shockley and Frank partial dislocations are listed, with the observed partial dislocation contrast consistent with that of Shockley dislocations.

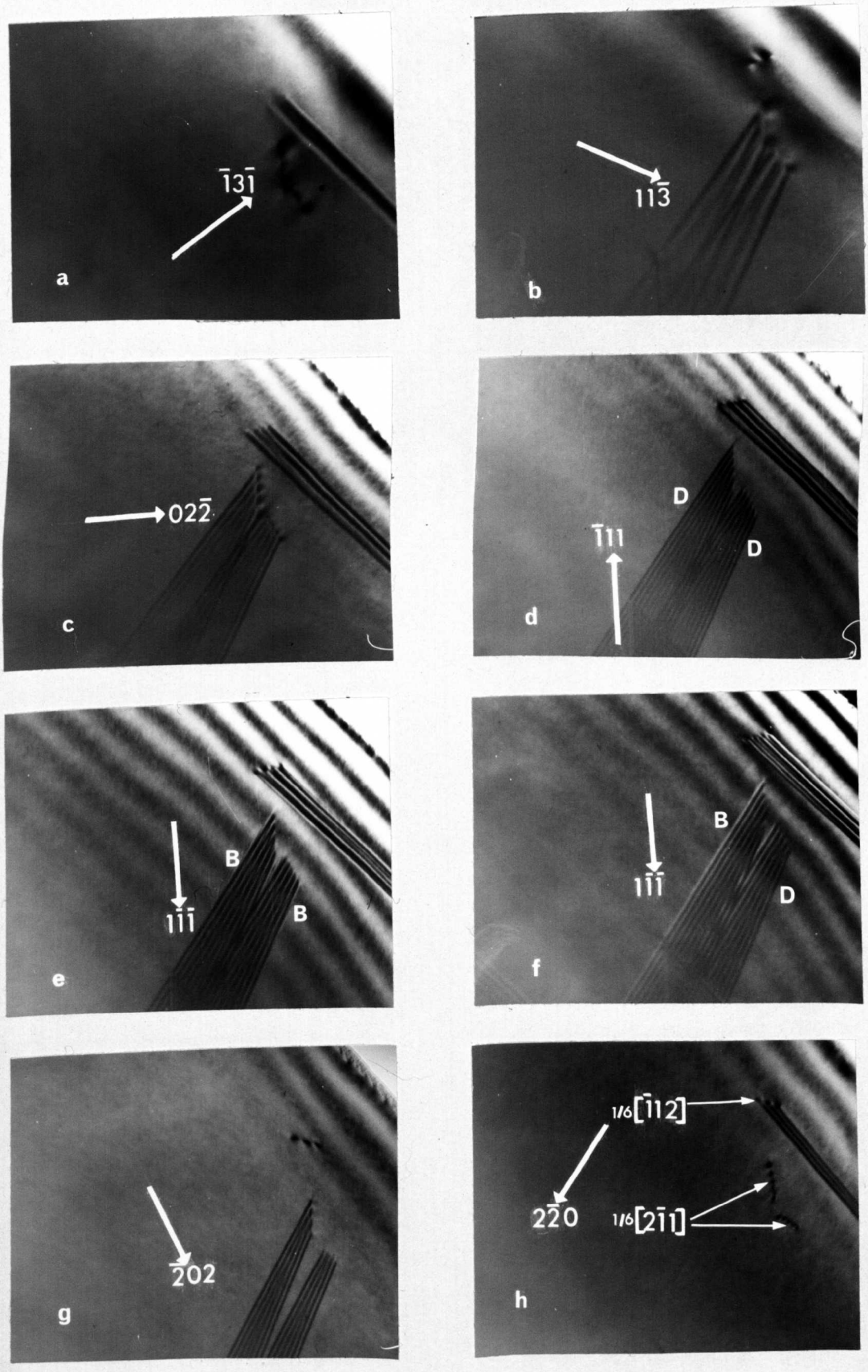

Fig. 5.2.7 Intrinsic stacking faults and partial dislocations in $TiN_{0.60}$. (a) to (f) (211) orientation, (g) and (h) (111) orientation.

TABLE 5.3

$(11\bar{1})$

g \ b	1/6 $[\bar{1}\bar{1}2]$	1/6 $[\bar{1}21]$	1/6 $[2\bar{1}\bar{1}]$	1/3 $[\bar{1}1\bar{1}]$
$\bar{1}3\bar{1}$	0	+1	-1	+1
$11\bar{3}$	+2/3	-1/3	-1/3	+5/3
$02\bar{2}$	+1/3	+1/3	-2/3	+4/3
$\bar{1}11$	-1/3	+2/3	-1/3	-1/3
$1\bar{1}\bar{1}$	-1/3	-2/3	+1/3	+1/3
$\bar{2}02$	-1/3	+2/3	+1/3	+4/3
$2\bar{2}0$	0	-1	+1	0

$(1\bar{1}1)$

g \ b	1/6 $[21\bar{1}]$	1/6 $[\bar{1}2\bar{1}]$	1/6 $[\bar{1}12]$	1/3 $[\bar{1}\bar{1}1]$
$\bar{1}3\bar{1}$	+1/3	-2/3	+1/3	-5/3
$11\bar{3}$	+1	0	-1	-1
$02\bar{2}$	+2/3	-1/3	-1/3	-4/3
$\bar{1}11$	-1/3	-1/3	+2/3	-1/3
$1\bar{1}\bar{1}$	+1/3	+1/3	-2/3	+1/3
$\bar{2}02$	-1	0	+1	0
$2\bar{2}0$	+1/3	+1/3	-2/3	+4/3

5.2.3 Discussion of Stacking Fault Configurations

(i) Summary of electron microscope observations

The contrast analysis given in the previous section shows that intrinsic stacking faults form by the splitting of perfect dislocations on close-packed planes into two Shockley partial dislocations. This observation is in agreement with the two previous electron microscope studies of stacking fault formation in this type of compound, made by Billingham and Lewis (18) for $VC_{0.73}$, and by Martin et al. (19) for $TaC_{0.75}$. In the compounds with the NaCl-type structure (NbC, VN, TiN) the partial dislocations always appear widely separated. This implies a very low stacking fault energy as the nonmetal content is reduced towards the MX/M_2X phase boundary. In the fcc vanadium - carbon alloys studied in (18), the stacking faults appeared as sections through large loops of Shockley dislocations, thus the segments of partial dislocation associated with each fault were usually curved and had the same Burgers vector. Also, the density rather than the extent of dissociation of the faults increased with decreasing carbon content, suggesting that the loops were formed by spontaneous nucleation. This mechanism for fault formation will be discussed in section 5.3.4(iii).

In V_2C and Nb_2C stacking faults were observed only in specimens quenched from high temperatures, while for V_2N slight dislocation dissociation was seen, although the nature of the resulting faults was not identified.

(ii) The accommodation of nonmetal atoms at stacking faults

It is now necessary to examine the effect that local changes in the metal-atom stacking sequence have on the nonmetal-atom environment. The stacking sequence for

the perfect NaCl-type structure is given by,

...AγBαCβAγBαCβAγB ...

At the composition where stacking faults are observed about 75% of the nonmetal sites are occupied. Although the selection of occupied sites is non-random, as evidenced by the diffuse electron scattering (except $VN_{0.72}$), there is no long-range order in the nonmetal-atom sublattice.
The formation of an intrinsic fault via the motion of a Shockley partial dislocation will give the following sequence,

...AγBαCβAγBαAγBαC ...

The nonmetal atoms in the sequence ...BαA... have tetrahedral coordination. This must be considered as an unfavourable configuration which may be eliminated in two ways.
Firstly, the tetrahedrally coordinated atoms may diffuse away into neighbouring vacant sites leaving the sequence ...B□A... (where □ represents an unoccupied layer).
This will produce a thin lamella with a structure characteristic of the ordered phase in Ta_2C (20) (...AγB□AγB□A...).
Removal of the layer of nonmetal atoms should result in a relaxation of the metal-atom layers on either side of the fault, which will then influence the associated electron microscope contrast. The invisibility criterion for stacking faults observed with certain 311 g-vectors is $\mathbf{g}.\mathbf{R} = \pm 1$. When R changes from 1/3⟨111⟩ due to relaxation, the fault should become visible if g.R differs from an integer by more than 0.02 (21). In the present case, for the fault to become visible using this type of reflection a relaxation of about 3% is required. As no fringes are observed for the 311 reflection, this mechanism for the removal of tetrahedral coordination is unlikely since a relaxation greater than 3% is expected.

The probable mechanism for the removal of the tetrahedral coordination is related to the suggestion of Kelly and Rowcliffe (22) for slip in titanium carbide. This is based on the concept of synchro-shear developed by Kronberg (23). The nonmetal atoms at the partial dislocation core must move independently in a direction at 60° to that of the slipping metal atoms. The stacking sequence then becomes,

...AγBaCβAγBγAγBaCβA...
↑

where the arrow indicates the nonmetal-atom layer involved in the synchro-shear. Even this stacking sequence is not entirely satisfactory. For a statistical nonmetal-atom distribution the three γ-planes will be more than half-full, and the rule regarding the occupancy of interstices directly above each other will be violated. However, only a small number of nonmetal atoms need diffuse away from the fault into neighbouring vacant sites in order to produce a more favourable nonmetal-atom configuration.

The accommodation of the nonmetal atoms at stacking faults in the hcp compounds may be explained in a manner similar to that in the fcc compounds. The stacking sequence for the perfect hcp (NiAs-type) structure is given by,

...AγBγAγBγA...

The motion of a partial dislocation will then give the sequence,

...AγBγAγCaBaC

This contains the unfavourable ...AγC... tetrahedral coordination. By the process of synchro-shear this may then

be eliminated to give,

...AγBγAβCaBaC...

Unlike stacking fault formation in the fcc structure, this sequence will not violate the nonmetal-atom stacking rule since the fault is a thin region of fcc crystal.

5.3 Structures with Mixed Metal-Atom Stacking

5.3.1 Analysis by Electron Diffraction

Identification of the low-order polytypes described in section 5.1 can be readily made by electron diffraction. The reciprocal lattices for all these structures (fig. 5.1.1) are best described in terms of three different types of rows of points with $(h-k) = 3n$ and $3n\pm1$ (24). When the hexagonal c-axis is perpendicular to the electron beam, these rows will lie in the plane of the diffraction pattern. Indexing a $(11\bar{2}0)$-type pattern in the c-direction will then immediately give the number of close-packed layers comprising the unit cell height. Differences in the spacing or the composition of layer planes will give rise to extra reflections in $(1\bar{1}00)$ sections (containing only $h-k = 3n$ type rows) with values of l that are fractional multiples of the number of planes in the unit cell.

Mistakes in the correct stacking sequence of layer planes are evidenced by diffuse streaking along the rows with $(h-k) = 3n\pm1$, the $(h-k) = 3n$ rows being unaffected. The extent of this streaking will depend on the frequency of stacking mistakes.

5.3.2 Previous Observation of Structures with Mixed Metal-Atom Stacking

The possible occurrence of a phase with composition

between the hcp-M_2X and fcc-MX phases was first noted by Lesser and Brauer (25) in X-ray work on the Ta-C system. The evidence of a new phase was the appearance of one extra reflection in a specimen containing the hexagonal and cubic phases. These workers found similar evidence in the Nb-C and Ta-C-N systems (26,27). Storms and McNeal (28) identified an additional phase in vanadium carbide, which was confirmed by metallographic work of Rudy et al. (29). The structural characteristics of these intermediate phases were found simultaneously by Yvon and Parthé (30), who showed the ζ-phase vanadium, niobium, and tantalum carbides were based on $(hhcc)_3$ metal stacking, and by Rudy (31,32), who showed that the metal layers in Ta_2VC_2 and Hf_3N_2 were stacked according to $(hhc)_3$, and that Hf_4N_3 was similar to the carbide ζ-phases.

In a recent electron microscope examination of the ζ-phase in tantalum carbide by Martin et al. (33), the metal-atom stacking sequence was confirmed, and from additional diffraction evidence a possible scheme for carbon-atom ordering was proposed. In this present investigation the specimens were given prolonged low-temperature anneals in order to enhance the possible formation of long-range order in the carbon-atom sublattice.

5.3.3 Observation of Structures With Mixed Metal-Atom Stacking

(i) ζ-phase vanadium carbide

The hexagonal, cubic, and ζ-phases were present in a specimen with composition $VC_{0.67}$ in the as-grown (slowly cooled) condition. Some regions of thin-foil specimens were completely ζ-phase as shown in fig. 5.3.1. The narrow bands parallel to the traces of the layer planes

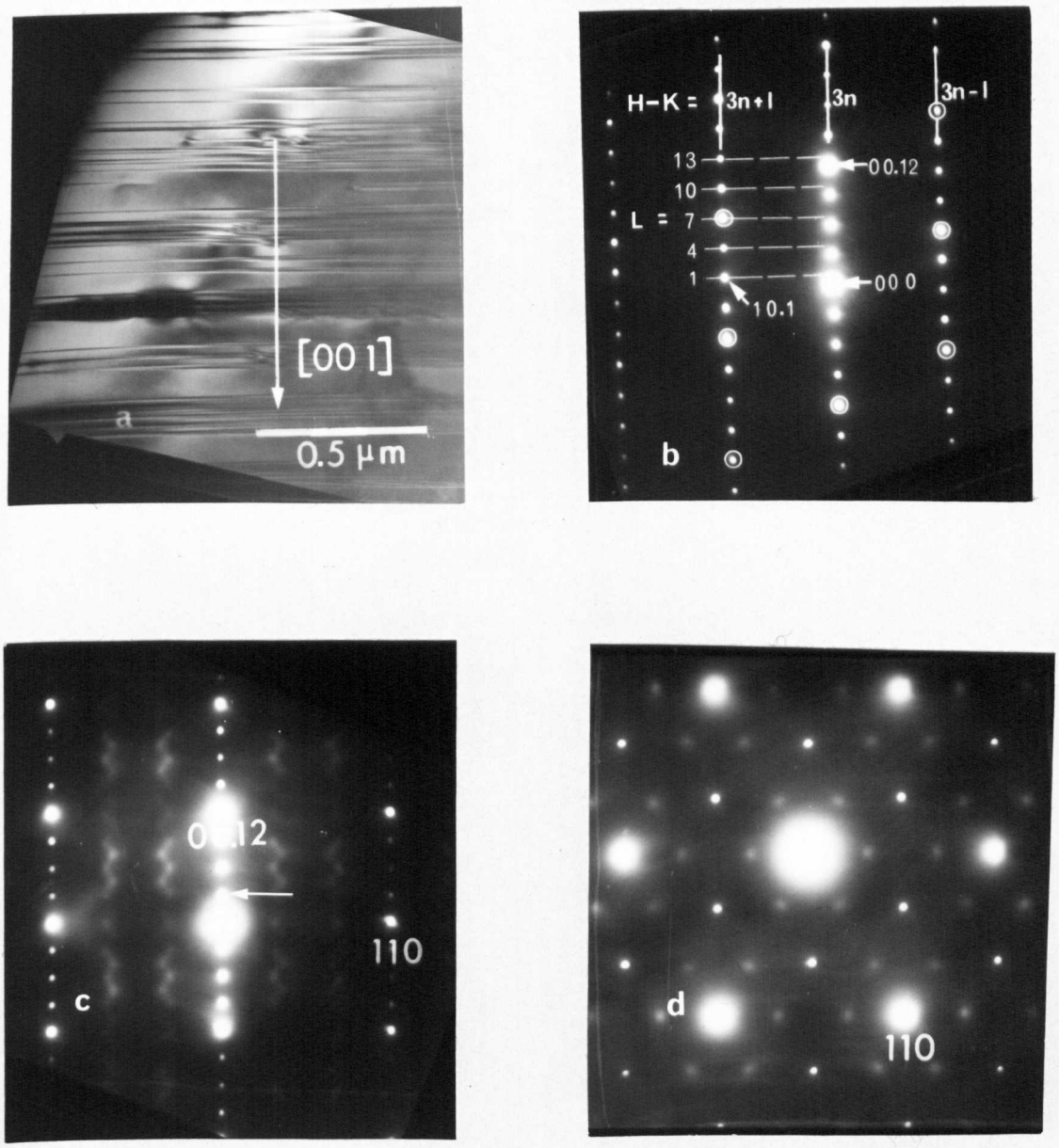

Fig. 5.3.1 ζ-phase in $VC_{0.67}$. (a) DF from indicated reflection, (b) $(11\bar{2}0)$, (c) $(1\bar{1}00)$, and (d) (0001) sections.

may be single stacking faults or very thin lamellae of the hexagonal and cubic phases. The three diffraction patterns in this figure from the $(11\bar{2}0)$, $(1\bar{1}00)$, and (0001) sections, may be correctly indexed for the ζ-phase, as shown in (b). In the $(1\bar{1}00)$ section the presence of reflections with $l = 3n$ in the $(h-k) = 3n$ type rows would indicate that differences in layer spacing or some degree of carbon sublattice order exist*. The second possibility of sublattice order is further supported by the zigzag diffuse scattering in this pattern. The intersection of this diffuse scattering with the (0001) section gives rise to the very weak reflections in (d).

A region containing the hexagonal and cubic phases as well as ζ-phase is shown in fig. 5.3.2. In the $(11\bar{2}0)$ diffraction pattern the diffuse scattering characteristic of the cubic phase was just visible (see for example fig. 3.2.2). This pattern has been schematically redrawn in (d). The ratio of the (111)-VC and (00.12)-ζ-phase d-spacings given by the measured splitting of the reflections is 1.03, compared to 1.025 calculated from the X-ray values for $VC_{0.73}$ (28) and ζ-phase (30). The splitting of the hexagonal V_2C and ζ-phase reflections is also just resolved. The $(1\bar{1}00)$ section in this figure shows, apart from the split reflections, faint diffuse streaks which are centred on the positions of the allowed reflections for the high-temperature form of V_2C (see fig. 4.2.2(b)).

Annealing at successively lower temperatures did not promote the formation of long-range order in the carbon

* These reflections will be present in the $(h-k) = 3n$ rows in all other (hki0) sections due to multiple diffraction from $(h-k) = 3n \pm 1$ rows.

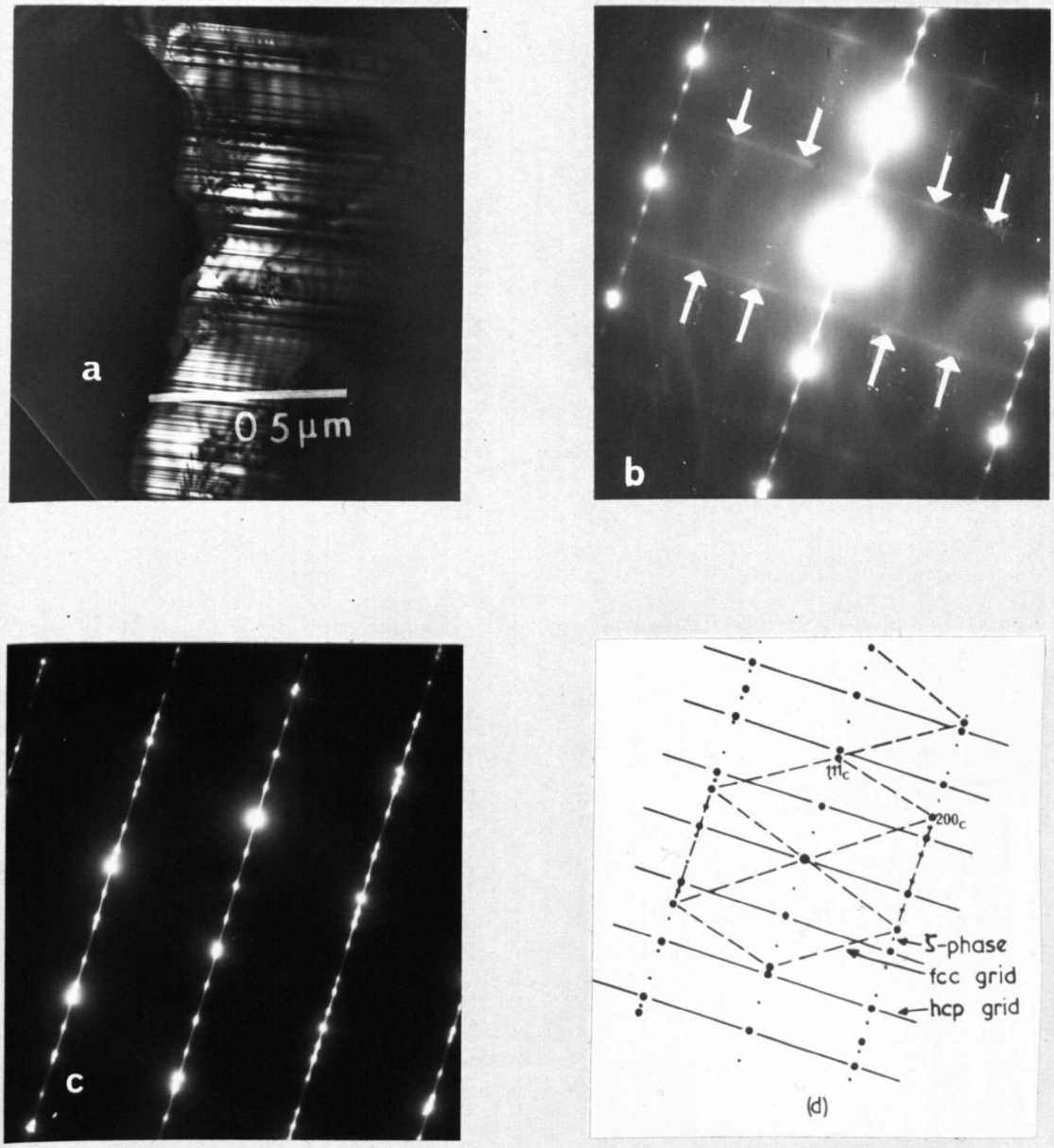

Fig. 5.3.2 Coexisting hexagonal, cubic, and ζ-phase in $VC_{0.67}$. (a) DF showing ζ-phase regions, (b) $(1\bar{1}00)$ section showing weak intensity (arrowed) at the superlattice reflection positions for the high-temperature form of V_2C, (c) $(110)_c/(11\bar{2}0)_h$ section showing reflections from the three phases, redrawn in (d).

sublattice, or alter the diffuse scattering intensity, but the fraction of ζ-phase increased considerably down to 750°C. Below 750°C the ζ-phase transformed to the hexagonal V_2C-phase. Fig. 5.3.3 shows such a transformed area containing many narrow banded regions. The diffraction patterns of the transformed hexagonal phase show continuous strong streaking in the c-direction. In the $(1\bar{1}00)$ and $(11\bar{2}0)$ sections of this figure diffuse streaks near the positions of the superlattice reflections for the high-temperature form of V_2C are seen. Fig. 5.3.4 shows a region where the transformation is incomplete. The diffraction patterns show only hexagonal and ζ-phase reflections, and the dark-field images show thin bands of these two phases.

(ii) ζ- and ε-phase niobium carbide

A ζ-phase similar to that in vanadium carbide, and a previously unobserved ε-phase were found in the Nb-C system for compositions within the nominal hcp-Nb_2C and fcc-NbC two-phase region. The different conditions influencing the formation of one or other of these two mixed metal-atom stacking phases were not clearly established. The ε-phase occurred in a much smaller fraction than the ζ-phase. Fig. 5.3.5 shows a region of ζ-phase containing a high density of faults giving rise to continuous streaking through the diffraction spots. The ε-phase is shown in fig. 5.3.6, where again a high density of faults produces continuous streaking. Occasionally both ζ- and ε-phases were found together in the form of an irregular intergrowth as shown in fig. 5.3.7. The $1/3$ and $1/4(002)_h$ reflections have merged to form an extended spot, while the reflection at $1/2(002)_h$ is still distinct. Dark-field images reveal the same broad bands in bright contrast, but within each

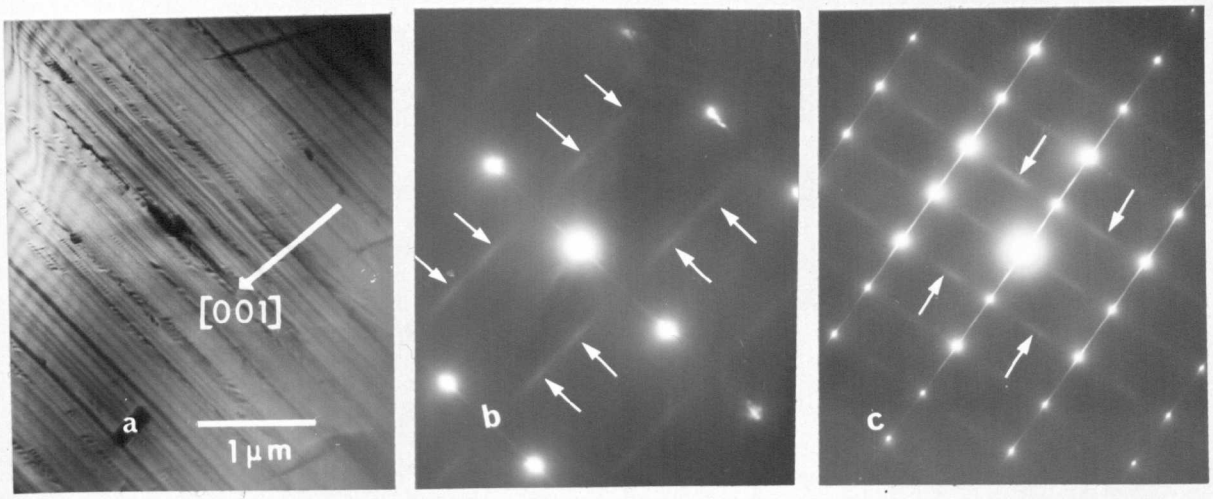

Fig. 5.3.3 Transformation from ζ-phase to hexagonal V_2C in $VC_{0.67}$, 200h at 750°C. (a) hexagonal phase containing many faulted regions, (b) $(1\bar{1}00)$ and (c) $(11\bar{2}0)$ sections showing diffuse superlattice reflections characteristic of the high-temperature form of V_2C.

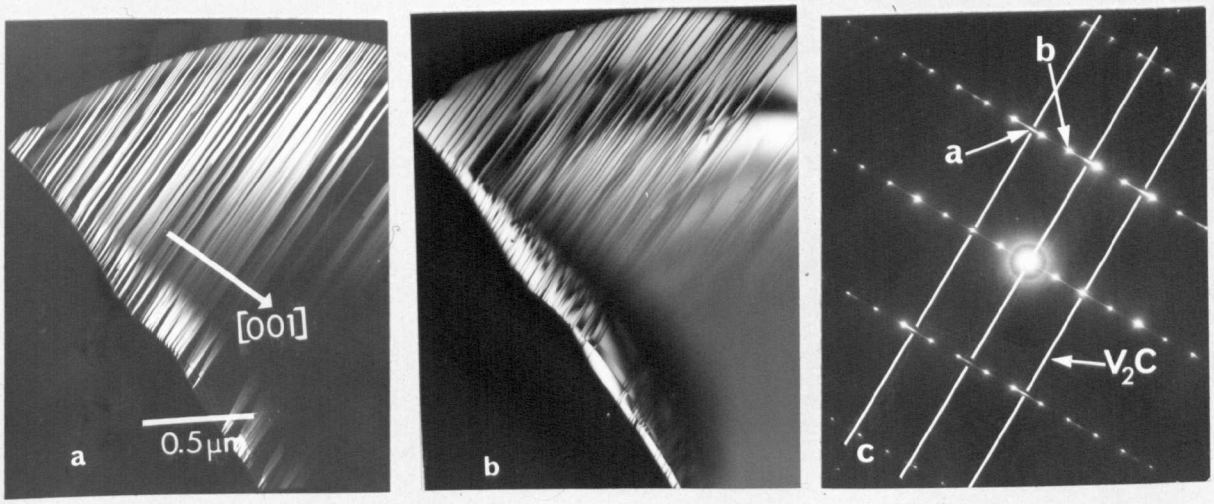

Fig. 5.3.4 Partial transformation to hexagonal V_2C. (a) DF hexagonal phase, (b) DF ζ-phase, (c) $(11\bar{2}0)$ section showing hexagonal and ζ-phase reflections.

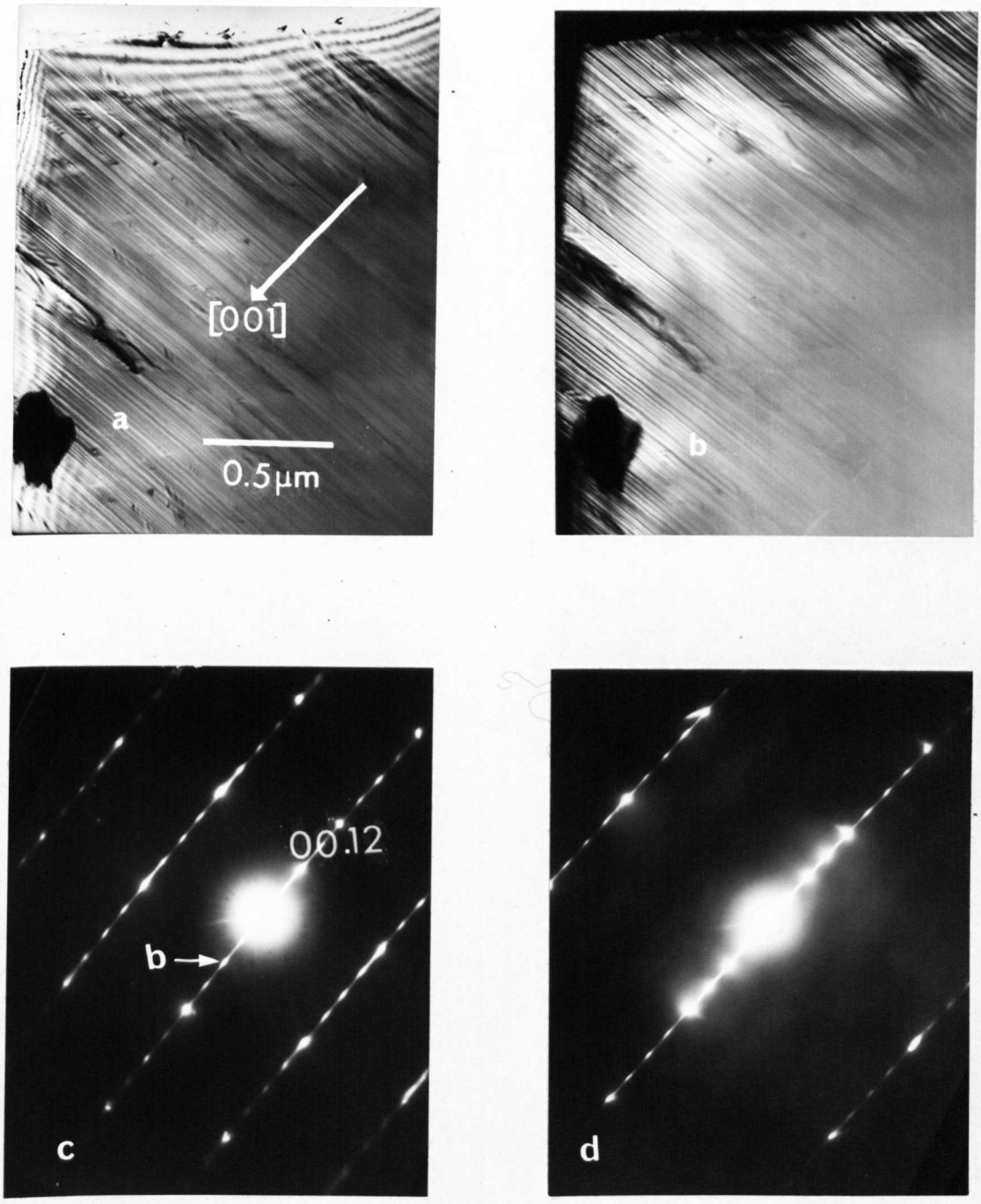

Fig. 5.3.5 ζ-phase niobium carbide. (a) BF, (b) DF from indicated reflection, (c) $(11\bar{2}0)$ and (d) $(1\bar{1}00)$ sections.

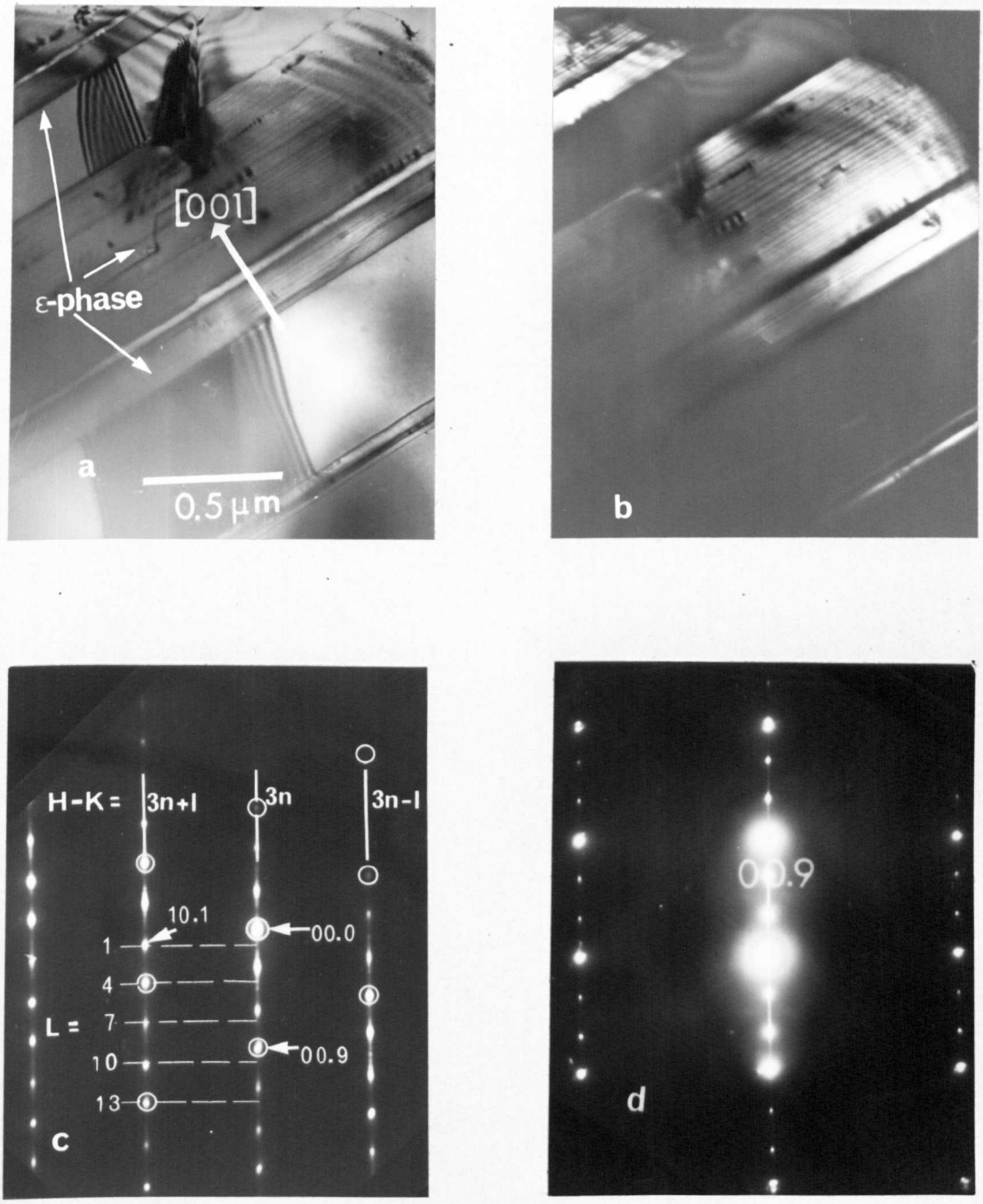

Fig. 5.3.6 ε-phase niobium carbide. (a) BF, (b) DF, (c) $(11\bar{2}0)$ section, (d) $(1\bar{1}00)$ section.

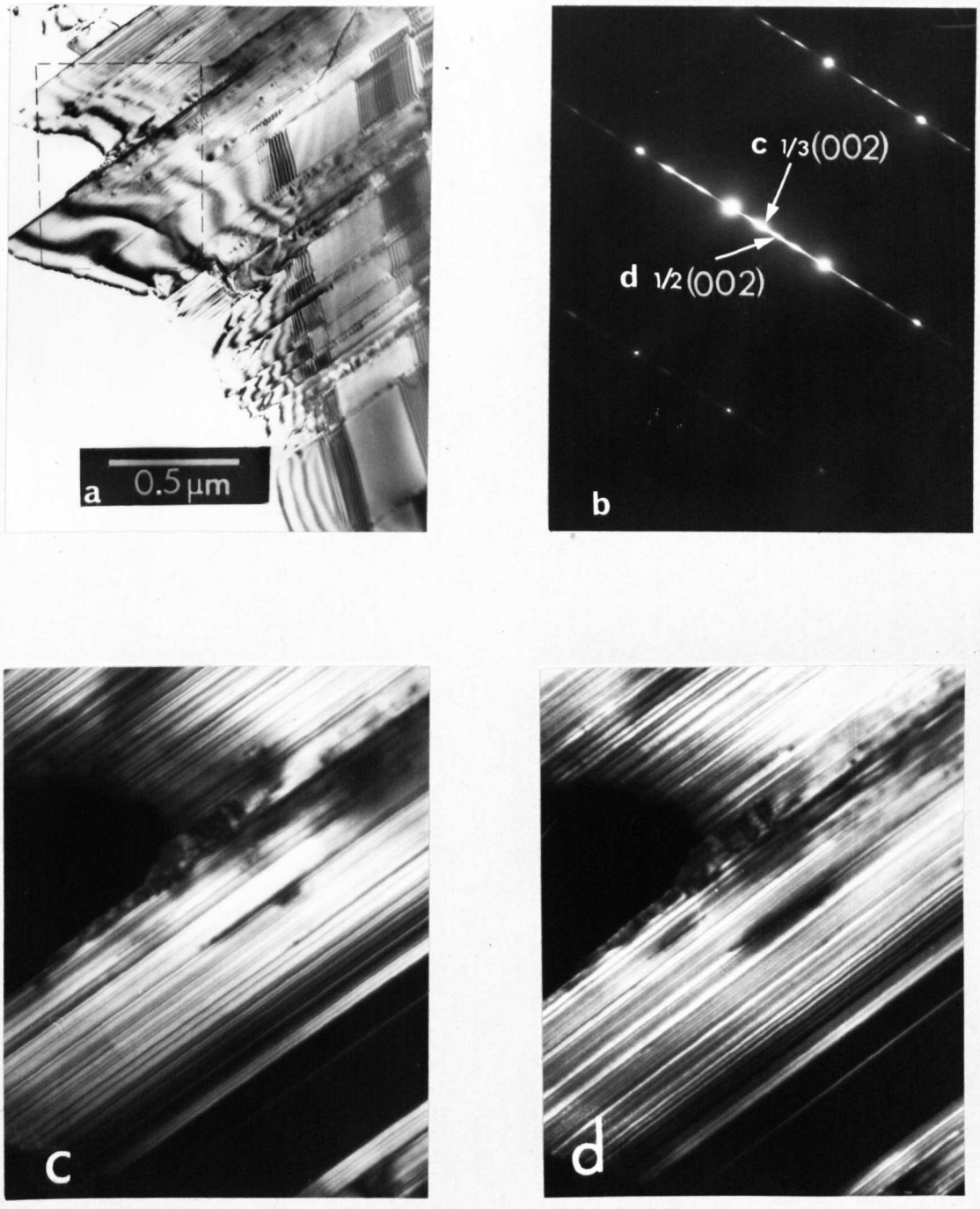

Fig. 5.3.7 Irregular intergrowth of ζ- and ε-phase niobium carbide. (a) BF, (b) $(1\bar{1}00)$ section, (c) and(d) DF from area outlined in (a), taken using beams indicated in (b).

band different sets of much narrower lamellae are visible. Below 715°C transformation to the hexagonal Nb_2C-phase occurred, shown in fig. 5.3.8. The area containing stacking fault contrast is fcc-NbC which has remained unchanged during the heat-treatment. The dark-field image from the maximum in the diffuse streaking shows that the adjacent region contains a small amount of ζ-phase (or possibly ε-phase). Tilting to another orientation showed that reflections characteristic of Nb_2C were present, which in dark-field gave the regions of bright contrast between the remaining ζ-phase lamellae. In this case there was no evidence for carbon-atom order in the Nb_2C, unlike the transformed V_2C.

In the $(1\bar{1}00)$ section diffraction pattern of fig. 5.3.9(a), which has been deliberately overexposed, the parallel straight lines of diffuse intensity which lie at one-third and two-thirds of the distance between adjacent rows with $(h-k) = 3n$, suggest that some form of carbon-atom order exists in the ζ- and ε-phases. The occurrence of reflections with $l = 3n$ on the $(h-k) = 3n$ rows gives further support to this idea. However, prolonged annealing did not result in an increase in the degree of order in the carbon sublattice.

5.3.4 Discussion of ζ- and ε-phases

(i) Stability with respect to temperature and composition

In the previous work mentioned in section 5.3.2, it was shown that the upper temperature limits for the formation of ζ- and ε-phases occurred below the respective solidus temperatures. The possibility of a lower limiting temperature has not been examined. The present results show that these vanadium and niobium compounds with mixed

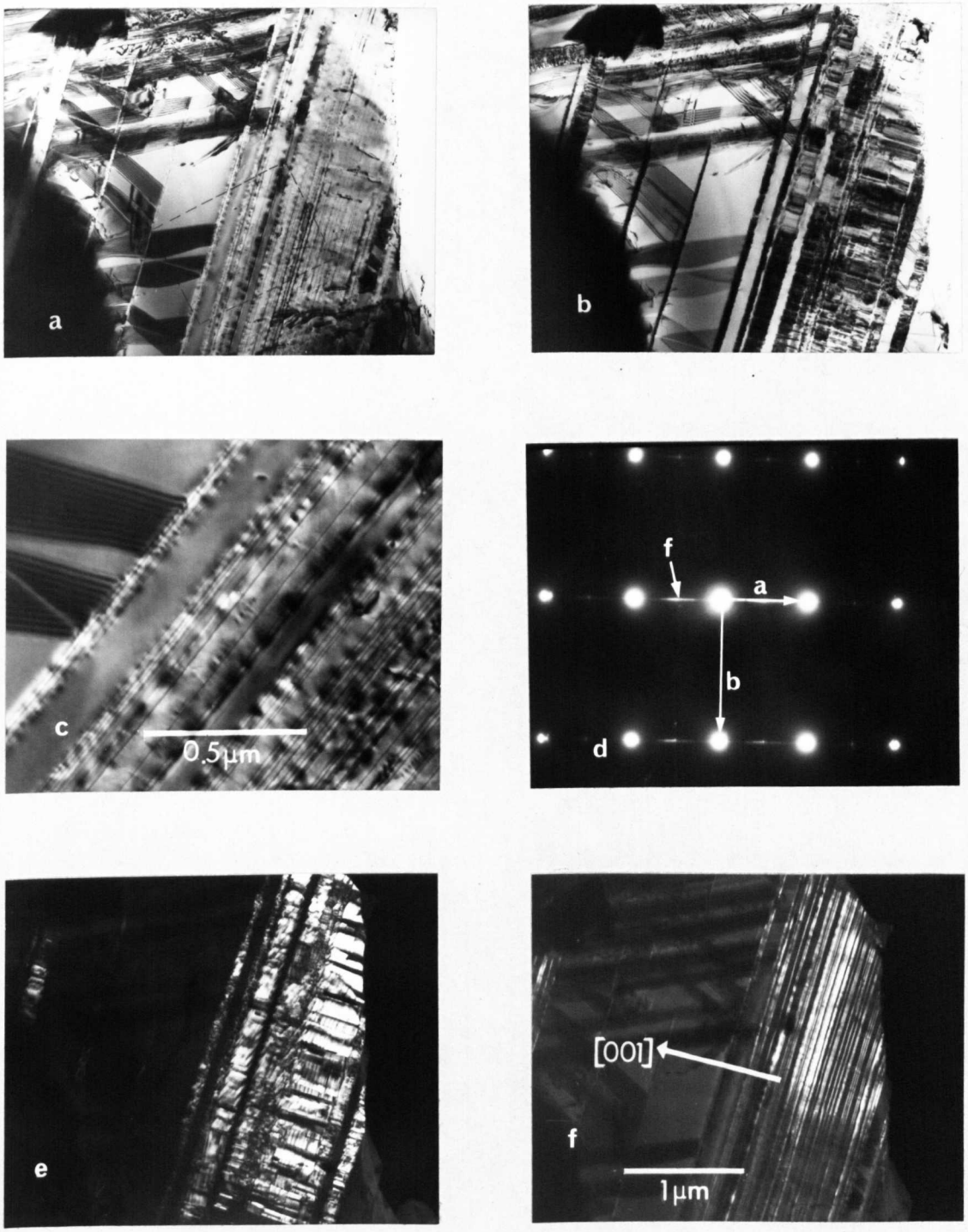

Fig. 5.3.8 Transformation of ζ-phase to hexagonal Nb_2C. (a) and (b) BF from reflections indicated in (d), (c) enlarged area of (a) showing mottled dislocation contrast, (d) $(1\bar{1}00)$ section, (e) DF from hexagonal Nb_2C reflection (specimen tilted from orientation of (d)), (f) DF showing a small amount of residual ζ-phase.

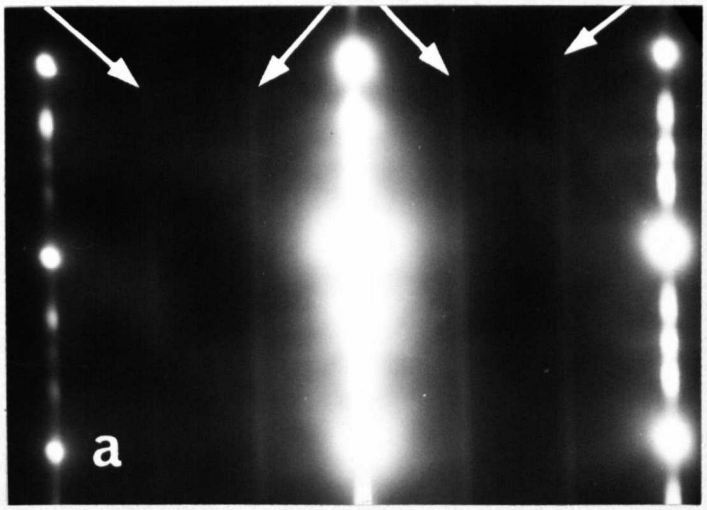

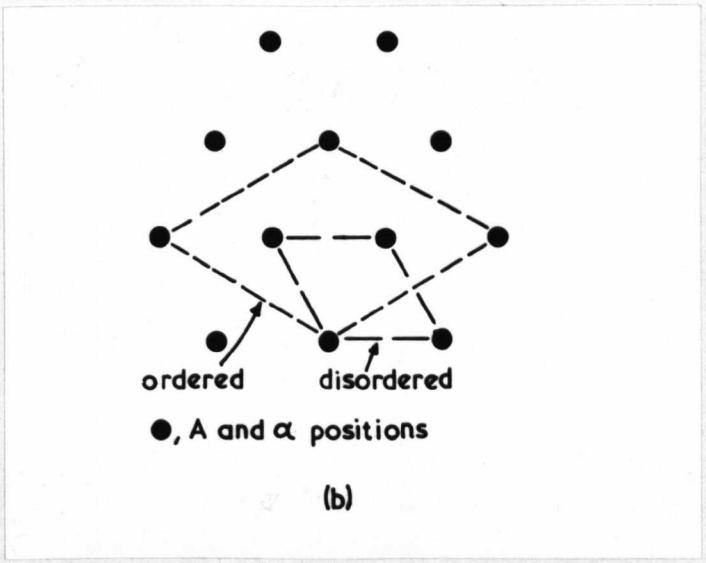

Fig. 5.3.9 (a) $(1\bar{1}00)$ section showing lines of diffuse intensity indicative of a non-random carbon-atom distribution, (b) modified basal plane unit cell axes.

metal-atom stacking transform at about 750°C to the respective hexagonal phases.

The carbon deficiency from the ideal compositions, and the narrow homogeneity ranges of the ζ- and ε-phases are confirmed. Thus these compounds, with ideal compositions V_4C_3, Nb_4C_3, and Nb_3C_2, were invariably found within small regions of crystal adjacent to both the mono- and hemicarbides, and in specimens with overall composition below $MC_{0.7}$. Only ζ-Ta_4C_3 (34) and Hf_4N_3 (32) exist near the ideal compositions, $MX_{0.75}$. ζ-V_4C_3 was found at V_4C_{3-x}, with x = 0.33, by Yvon and Parthé (30), who also showed that the lattice parameters of the ζ-phase in specimens with different V_2C/VC ratios were identical, i.e. the ζ-phase must have a very narrow homogeneity range. If as observed, only the hexagonal M_2C-phase results from the low-temperature transformation of the ζ- and ε-phases, excess carbon atoms must be present in the hemicarbides above the $MC_{0.5}$ composition. Although the stoichiometric M_2C composition is found, higher carbon-atom concentrations in the hexagonal phase have not been reported. However, the diffraction patterns from the transformed V_2C show weak diffuse superlattice reflections, indicating a low degree of long-range order. This would be likely to occur if the composition deviated from $VC_{0.5}$, since at the temperature for the transformation from the ζ-phase, carbon-atom ordering would readily occur for specimens with more nearly stoichiometric compositions. Similarly carbon-atom concentrations in excess of $NbC_{0.5}$ are indicated for the transformed Nb_2C, since there is no indication of the long-range order expected for stoichiometric compositions.

(ii) The accommodation of carbon atoms in structures with mixed metal-atom stacking

The full stacking sequences of the ζ- and ε-phases are given by,

...AγBγAγBαCβAβCβAγBαCαBαCβA... ζ-phase

...AγBγAγBαCαBαCβAβCβA... ε-phase

Both structures have the same space group, $R\bar{3}m$. The non-metal-atom positions are; hexagonal environment γγγ, point position 3(b), mixed environment γγα, 6(c), and cubic environment (ζ-phase only) βγα, 3(a). These positions are shown in fig. 5.3.10. In the previous X-ray investigations, reflections resulting from an ordered arrangement of nonmetal atoms and vacancies distributed over these positions were absent, and a statistical arrangement was assumed (30,32). However these results did not eliminate the possibility of ordering, since the reflections would have probably been too weak to observe, and a possible form of order involving vacant sites at the 3(b) positions was proposed. This would lead to structures with the ideal M_4X_3 and M_3X_2 compositions. Such an ordered distribution would give rise to superlattice reflections with $l = 3n$ on $(h-k) = 3n$ rows. From an intensity analysis of the fundamental reflections from ζ-phase vanadium carbide, Yvon and Parthé (30) found the distance between two layer planes enclosing nonmetal atoms in hexagonal environment was slightly less, 2.26Å, than that between the other layer planes, 2.34Å. This difference in spacing could indicate the presence of carbon vacancies in the 3(b) positions. However, the hexagonal environment of these metal-atom planes could in itself give a variation in the layer-plane

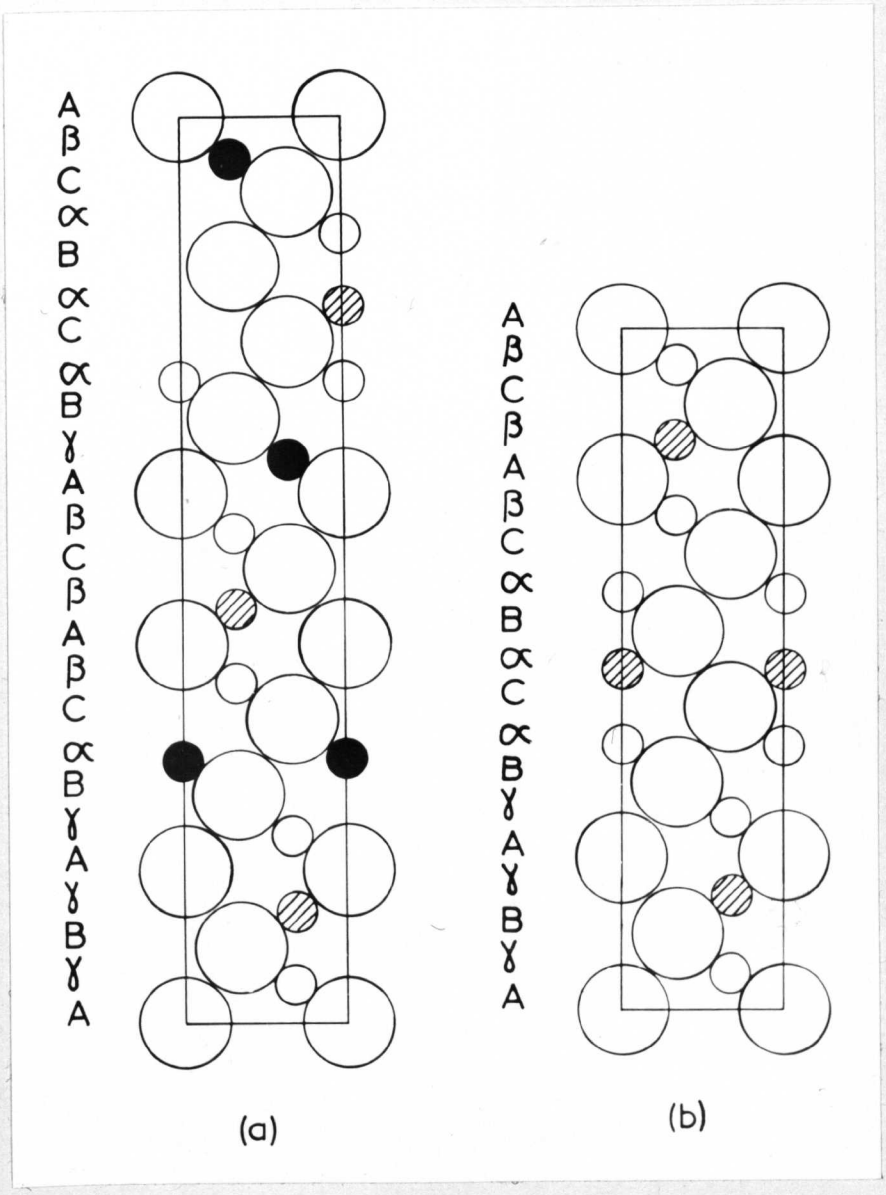

Fig. 5.3.10 (a)ζ-, and (b) ε-phase hexagonal unit cells viewed as sections through the $(11\bar{2}0)$ plane. Large open circles, metal atoms; filled circles, carbon atoms in 3(a) positions; shaded circles, carbon atoms in 3(b) positions; small open circles, carbon atoms in 6(c) positions.

spacing, even for a statistical distribution of carbon atoms.

Apart from Ta_2C which has the CdI_2-type structure, completely vacated nonmetal-atom layers are not found in the fcc or hcp Group IVa and Va compounds with carbon and nitrogen. In the ordered compounds, 1/4, 1/3, 2/3, and 3/4-filled close-packed nonmetal-atom layers are found. In this respect it is interesting to note that ζ-phase Ta_4C_3 and fcc-TaC exist at the ideal compositions, i.e. $TaC_{0.75}$ (34) and $TaC_{1.0}$ (35), and that the ordering of carbon atoms in Ta_4C_3 may involve the vacation of the 3(b) positions, giving a structure consisting of blocks of Ta_2C and $TaC_{1.0}$.

The presence of strong reflections for $l = 3n$ on $(h-k) = 3n$ rows in $(1\bar{1}00)$ sections would indicate a non-random distribution of carbon atoms between layer planes, rather than just small differences in layer-plane spacing. Bearing in mind the carbon deficiency of the ζ-phases from the ideal composition, a possible ordering scheme could be,

...Aγ"Bγ'Aγ"BαCβ"Aβ'Cβ"Aγ Bα"Cα Bα"CβA...

A single prime indicates a 1/3-full layer and a double prime a 2/3-full layer. Thus, point position 3(a) is fully occupied, 3(b) is 1/3-occupied, and 6(c) is 2/3-occupied. The atom positions in the 2/3-full layers project in the c-direction onto the vacant sites of the neighbouring 1/3-full layer to form a small element with the ε-Fe_2N type structure (fig. 4.1.2). The modified basal plane unit cell axes consistent with this ordered distribution are shown in fig. 5.3.9(b). For this ordering scheme

the number of vacancies is increased to give a composition very close to that observed for the ζ-phase, i.e. $MC_{0.67}$.

A similar arrangement can be devised for the ε-phase, thus,

...Aγ"Bγ'Aγ"Bα"Cα'Bα"Cβ"Aβ'Cβ"A...

This gives a composition $MC_{0.55}$.

Although a highly feasible and unique regular sequence in the occupation of the nonmetal-atom layers of the ζ- and ε-phases can be found, the same problem, as found for V_6C_5 and Nb_6C_5, will arise concerning the various possible lateral displacements of these layers within each nonmetal-atom plane. Thus the hexagonal net formed by the atoms in the 1/3- and 2/3-full layers may be translated to one of three equivalent positions within the layer plane. If one of these positions is arbitrarily chosen for the first (γ') layer, then the atom positions in the adjacent (γ") planes will be fixed, i.e. to form the ε-Fe_2N-type nonmetal-atom stacking. However the question arises as to which of the three equivalent positions the atoms will occupy in the next (α") 2/3-full layer.

Even in the presence of a high density of irregular lateral displacements of carbon-atom layers, the extra reflections in the $(1\bar{1}00)$ sections will remain sharp and strong, since their intensity will only be determined by the relative occupation of the carbon-atom layers, which will in turn depend on the perfection of the metal-atom stacking. These reflections are similar to those of the 1/2(111) type in V_6C_5 and Nb_6C_5. For these last two compounds there is perfect fcc metal-atom stacking, and the intensity of the 1/2(111) superlattice reflections will

be unaffected by lateral displacements of the carbon-atom planes, provided the 2/3-occupancy of alternate planes is maintained. Although the metal-atom stacking in the ζ- and ε-phases does contain a number of stacking faults, sufficiently large perfect crystal regions exist, so that sharp reflections will result from the differences in occupancy of the carbon-atom planes.

The diffuse streaks in fig. 5.3.9(a) may then be explained in terms of frequent irregular lateral displacements of successive 1/3-, and their adjacent 2/3-full layers. A similar effect was found in unannealed specimens of Nb_6C_5, where a high density of these displacements resulted in continuous streaking in (211) sections (see fig. 3.2.5).

The $(1\bar{1}00)$ section of ζ-phase vanadium carbide (fig. 5.3.1(c)) shows a complex diffuse scattering pattern. Although the zigzag lines of scattering are centred at one-third and two-thirds the distance between rows of reflections, they contain peaks displaced slightly from these positions. If a high degree of long-range order could develop, and the resulting superlattice reflections were at approximately the same positions as the diffuse peaks, then a large basal plane cell parameter would be needed in order to index these reflections.

(iii) Mechanisms for the transformation between structures with different stacking sequences

A notable feature of transformations which only involve changes in the stacking sequence of close-packed planes, is their capacity to propagate at temperatures below those needed for transformations known to require long-range atomic diffusion. Although the ζ- and ε-phases form at high temperatures, their transformation to hcp

structures at 750°C is typical of this type of transformation, the simplest example being the fcc to hcp transformation in cobalt. The driving force for the cobalt transformation is the negative stacking fault energy for the fcc structure below the equilibrium temperature of 420°C, and the negative stacking fault energy for the hcp structure above this temperature. A large temperature hysteresis is frequently found, especially on cooling, for the fcc to hcp transformation. Although the stacking fault energies for the structures presently considered, fcc, hcp, ζ and ε, are low, the simple criterion for the cobalt transformation will not be directly applicable, since the ζ- and ε-phase unit cells contain sequences of layer planes with fcc and hcp configurations. However, the mechanisms for the transformations between the various stacking sequence structures and those previously examined for the fcc to hcp transformation are likely to be similar.

It is instructive to consider the partial shear displacement sequences necessary to transform one structure into another. For the fcc to hcp transformation (and its reverse) partial shear displacements of the same type on alternate planes are required as shown,

...A̲BC̲AB̲C̲AB̲C̲... gives
...ABABABABA...

To transform the fcc structure to the ζ-phase, shear displacements on every fourth plane are required,

...A̲BCA̲BCAB̲CABC̲ABC...
...ABCACABCBCABABC...

However, not all of the possible transformations have evenly spaced shear displacements. A simple notation can be used

to describe the sequence of displacements. Thus fcc to hcp will be (-.), and fcc to ζ (-...). Using this notation the transformations between various pairs of structures are shown in Table 5.4 below.

TABLE 5.4

structure pair		displacement
fcc	hcp	(-.)
fcc	fcc(twin)	(-)
fcc	ζ	(-...)
fcc	ε	(-..)
fcc	$(cch)_2$	(---...)
hcp	ζ	(-...)
hcp	ε	(---...)
hcp	$(cch)_2$	(-..)
ε	ζ	(.....--.-.--)

The same symbol will represent the transformation in the reverse direction, and to produce a twin-related structure the dots are replaced by dashes and vice versa (for the hcp and $(cch)_2$ sequences the basal plane is not a twin plane).

As there is a very small volume free energy change accompanying this type of transformation (36), possible nucleation and growth processes must therefore

involve very small expenditures of energy. Apart from the occurrence of the transformations at low temperatures, the possibility of stacking rearrangements by atomic diffusion at extended disordered boundaries is unlikely, since such a boundary will have an energy comparable with that of a grain boundary. The following transformation theories have been devised, and are discussed below with reference to the present observations.

(a) In the simplest mechanism a loop of partial dislocation forms spontaneously and expands through the crystal. Subsequent loops then nucleate on the correct planes to give the required stacking sequence. Bollmann (37) noted a serious objection to this mechanism in that the critical loop radius, obtained from a free energy sum involving a negative stacking fault energy balanced against a positive dislocation energy, was approximately 1600Å, and thus spontaneous formation would be improbable. However, de Lamotte and Altstetter (38) suggested that spontaneous nucleation could be aided by an applied stress, and that a new fault would be more likely to form near a pre-existing fault, since this would result in a greater gain in volume free energy.

It was previously mentioned that the stacking faults observed by Billingham and Lewis (18) in vanadium carbide were apparently in the form of loops, since the bounding partial dislocations had the same sign. The loops were very large (much greater than the critical size) and may have formed spontaneously as a result of cooling stresses within the single crystal rods. The increase in fault density for the lower carbon-content specimens would then result from the higher probability of

surmounting the nucleation barrier as the stacking fault energy is reduced. In the present work loops were not seen, and in the absence of a means to overcome the loop nucleation problem, this mechanism seems unlikely, although in principle it could apply to the transformation between any pair of structures.

(b) The mechanism devised by Seeger (39) requires a pole dislocation with a Burgers vector screw component perpendicular to the close-packed planes, which then form a set of interleaved helicoidal surfaces. An expanding partial dislocation will wind up the pole dislocation giving repeated shear with a period that depends on the magnitude of the screw component. In the application of this mechanism to the cobalt transformation, the required screw component is $2a/3[111]$, and the partial dislocations require kinetic energy to overcome their mutual repulsion after the first half-revolution. In metallic crystals the necessary pole dislocations have not been observed, and their existence is unlikely due to their high energy. For the fcc to ζ-phase transformation this mechanism would require an even larger screw component, $4a/3[111]$. This mechanism has however satisfactorily explained the abundance of zinc sulphide polytypes, where screw dislocations with very large Burgers vectors have recently been observed (40).

(c) In the mechanism suggested by Aaronson (41) the growth of a new phase takes place by the propagation of a step across a close-packed plane. Rearrangement of the atom positions occurs at the edges of the steps which are small regions of atomic disorder. The lateral motion of the step is then controlled by short-range diffusion.

The formation of the steps presents a problem of classical two-dimensional nucleation, similar to the spontaneous nucleation of a stacking fault loop, unless nucleation at defects is possible. A dislocation that passes obliquely through the two-phase interface to give a step which is not an integral number of atomic layers in height, will form an inexhaustible supply of nucleation sites for partial dislocations in the interface plane (42).

The fcc to hcp transformation in Al- 4.2at.% Ag alloys (43) is one example which has been found to proceed by this mechanism. The interfacial partial dislocations must lie in alternate planes in order to produce the correct stacking sequence. For the ζ to hcp transformation, partial dislocations would be required on every fourth plane. In figs. 5.3.3(a) and 5.3.8(c) there are many dislocations, giving the mottled contrast, and short lengths of stacking fault are seen which intersect the phase boundaries. Thus the necessary conditions exist for the operation of this step mechanism.

(d) The dislocation reflection mechanism, where one stacking fault can develop into a series of faults on neighbouring planes, was originally proposed by Christian (44), and later extended by Bollmann (45). For this mechanism to operate, a partial dislocation must have sufficient kinetic energy such that when it strikes an inclined fault a local stress field is produced. This stress can be relieved, and the momentum of the initial fault conserved, by the nucleation of another partial dislocation with opposite sign, as shown schematically in fig. 5.3.11. Although the original treatment dealt with the fcc to hcp transformation, the nucleation of new partial dislocations separated by three layers of the original fcc structure

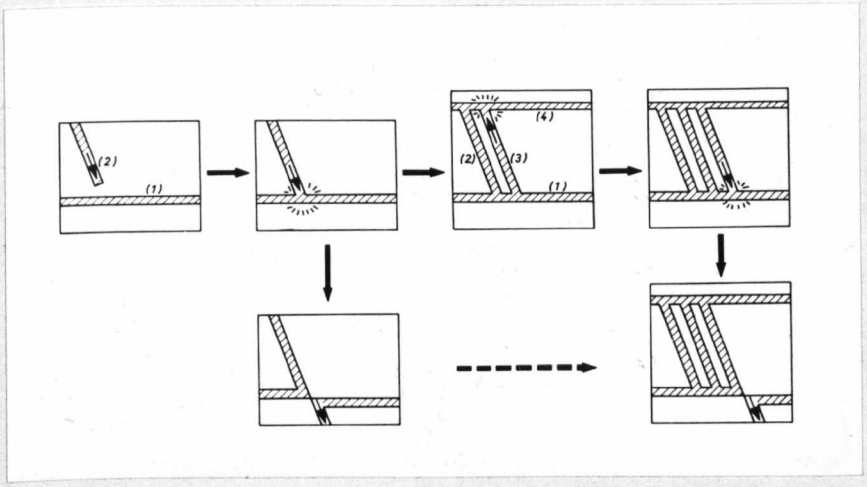

Fig. 5.3.11 Stages in the operation of the stacking fault reflection mechanism, after Bollmann (45).

to give the ε-phase, or four layers to give the ζ-phase, should be possible. Cooling stresses are thought to provide the partial dislocations and their necessary kinetic energy. This mechanism should produce thick regions of perfect stacking. When several travelling partial dislocations nucleate and move independently on the same slip plane, thin faulted lamellae will result where the transformed regions meet.

The observed orientations of the ζ- and ε-phases with respect to the fcc matrix are always those that result from the (-...) and (-..) transformations, i.e. the faults are evenly spaced. Twin-related orientations were never seen. If during the motion of the partial dislocations in the fcc monocarbides, carbon atoms diffuse away from the resulting hexagonal layer into the neighbouring planes, reflection giving another hexagonal layer may be favoured at the third or fourth next plane to avoid forming the new fault in a region with a locally higher carbon-atom concentration.

A brief summary of these transformation modes may be given. The ledge and reflection mechanisms would appear most likely for respectively, the low-, and high-, temperature transformations between carbides with various metal-atom stacking arrangements. Both of these mechanisms depend on the nucleation of a new partial dislocation at an inclined stacking fault. For the low-temperature transformation of the ζ- and ε-phases to the hcp structure, the initial hexagonal nuclei are present in the stacking arrangements of the ζ- and ε-phases. The formation of the ζ- and ε-phases at high temperatures would appear to be initiated by single high velocity partial dislocations, produced by cooling stresses, which are then reflected back and forth between inclined stacking faults.

REFERENCES

1. F.C.Frank, Phil. Mag., 42, 1014 (1951).
2. G.S.Zhdanov, C. R. Acad. Sci. URSS, 48, 43 (1945).
3. G.S.Zhdanov and Z.V.Minervina, C. R. Acad. Sci. URSS, 48, 182 (1945).
4. H.Jagodzinski, Acta Cryst., 2, 201 (1949).
5. H.Hashimoto, A.Howie and M.J.Whelan, Proc. Roy. Soc., A269, 8 (1962).
6. A.Art, R.Gevers and S.Amelinckx, Phys. Stat. Sol., 3, 697 (1963).
7. R.Gevers, A.Art and S.Amelinckx, Phys. Stat. Sol., 3, 1563 (1963).
8. J.Van Landuyt, R.Gevers and S.Amelinckx, Phys. Stat. Sol., 18, 167 (1966).
9. W.L.Bell and G.Thomas, Phys. Stat. Sol., 12, 843 (1965).
10. A.K.Head, Aust. J. Phys., 22, 569 (1969).
11. G.S.Woods, Phil. Mag., 23, 473 (1971).
12. J.Van Landuyt, R.Gevers and S.Amelinckx, Phys. Stat. Sol., 7, 519 (1964); 9, 135 (1965).
13. A.Howie and M.J.Whelan, Proc. Roy. Soc., A267, 206 (1962).
14. J.M.Silcock and W.J.Tunstall, Phil. Mag., 10, 361 (1964).
15. L.M.Clarebrough, Aust. J. Phys., 24, 79 (1971).
16. M.J.Whelan and P.B.Hirsch, Phil. Mag., 2, 1121 (1957).
17. P.Humble, Phys. Stat. Sol., 30, 183 (1968).
18. J.Billingham and M.H.Lewis, Phil. Mag., 24, 231 (1971).
19. J.L.Martin, B.Jouffrey and P.Costa, Phys. Stat. Sol., 22, 349 (1967).
20. A.L.Bowman, T.C.Wallace, J.L.Yarnell, R.G.Wenzel and E.K.Storms, Acta Cryst., 19, 6 (1965).

21. G.R.Booker and A.Howie, unpublished work quoted by, A.Howie and B.Jouffrey, Phil. Mag., 14, 201 (1966).
22. A.Kelly and D.J.Rowcliffe, Phys. Stat. Sol., 14, K29 (1966).
23. M.L.Kronberg, Acta Met., 5, 507 (1957).
24. M.S.Paterson, J. Appl. Phys., 23, 805 (1952).
25. R.Lesser and G.Brauer, Z. Metallk., 49, 622 (1958).
26. G.Brauer and R.Lesser, Z. Metallk., 50, 8 (1959).
27. G.Brauer and R.Lesser, Z. Metallk., 50, 512 (1959).
28. E.K.Storms and R.J.McNeal, J. Phys. Chem., 66, 1401 (1962).
29. E.Rudy, St.Windisch and C.E.Brukl, Planseeber. Pulvermet., 16, 3 (1968).
30. K.Yvon and E.Parthé, Acta Cryst., B26, 149 (1970).
31. E.Rudy, J.Less-Common Metals, 20, 49 (1970).
32. E.Rudy, Met. Trans., 1, 1249 (1970).
33. J.L.Martin, A.Rocher, B.Jouffrey and P.Costa, Phil. Mag., 24, 1355 (1971).
34. W.F.Brizes and J.M.Tobin, J. Amer. Cer. Soc., 50, 115 (1967).
35. E.K.Storms, "The Refractory Carbides", (Academic Press, New York, 1967).
36. E.E.Havinga, J.H.N.van Vucht and K.H.J.Buschow, Philips Res. Repts., 24, 407 (1969).
37. W.Bollmann, "Crystal Defects and Crystalline Interfaces", (Springer-Verlag, Berlin, 1970).
38. E.de Lamotte and C.Altstetter, in "The Mechanism of Phase Transformations in Crystalline Solids", Inst. of Metals Monograph, No33, 189 (1968).
39. A.Seeger, Z. Metallk., 44, 247 (1953); 47, 653 (1956).
40. S.Mardix and A.R.Lang, Phil. Mag., 24, 683 (1971).
41. H.I.Aaronson, "Decomposition of Austenite by Diffusional Processes", (Interscience, New York, 1962).

42. H.I.Aaronson and C.Laird, Met. Trans., 242, 1437 (1968).
43. C.Laird and H.I.Aaronson, Acta Met., 17, 505 (1969).
44. J.W.Christian, Proc. Roy. Soc. Lond., 206, 51 (1951).
45. W.Bollmann, Acta Met., 9, 972 (1961).

CHAPTER SIX

TRANSITION-METAL NITRIDES

6.1 Introduction

The transition-metal nitrides have previously been examined to a far smaller degree than either the carbides or oxides. Their use as high temperature structural materials is secondary to that of the carbides mainly because of their inferior resistance to chemical attack, and lack of stability with respect to dissociation at high temperatures.

The free energies of formation of various carbides and nitrides are shown for comparison in fig. 6.1.1. For a constant composition, the nitrogen vapour pressure, which is considerably higher than the metal vapour pressure, shows a logarithmic dependence on reciprocal temperature (3-8), and thus dissociation to a composition lower in nitrogen readily takes place. For carbides, the vapour pressures of metal and nonmetal are comparable, and much lower than for nitrides at elevated temperatures, and thus a given composition is moderately stable with respect to the loss of an excess of one atomic species. The equilibrium nitrogen pressure shows a very strong dependence on composition, for a constant temperature. From the combination of these thermodynamic factors, the preparation of higher nitrides from the melt may require ambient nitrogen pressures of up to several hundred atmospheres.

The objective of most previous work on nitrides has been the determination of phase relationships, many of which are still doubtful. The present work was undertaken to establish whether ordered compounds such as

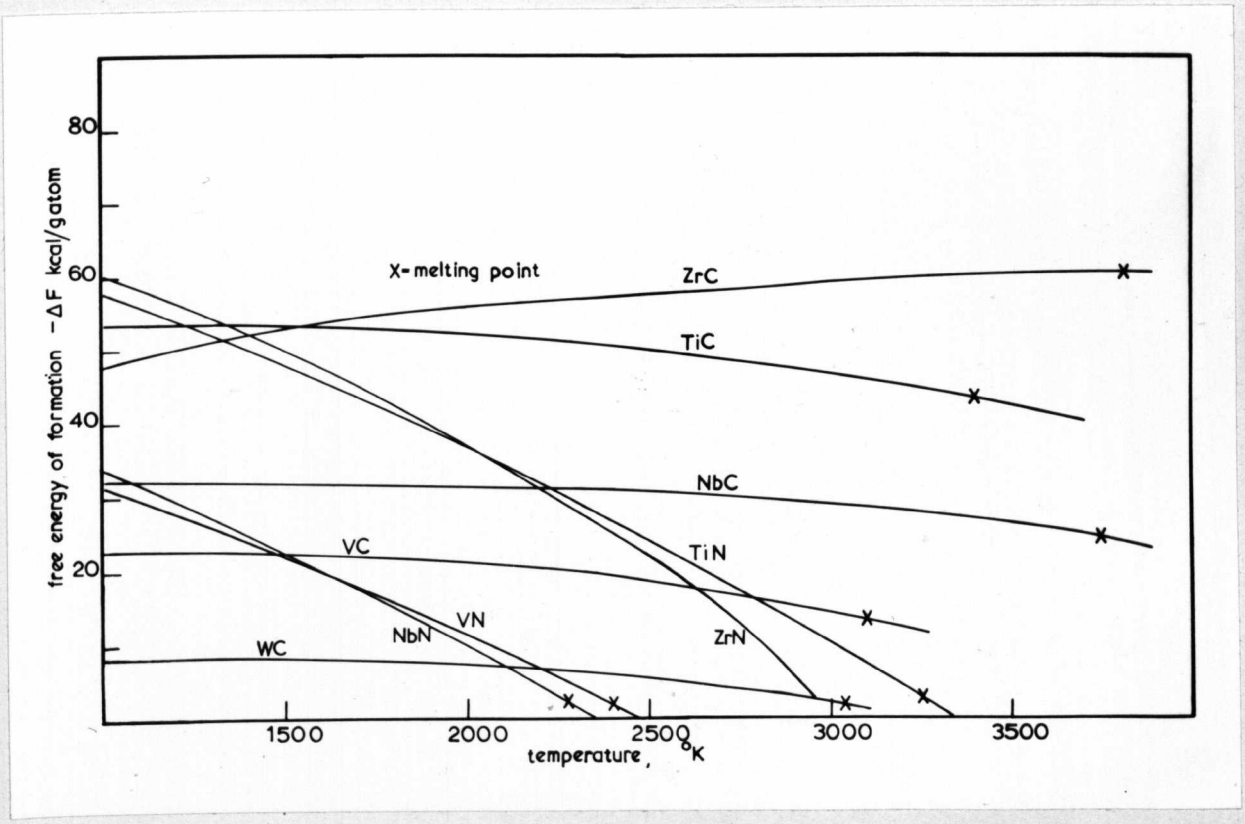

Fig. 6.1.1 Free energy of formation of various Group 1Va and Va metal carbides and nitrides as a function of temperature. VC and VN from Mah (1), others from Gerasimov et al. (2).

M_2X, M_6X_5, and M_8X_7 might exist in the mononitride phase fields of vanadium and titanium, in view of the similar nonstoichiometric deviations of these phases to the corresponding monocarbides.

6.1.1 Phase Relationships in Transition-Metal Nitrides

(i) Titanium nitride

The most recent phase diagram for this system (3) is shown in fig. 6.1.2. Two intermediate phases are known. The NaCl-type mononitride shows the largest composition range for any carbide or nitride. The ε-phase, with ideal composition Ti_2N, has very narrow composition limits and exists below about 1000°C. It has been reported (9) that nitrogen-atom ordering in the α-Ti solid solution at 20at.% N results in a CdI_2-type superstructure.

(ii) Vanadium nitride

A complete phase diagram for the vanadium - nitrogen system has not been determined, due mostly to the very high nitrogen pressures encountered at high temperatures. The most systematic survey of the sub-solidus equilibria has been made by Schnell (10), who showed the existence of the hcp heminitride V_2N, between $VN_{0.48}$ and $VN_{0.50}$, and the NaCl-type mononitride between $VN_{0.72}$ and $VN_{1.0}$.

Two examples of nitrogen-atom order have been found. The compound $V_{16}N$, whose structure was determined by electron diffraction (11), is based on a distorted bcc vanadium metal lattice. Yvon et al. (12), using neutron diffraction, found the ordered nitrogen-atom arrangement in hcp-V_2N was similar to that in ε-Fe_2N (see fig. 4.1.2).

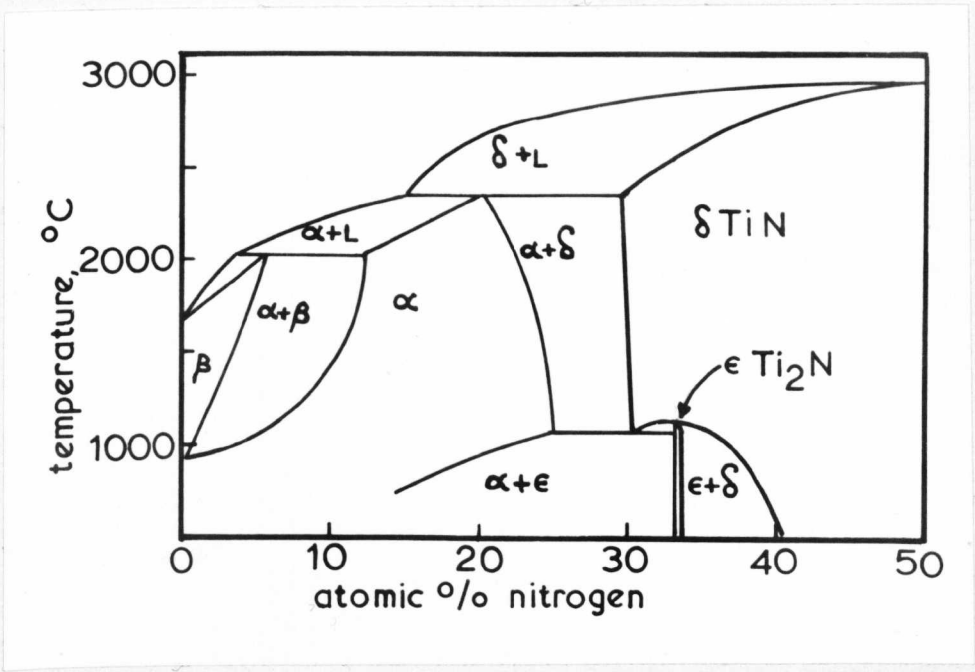

Fig. 6.1.2 Phase diagram for the titanium - nitrogen system, after McClaine and Coppel (3).

(iii) Comparison with other nitrides

Apart from the Zr-N system which contains only the NaCl-type mononitride (13), the other nitride systems of the Group IVa and Va metals which have received noteworthy attention, Nb-N and Ta-N, show many intermediate phases. In the Nb-N system the NaCl-type mononitride is of limited extent, and three other phases are found in the range $NbN_{0.8}$ to $NbN_{1.0}$ (14). In the Ta-N system there is no NaCl-type mononitride. Recent electron diffraction results using vapour-grown polycrystalline films (15) have shown a series of isomorphous niobium and tantalum nitrides containing excess nitrogen, i.e. M_5N_6, M_4N_5, as well as Ta_3N_5. The isolated occurrence of Hf_4N_3 and Hf_3N_2 with mixed metal-atom stacking has already been noted in Chapter 5.

6.2 Titanium Nitride

6.2.1 Electron Microscopy and Diffraction

Mononitride specimens with compositions from $TiN_{0.5}$ to $TiN_{1.0}$ failed to show any form of long-range order, even after prolonged heat-treatments at temperatures down to 500°C. However, the diffraction patterns from specimens with nitrogen concentrations below $TiN_{0.75}$ did reveal a characteristic type of diffuse scattering with a similar distribution to that found in the monocarbides. In this case the intensity of the scattering was much weaker than for example in niobium carbide, and satisfactory photographic reproduction was impossible.

The presence of this diffuse scattering for similar compositions as in titanium carbide might indicate that an ordered compound, isostructural with Ti_2C, would be formed at slightly lower temperatures, though its observation will be denied due to the very low diffusion rates.

6.3 Vanadium Nitride

6.3.1 The VN/V_2N Eutectic

A transverse section from an as-grown rod is shown in fig. 6.3.1. The areas in light and dark contrast are the cubic and hexagonal phases respectively. Within the mononitride lamellae a fine scale precipitation of V_2N is observed. The formation of a eutectic between the hexagonal M_2X and cubic MX phases is so far unique for this type of transition-metal - interstitial-atom system. However, the presence of the two different V_2N lamellae sizes indicates the formation of a eutectic, since the large lamellae have grown from the melt, while the fine lamellae have precipitated from the cubic mononitride on post-solidification cooling.

By prior optical examination of perforated disc specimens, it was possible to select for electron microscopy boundaries that resulted from solidification or solid-state precipitation. Although the interface relationship for the two phases was the same in both cases, the boundaries resulting from solidification show slight irregularities (see fig. 5.2.4(c)), while those resulting from solid-state precipitation are straight, as shown in fig. 6.3.2. The orientation relationship is given by,

$$(111)VN \parallel (0001)V_2N$$
$$\langle 110\rangle VN \parallel \langle 11\bar{2}0\rangle V_2N$$

From the lattice parameter data of Schnell (10) there is good matching in the interface plane, thus,

$$\frac{d\text{-}(110)VN}{d\text{-}(11\bar{2}0)V_2N} = 1.012$$

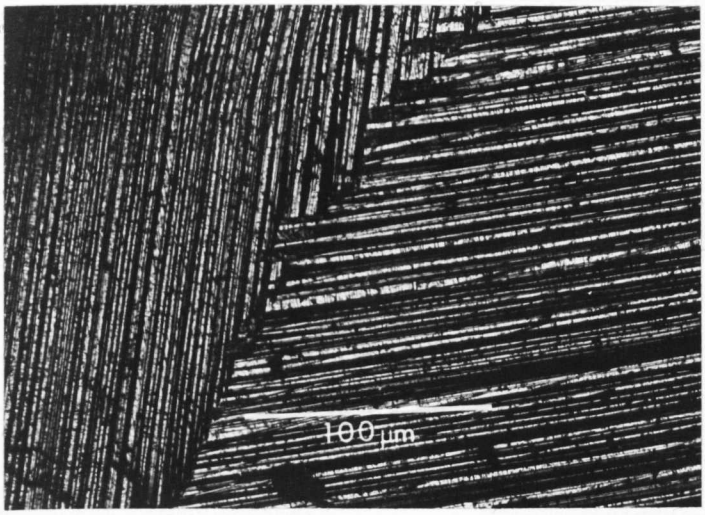

Fig. 6.3.1 Transverse section through an as-grown crystal rod of the VN/V_2N eutectic. Light phase VN, dark phase V_2N. (optical micrograph)

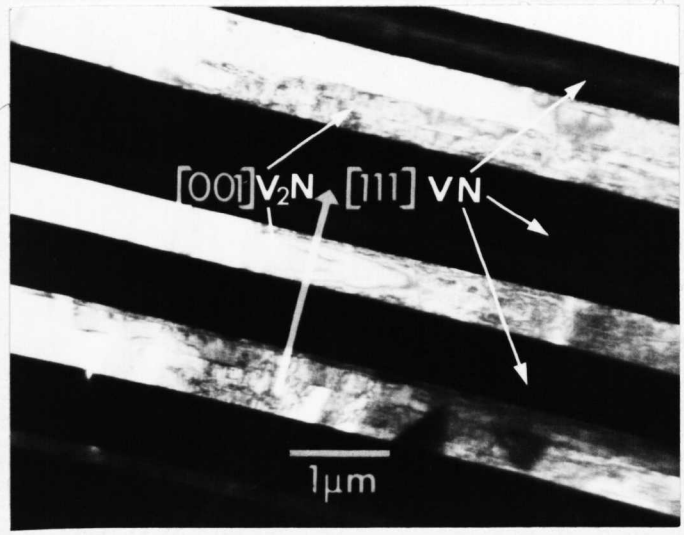

Fig. 6.3.2 Precipitate lamellae of V_2N in as-grown eutectic. The mononitride phase is not sufficiently thin to be electron transparent.

Although melting point data for the V-N system is unavailable, the inability to produce single phase V_2N from the melt implies that the equilibrium nitrogen pressure for the eutectic composition will be less than for V_2N, due to the lower melting point of the eutectic, despite having a higher overall nitrogen concentration. Increasing the nitrogen pressure will then tend to produce single-phase mononitride. On the other hand, when the nitrogen pressure is reduced just below that necessary for the eutectic, the composition of the solidifying phase will then be displaced discontinuously to a composition with nitrogen concentration below that for single phase V_2N.

By a chemical analysis method similar to that used for vanadium monoxide (Appendix 7.1), the composition of the eutectic specimens was $VN_{0.63}$, while the specimen grown below the critical eutectic nitrogen pressure (about two atmospheres) was $VN_{0.40}$.

6.3.2 Electron Microscopy and Diffraction

(i) Vanadium mononitride

When thin discs of the eutectic were heated under two atmospheres of nitrogen at 1000°C single phase mononitride was formed. The highest composition produced in this way was $VN_{0.95}$, as measured by weight gain and chemical analysis. Subsequent electron microscope examination of annealed mononitride specimens showed that this phase was exceptional in that it contained no long- or short-range order at any composition.

(ii) Vanadium heminitride

The previously proposed ε-Fe_2N-type ordered structure (9) was confirmed by electron microscopy and

diffraction. The upper temperature limit for the formation of this superlattice could not be determined because ordering took place when bulk specimens were quenched.
It was possible to melt specimens of the eutectic in the electron microscope by 'beam heating'. The ensuing loss in nitrogen gave single-phase heminitride, which even after rapid quenching, by shutting off the electron beam, still showed the presence of the ordered structure. Fig. 6.3.3 shows a region of heminitride containing antiphase boundaries, and the associated diffraction patterns. This specimen had been converted wholly into V_2N by normal vacuum annealing.

Since it was suggested in Chapter 4 that the high-temperature modifications of V_2C and Nb_2C did not have the ε-Fe_2N-type structure, the diffraction patterns from V_2N provide a useful reference on which to base this argument. The exact $(1\bar{1}00)$ section diffraction patterns from V_2N, and V_2C and Nb_2C are identical (see figs. 4.2.1(b) and 4.3.1(b)). However the 001 reflection of V_2N is allowed, since its intensity remains unaltered when the specimen is rotated about the hexagonal c-axis (fig. 6.3.3(c)). The (0001) section diffraction patterns from V_2C, Nb_2C, and V_2N show one particular feature in common, in that they contain the anomalous group of 1/3(110) reflections round the origin. As for V_2C and Nb_2C, these reflections may be explained by the multiple diffraction that results from the intersection of the Ewald sphere with the first-order Laue zone, where the 1/3(110) type of reflections are allowed.

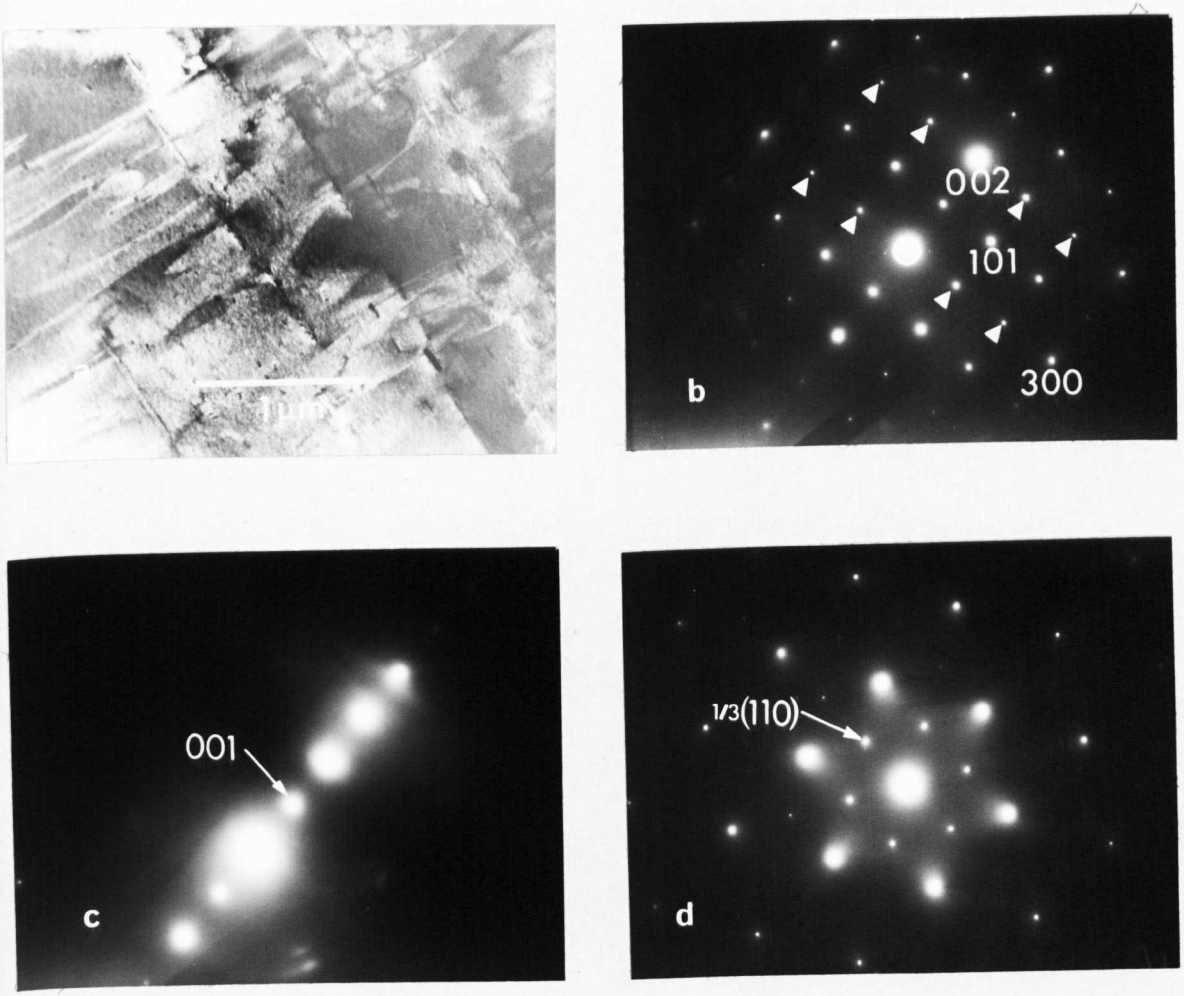

Fig. 6.3.3 Ordered domain structure in V_2N. (a) DF showing antiphase boundary structure characteristic of hexagonal superlattice, (b) $(1\bar{1}00)$ section with hexagonal superlattice reflections (multiple diffraction reflections marked), (c) rotated $(1\bar{1}00)$ section showing allowed intensity of 001 reflection, (d) (0001) section showing anomalous group of 1/3(110) reflections round the origin.

REFERENCES

1. A.D.Mah, U.S. Bur. Mines Rept., RI6177 (1963).
2. Ya.Gerasimov, A.N.Kestovnikov and A.S.Shakov, "Chemical Thermodynamics in Nonferrous Metallurgy", vol. 3 (Israel Program for Scientific Translations, Jerusalem, 1965).
3. L.A.McClaine and C.P.Coppel, Tech. Rept., AFML-TR-65-299, Part 1 (1965).
4. G.Brauer and W.-D.Schnell, J. Less-Common Metals, 6, 326 (1964).
5. F.J.Krieger, Rand Memorandum, RM-6295-PR (1970).
6. C.A.Stearns and F.J.Kohl, High Temp. Sci., 2, 146 (1970).
7. T.Mills, J. Less-Common Metals, 22, 373 (1970).
8. N.R.McDonald and G.R.Wallwork, Oxidation of Metals, 2, 263 (1970).
9. H.Nowotny, F.Benesovsky, C.E.Brukl and O.Schob, Monatsh. Chem., 92, 403 (1961).
10. W.-D.Schnell, PhD thesis, University of Vienna (1964).
11. D.Potter and C.Altstetter, Scripta Met., 4, 849 (1970).
12. K.Yvon, H.Nowotny and R.Kieffer, Monatsh. Chem., 98, 34 (1967).
13. E.K.Storms, Tech. Rept., LAMS-2674, Part 2 (1962).
14. N.Terao, Japanese J. Appl. Phys., 4, 353 (1965).
15. N.Terao, Japanese J. Appl. Phys., 10, 248 (1971).

CHAPTER SEVEN

OXIDES WITH AN FCC METAL-ATOM STRUCTURE

7.1 Introduction

In this Chapter the titanium and vanadium monoxide phase fields are examined. The phase relationships in the Ti-O and V-O systems show many similarities. Thus at low oxygen concentrations there are several phases whose structures are based on those of the parent metals, while at high oxygen concentrations both systems contain a complex series of shear structures. However, in the neighbourhood of the equiatomic compositions the nominal NaCl-type monoxides are found with large nonstoichiometric deviations on both sides of the composition $MO_{1.0}$. Complete phase diagrams do not exist, partly because of the inherent complexity of the systems, but mainly due to the difficulty in structure determination by X-ray diffraction techniques when weakly scattering atoms are involved.

An additional feature of these monoxides, which is not encountered with either the carbides or nitrides, is that appreciable vacancy concentrations may exist in both the metal and nonmetal sublattices. This will then lead to the possibility of ordering of the remaining metal and nonmetal atoms.

The major part of this Chapter is concerned with the vanadium-atom order in oxygen-rich vanadium monoxide, and for this reason a departure will be made from the natural order of description by giving the results for this compound before those of the Group IVa metal compound. The work on titanium monoxide was undertaken

in order to check the previous electron microscope observations of vacancy order, and to examine certain aspects of this ordering which have remained in doubt.

7.2 Vanadium Monoxide

7.2.1 Previous Work

Much of the earlier work on vanadium monoxide was made in order to establish the extent of the single-phase field. Although the phase boundaries show little deviation with temperature, different values of these limits have been reported. Schönberg (1) and Andersson (2) gave the single-phase limits as $VO_{0.80}$ to $VO_{1.20}$, Gel'd et al. (3) $VO_{0.85}$ to $VO_{1.24}$, and Westman and Nordmark (4) $VO_{0.89}$ to $VO_{1.26}$. More recently Stenstrom and Westman (5) put the limits as $VO_{0.68}$ to $VO_{1.26}$. Banus and Reed (6) found the homogeneity limits at 1300°C were from $VO_{0.79}$ to $VO_{1.28}$, although single-phase material up to $VO_{1.32}$ could be cast from the melt.

At the stoichiometric composition the concentrations of vanadium and oxygen vacancies are equal at about 15%, while the total number of vacancies decreases smoothly across the phase field. Taylor and Doyle (7) have found that the number of vacancies can be reduced under pressure at high temperatures, as evidenced by the increase in lattice parameter.

Several workers have reported the occurrence of another phase between the monoxide and monoxide plus sesquioxide (V_2O_3) phase fields. Klemm and Grimm (8), and Gurevich and Ormont (9), noted a bcc phase at $VO_{1.30}$, and between $VO_{1.20}$ and $VO_{1.37}$ respectively. Magnéli et al. (10) reported an ordered defect structure at $VO_{1.20}$ which formed below 900°C and was based on the NaCl-type

structure. Further work by Westman and Nordmark (4) showed this phase was tetragonally distorted and had a unit cell four-times that of the basic NaCl cell. Attempts to determine the structure were unsuccessful (11), although the space group Ia3 was assigned, and two unit cells with contents $V_{200}O_{256}$ ($VO_{1.28}$) and $V_{192}O_{256}$ ($VO_{1.31}$) were considered.

Two recent electron microscope examinations have been made. The first, by Andersson and Gjønnes (12), showed the presence of an ordered phase, $V_{52}O_{64}$ ($VO_{1.23}$), belonging to the space group $I4_1/amd$. The structure was determined by combining electron diffraction patterns, which gave the positions of the superlattice reflections, with X-ray diffraction intensities. The unit cell, shown in fig. 7.2.12, contains four vanadium atoms in interstitial sites (tetrahedrally coordinated by oxygen atoms) with the four neighbouring vanadium sites vacant. Comparison of the calculated and observed X-ray intensities gave an R-factor of 0.08. Another tetragonal phase, which gave other superlattice reflections as well as those of $V_{52}O_{64}$, was found near $VO_{1.17}$, but in this case no structure determination was made. In the second electron microscope investigation, by Saeki and Nakahira (13), similar electron diffraction patterns and the same space group were found as for $V_{52}O_{64}$. However, the previous structure was challenged, and a vacancy distribution consisting of planar groups of four vacant nearest-neighbour vanadium sites lying on the (001) plane perpendicular to the tetragonal axis was suggested.

It is worth noting at this point that in the structure considered by Andersson and Gjønnes (12) the

presence of the interstitial vanadium atoms lowers the intensity of certain fundamental reflections over those for a distribution on normal fcc sites. This reduction amounts to almost 20% for the 200 reflection, and a much higher R-factor would have resulted if the actual structure did not contain the interstitial vanadium atoms.

7.2.2 Characterization of Vanadium Monoxide

(i) Chemical analysis

A suitable method of composition analysis was found desirable in view of the widely differing reported values for the phase limits. Also, a crystal growth method from the melt had been used, where significant changes in composition from that of the starting material would be likely to occur.

A detailed description of the various methods that were used for this analysis is given in Appendix 7.1 at the end of this Chapter. The method finally adopted was accurate and reproducible to within $\pm 0.3\%$ in the weight of vanadium. This will then give an error in the composition of $VO_{x \pm 0.02}$. Two determinations were made on each slice cut from the bulk crystals.

(ii) Density and lattice parameter measurements

By combining measurements of the variation of pycnometric density and lattice parameter with composition, the numbers of metal and nonmetal vacancies may be found. The specimens used for these measurements were in the as-grown (disordered) condition.

The lattice parameter measurements were made by the standard Debye-Sherrer powder technique using an 11.54cm diameter camera and Cu-Kα radiation.

As suggested in (4) a 40μm thick aluminium sheet was placed over the film to reduce fogging by fluorescent radiation from the specimens. Potassium chloride was used as an internal standard. The values obtained are plotted in fig. 7.2.1*, and compare favourably with the later results of Banus and Reed (6).

Density measurements were made using a simple displacement method. The liquid used, ethylene dibromide density approximately 2.17gcm^{-3}, was calibrated for each measurement with a piece of brass having accurately known dimensions, and approximately the same weight as the test specimens (about 10g). The specimens were supported from the balance by a thin wire, and held under the liquid in a wire cage. These results are shown in fig. 7.2.2.

The method used to determine the fraction of vacant metal and nonmetal sites is given in Appendix 7.2. The calculated percentages of vacancies in each sublattice are shown in fig. 7.2.3. At $VO_{1.30}$ the oxygen sublattice is fully occupied and there are 22% metal-atom vacancies. With decreasing oxygen concentration the total number of vacancies increases, and at the lower phase boundary, near $VO_{0.80}$, 10% vacancies remain in the metal sublattice, while the oxygen sublattice contains 28% vacancies.

The largest source of error in the lattice parameter and density functions is in the determination of the composition, i.e. x in VO_x. The results of Westman and Nordmark (4) suggest a systematic error in this quantity, giving consistently low values for the density, and high values for the lattice parameter.

* Although a straight line has been drawn through the plotted points, a linear relationship is not necessarily predicted.

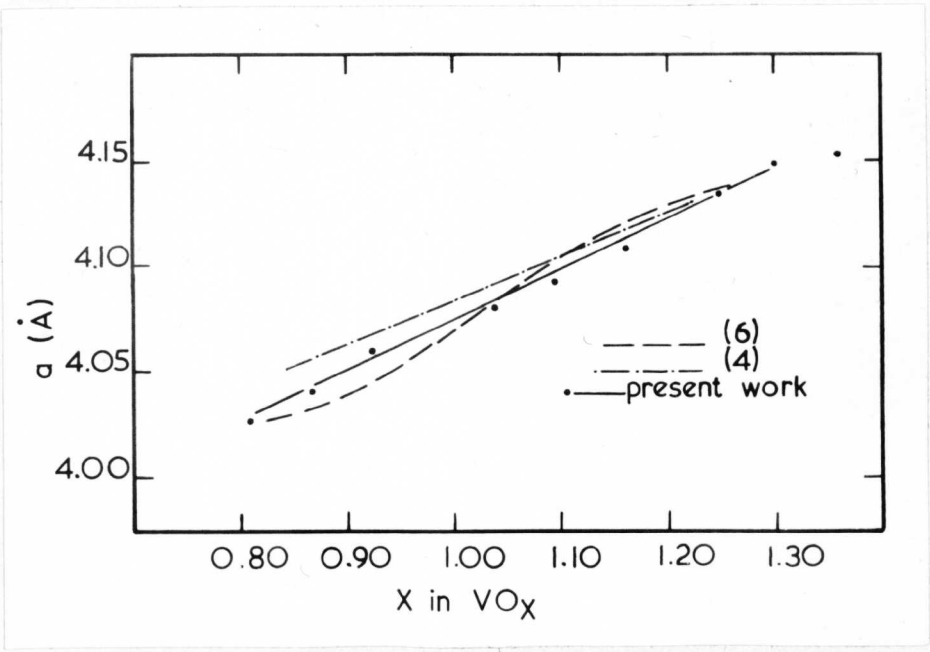

Fig. 7.2.1 Variation in lattice parameter against composition for vanadium monoxide.

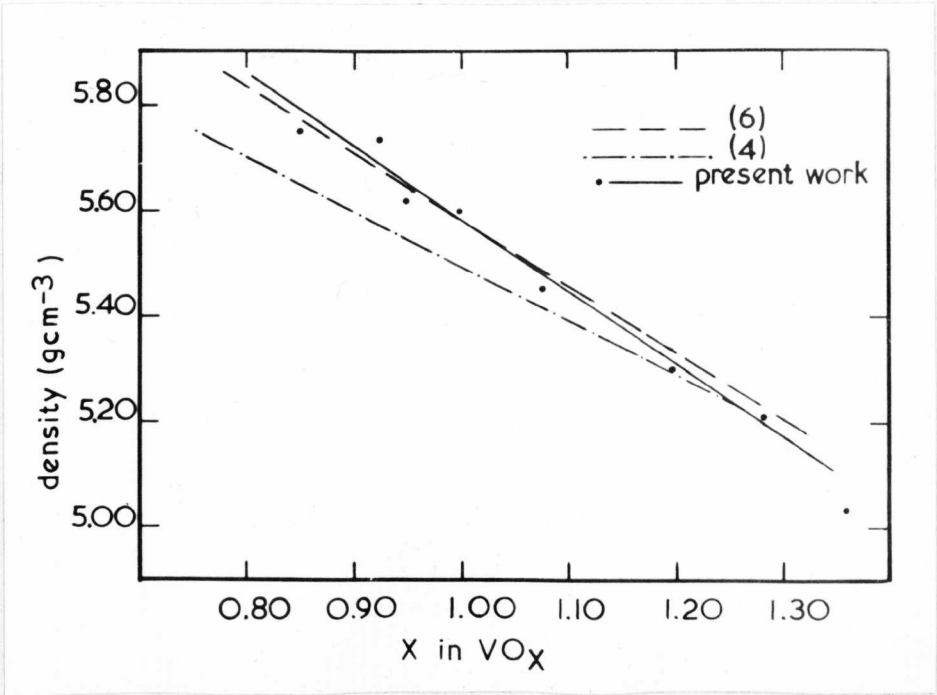

Fig. 7.2.2 Variation in density against composition for vanadium monoxide.

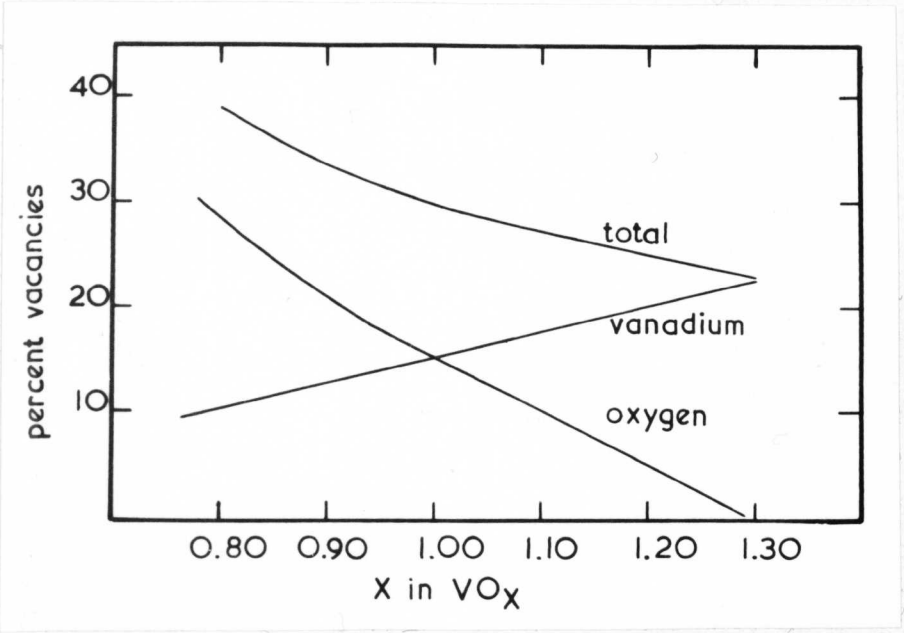

Fig. 7.2.3 Variation in vacancy concentrations against composition for vanadium monoxide.

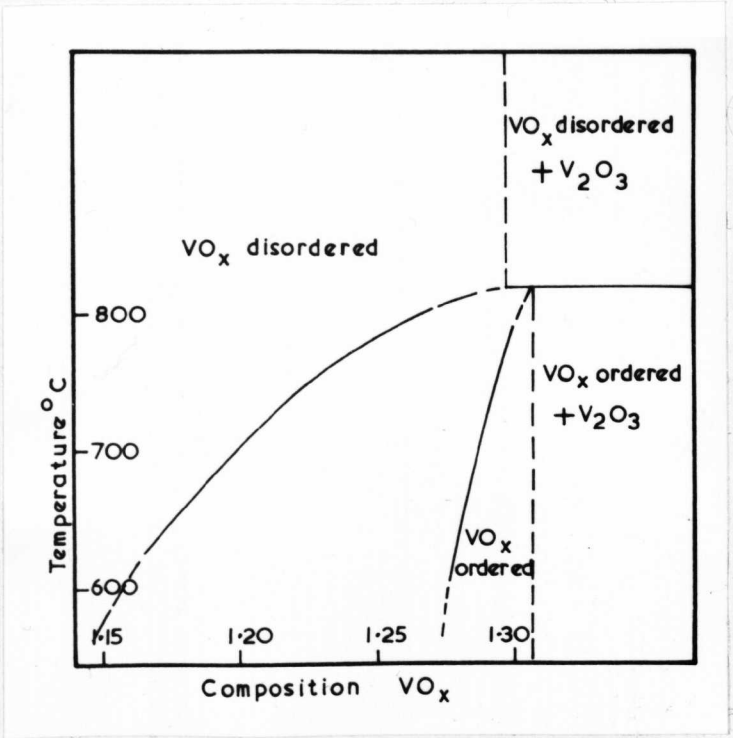

Fig. 7.2.4 Partial phase diagram showing the limits of the ordered compound $V_{244}O_{320}$.

7.2.3 Electron Microscope Observations on Vanadium Monoxide

An examination was made on thin-foil specimens, with compositions ranging over the entire cubic phase field, which were annealed at various temperatures down to 500°C. One ordered phase was found in specimens within the composition limits $VO_{1.15}$ to $VO_{1.31}$, having a maximum in the order - disorder transformation temperature of 810°C at the upper composition limit. The decomposition of this phase was observed below 600°C into one, or possibly two, other ordered structures. The diffraction patterns and domain morphology of this first ordered structure are described in section 7.2.4(i), and the structure of this phase, which has a unit cell composition of $V_{244}O_{320}$, in section 7.2.4(ii).

The low temperature for the decomposition of $V_{244}O_{320}$ gave a reaction product on a fine scale, thus making a complete structure analysis impossible. Several other features observed during electron microscope examination, such as diffuse electron scattering, complex dislocation configurations, and the precipitation of V_2O_3, are also discussed.

7.2.4 The Ordered Compound $V_{244}O_{320}$

(i) Electron microscopy and diffraction

In discussing the formation of $V_{244}O_{320}$ it is convenient to refer to the partial phase diagram shown in fig. 7.2.4. This has been constructed from a series of isothermal heat-treatments, and indicates the stability region of the ordered phase. The decomposition of this phase below 600°C is not shown.

Domains of the long-range-ordered phase formed by a process of nucleation and growth. The distribution

and size of the domains varied with composition, and heat-treatment time and temperature. Preliminary examination of the diffraction patterns from isolated domains showed that the superlattice has tetragonal symmetry, with the c-axis aligned along one of the three possible cube axes of the parent disordered matrix. This type of symmetry is evident from the diffraction patterns of fig. 7.2.5; thus in a (100) orientation foil one four-fold symmetric pattern consisting of strong superlattice reflections and ringed arrays of weak superlattice reflections, and two two-fold symmetric patterns rotated relatively by 90° are observed. A (110) orientation shows two different patterns, while a (111) orientation shows three identical patterns rotated relatively by 60°. In the two remaining diffraction patterns of this figure, the (310) section contains the weak reflections observed in (a), and the (210) section shows additional reflections which are not contained in either the (100), (110) or (111) sections.

Short anneals just below the disordus* temperature resulted in the uniform distribution of small domains illustrated in fig. 7.2.6. Dark-field images from the indicated superlattice reflections show the three domain orientations. Slow cooling (5°C/h) through the disordus and longer annealing times resulted in the inhomogeneous distribution of domains shown in fig. 7.2.7. The domains in light contrast in (a), (100) orientation, have similar c-axes which are aligned parallel to the electron beam, while for those in (c), (110) orientation, the c-axes are

* The disordus and ordus lines on the phase diagram (fig. 7.2.4) delineate the start and completion of the ordered phase formation.

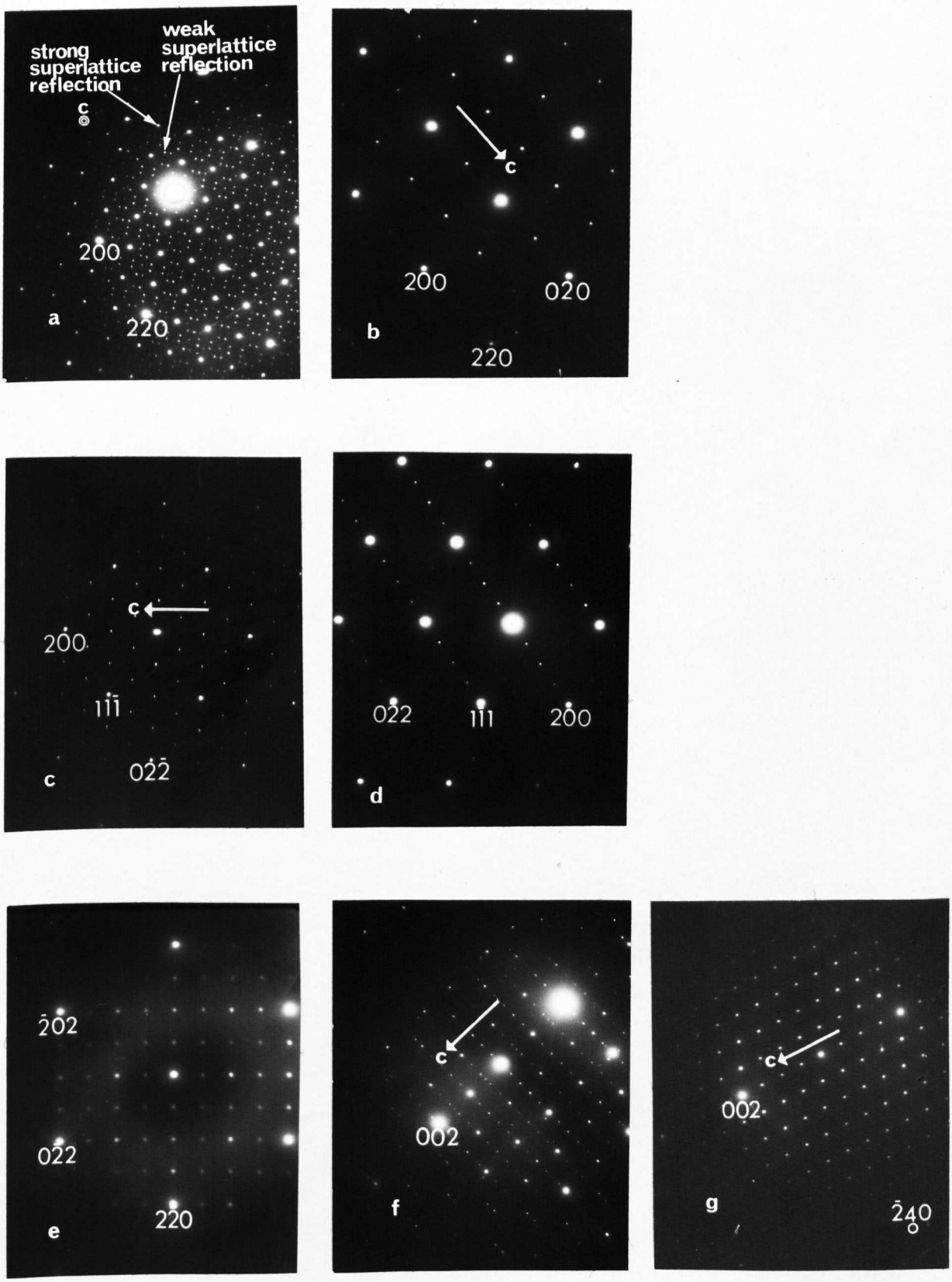

Fig. 7.2.5 Diffraction patterns from the ordered compound $V_{244}O_{320}$. (a) and (b) (100) sections, (c) and (d) (110) sections, (e) (111), (f) (310), and (g) (210) sections. The direction of the tetragonal c-axis is marked on some patterns.

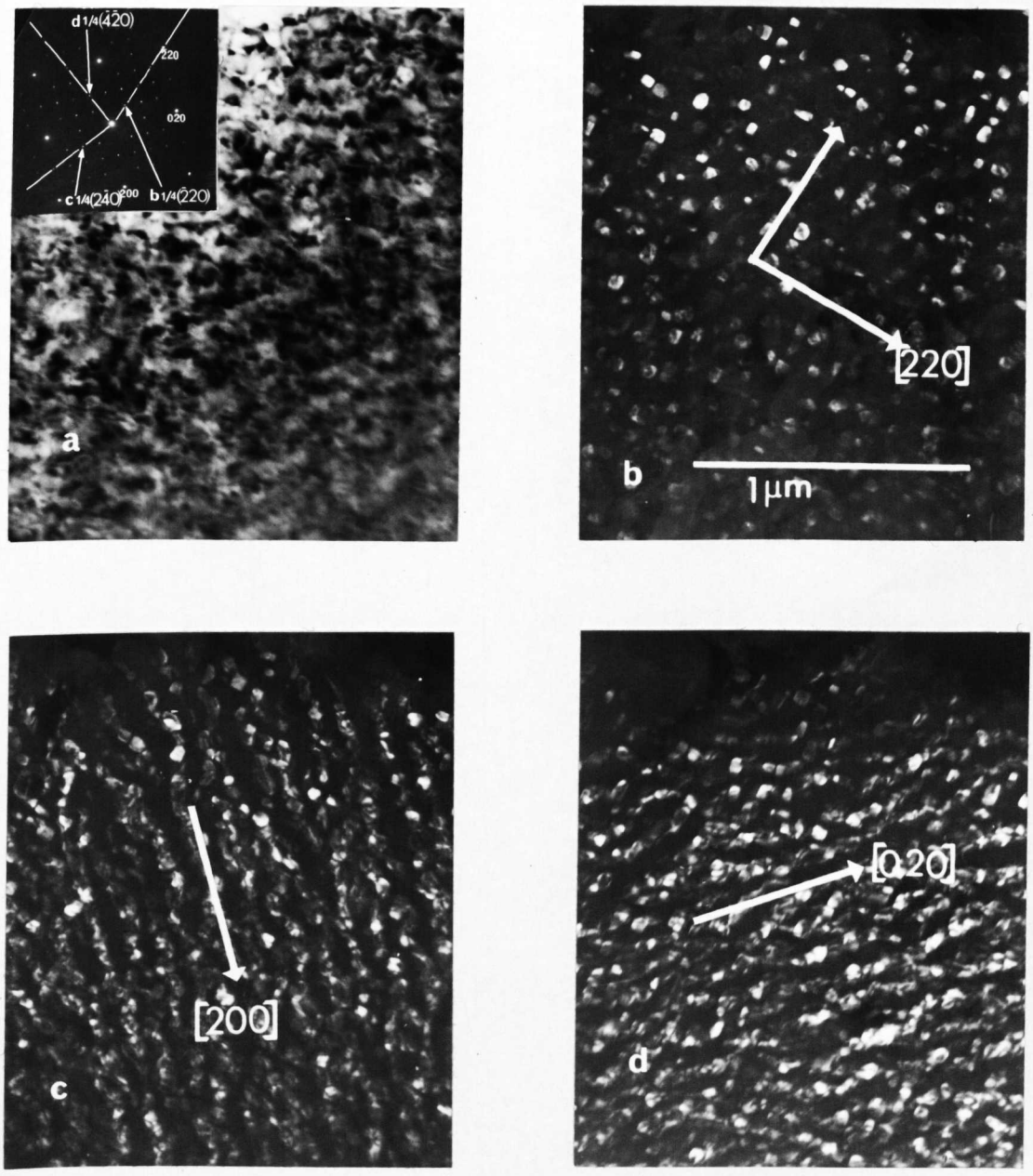

Fig. 7.2.6 Distribution of ordered domains in $VO_{1.25}$ annealed for 30h at 700°C. (a) BF, inset shows correctly orientated (100) section pattern (the weak superlattice reflections do not appear in this pattern due to the low beam intensity). (b), (c) and (d) DF from indicated strong superlattice reflections.

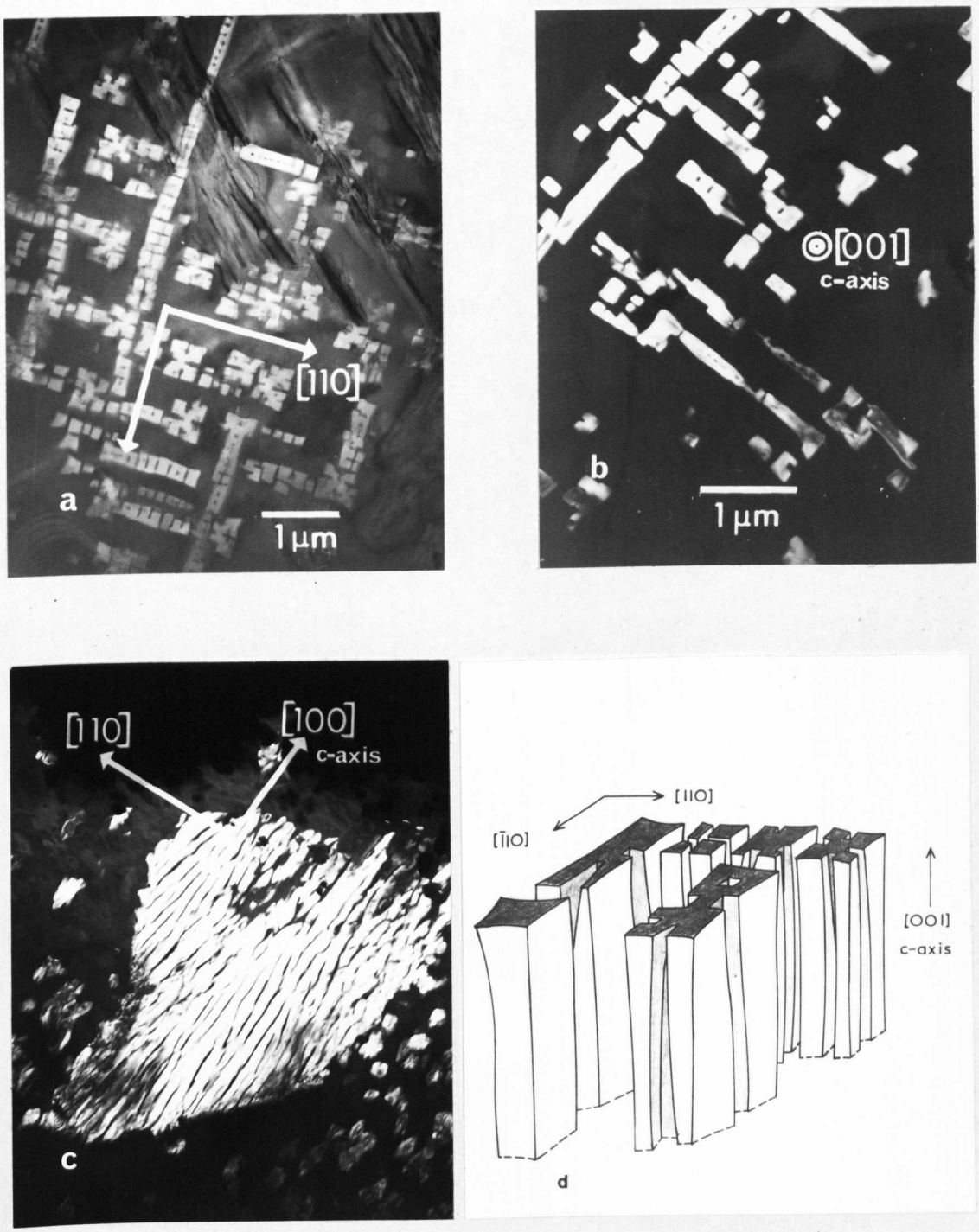

Fig. 7.2.7 Selective coarsening of ordered domains. (a) BF and (b) DF (different area from (a)) (100) orientation. (c) DF (110) orientation. (d) schematic representation of coarsened distribution.

aligned perpendicular to the beam.

In these well annealed specimens the individual domains have a square-sectioned rod-like shape, with the rod axis the [001] c-axis and orthogonal {110} interfaces. The coarsening process from the homogeneous distribution of fig. 7.2.6 involves grouping of the domains along ⟨110⟩ directions, shown schematically in fig. 7.2.7(d), thus accounting for their unusual change in aspect when viewed in different orientations. A selective dissolution and growth process is thought to be responsible for the formation of the aligned groups of domains. A similar explanation has been suggested to account for the aligned arrays of Ni_3Al (γ') coherent precipitates in nickel alloys (14). An attractive elastic interaction between neighbouring γ' precipitates arises from differences in the elastic moduli between the precipitate and the matrix. This interaction then affects the coarsening process by selecting aligned particles for growth at the expense of non-aligned particles which will dissolve. In the present case favourably aligned particles will be those domains with similarly directed c-axes. The main driving force for coarsening is the overall reduction in interfacial energy. When this energy is large, the coarsening rate will be too rapid for the elastic interaction to exert any influence. The coarsening rate for $V_{244}O_{320}$ domains is particularly slow, as evidenced by the long annealing times required to develop the aligned microstructure.

A striking illustration of the long-range nature of the elastic interaction is shown in fig. 7.2.8. This specimen was annealed just below the disordus to

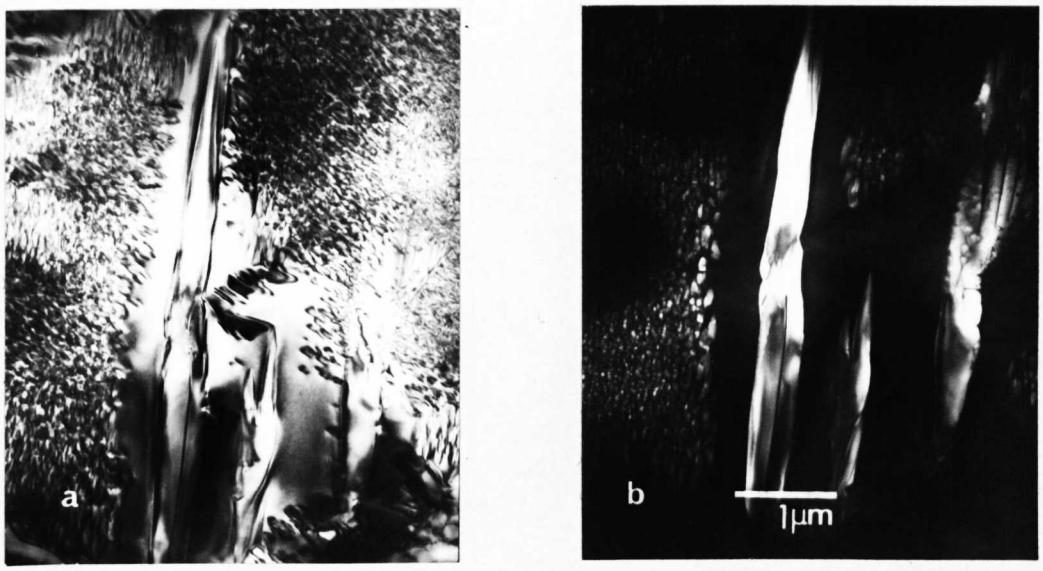

Fig. 7.2.8 Nucleation of new ordered domains with the same orientation as large pre-existing domains in $VO_{1.25}$, annealed for 200h at 750°C, quenched to 600°C and annealed for 50h. (a) BF and (b) DF (110) orientation.

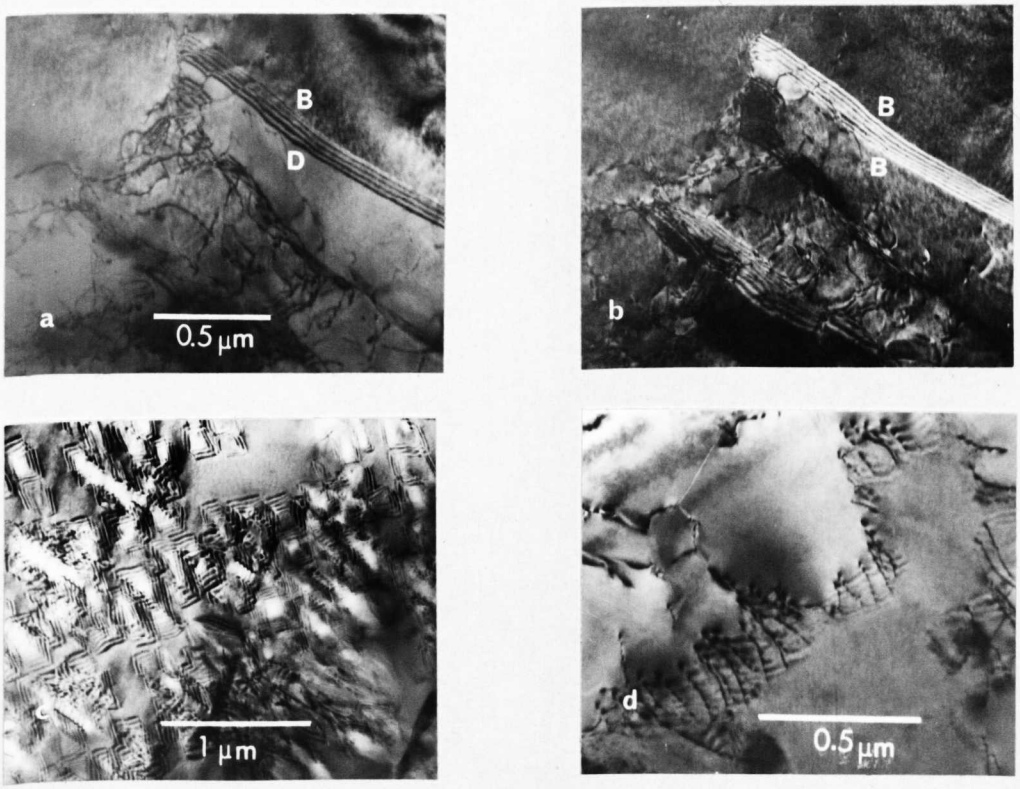

Fig. 7.2.9 Interface contrast associated with ordered domains. (a) BF antisymmetric, (b) DF symmetric δ-fringes at domain-domain interface. (c) BF domain-matrix interfaces δ-fringes, (d) BF fringes associated with dislocations in domains.

produce a sparse distribution of very large domains. Quenching to a lower annealing temperature resulted in the nucleation of domains with c-axes in the same direction as the large neighbouring domains. The zone which is free from newly nucleated domains in the close vicinity of the large domains is probably caused by the depletion of metal vacancies from the matrix in this region.

The tetragonal distortion introduced by the vacancy ordering, though too small to be detected directly by electron diffraction, was apparent in interface contrast. This is shown in fig. 7.2.9, where typical δ-fringes are observed at both domain-domain and domain-matrix interfaces. The specimen showing domain-domain interface contrast is fully ordered, and also contains large precipitates of V_2O_3. This precipitation, which took place above the annealing temperature, generated a high density of dislocations, and fringe contrast is seen associated with these dislocations in an ordered domain (fig. 7.2.9(d)). This contrast is expected when the dislocation produces an 'out-of-step' antiphase boundary with respect to the superlattice unit cell. Antiphase boundaries formed as a result of growth accidents were not seen in the domains when the image was formed in dark-field from one of the strong superlattice reflections.

Domains found in specimens with compositions below about $VO_{1.20}$ frequently had dislocation arrays at their interface with the matrix, while larger domains formed at the same temperature in specimens with compositions higher than $VO_{1.20}$ remained fully coherent. The dislocations lie along the c-axis direction, and

contrast experiments showed they had Burgers vectors of the form a/2⟨110⟩. The domains in fig.7.2.10(a) have an irregular array of dislocations, while in (b) some domains have no associated dislocations, and others, which are much larger, have a closely spaced array. Domains having an interface with the more disordered dislocation configuration will grow more rapidly if short-range diffusion across the interface is a significant barrier to domain growth.

Several mechanisms have been proposed for introducing misfit dislocations. Except in the case of prismatic punching, for large lattice misfit strains, spontaneous bursting at the interface is unlikely (15,16). Usually the observed misfit dislocation structure is the one that can develop most rapidly, and is not necessarily the predicted equilibrium configuration. One such mechanism involves the attractive interaction between the strain fields of a precipitate particle and grown-in dislocations (17). These matrix dislocations are then trapped at the precipitate-matrix interface. In the present case, specimens with compositions below $VO_{1.20}$ contained a large number of grown-in dislocations, while those with higher compositions were virtually dislocation-free (except where V_2O_3 precipitation had taken place as mentioned above). Furthermore, there was no evidence for splitting of the matrix dislocations which would inhibit their climbing into a suitable orientation at the domain-matrix interface.

During the examination of the (100) section diffraction patterns from domains with c-axes parallel to the electron beam, patterns such as those shown in

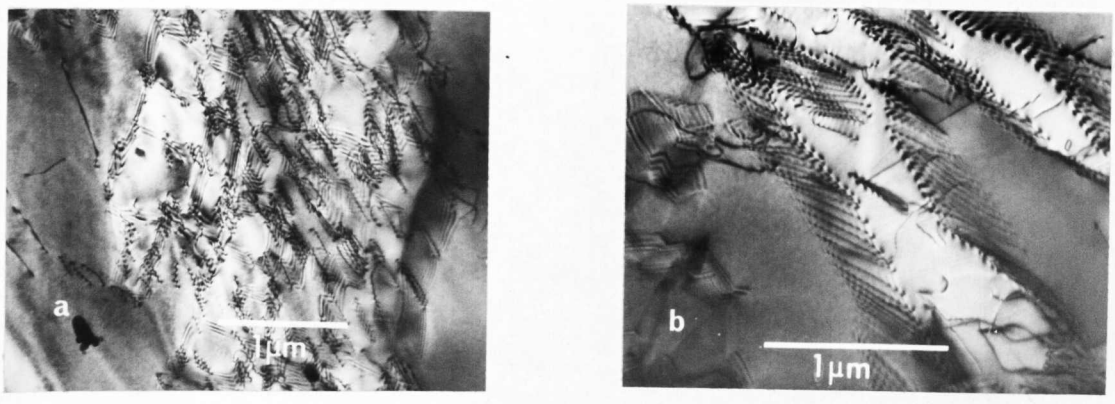

Fig. 7.2.10 Dislocations at domain-matrix interface in $VO_{1.19}$.

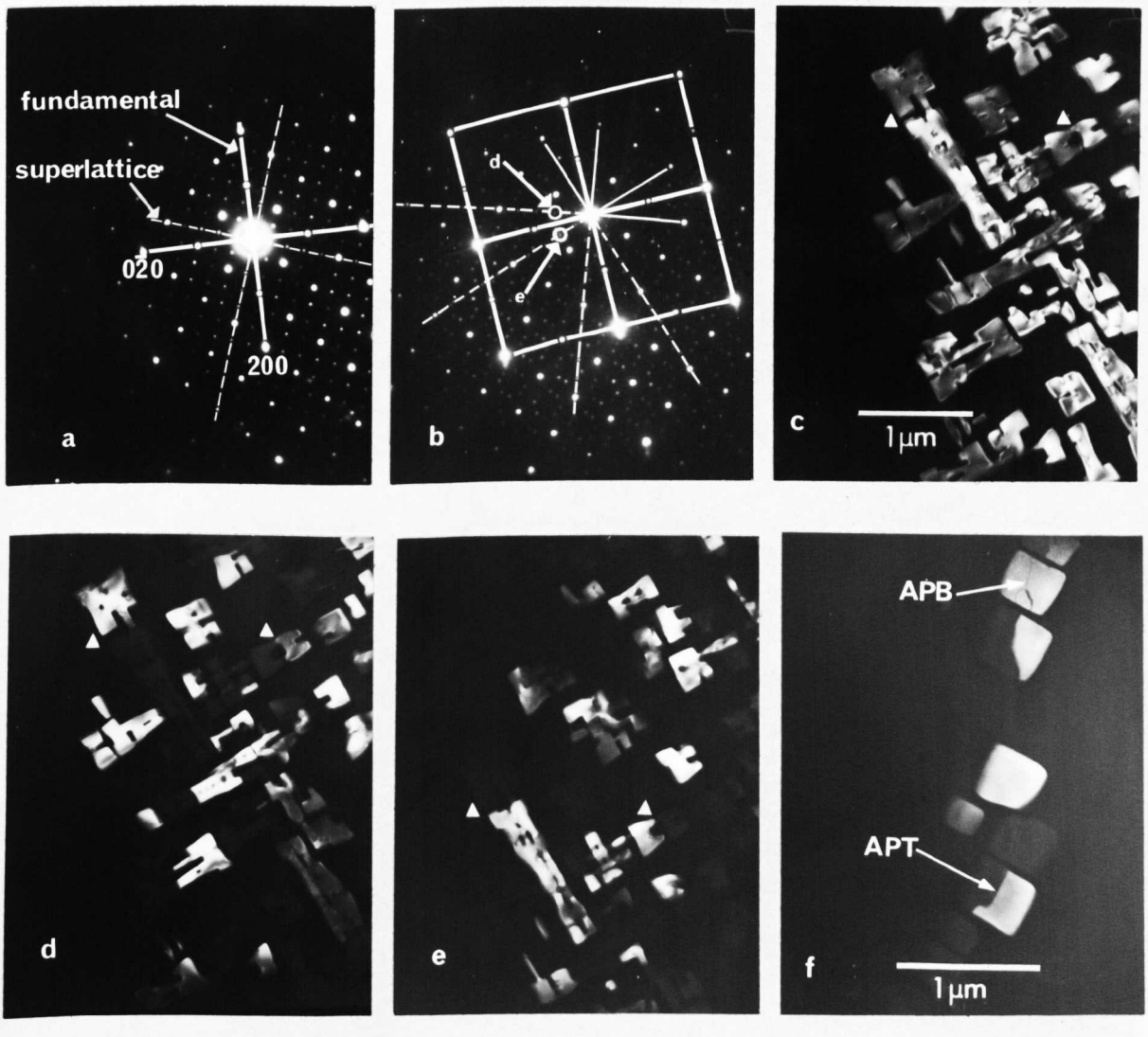

Fig. 7.2.11 Twin-related 'sub-domains' in vanadium monoxide. (a) (100) section from one twin orientation, (b) (100) section with superimposed patterns from both twin orientations, i.e. from whole area shown in (c) DF from strong superlattice reflection. (d) and (e) DF showing separate twin orientations, (f) DF from weak reflection. APT, anti-parallel twin.

fig. 7.2.11(a) were obtained. This pattern contains half of the weak reflections which formed the ringed arrays of fig. 7.2.5(a). The fundamental, strong, and weak superlattice reflections now form a square grid. A similar grid, but rotated by $2\tan^{-1}1/3$ about the beam direction, could then be obtained containing the remaining weak reflections, as well as the fundamental and strong superlattice reflections as before. Dark-field images, figs. 7.2.11(d) and (e), from the weak reflections on the two grids, showed that the domains with a common c-axis were actually comprised of two orientations of domains in twin-relation. These two 'sub-domain' orientations share the same strong superlattice reflections, but are distinguished by the positions of their respective weak superlattice reflections.

Fig. 7.2.11(f) shows a group of domains observed in dark-field using one of the weak superlattice reflections. Within each domain, which appears to have formed from a single nucleus, growth accidents have occurred which result in the formation of different twin orientations or anti-phase boundaries.

(ii) Structure of the ordered compound $V_{244}O_{320}$

The two ordered phases previously found by Andersson and Gjønnes (12), $V_{52}O_{64}$, giving rise to the strong superlattice reflections, and a superlattice at $VO_{1.17}$, with unknown structure giving rise to the same strong superlattice reflections plus the additional weak reflections, can now be identified as a single superlattice. Thus the same weak and strong superlattice reflections are always observed together in specimens that show the ordered-domain microstructure. The distribution of

allowed superlattice reflections was found by combining the information obtained from the various single crystal diffraction patterns. From the general conditions for these reflections,

$$\begin{aligned} hkl, \quad & h+k+l = 2n, \\ hk0, \quad & h,(k) = 2n, \\ 00l, \quad & l = 4n, \end{aligned}$$

the superlattice may be assigned to the space group $I4_1/a$. The tetragonal unit cell a-axes are directed along orthogonal ⟨310⟩ directions with $a_t = 2\sqrt{10}a_c$, c_t lies along a ⟨100⟩ direction with $c_t = 2a_c$. This gives a unit cell containing 320 metal and nonmetal atom sites. Andersson and Gjønnes (12) suggested that their structure observed at $VO_{1.17}$ was based on $V_{52}O_{64}$, but that the weak superlattice reflections were due to the ordering of additional vacancies in either the vanadium or oxygen sublattice. In view of the progressive increase in the disordus temperature with increase in oxygen concentration, and the extremely narrow homogeneity range for the ordered structure, it is believed that the superlattice is based on $V_{52}O_{64}$ ($VO_{1.23}$) but with a composition near $VO_{1.30}$, i.e. with an additional ten to twenty vanadium vacancies in the larger unit cell

The structure factors for the $V_{52}O_{64}$ unit cell were computed, and the positions of the reflections were found to be consistent with the strong superlattice reflections. Extra vanadium atoms were then removed from the larger unit cell and the computed structure factors were compared with all the observed superlattice reflections. Only two arrangements were found to be consistent with the observed reflections. The extra vanadium vacancies

in the unit cell form four helices with axes directed parallel to c_t. The difference between the two possible structures lies in the z-coordinate (parallel to c_t) of the extra vacancies. When the calculated structure factors for the two arrangements were compared, differences were found for similarly indexed weak superlattice reflections (those in the (310) section, see fig. 7.2.5(f)). However, a distinction between the two structures could not be made using this information, since the relative intensities of the weak reflections were extremely sensitive to the specimen orientation. X-ray analysis would be of no use since the calculated ratio of the weak to fundamental intensities was about $1:4X10^3$.

An alternative method based on the electrostatic lattice energy was used to distinguish between the two structures. The observed lattice energy of vanadium monoxide (18) is found to be close to the value calculated from the equation,

$$U = - \frac{NAe^2z^2}{r} + \frac{B}{r^m}$$

The first term gives the attractive electrostatic energy of a distribution of point charges, where, N is the number of molecules, e the electronic charge, z the charge on each ion, r the interionic distance, and A is the Madelung constant characteristic of the particular lattice geometry. The second term is a repulsive energy, where B is a constant, and m depends on the type of ion, i.e. m = 6 for V^{2+} and O^{2-}.

The Madelung constant, A, is the limiting value as n (number of the coordination sphere) tends to infinity, of a series of positive and negative terms (electrostatic

attraction and repulsion respectively). This limiting value may be calculated theoretically, thus for the NaCl structure A is given by,

$$6 - \frac{12}{\sqrt{2}} + \frac{8}{\sqrt{3}} - \frac{6}{2} \ldots (-1)^{n-1} \frac{(\text{no. of ions in the } n^{th} \text{ shell})}{(\text{radius of the } n^{th} \text{ shell})} \ldots, \quad n=\infty$$

Thus the favoured structure will be the one with the larger value of A. The computer programme written to calculate A started with the atom and vacancy positions in the unit cell of $V_{244}O_{320}$, i.e. all the vacancies associated with the interstitial vanadium atoms and those in the chosen helix arrangement. One of the vacancy positions in a helix is made the origin of a new unit cell, and further similar unit cells are then added to make a large cube with the specified vacancy at the centre. Previous computer runs for a fully dense lattice showed that in order to obtain a value for A close to that for $n = \infty$, about 10^6 atom sites were required. The positive and negative parts of the Madelung constant are then summed, assuming a metal ion has been placed in the vacancy position at the origin. This procedure is then repeated for the other vacancies comprising the helix. The summation will be a measure of the energy needed to remove the atom on the origin to create the required vacancy. The favoured vacancy arrangement which gave the smallest loss in electrostatic energy on removal of the vanadium ions is shown in fig. 7.2.12.

7.2.5 Low-Temperature Structure in Vanadium Monoxide

(i) Electron microscopy and diffraction

When specimens containing the ordered tetragonal domains (with compositions near the upper phase boundary)

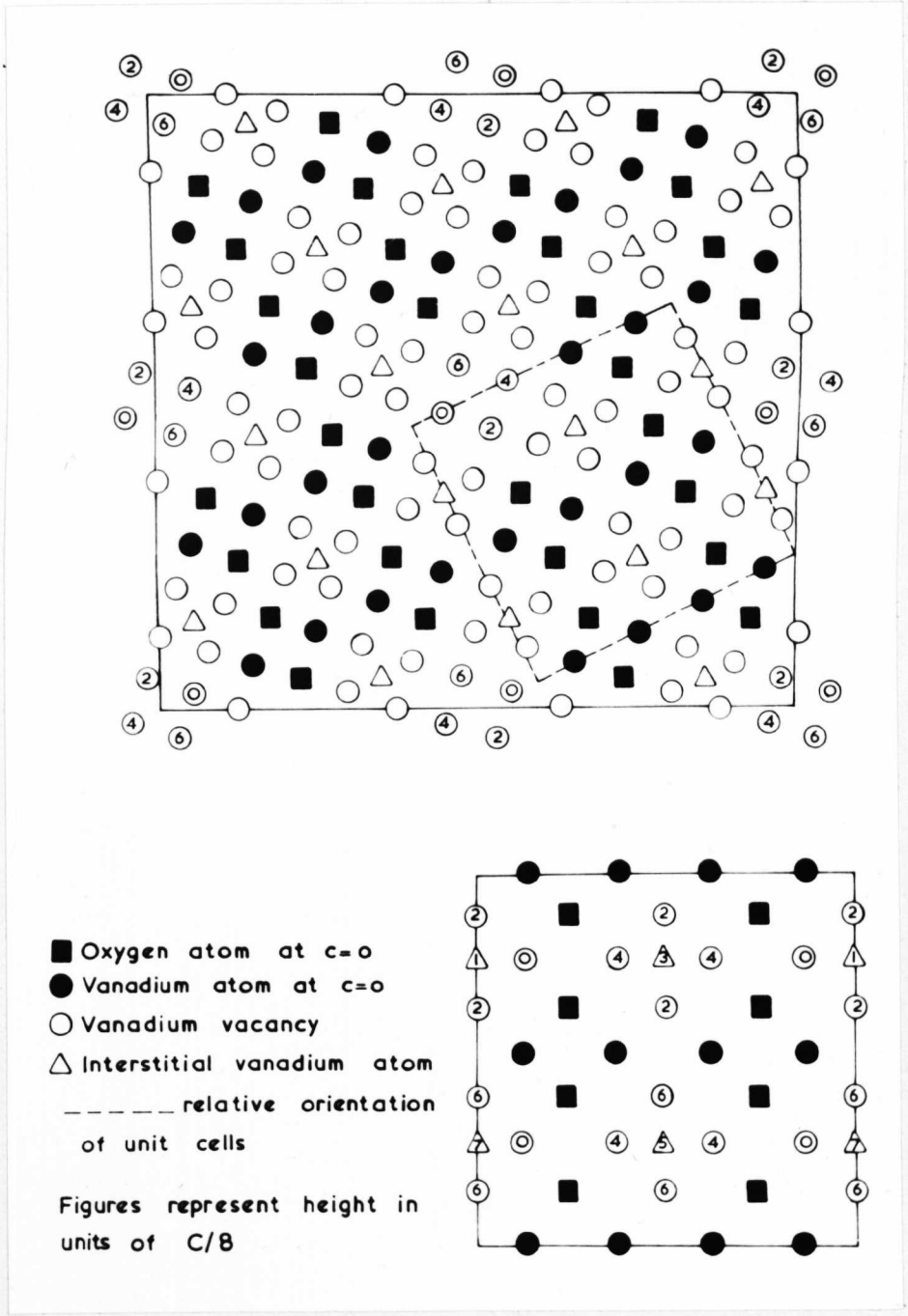

Fig. 7.2.12 The unit cells of $V_{244}O_{320}$ (top) and $V_{52}O_{64}$ (bottom) shown as projections along the tetragonal c-axis.

were annealed at temperatures below about 600°C many new reflections were observed in the diffraction patterns. Fig. 7.2.13 shows the early stages of this transformation in a specimen with (100) orientation that was almost fully ordered after a previous heat-treatment at a higher temperature. In (a) the dark-field image was recorded from a 1/2(220) reflection. This would normally show in bright contrast only those $V_{244}O_{320}$ domains with c-axes parallel to the beam. However, these domains now have a mottled appearance, and irregular striations are seen in some domains which have c-axes perpendicular to the beam. In (b) the image was formed from a 1/4(420) reflection. This would normally show in bright contrast one set of domains with c-axes perpendicular to the beam. Now, some of these domains are seen in which no transformation has occurred, while the weak striations in other areas show what remains of the original domains that have undergone partial transformation to the low-temperature structure.

Fig. 7.2.14 shows the analysis of a (100) orientation specimen where the transformation has gone to completion, as evidenced by the disappearance of the 1/4(420) reflections of $V_{244}O_{320}$ (some reflections, such as those at 1/2 and 1/4(220) are characteristic of both structures). In (c) the large areas in bright contrast were originally domains of $V_{244}O_{320}$ with tetragonal c-axes parallel to the beam. Within these areas there are small rectangular regions which appear to be concentrated towards the centre of the areas in bright contrast. It would thus seem reasonable to suppose that a single $V_{244}O_{320}$ domain has not decomposed into two orientations of one structure,

Fig. 7.2.13 Partial transformation of $V_{244}O_{320}$ domains in $VO_{1.30}$ annealed for 120h at 580°C. (a) and (b) DF from reflections marked in (c)

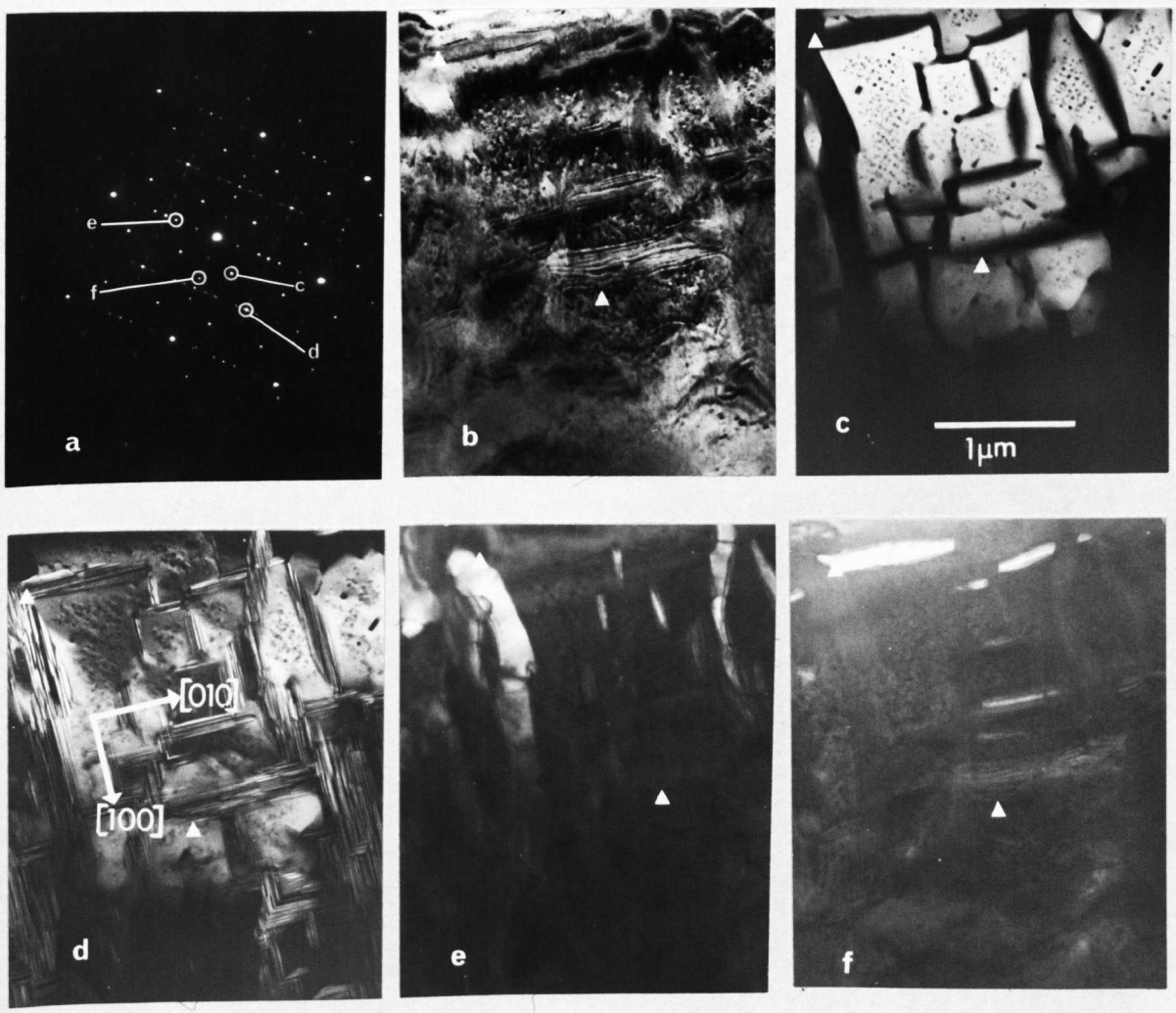

Fig. 7.2.14 Analysis of a fully transformed region in $VO_{1.30}$ annealed for 400h at 540°C. (a) (100) section, (b) BF, (c) DF from 1/4(220), other similar reflections give the same image, (d) DF from 1/2(220), again other similar reflections give the same image, (e) and (f) DF from 2/5(200).

but rather two new structures are formed, with one, i.e. the small rectangular regions, occupying a much smaller volume fraction than the other.

A particular feature of the diffraction patterns from (100) sections is the division of the 200 reflections into fifths, and the streaking parallel and between the 200 reflections. Rotating the specimen greatly reduces the intensity of the 1/5 and 4/5(200) reflections ((b) in fig. 7.2.15). This suggests that these reflections are formed by multiple diffraction, while the 2/5 and 3/5(200) reflections persist after tilting. Difficulty was encountered with these transformed specimens when thinned electrochemically, in that the disc often shattered before perforation. Since the fragmentation technique did not provide suitably thin areas, a more extensive analysis was impracticable. However, several other diffraction patterns obtained from various reciprocal lattice sections are shown in fig. 7.2.15.

(ii) Structure of the low-temperature forms of vanadium monoxide.

The possibility that two new phases are formed from the decomposition of $V_{244}O_{320}$ below 600°C received further support after attempts were made to index the diffraction patterns on the basis of a single phase. The partial reciprocal lattice construction shown in fig. 7.2.15(f) is based on the following argument. Fig. 7.2.15(a), (100) section, shows that two parallel edges of a unit body-centred cube of the fcc reciprocal lattice have reflections at the 2/5 and 3/5(200) positions. Thus the two other edges of the cube, parallel to the first edges, will also contain these reflections.

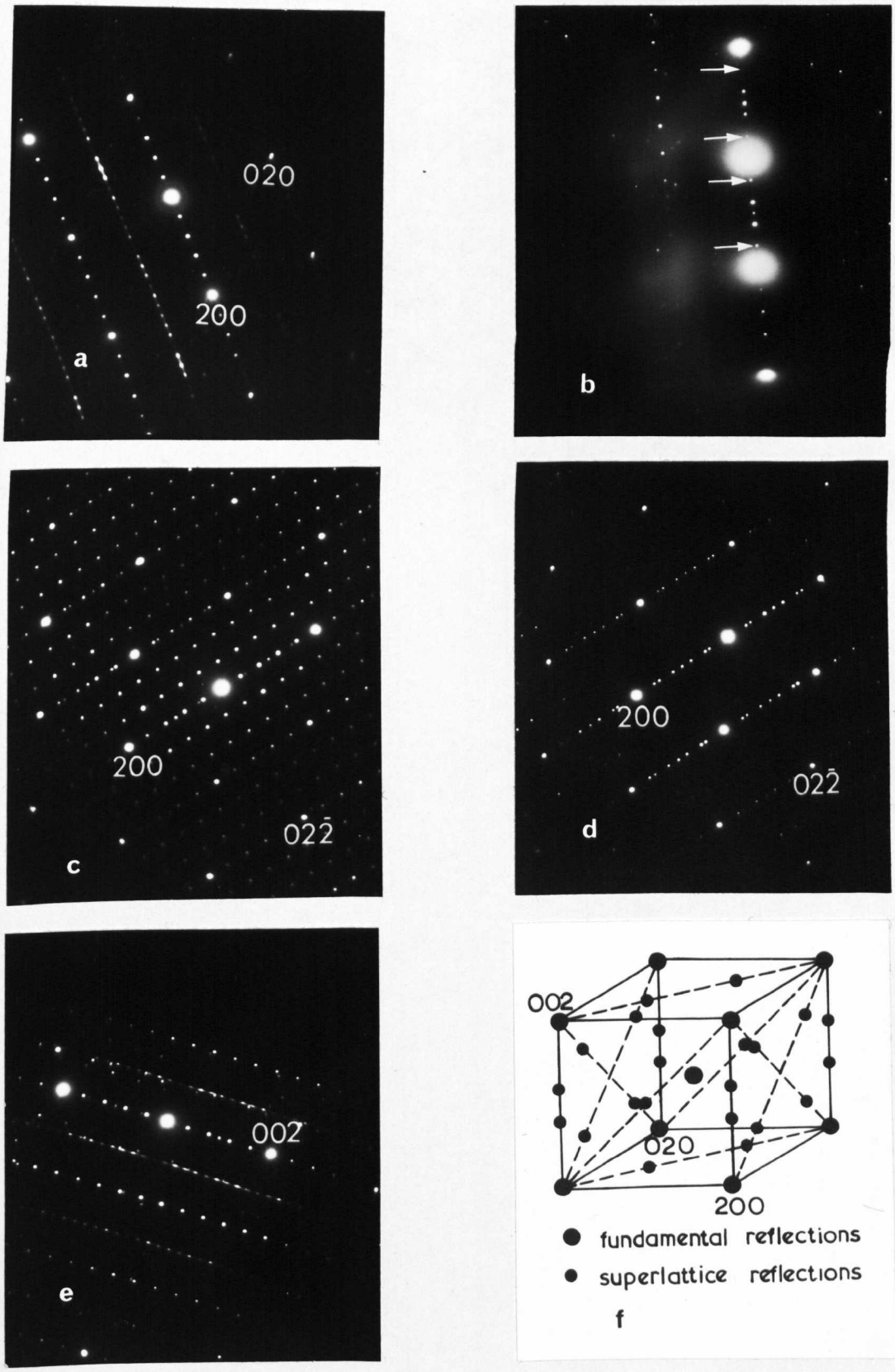

Fig. 7.2.15 Diffraction patterns from transformed regions. These are believed to be single crystal patterns except for the reflections at 1/4 and 1/2(200), which probably arise from untransformed $V_{244}O_{320}$. (a) (100) section, (b) after tilting about 200 showing extinction of 1/5 and 4/5(200) reflections. (c) and (d) (110) sections, (e) (210) section, (f) partial reciprocal lattice construction.

Figs. 7.2.15 (c) and (e), (110) and (210) sections, show that the cube faces perpendicular to the edges containing the 2/5 and 3/5(200) reflections will have reflections at 1/3 and 2/3(220). The other two pairs of parallel faces will contain reflections at 1/4 and 3/4(220) (see fig. 7.2.14(c)), and at 1/2(220) (see fig. 7.2.14(d)) respectively. At this stage the latter two pairs of faces will have reflections at 2/5 and 3/5(200) along one set of parallel edges. Fig. 7.2.14 shows that the regions giving the 1/4 and 3/4(220) reflections do not however appear in bright contrast when using a 2/5(200) reflection for the dark-field image. It is interesting to see that the dark-field images from the 2/5(200) reflections (figs. 7.2.14 (e) and (f)) show in bright contrast areas that may be identified as having been single domains of $V_{244}O_{320}$ with c-axes perpendicular to the beam. If, as suggested, two new phases are contained within these original areas, then they must both have allowed reflections at 2/5 and 3/5(200), i.e. it is expected that the two phases will have certain close similarities in structure.

7.2.6 Further Electron Microscope Studies on Vanadium Monoxide

(i) Diffuse electron scattering

Diffraction patterns from the cubic matrix, existing either as a single phase or in equilibrium with ordered domains, showed strong diffuse electron scattering. Two types of distribution of diffuse scattering were seen according to whether the composition was above or below $VO_{1.0}$. These distributions are shown in figs. 7.2.16 and 7.2.17. Approaching the stoichiometric composition from either

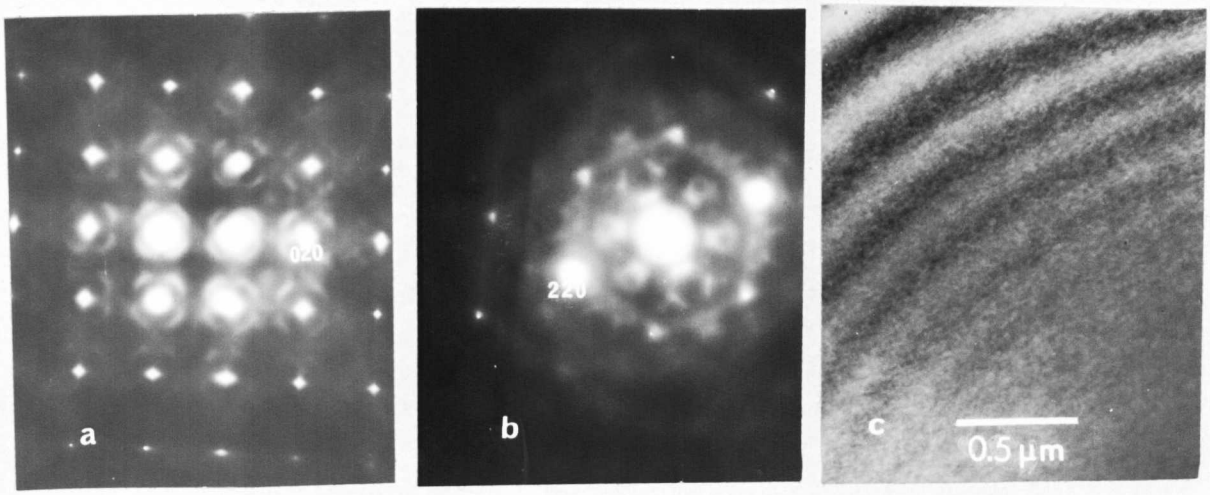

Fig. 7.2.16 Diffuse electron scattering from the cubic matrix for compositions above $VO_{1.0}$.
(a) (100) section, (b) near a (111) section, (c) BF showing fine-scale mottling.

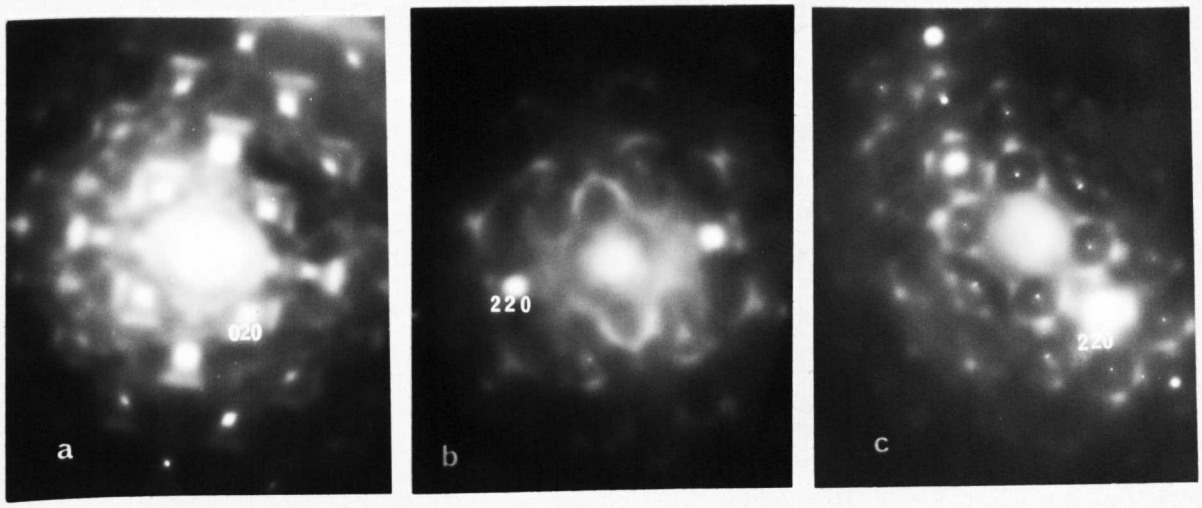

Fig. 7.2.17 Diffuse electron scattering from the cubic matrix for compositions below $VO_{1.0}$.
(a) near a (100) section, (b) near a (111) section, (c) near a (110) section.

side showed no apparent change in these two distributions. Thus specimens near $VO_{1.0}$ always showed one or other of the distributions, with no intermediate forms.

Contrary to the observations in the carbides (TiC, VC, NbC), the superlattice reflections in vanadium monoxide do not appear at the exact positions of the diffuse intensity maxima. Bright-field images recorded with the deviation parameter near zero showed a dense black and white dot contrast. The size of these dots (fig. 7.2.16) is of the order of 100Å. Dark-field images formed from one of the diffuse intensity maxima showed very weak dot contrast (this could not be photographically reproduced).

The form of the diffuse scattering and the associated contrast were not altered by heat-treatment, even in one extreme instance where a specimen was beam heated to its melting point and then rapidly quenched, the effect still persisted.

(ii) Microstructure within the range $VO_{1.10}$ to $VO_{1.15}$

It was previously mentioned in connection with the formation of interface dislocations, that the matrix contained a large number of grown-in dislocations at compositions below about $VO_{1.20}$. Fig. 7.2.18 shows a complicated dislocation array containing several forms such as loops, helices, and heavily jogged segments. When these specimens were annealed an unusual type of configuration was frequently observed where several dislocations became aligned along the sides of a rectangle. A group of these dislocation rectangles is shown in fig. 7.2.19. The rectangles lie on {100} planes with sides in ⟨110⟩ directions, and in the (100) orientation

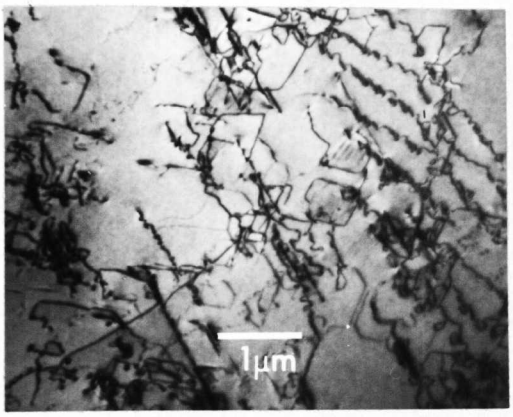

Fig. 7.2.18 Complex dislocation structure in $VO_{1.15}$.

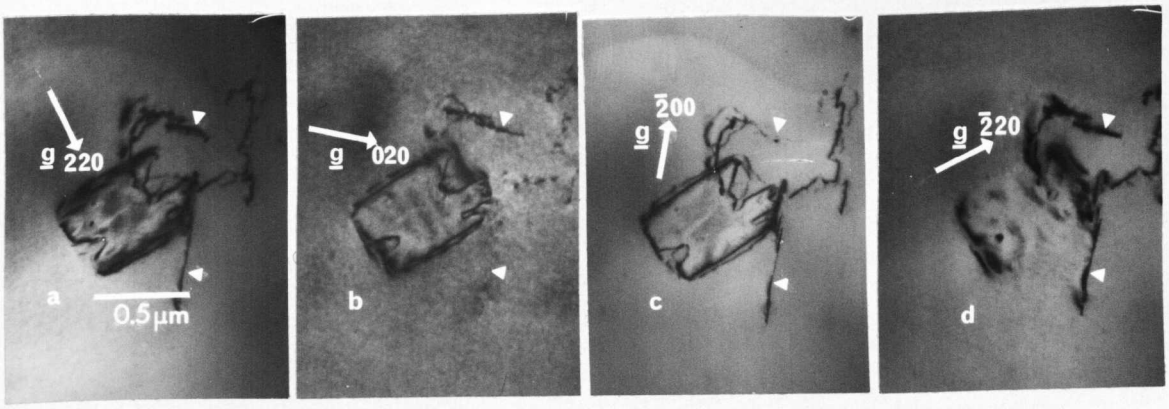

Fig. 7.2.19 Rectangular dislocation arrays on {100} planes in $VO_{1.17}$, 50h 750°C, BF images (100) orientation.

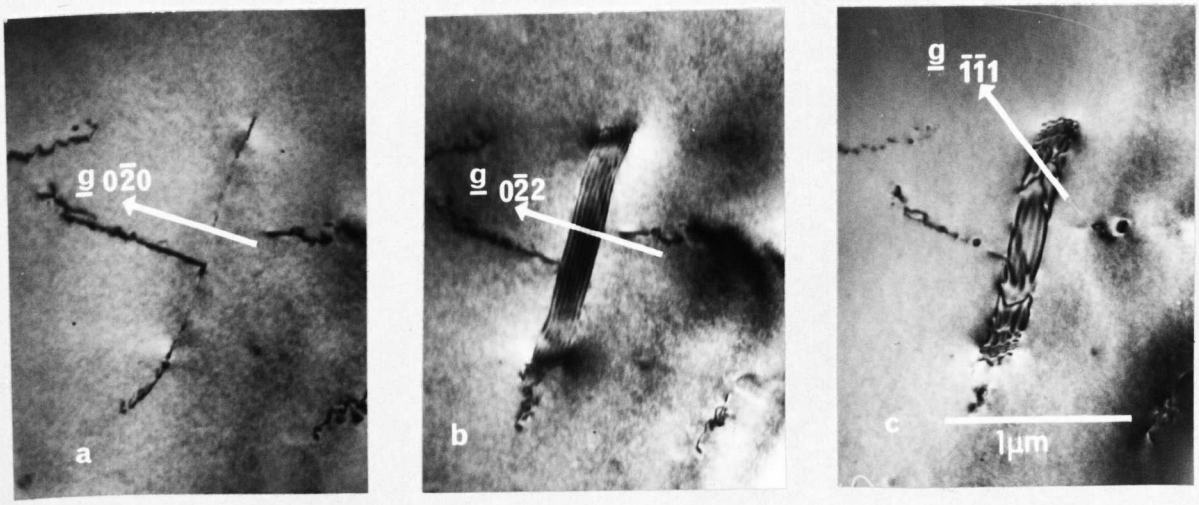

Fig. 7.2.20 Rectangular defect containing several dislocations, showing displacement fringe contrast. (a) (100) orientation, (b) and (c) (110) orientation.

of this foil, two of the rectangles lie on (100) planes parallel to the electron beam. Contrast analysis shows that the dislocations have Burgers vectors of the type $a/2\langle 110\rangle$ in the plane of the rectangle. The very weak fringe contrast in fig. 7.2.19 should be compared with that in fig. 7.2.20. In this example the foil makes a section through the rectangle which contains five dislocations along one set of sides.

The exact structure of these large defects is not certain. The fringe contrast is similar to the displacement fringes at thin plate precipitates, and it may be supposed that in the region enclosed by the dislocation rectangle composition changes have occurred which cause displacements of the surrounding perfect crystal. Planar defects which bear some resemblance to those presently observed have also been seen in other nonstoichiometric materials, e.g. UO_2 (19) and NiAl (20).

(iii) Precipitation of V_2O_3

Specimens with compositions greater than about $VO_{1.31}$ contained precipitates of V_2O_3. From their size it was apparent that the precipitation took place at high temperatures, probably while cooling from the crystal growth temperature, and no new precipitation was observed after the heat-treatments used to develop the long-range-ordered structures. The precipitates formed as thick plates parallel to {111} matrix planes. Fig. 7.2.21(a) shows two orientations of plates lying parallel to the beam in a (110) orientation foil, while in (b) both δ-fringe and interface dislocation contrast are seen at an inclined boundary. The diffraction patterns from the precipitates

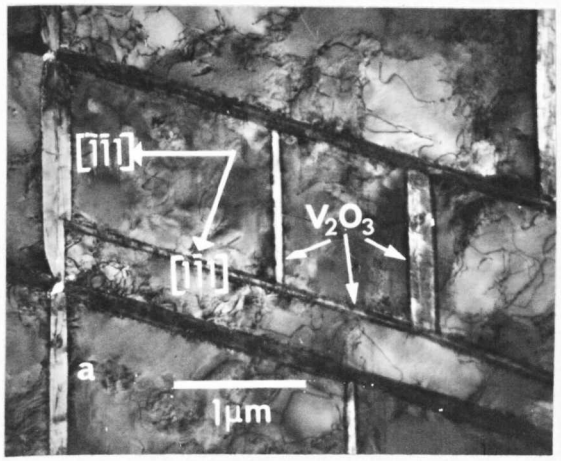

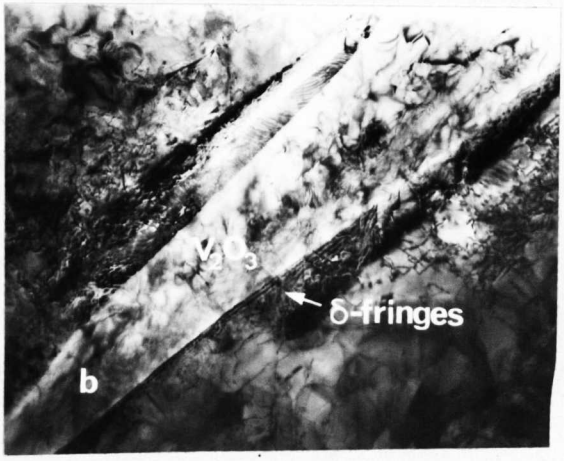

Fig. 7.2.21 Precipitation of V_2O_3 in the cubic vanadium monoxide matrix. (a) BF (110) orientation, (b) BF (100) orientation, precipitate-matrix interface inclined to beam direction showing δ-fringes and interface dislocations.

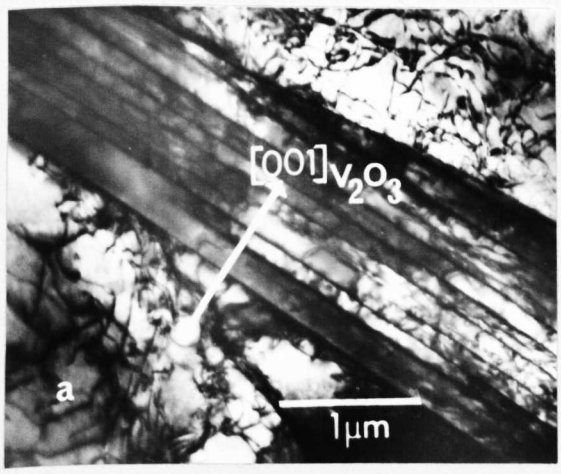

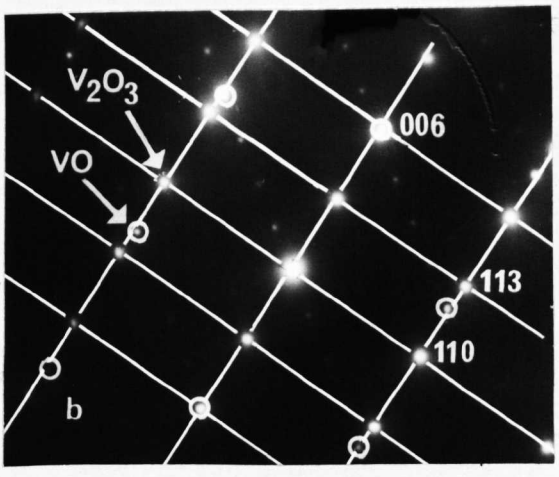

Fig. 7.2.22 Bands of V_2O_3 precipitates. (a) (110) orientation, (b) indexed diffraction pattern showing orientation relation between precipitate and matrix, weak spots are $V_{244}O_{320}$ superlattice reflections.

contained the corundum reflections of V_2O_3.
From fig. 7.2.22 the orientation relation is found to be,

$$(111)VO \parallel (001)V_2O_3$$
$$[1\bar{1}0]VO \parallel [1\bar{1}0]V_2O_3$$

From the quoted lattice parameters of V_2O_3 (21) the matching of planes perpendicular to the interface is,

$$\frac{d\text{-}(220)VO}{d\text{-}(300)V_2O_3} = 1.02$$

and parallel to the interface,

$$\frac{d\text{-}(111)VO}{d\text{-}(006)V_2O_3} = 1.01$$

These values are in close agreement with those measured from the diffraction patterns.

7.2.7 Electrical Measurements on Vanadium Monoxide

(i) Previous work

The electrical properties of vanadium monoxide have been investigated, although to a smaller extent than the dioxide (VO_2) or sesquioxide. The original stimulus came from the work of Morin (22) who claimed that vanadium monoxide underwent an electrical transition from metallic to semiconducting behaviour at about 125°K. Further support for this transition was given by Austin (23). However, in both these examples no chemical analysis was made, and it is now thought that these specimens were V_2O_3, where a well characterized transition is observed.

Recent conductivity measurements down to liquid nitrogen temperature (6,24,25) have shown that vanadium monoxide is semiconducting over the whole composition

range. The conductivity is high with a small activation energy which increases with oxygen concentration. Measurements down to 4.2°K (26) on specimens with compositions below $VO_{1.0}$ showed a continuation of the semiconducting behaviour with no electrical transitions.

Although the present investigation is centred on the ordering phenomonen associated with defective sublattices, it was considered worthwhile to make a brief study of the electrical properties of vanadium monoxide. In particular, resistance against temperature measurements could easily be made and would show the possible existence of a metal to semiconductor transition.

(ii) Experimental results

Disc specimens approximately 2mm thick and 3mm in diameter were used. These were all as-grown single-phase monoxide except for the $VO_{1.36}$ specimen which contained a small amount of V_2O_3. The discs were clamped between two copper plates which served as electrical contacts, and the resistance was measured with an Avometer. This simple arrangement was justified in view of the measured resistances, between 0.1 and 1000 ohms, where errors due to contact resistance would not be appreciable, and where the Avometer was sufficiently sensitive. A copper/constantin thermocouple was used to measure the temperature of the iso-pentane bath which was cooled from room temperature to 77°K by liquid nitrogen.

The resistivity-reciprocal temperature plots of fig. 7.2.23 were obtained from a number of discs with different compositions. There is no indication of an electrical transition. The temperature coefficient of

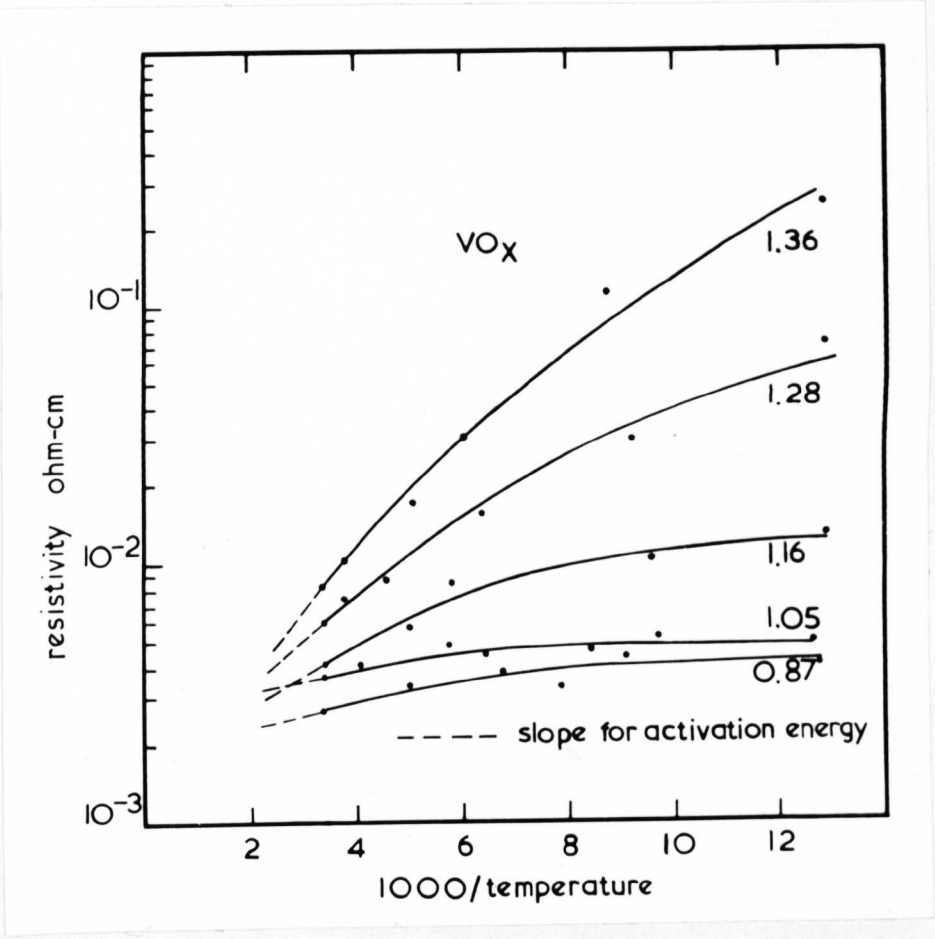

Fig. 7.2.23 Resistivity against reciprocal temperature for vanadium monoxide.

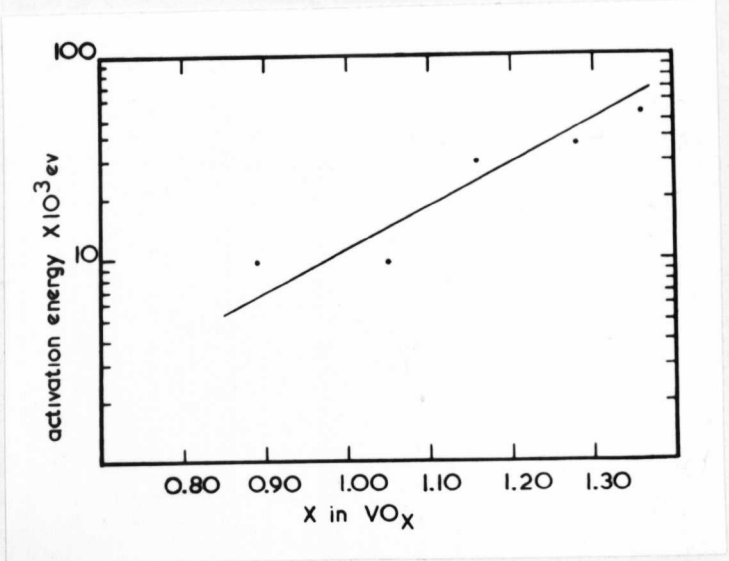

Fig. 7.2.24 Activation energy for the conduction mechanism against composition for vanadium monoxide.

resistivity is negative, indicating semiconducting behaviour, although the resistivities at room temperature are comparable with those of metallic conductors.
For ideal semiconducting behaviour the resistance is related to the temperature according to the equation,

$$\rho = \rho_o \exp E/kT$$

where E is the activation energy associated with the conduction mechanism. The values of E found from the room temperature gradients of logρ versus 1/T are shown in fig. 7.2.24. The activation energy, which increases rapidly with oxygen concentration, is drawn on a logarithmic scale, although this type of dependence is not readily interpreted.

(iii) Discussion of the electrical properties of vanadium monoxide

The reversal in sign of the Hall coefficient and thermoelectric power (25) from negative to positive on going from hypo- to hyperstoichiometric compositions, indicates that the majority of carriers are n-type (electrons) below $VO_{1.0}$, and p-type (holes) above. From the small value of the Hall coefficient, the number of carriers is very large, while their mobility is low. Thus the type of semiconducting behaviour shown by vanadium monoxide is different from that of a normal semiconductor such as germanium, in that for the latter the number of carriers is the temperature dependent variable, while for vanadium monoxide the mobility would appear to be the temperature activated variable.

The ordering of metal vacancies in vanadium monoxide, described in detail above, could create subbands resulting in new energy gaps at the Fermi level.

However from the partial phase diagram of fig.7.2.4, the narrow homogeneity range of the ordered phase would make single-phase ordered material difficult to obtain. Thus any transitions associated with the ordered phase would be partly masked by the presence of either untransformed cubic vanadium monoxide or V_2O_3. Although some larger rectangular specimens were prepared containing the ordered phase, the more sophisticated measuring equipment necessary was not readily available. However this work is being continued* and measurements on these specimens down to 4.2°K are anticipated.

7.3 Titanium Monoxide

7.3.1 Previous Work

The physical parameters defining nonstoichiometric titanium monoxide are similar in many respects to those of vanadium monoxide. At 1400°C the range of compositions extends from $TiO_{0.64}$ to $TiO_{1.25}$ (27), and at 900°C from $TiO_{0.90}$ to $TiO_{1.25}$ (28). The variation in the number of titanium and oxygen vacancies with composition is almost identical to that of the vanadium and oxygen vacancies in vanadium monoxide, except that at the lowest oxygen composition the metal-atom sublattice is fully occupied.

Two ordered superlattices have been positively indentified by the electron diffraction studies of Watanabe and coworkers (29-31). The superlattice based on the composition $TiO_{1.0}$ has monoclinic symmetry and forms below about 950°C. In every third (110) plane (see fig. 7.3.1(a)) half the titanium and oxygen atoms are missing, and the remaining atoms occupy alternate positions along the close-

* M.D.Ball, University of Warwick.

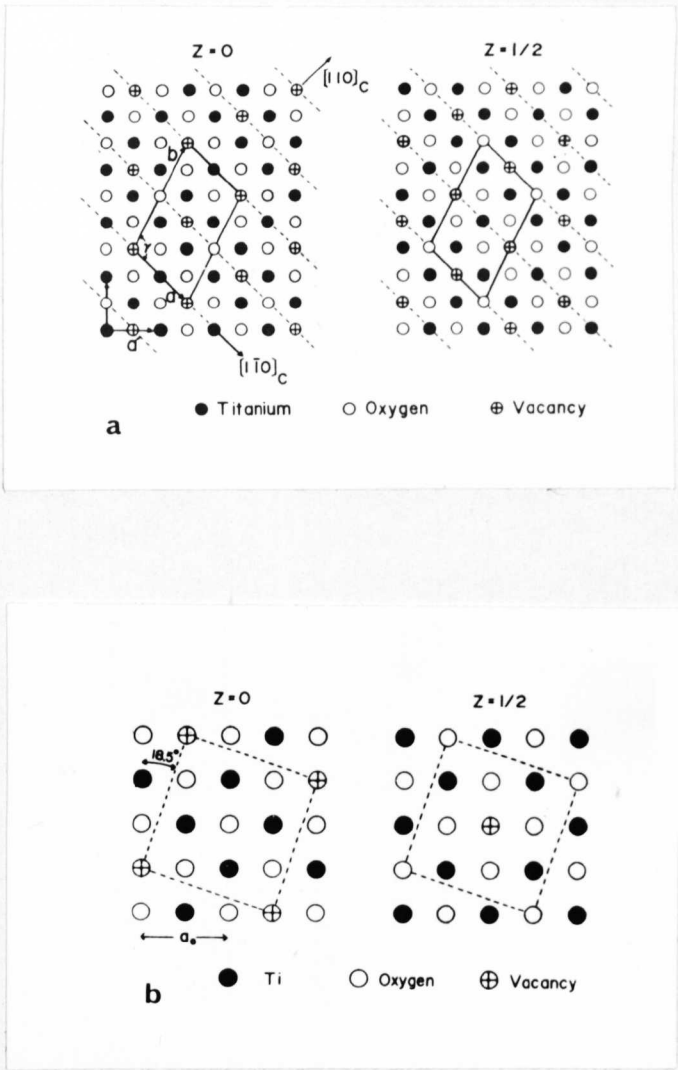

Fig. 7.3.1 (a) the structure of the monoclinic superlattice $TiO_{1.0}$, (b) the structure of the tetragonal superlattice $TiO_{1.25}$, after Watanabe et al. (31).

packed rows. The observation of this superlattice as a single-phase microstructure over the range $TiO_{0.90}$ to $TiO_{1.10}$, implies that an excess or deficit of titanium and oxygen vacancies can be tolerated. When observed in the electron microscope the morphology of this superlattice appears as contiguous domains, each of which contains a set of parallel bands. Each set of bands is characterized by a common $[100]_c$ direction of the monoclinic c-axis, while the respective monoclinic a- and b-axes are differently orientated.

At higher oxygen concentrations a tetragonal superlattice based on the composition $TiO_{1.25}$ is formed below about 800°C. This structure (see fig. 7.3.1(b)) results from the ordering of only titanium atoms. The arrangement of metal atoms and vacancies on the distorted fcc titanium sublattice is identical to that of the nickel and molybdenum atoms respectively in the ordered compound Ni_4Mo. The crystallographic relationship of this superlattice with respect to the parent fcc matrix is similar to that of $V_{244}O_{320}$. Thus for each $[100]_c$ direction of the tetragonal c-axis, two sets of domains exist in twin-relation. The most recent examination of this superlattice (31) showed a microstructure consisting of very small randomly orientated domains, rather like that of vanadium monoxide after short anneals (fig. 7.2.6).

A third type of ordered structure known as the 'transition' structure has been observed in the region $TiO_{0.7}$ to $TiO_{0.9}$ (29-32), and more recently (33) in coexistance with ordered $TiO_{1.25}$. This structure has orthorhombic symmetry and is thought to involve a random

arrangement of vacancies on every third (110) plane. No microstructural evidence has been produced showing this superlattice, and its existence has largely stemmed from the observation of diffraction patterns containing extra reflections at only the 1/3 and 2/3(220) positions. Furthermore, this pattern has been observed after beam heating specimens in the electron microscope. In the present work beam heating experiments were made on thin foils of several compounds. It was found that reaction with the residual gas in the microscope column and preferential evaporation of one component gave rise to changes in composition, and frequently the type of microstructure found after beam heating could not be reproduced in bulk annealed specimens. Thus the observation of new structures formed by beam heating must be open to question.

The diffuse electron scattering observed in disordered specimens of titanium monoxide has been studied in a recent paper by Castles et al. (34). The form of the scattering is found to be composition dependent, and the possibility that it arises from short-range ordering of vacancies under the influence of a long-range electronic interaction was examined.

The objectives of the present work on this compound were to examine more closely the formation of the transition structure, and to obtain equilibrium domain distributions of the ordered compound $TiO_{1.25}$.

7.3.2 Electron Microscopy and Diffraction

(i) The ordered compound $TiO_{1.0}$

Thin-foil specimens with compositions near $TiO_{1.0}$ showed the presence of the monoclinic superlattice.

The diffraction patterns shown in fig. 7.3.2 are identical to those obtained previously by Watanabe (31). The (111) section, (a), shows three superposed superlattice patterns, and the two (110) sections, (b) and (c), show single crystal patterns.

(ii) The ordered compound $TiO_{1.25}$

Long anneals of up to 500h were required to produce the ordered domain distributions shown in fig. 7.3.3 from the small irregularly shaped domains previously observed. In (a) the domains of $TiO_{1.25}$ coexist with ordered $TiO_{1.0}$, while in (b) they coexist with the disordered cubic matrix. In fig. 7.3.4(a) the (100) section diffraction pattern shows the superlattice reflections from one twin orientation which has its c-axis parallel to the beam. When the specimen is rotated from the (100) orientation about the 002 reciprocal lattice vector so that the beam direction is [310] (see (d)), superlattice reflections from one twin orientation of domains having c-axes parallel to the original 002 g-vector will be intersected as shown in (b). Further rotation of the specimen about the same axis until the beam direction is [210] will result in the intersection of superlattice reflections from the second twin orientation of domains with this c-axis (c). When combined with dark-field imaging, this tilting technique provides a convenient way of identifying all six crystallographic variants of $TiO_{1.25}$.

The domains shown in fig. 7.3.3 have a distinct lozenge shape with the long dimensions lying near one of the three possible ⟨100⟩ directions. Large areas of the thin-foil specimens contained domains lying in only one

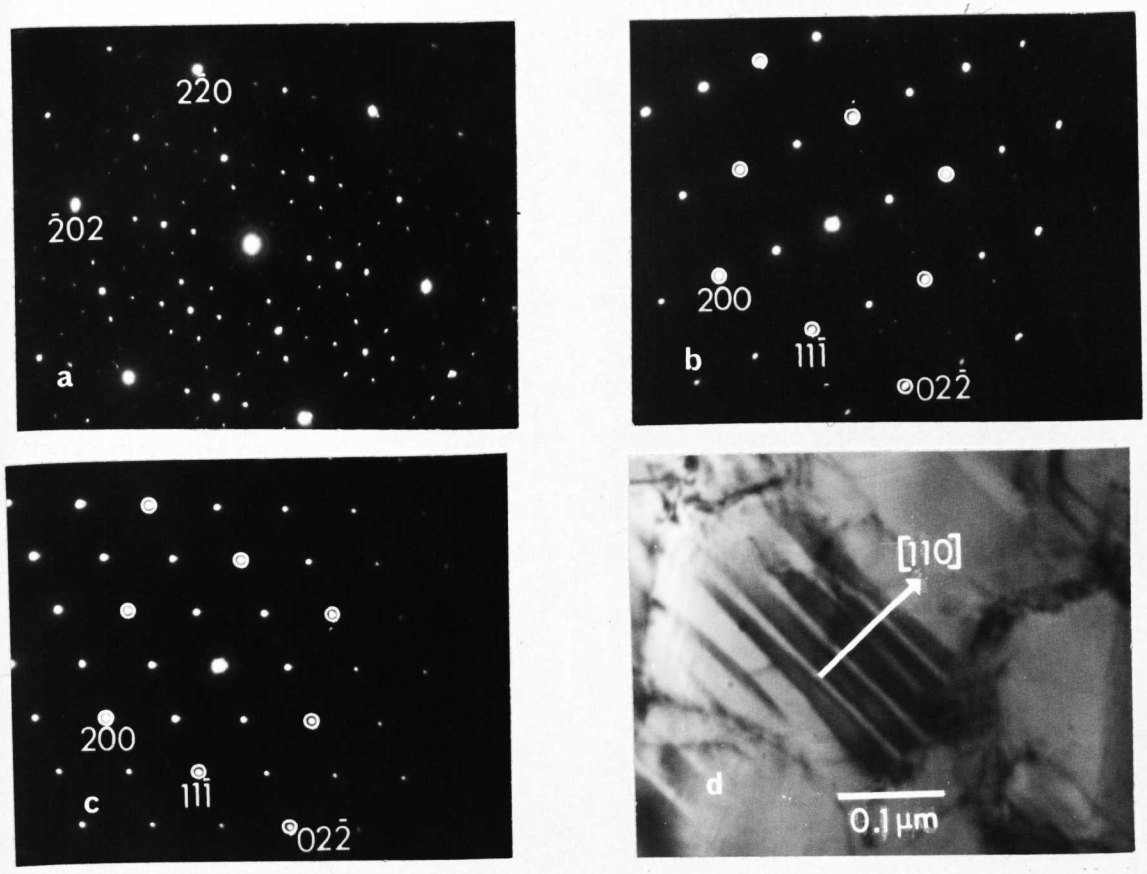

Fig. 7.3.2 The monoclinic superlattice $TiO_{1.0}$. (a) (111) section containing three superposed patterns, (b) and (c) (110) sections from single domain orientations, (d) BF showing one set of parallel bands.

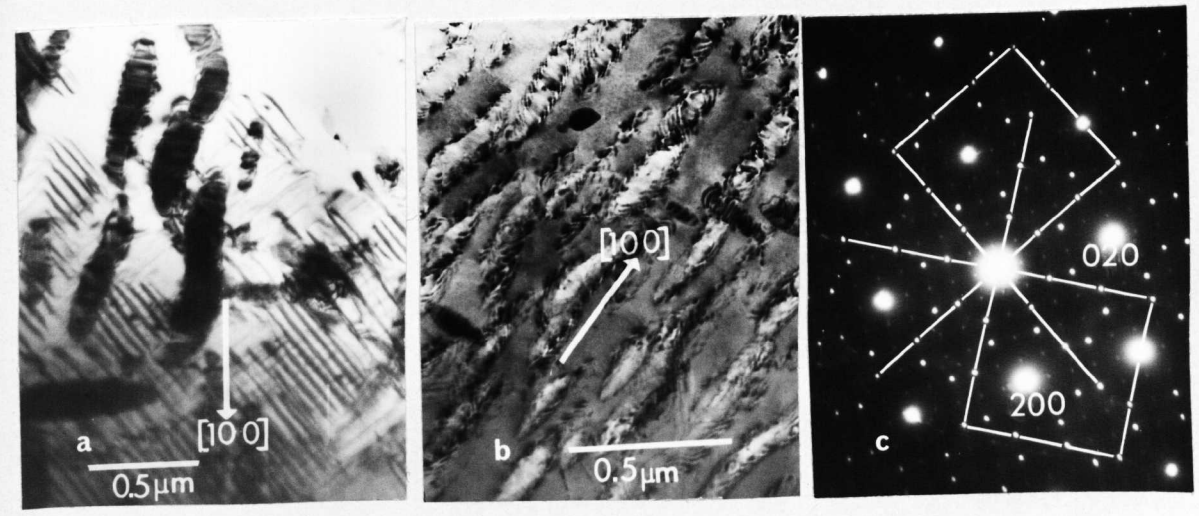

Fig. 7.3.3 The tetragonal superlattice $TiO_{1.25}$, specimen annealed for 480h at 700°C. (a) and (b) BF (100) orientation, $TiO_{1.25}$ coexisting with $TiO_{1.0}$ and cubic matrix respectively, (c) (100) section showing superlattice reflections from both twin orientations.

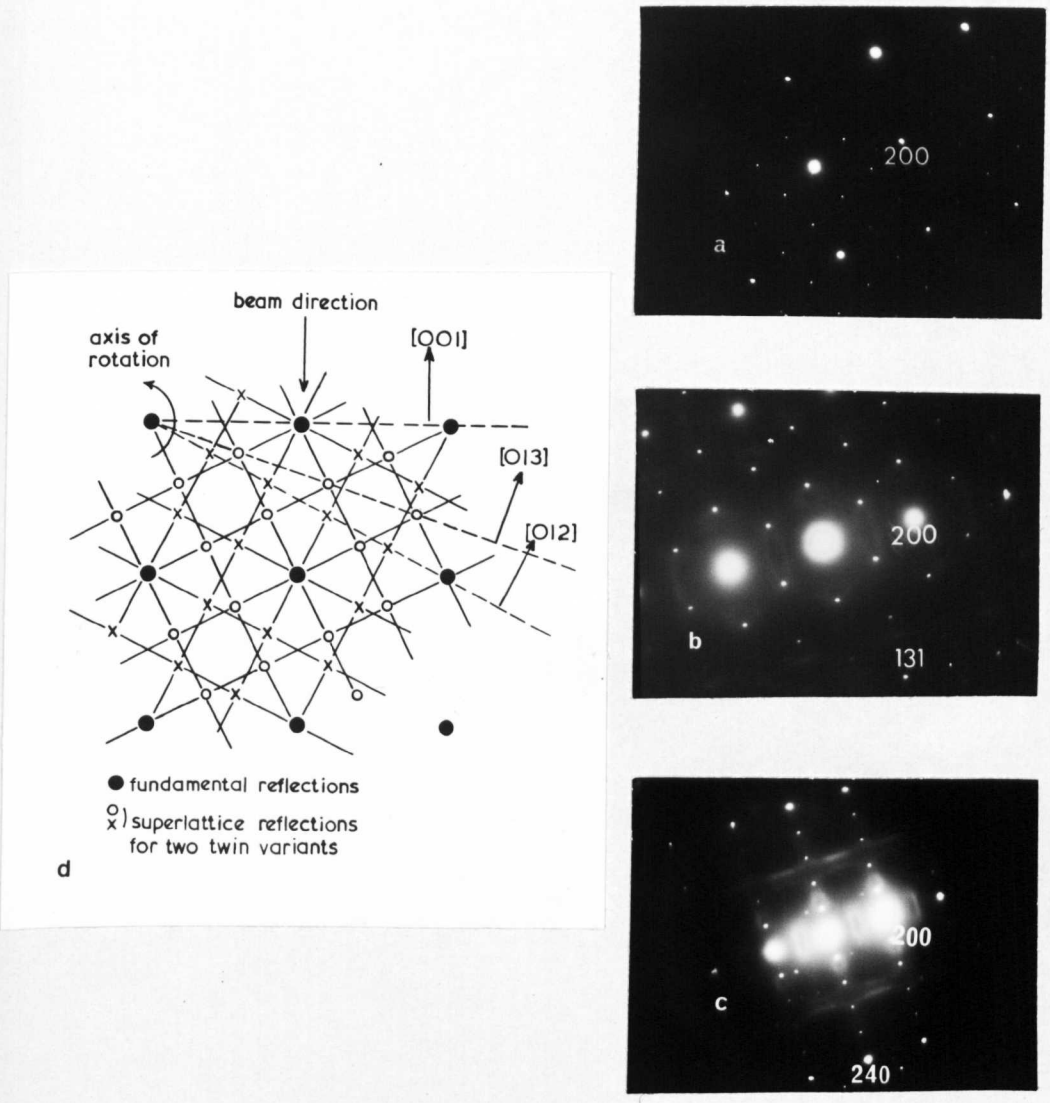

Fig. 7.3.4 Diffraction patterns from the superlattice $TiO_{1.25}$. (a) (100) section from single twin orientation, (b) (310) and (c) (210) sections, (d) shows how rotation of the specimen will result in the reciprocal lattice sections shown in (b) and (c).

of these directions, i.e. the distribution of domains is inhomogeneous. Dark-field images (fig. 7.3.5) show that each lozenge is in fact made up from several segments of single domain orientations. Each group of similarly aligned lozenges contains both twin orientations of domains having only two of the three possible c-axis orientations, with both of these c-axes perpendicular to the direction of alignment. These segments appear to be in a regular sequence, although the exact sequence was not determined because in the foil orientation where the dark-field analysis was possible the segments partly overlapped.

The alignment and distribution of the $TiO_{1.25}$ domains is perhaps even more striking than that of $V_{244}O_{320}$. No doubt similar arguments involving elastic strain interaction can account for this highly selective coarsening process. The bright-field images of these domains (see fig. 7.3.3(b)) show an unusual type of domain-matrix interface contrast in the form of black and white lines. These lines might be mistaken for interface dislocations. However, a pair of lines appears to be associated with each domain segment, and it is therefore probable that each segment produces a strain in the matrix which can then be partially relieved during the growth process by the presence of an adjacent domain segment in a different orientation. A similar type of distribution has been observed for V_6C_5 ordered domains in a vanadium carbide matrix (35).

(iii) Transition structures

Specimens quenched from high temperatures (near 1600°C) exhibited diffuse electron scattering. For oxygen-rich compositions the form of this scattering, shown in fig. 7.3.6, is characterized by pairs of diffuse

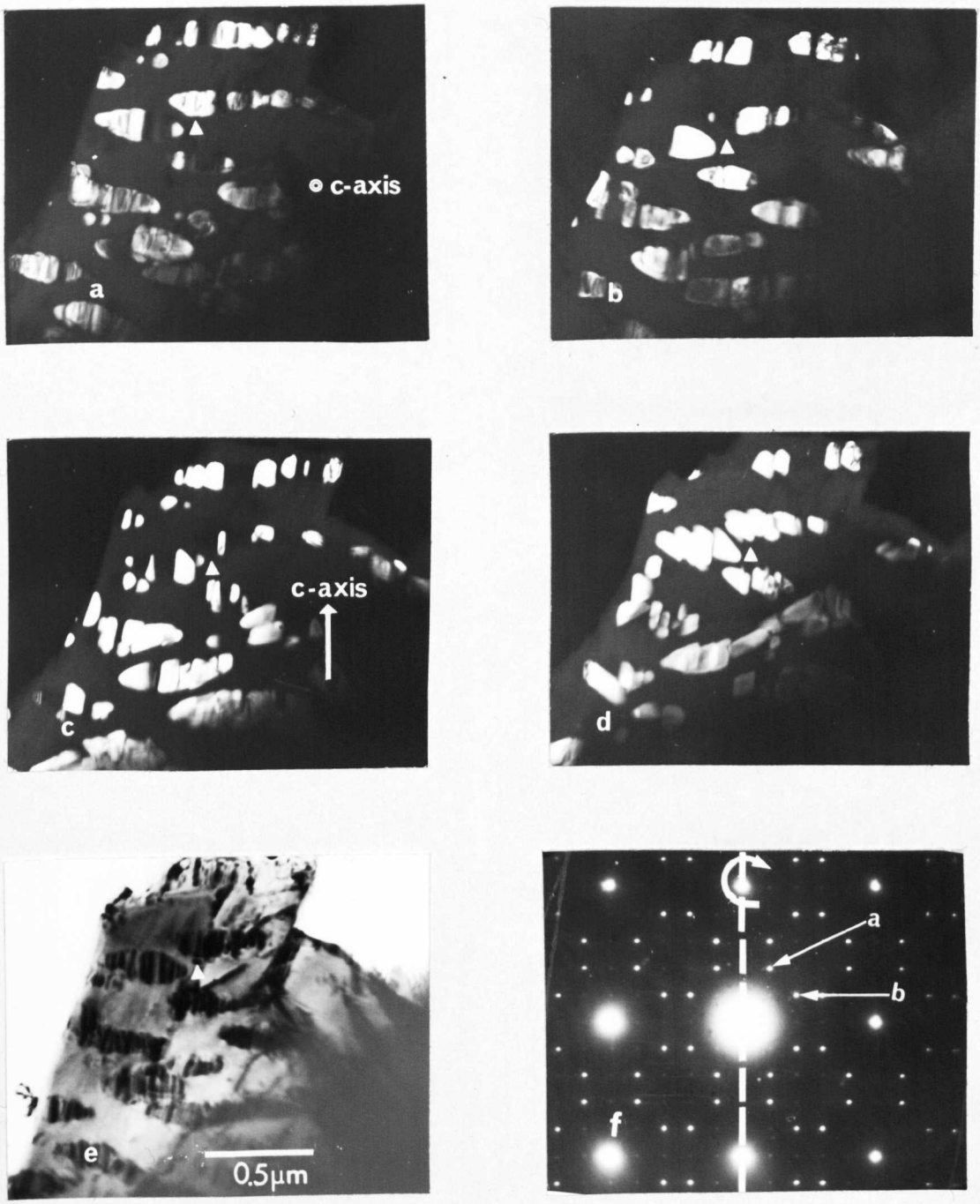

Fig. 7.3.5 Analysis of lozenge shaped domains of $TiO_{1.25}$. (a) and (b) DF (100) orientation show the two twin orientations of domains with c-axes parallel to the beam, (c) DF (310) orientation and (d) DF (210) orientation show the two twin orientations of domains with the indicated c-axis perpendicular to the beam. (e) BF (100) orientation, (f) shows axis of tilt to orientations of (c) and (d). Tilting about the other cube axis gives (310) and (210) sections with no superlattice reflections.

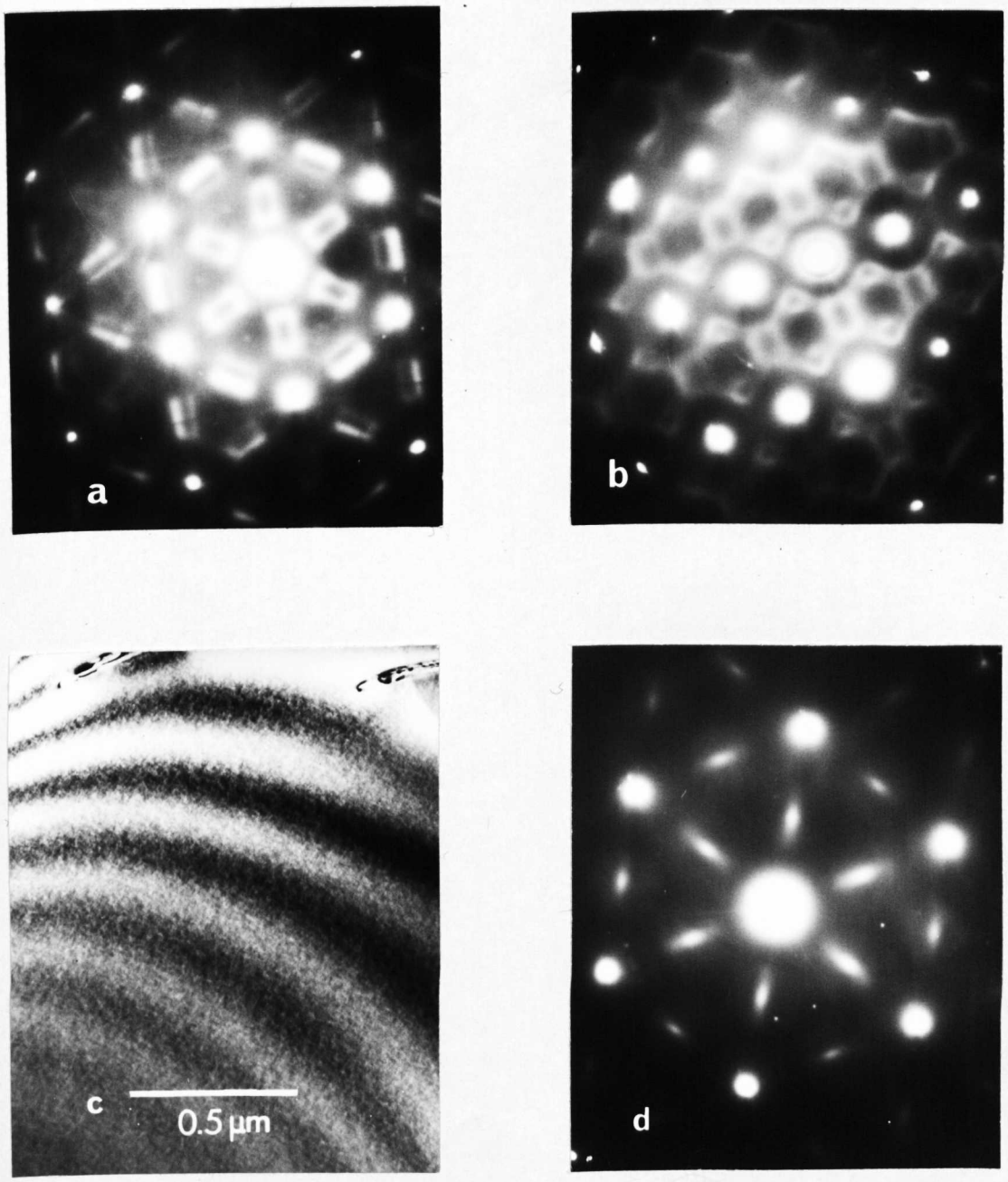

Fig. 7.3.6 Diffuse electron scattering in titanium monoxide. (a) (111) and (b) (211) sections $TiO_{1.25}$, (c) BF shows fine-scale mottling, (d) (111) section $TiO_{0.95}$.

maxima lying parallel to 220-type reciprocal lattice vectors in (111) sections. The bright-field image (fig. 7.3.6(c)) recorded with the deviation parameter nearly zero, shows a similar type of black and white dot contrast to that seen in vanadium monoxide. As the oxygen concentration is reduced, the pairs of diffuse maxima gradually close-up until the type of distribution shown in fig. 7.3.6(d) is obtained at about $TiO_{0.95}$.

Quenched specimens with compositions below about $TiO_{0.90}$ down to the lower phase boundary $TiO_{0.7}$, showed a splitting in the diffuse maxima into well defined peaks at 1/3 and 2/3(220) and 1/2(220) positions. The dark-field images shown in fig. 7.3.7 reveal a fine-scale mixture of small regions contributing separately to either the 1/3 and 2/3(220), or the 1/2(220) reflections. When these specimens were annealed at lower temperatures, precipitation of the close-packed hexagonal Ti_2O-phase (anti-CdI_2-type) occurred. This precipitation was accompanied by a marked decrease in the intensity of the reflections along 220-type reciprocal lattice vectors. Thus the small ordered domains found in quenched specimens could not be retained after annealing.

The mode of Ti_2O precipitation is similar to that of the other hexagonal phases observed in this work. Fig. 7.3.8 shows two orientations of precipitates lying parallel to {111} planes in a foil with (110) orientation. Stacking faults having contrast of both intrinsic and extrinsic type were observed in these specimens with compositions near the lower phase boundary. A complete analysis of these faults and their bounding partial dislocations

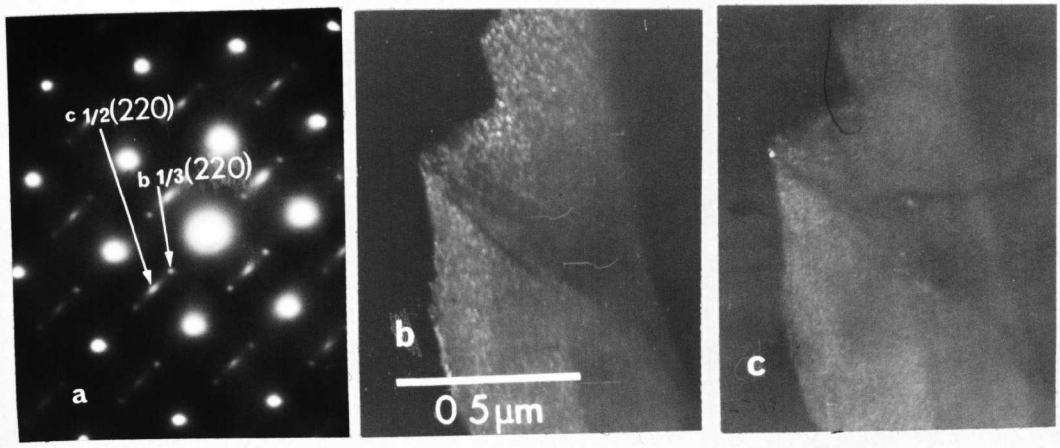

Fig. 7.3.7 Small domains formed on quenching specimens with composition $TiO_{0.7}$ to $TiO_{0.9}$. (a) (110) section showing reflections at 1/3 and 2/3(220) and 1/2(220) positions, (b) DF from 1/3(220) and (c) DF from 1/2(220).

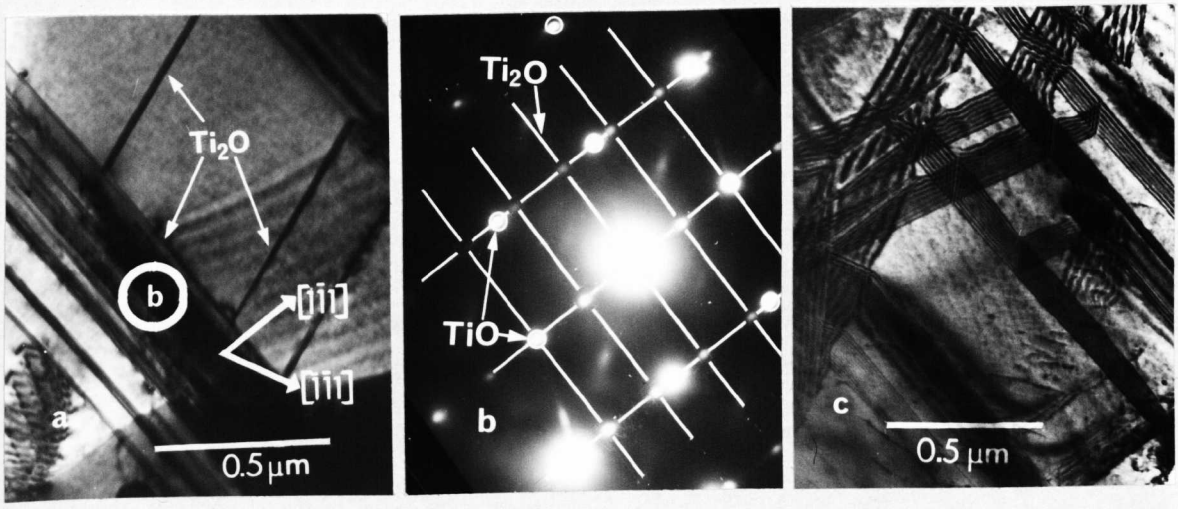

Fig. 7.3.8 Precipitation of hexagonal Ti_2O in annealed specimens with composition $TiO_{0.7}$ to $TiO_{0.9}$. (a) (110) orientation showing precipitates lying in (111) planes, (b) diffraction pattern with $(11\bar{2}0)$ hexagonal grid outlined, (c) stacking faults observed in specimens in this composition range.

could not be made due to the poor quality of the thin-foil specimens.

For compositions near $TiO_{1.20}$ a domain structure was observed, shown in fig. 7.3.9, which was different from either ordered $TiO_{1.0}$ or $TiO_{1.25}$. This would appear to be a stable structure, since specimens containing these domains had been annealed for 500h at 700°C. The diffraction patterns from these domains indicate that the structure is similar to the orthorhombic modification found by the X-ray analysis of Hilti (33).

Beam heating in the electron microscope produced a rapid transformation in thin-foil specimens (fig. 7.3.10) that propagated from lamellae which nucleated at the edge of the foil and then spread into the thicker areas. Composition changes at the edge of the foil will readily take place because this material has a large surface to volume ratio, also, the relaxation of stresses at the foil edge and the presence of a free surface will allow transformations to take place which are unobserved in bulk specimens. The diffraction patterns from specimens transformed by beam heating were rather variable, although usually reflections at 1/3 and 1/2(220) positions were seen.

7.3.3 Discussion of the Transition Structures

The very small domains observed in the quenched specimens ($TiO_{0.7}$ to $TiO_{0.9}$) represent a non-equilibrium state. These domains form by the segregation of vacancies (mainly in the oxygen sublattice) onto every third or second (110) plane during the quench. This state is then metastable with respect to decomposition into a two-phase mixture of Ti_2O and $TiO_{0.9}$, which forms after annealing.

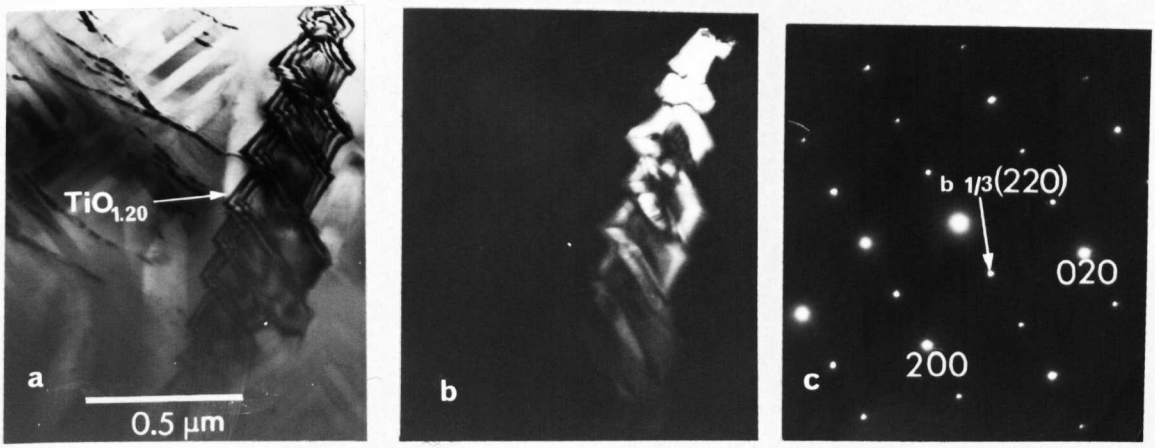

Fig. 7.3.9 Domains of an orthorhombic superlattice, $TiO_{1.20}$. (a) BF (100) orientation (background ordered $TiO_{1.0}$), (b) DF from 1/3(220) reflection in (c) (100) section.

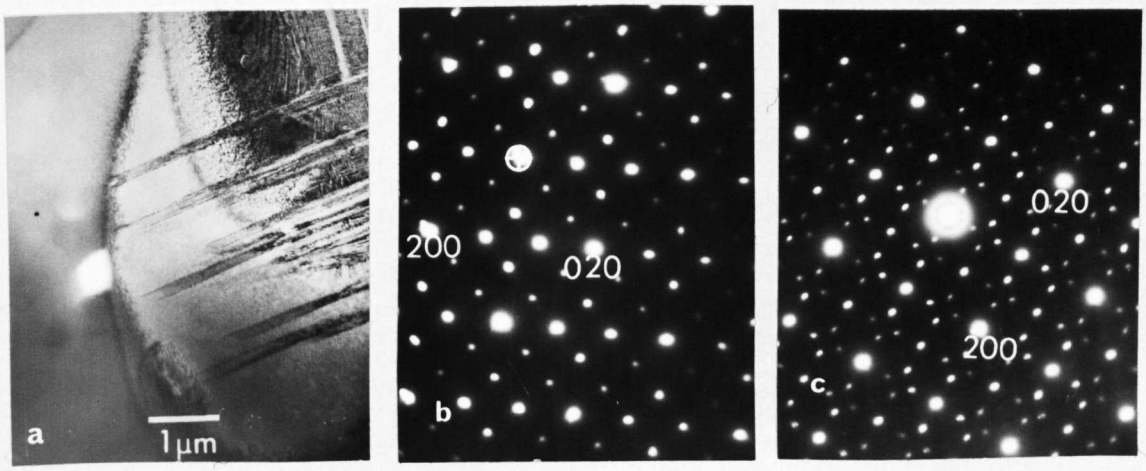

Fig. 7.3.10 Effect of beam heating on titanium monoxide. (a) BF typical microstructure showing lamellae extending into foil from edge, (b) and (c) (100) sections.

It seems unlikely that Watanabe et al. (31) would have used the term 'transition' structure if they had observed the type of domains presently seen in the specimens with compositions near $TiO_{1.20}$ (fig. 7.3.9). In their definition the transition structure forms at high temperatures, and is the precursor of either ordered $TiO_{1.0}$ or $TiO_{1.25}$. The orthorhombic structure observed near $TiO_{1.20}$ was not seen after quenching from high temperatures, but only after annealing below 800°C. This structure is similar to that of ordered $TiO_{1.0}$, except that while the vacancies are restricted to every third (110) plane, they are randomly arranged on these planes.

The structure produced by beam heating is probably a higher oxide which happens to possess some fortuitous similarities to the diffraction patterns from quenched $TiO_{0.7}$ to $TiO_{0.9}$ and the orthorhombic modification near $TiO_{1.20}$.

APPENDIX 7.1

The Chemical Analysis of Vanadium Monoxide

Because gravimetric techniques are in theory more accurate than wet chemical analysis, several investigators have used the method of weight gain after oxidation to the highest oxide, V_2O_5. For titanium oxides (TiO) this method is suitable, since, oxidation to TiO_2 is virtually complete, the dioxide has a low vapour pressure at temperatures where the reaction is rapid, and the end-point may be ascertained from the white colour of TiO_2 as opposed to the grey of slightly reduced samples. However, V_2O_5 melts at 670°C and has an appreciable vapour pressure at 800°C.

Tests under various oxidation conditions showed this method was both inaccurate (V_2O_5 never being produced), and unreproducible, i.e. different degrees of final oxidation. A variation on this technique was tried where the sample was oxidized by concentrated nitric acid. This method gave a fine residue of V_2O_5 and resulted in improved accuracy. However, one drawback with this specific type of gravimetric method is that the accuracy decreases for specimens with compositions which are near that of the final oxidation product. The titrimetric method used by Westman and Nordmark (4) employing oxidation of the sample in solution by cerium(IV) sulphate followed by back titration with ferrous ammonium sulphate, and a gravimetric precipitation using oxine were both tried, but again the desired accuracy was not achieved.

If the vanadium could be brought into solution

in the V^{5+} state, then in the absence of other red-ox ions, titration with ferrous ammonium sulphate followed by back titration of the excess Fe^{2+} with dichromate could be used. The exact procedure was as follows;

Weigh sample containing approximately 0.03g vanadium.
Dissolve sample in 10ml 50% sulphuric acid.
Dilute to 200ml.
Add potassium permanganate, 0.1N, until pink (V^{5+}).
Add excess 5 wt.% solution sodium nitrite to destroy excess permanganate.
Add 5ml 5 wt.% solution of sulphamic acid to destroy excess nitrite.
Add 5ml concentrated phosphoric acid to remove green colour of ferric ions.
Pipette 25ml 0.02N ferrous ammonium sulphate,

$$Fe^{2+} + V^{5+} \longrightarrow Fe^{3+} + V^{4+}$$

Add five drops diphenylaminesulphonic acid indicator, made from five drops of supplied solution in 100ml water.
Titrate with standard 0.005N potassium dichromate until green to purple colour change,

$$Cr^{6+} + 3Fe^{2+} \longrightarrow Cr^{3+} + 3Fe^{3+}$$

Make a blank run using reagents to standardize ferrous ammonium sulphate.
Make control tests on vanadium metal powder and V_2O_5.

APPENDIX 7.2

Calculation of Vacancy Concentrations

The fraction of occupied vanadium sites F_v, and oxygen sites F_o, in a sample with composition VO_x and lattice parameter a, may be calculated thus;

No. of metal atoms in one unit cell VO_x = $4F_v$

No. of metal atoms in one g. mole VO_x = N (Avogadro's No.)

Volume of one g. mole VO_x = $Na^3/4F_v$

Wt. one g. mole VO_x, where w refers to atomic wt. = $w_v + xw_o$

When d is the pycnometric density the fraction of occupied sites is then,

$$F_v = \frac{Na^3 d}{4(w_v + xw_o)}$$

and $F_o = xF_v$

The calculated percentages of vacancies in each sublattice will then be, $(1-F_v)100$, and $(1-F_o)100$.

REFERENCES

1. N.Schönberg, Acta Chem. Scand., 8, 221 (1954).
2. G.Andersson, Acta Chem. Scand., 8, 1599 (1954).
3. P.V.Gel'd, S.I.Alyamovskii and I.I.Matveenko, Zh. Strukt. Khim., 2, 301 (1961).
4. S.Westman and C.Nordmark, Acta Chem. Scand., 14, 465 (1960).
5. G.Stenstrom and S.Westman, Acta Chem. Scand., 22, 1712 (1968).
6. M.D.Banus and T.B.Reed in "The Chemistry of Extended Defects in Non-Metallic Solids", eds. L.Eyring and M.O'Keeffe (North-Holland, Amsterdam, 1970).
7. A.Taylor and N.J.Doyle in "The Chemistry of Extended Defects in Non-Metallic Solids", eds. L.Eyring and M.O'Keeffe (North-Holland, Amsterdam, 1970).
8. W.Klemm and L.Grimm, Z. Anorg. Allg. Chem., 250, 42 (1942).
9. M.A.Gurevich and B.F.Ormont, Zh. Neorg. Khim., 2, 2581 (1957).
10. A.Magnéli, S.Andersson, S.Asbrink, S.Westman and B.Holmberg, Final Tech. Rept. No.1, U.S. Dept. of Army, DA-91-508-EUC-245 (Sept. 1958).
11. S.Westman, Final Tech. Rept. No.1, U.S. Dept. of Army, DA-91-591-EUC-13139 (Dec. 1960).
12. B.Andersson and J.Gjønnes, Acta Chem. Scand., 24, 2250 (1970).
13. M.Saeki and M.Nakahira, Mater. Res. Bull., 6, 603 (1971).
14. A.J.Ardell and R.B.Nicholson, Acta Met., 14, 1295 (1966).
15. G.C.Weatherly, Phil. Mag., 17, 791 (1963).

16. K.E.Easterling and T.Johannesson, Phil. Mag., 24, 981 (1971).
17. G.C.Weatherly and R.B.Nicholson, Phil. Mag., 17, 801 (1968).
18. C.S.G.Phillips and R.J.P.Williams, "Inorganic Chemistry", Vol. 1, p.174 (Clarendon, Oxford, 1965).
19. K.H.G.Ashbee in "The Chemistry of Extended Defects in Non-Metallic Solids", eds. L.Eyring and M.O'Keeffe (North-Holland, Amsterdam, 1970).
20. A.Ball, Phil. Mag., 20, 113 (1969).
21. R.E.Newnham and Y.M. de Haan, Z. Krist., 117, 235 (1962).
22. F.J.Morin, Phys. Rev. Letts., 3, 341 (1959).
23. I.G.Austin, Phil. Mag., 7, 961 (1962).
24. S.Kawano, K.Kosuge and S.Kachi, J. Phys. Soc. Japan, 21, 2744 (1966).
25. R.Steinitz, GT&E Tech. Rept., TR-186.2 (Aug. 1967).
26. J.M.Honig, W.E.Wahnsiedler, M.D.Banus and T.B.Reed, J. Sol. State Chem., 2, 74 (1970).
27. S.Andersson, B.Collén, U.Kuylenstierna and A.Magnéli, Acta Chem. Scand., 11, 1641 (1957).
28. H.Iwasaki and N.F.H.Bright, J. Less-Common Metals, 21, 353 (1970).
29. D.Watanabe, J.R.Castles, A.Jostons and A.S.Malin, Acta Cryst., 23, 307 (1967).
30. D.Watanabe, O.Terasaki, A.Jostons and J.R.Castles, J. Phys. Soc. Japan, 25, 292 (1968).
31. D.Watanabe, O.Terasaki, A.Jostons and J.R.Castles in "The Chemistry of Extended Defects in Non-Metallic Solids", eds. L.Eyring and M.O'Keeffe (North-Holland, Amsterdam, 1970).

32. D.Watanabe, J.R.Castles, A.Jostons and A.S.Malin, Nature, 210, 934 (1966).
33. E.Hilti, Naturwissenschaften, 55, 130 (1968).
34. J.R.Castles, J.M.Cowley and A.E.C.Spargo, Acta Cryst., A27, 376 (1971).
35. J.Billingham and M.H.Lewis, Proc. 7th. Int. Conf. on Electron Microscopy, Grenoble (1970).

CHAPTER EIGHT

THE EFFECT OF ELECTRON IRRADIATION ON VANADIUM MONOXIDE

8.1 Introduction

After prolonged irradiation in the electron microscope with 200kev electrons, all the superlattice structures underwent disordering. Usually this did not interfere with the examination of a specific area of a thin-foil specimen, as a long time was required for a significant amount of disordering. However, for thin-foil specimens of vanadium monoxide, containing domains of the $V_{244}O_{320}$ superlattice, the disordering process proceeded in two distinct steps. Thus, after relatively short times the weak superlattice reflections disappeared (see fig. 7.2.5(a)), then after further irradiation, the strong superlattice reflections disappeared. This unusual disordering behaviour prompted a quantitative investigation to determine the mechanism of the disordering process.

8.2 Experimental

The accelerating voltages used in the JEM 200 electron microscope are from 100kev to 200kev in 25kev steps. The electron current reaching the specimen was varied by changing the bias potential on the electron gun, and by using different sizes of condenser lens aperture. The electron current was measured with a Keighly picoammeter connected to a removable probe above the viewing screen. The electron flux was found from the measured current and the area of the focused illumination spot. Domains having the tetragonal c-axis parallel to the electron beam were

selected for examination. In this orientation both the weak and strong superlattice reflections are clearly visible. Where possible, only the thinnest parts of the foils were used, in order to minimize the heating effect of the electron beam.

8.3 Radiation Induced Disordering

(i) Electron microscope observations

At microscope operating voltages of 150, 175, and 200kev, disordering was observed, where only the area of thin-foil section covered by the focused electron beam was affected. At 100kev and 125kev the intensity of both types of superlattice reflection remained constant after long periods of irradiation. The period of irradiation needed to produce partial disorder (disappearance of weak superlattice reflections) and complete disorder was recorded visually from the microscope screen. This time could be measured accurately because of the sharp cut-off in the visibility of the diffraction spots. These times, estimated to the nearest half minute when less than 10 minutes, and to the nearest minute for longer times, are summarized in Table 8.1.

The measurements at 200kev for different values of electron current show that the time required for complete disordering is inversely proportional to the flux. Thus thermal disordering due to heating of the specimen, which could possibly occur at the higher electron currents used, appears to be negligible.

From the electron microscope observations it would appear that disordering of the $V_{244}O_{320}$ structure

TABLE 8.1

Accelerating voltage kev	Flux, J electrons/cm^2/s	Time, t seconds	J x t	Superlattice reflection
200	$1X10^{20}$	240	$2.4X10^{22}$	strong
200	$6X10^{19}$	420	$2.5X10^{22}$	"
200	$7X10^{18}$	3120	$2.2X10^{22}$	"
175	$5X10^{19}$	720	$3.6X10^{22}$	"
150	$1X10^{20}$	1200	$1.2X10^{23}$	"
200	$8X10^{18}$	240	$2.0X10^{21}$	weak
175	$2X10^{18}$	1380	$2.8X10^{21}$	"
150	$1X10^{19}$	1020	$1.0X10^{22}$	"
125	$7X10^{18}$	5400	$3.8X10^{22}$	neither

proceeds in two stages. Firstly, the disappearance of the weak superlattice reflections indicates a destruction in the order associated with the vacancy spirals in the $V_{244}O_{320}$ unit cell (see fig. 7.2.12). The sequence of dark-field images shown in fig. 8.3.1 were obtained from a weak superlattice reflection, and show the progress of partial disordering. At this stage the structure of the partially disordered area is similar to that of the $V_{52}O_{64}$ sub-cell, although there will be some disorder within this smaller unit cell. On further irradiation the order associated with the interstitial vanadium atoms and vacancy

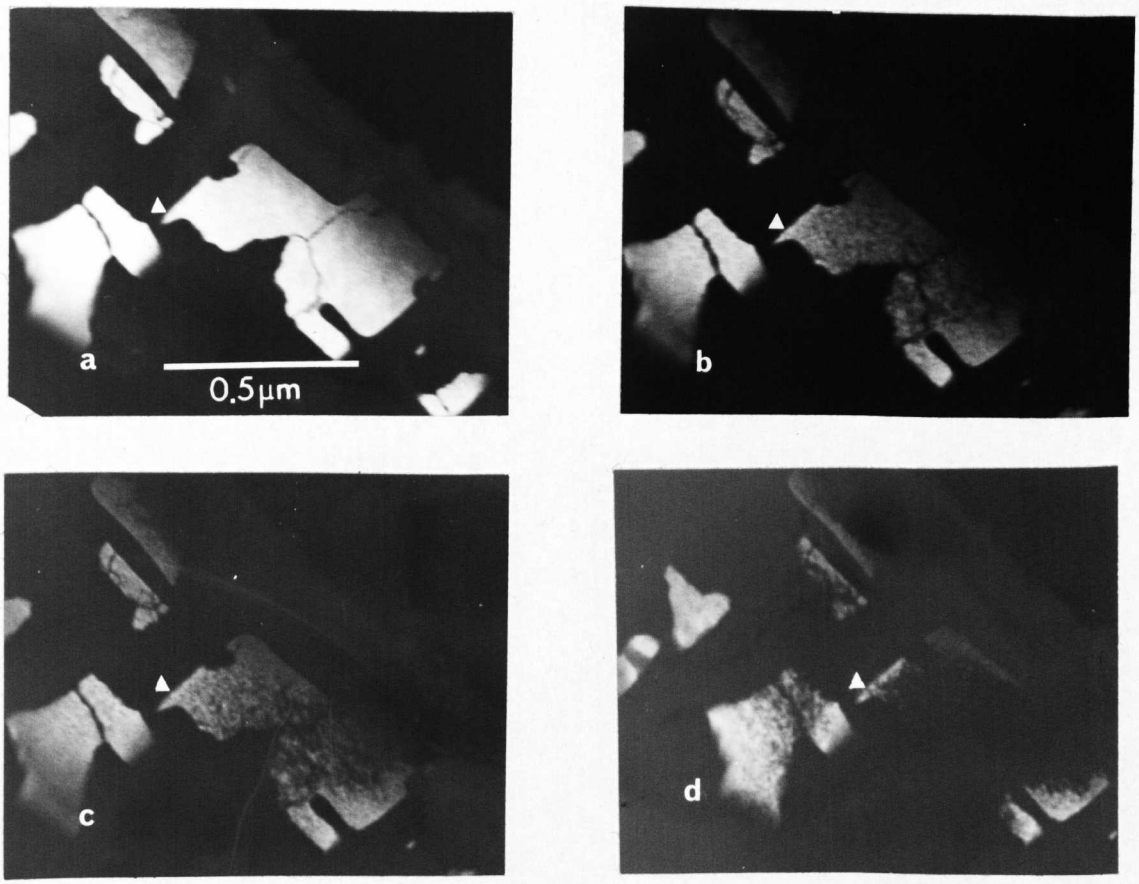

Fig. 8.3.1 Dark-field images recorded using a weak superlattice reflection showing progressive stages in partial disordering.

Fig. 8.3.2 Dark-field image recorded using a strong superlattice reflection showing a fully disordered region.

clusters of the $V_{52}O_{64}$ structure is destroyed. Fig. 8.3.2 is a dark-field image formed from a strong superlattice reflection, and shows a fully disordered region surrounded by domains which still show bright contrast. However, the arrangement of vacancies is never completely random, as the diffuse electron scattering, characteristic of the thermally disordered and quenched state, is still present in the diffraction patterns.

(ii) Mechanism for displacements in vanadium monoxide

It is believed that the disordering phenomonen is due to the displacement of atoms by energetic electrons. It is possible that the observed effects, viz. a diminution in superlattice reflection intensity and image contrast from ordered domains, could be explained by other processes, e.g. a surface contamination film, thermal disordering in the electron beam, or atomic rearrangements due to ion bombardment. The various reasons for discounting these possible mechanisms have been previously outlined (1), and as similar explanations are applicable in the present work, they will not be repeated.

An energetic electron can displace atoms in a crystal by various processes that depend on the nature of the crystal. The different mechanisms whereby ionization, induced by the electron beam, may result in atomic displacements are believed to be inapplicable to vanadium monoxide. Apart from the metallic behaviour of this compound, especially the good electrical conductivity, there is an enhanced disordering effect with increasing electron energy, and a threshold energy well above the level associated with ionization processes. Hence it will be assumed that the

primary displacement process arises from coulomb encounters between incident electrons and nuclei within the crystal.

The maximum energy, E_m, that can be imparted to a nucleus of mass M by an electron of energy E_e is given by,

$$E_m = \frac{(Mm_o)}{(M + m_o)^2} (1 + E_e/2m_oc^2)E_e \qquad ...1$$

where m_o is the electron rest mass, and c the velocity of light. When E_m reaches the displacement threshold energy, E_d, displacements will occur. The number of displacements depends on σ_d, the displacement cross-section. This quantity is given by the relationship derived by McKinley and Feshbach (2), for a single step displacement process,

$$\sigma_d = (Ze^2/m_oc^2)^2(\beta^4\gamma^2)^{-1}\left[(E_m/E_d - 1) - \beta^2 \ln(E_m/E_d) + \pi\alpha\beta\left\{2\left[(E_m/E_d)^{\frac{1}{2}} - 1\right] - \ln(E_m/E_d)\right\}\right] \qquad ...2$$

where Z is the atomic number of the displaced atoms, e the electronic charge, β the fractional electron velocity relative to the velocity of light, $\gamma = (1 - \beta^2)^{-\frac{1}{2}}$, and $\alpha = Z/137$.

The probability, p, of an atom being displaced in time t is then given by,

$$p = J\sigma_d\nu t \qquad ...3$$

where J is the electron flux, and the factor ν accounts for further atom displacements as a result of collisions with energetic primary displaced atoms. The value of ν is one when $E_m < 2E_d$, and increases slowly for $E_m > 2E_d$.

(iii) Vanadium atom displacement energy, E_{dv}

If the atomic displacements observed in vanadium monoxide are the result of electron-nucleus collisions,

then two processes may account for the vanadium atom displacements: (1), direct displacement of a vanadium atom by an incident electron, or (2), a secondary displacement process by a primary high energy displaced oxygen atom. Since both types of superlattice reflection remain unaltered during irradiation at 125kev, a lower limit of 6.5ev can be assigned to E_{dv} (vanadium atom displacement energy) for process (1), whereas the lower limiting value of E_{dv} can only be found for a given value of E_{do} (oxygen atom displacement energy) if process (2) is operative. It is possible that a combination of both processes may be responsible for the observed vanadium atom displacements. Their relative importance may be estimated from the following reasoning.

For process (1) the vanadium atom displacement probability will be given by eqn. 3. In this case the value of v will be unity, since $E_m < 2E_{dv}$ over the range of electron energies used (for E_{dv} = 6.5ev). For process (2) the vanadium displacement probability will be given by,

$$p = J\sigma_{do}(v - 1)t \qquad \ldots 4$$

For this process to operate v must be greater than unity. Here v will depend on the parameter x, given by,

$$x = \frac{0.73(E_{mo} - E_{do})}{E_{dv}} \qquad \ldots 5$$

The 0.73 factor is the fraction of its energy that an oxygen atom can impart to a vanadium atom. For different values of x it is possible to calculate v from the equations given by Seitz and Koehler (3), which are a combination of the earlier work of Snyder and Neufeld (4,5) and Harrison and Seitz (6).

Plots of displacement cross-section against incident electron energy for various values of E_{dv} and E_{do}, calculated from eqn. 2, are shown in figs. 8.3.3, and 8.3.4. From these values of σ_{dv} and σ_{do} it is found that at the lower limit of 6.5ev for E_{dv}, the number of vanadium displacements by process (2) would account for 12% and 3% of the total number (via process (1)) of vanadium displacements at 150kev, for E_{do} = 4ev and 8ev respectively. These suggested values for E_{do} are based on a value of 5.4ev for the threshold displacement energy of the carbon atoms in V_6C_5 found by Venables et al. (1).

It is necessary for the value of p to be $\geqslant 1$ for complete disordering of the vanadium sublattice to occur. For example, from the work of (1), p = 1.2 at 79kev for the disordering of the carbon-atom distribution in V_6C_5. The values of p for complete disordering in $V_{244}O_{320}$, calculated from the disordering time and the electron flux, are near to 2.4 for process (1), while much less than unity for process (2). The observed disordering is therefore almost entirely due to the first process, i.e. direct displacement of vanadium atoms by incident electrons.

If the electron accelerating voltage could be varied continuously over the range 100-200kev, it would be possible to determine the value of E_{dv} from the electron energy where damage just ceased to occur. However this was not possible, and an alternative method similar to that of (1) is used. In this latter work the theoretical expression for the variation of superlattice reflection intensity with time was found to be,

$$\frac{d\ln I}{dt} = -KJ\sigma_{dc}^{\nu} \qquad \ldots 6$$

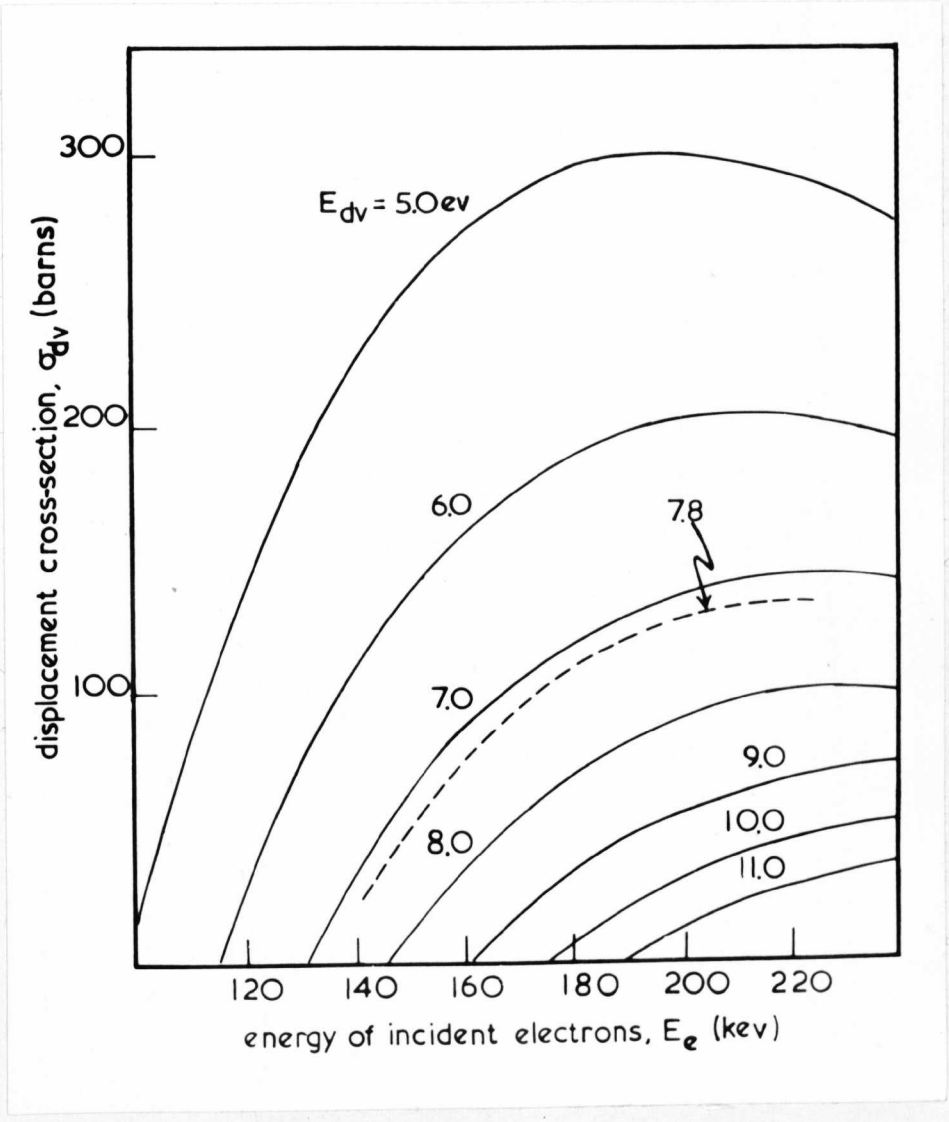

Fig. 8.3.3 Theoretical curves of displacement cross-section against incident electron energy for several values of vanadium atom displacement energy E_{dv}. The dashed curve for 7.8ev gives the best fit to the observed times for disordering..

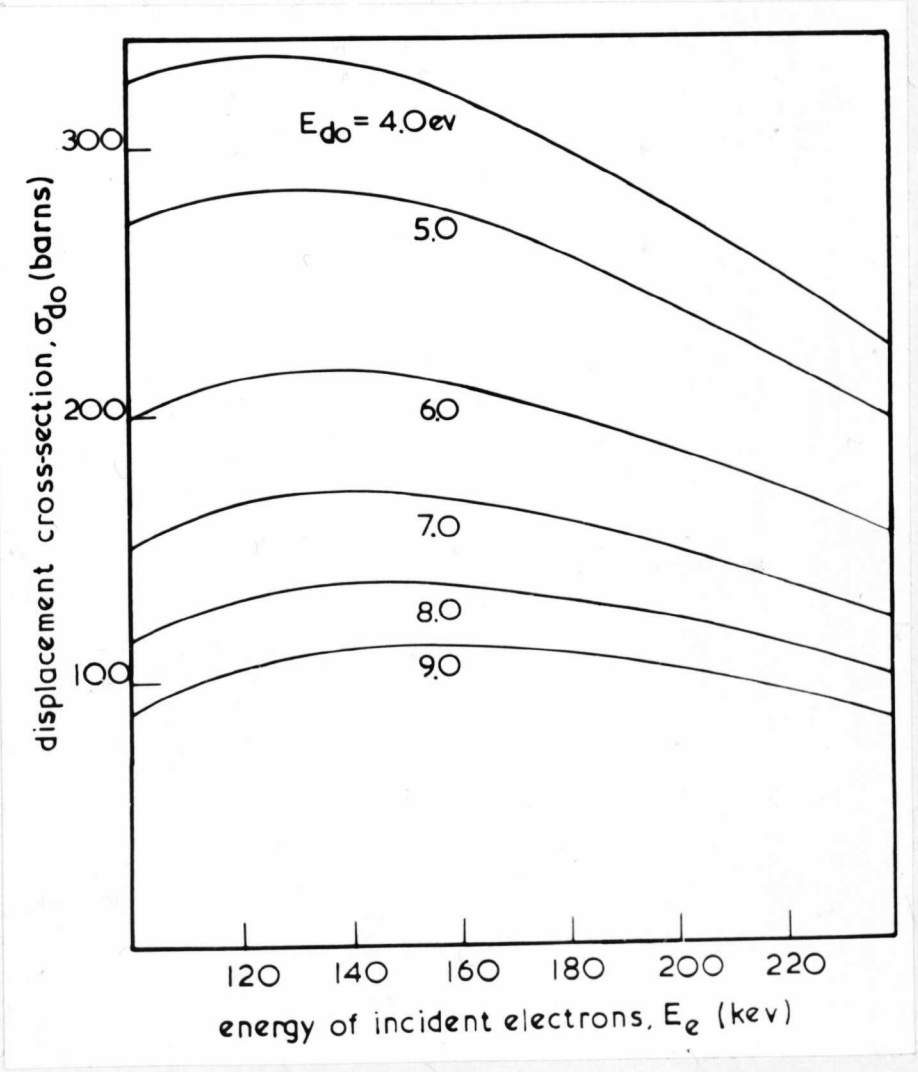

Fig. 8.3.4 Theoretical curves of displacement cross-section against incident electron energy for several values of oxygen atom displacement energy E_{do}.

From this equation σ_{dc} for a particular electron energy may be found from the measured value of dlnI/dt. The value of the constant K depends on the geometry of the ordered superlattice. In order to apply this expression to experimental observations, the measured value of I must not be influenced by dynamical diffraction effects. In the present method the value of ΔlnI from the state of order to disorder will be the same for all values of electron energy. Thus the ratio of the observed times for disordering at different electron energies will be inversely proportional to the ratio of the respective displacement cross-sections, for the same flux J, i.e.,

$$\frac{t_1}{t_2} = \frac{\sigma_{dv2}}{\sigma_{dv1}} \qquad \ldots 7$$

This method eliminates both the constant K, and measurement of the superlattice reflection intensity. By comparing the measured times for disordering at 150, 175, and 200kev, a value of 7.8ev for E_{dv} was found to give the best fit to the values of σ_{dv} against electron energy of fig. 8.3.3. It is fortunate that the values of σ_{dv}, and hence t, vary considerably over the range of electron energies used, making an accurate fit to the theoretical curves possible.

The value of E_{dv} is low compared to that for metal atoms in metallic structures (7-10) which contain only a small number of vacancies in thermal equilibrium. However, the displacement energy observed in the present case is that required to move a vanadium atom into a vacant site in the nearest-neighbour shell, and not the energy required to displace an atom well away from its original site in order to form a stable vacancy-interstitial pair.

8.4 Two-Stage Disordering Mechanism for Vanadium Monoxide

(i) Theory

The disordering process was observed to occur in two stages. It is of interest to try to correlate the theoretical disordering rates with this observation.

In the ordered vanadium sublattice two types of site may be distinguished, occupied β sites, and vacant α sites. The regular arrangement of vacant α sites (or occupied β sites) may be considered to give rise to the superlattice reflections. Under the influence of the electron beam atoms will be accumulated on the α sites, with a corresponding decrease in the superlattice reflection intensity, which will become zero when the occupancy of the α sites is equal to that for a random distribution of atoms over all the available sites. Only displacements of the type $\beta \rightarrow \alpha$ and $\alpha \rightarrow \beta$ will affect the superlattice reflection intensity, and in the present case these are restricted to displacements from an occupied site to a vacant site in the nearest-neighbour coordination shell. The rate $\beta \rightarrow \alpha$ will depend on the number of atoms on β sites, n_β, and the average fraction of vacant α sites that surround the β sites. The rate $\beta \rightarrow \alpha$ is then given by,

$$\frac{d\beta \rightarrow \alpha}{dt} = R n_\beta (1 - n_\alpha / N_\alpha) c_\alpha \qquad \ldots 8$$

where $R = J\sigma_{dV}\nu$, n_α = number of atoms on α sites, N_α = total number of α sites, and c_α is the average number of α sites surrounding a β site. The rate of accumulation of atoms on the α sites will be,

$$\frac{d\beta \rightarrow \alpha}{dt} - \frac{d\alpha \rightarrow \beta}{dt} \qquad \ldots 9$$

which may be rewritten as,

$$\frac{dn_\alpha}{dt} = Rn_\beta(1 - n_\alpha/N_\alpha)c_\alpha - Rn_\alpha(1 - n_\beta/N_\beta)c_\beta \qquad ...10$$

The terms n_β, N_β, and c_β are the β site equivalents to those terms with subscript α.

The total number of atoms in the unit cell, $(n_\alpha + n_\beta)$, and the total number of available sites, $(N_\alpha + N_\beta)$, are known, and the values of c_α and c_β may be found from the arrangement of α and β sites. The expression for the rate of displacements onto α sites can be reduced (ignoring very small terms in n_α^2) to an expression of the type,

$$\frac{dn_\alpha}{dt} = R(a - bn_\alpha) \qquad ...11$$

where a and b are constants depending on the size of the unit cell chosen and the superlattice geometry. Eqn. 11 may be integrated thus,

$$t = -\frac{1}{Rb}\ln(Ra - Rbn_\alpha) + \text{constant} \qquad ...12$$

(ii) Numerical calculation

For partial disordering the α sites will be those associated with the vacancy spirals. It will be assumed that the atoms on the remaining β sites are randomly arranged. The values of c_α and c_β are 0.038 and 0.83 respectively. Substitution into eqn. 10 and reduction gives,

$$\frac{dn_\alpha}{dt} = R(9.3 - 0.76n_\alpha) \qquad ...13$$

For random occupation of the α sites,

$$n_\alpha = (244/320).16 = 12.2 \qquad ...14$$

When this value of n_a is substituted into eqn. 13, dn_a/dt becomes zero.

To calculate the rate of disordering of the $V_{52}O_{64}$ structure, the same size unit cell is chosen as that used for the rate of partial disordering. A slight modification of this theory is now necessary due to the presence of vanadium atoms in interstitial sites in the ordered structure. In calculating the c_a and c_β coefficients it is assumed that displacements from these interstitial sites onto the four neighbouring a sites are possible. Reverse displacements, from these a sites onto the interstitial sites, are ignored on the basis that once the disordering starts the number of vacancy clusters that contain no atoms, i.e. which will readily accept an interstitial atom, is very small. The coordination coefficients, c_a and c_β, are now 0.23 and 0.77 respectively, and the rate equation is,

$$\frac{dn_a}{dt} = R(56 - 0.92n_a) \qquad \ldots 15$$

According to this theory the superlattice reflection intensity will become zero only after infinite time, when n_a will represent random occupation. Thus some cut-off value in the calculated intensity must be assumed (this will be the same for both weak and strong superlattice reflections), where the spots can no longer be regarded as visible on the screen. It is necessary to know the contribution to the structure factor of a given reflection per vacancy (excess number of vacancies over that for a random distribution) on an a site of the two different structures. The average structure factors for the two

types of superlattice reflection contained in a unit 020-200 square of the $(001)_t$ reciprocal lattice section were found from the calculated structure factors for perfect order, and then a linear relationship was assumed between the number of excess vacancies on a sites and these average values of the structure factors. It is now possible to calculate the time required for both types of superlattice reflection to diminish in intensity to some given value. For convenience this intensity I, will be expressed as a fraction of the original intensity of a weak superlattice reflection, I_w.

At 200kev, with J = $1X10^{20}$electrons/cm^2/s, R will equal 10^{-2}. The observed time for complete disordering was 240s, and for partial disordering 20s (extrapolated from a longer time at a lower flux). The times calculated from the above theory for both types of reflection to reach a given intensity are shown in fig. 8.4.1. The time lag for the intensity of the different reflections to reach values from 0.5 to $0.1I_w$ is in good agreement with the observed time of 220s. The absolute times for the two types of disordering will depend on an estimate for I at the point of invisibility. The best fit to the observed times obtained from fig. 8.4.1 gives $I = 0.5I_w$. This would appear too high for the limiting value of I, even so, for a more reasonable value of $I = 0.1I_w$, the calculated times are still in fair agreement with those observed experimentally.

The explanation as to why the observed times for disordering are shorter than the calculated times, is that the electron flux profile has a Gaussian intensity

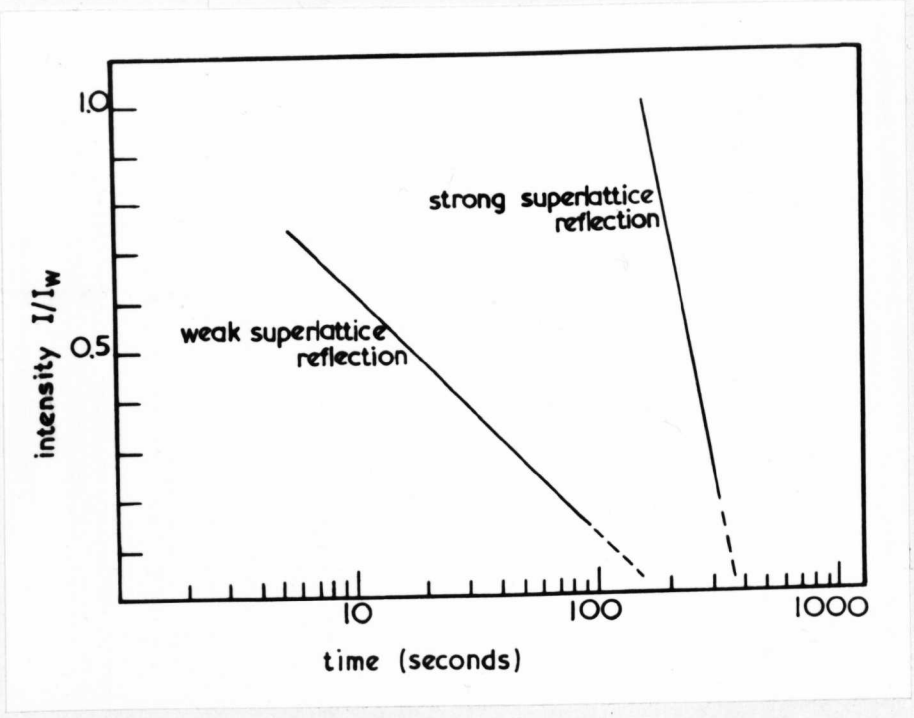

Fig.8.4.1 Theoretical values of the intensity of the strong and weak superlattice reflections of $V_{244}O_{320}$ against irradiation time. (incident electron energy E_e = 200kev, electron flux J = $1X10^{20}$ electrons/cm^2/s)

distribution across the focused illumination spot. The diffraction patterns were always taken from the centre of the illumination spot using a selected area aperture with small diameter. The electron flux is higher at the centre of the spot than the calculated average value of the flux. Increasing the value of the flux over the average measured value will lead to better agreement between the observed and calculated times for disordering. A non-uniform flux profile will not affect the value for E_{dv}.

8.5 Radiation Induced Ordering in Vanadium Monoxide

(i) Electron microscope observations

For thin-foil specimens of vanadium monoxide which did not contain ordered domains (formed by quenching from 1000°C or by previous irradiation) but within the approximate composition range $VO_{1.15}$ to $VO_{1.30}$, new superlattice reflections appeared in the diffraction patterns after long periods of irradiation at 175 and 200kev. These reflections could not be identified with those from thermally ordered specimens. No effect was observed at 150kev, or for crystals of lower oxygen content. After irradiating for about one hour at 200kev with a flux of $1X10^{20}$ electrons/cm^2/s there was a noticeable change in the diffraction pattern. The diffuse scattering became weaker, while new peaks appeared at the 1/2(220) positions, as shown in fig. 8.5.1. For irradiation times of up to about five hours the intensity of these new reflections continued to increase, but remained nearly constant after that time. A similar effect occurred at 175kev, but in this case the new reflections appeared at 1/3(220) positions. When an area previously irradiated at 200kev giving

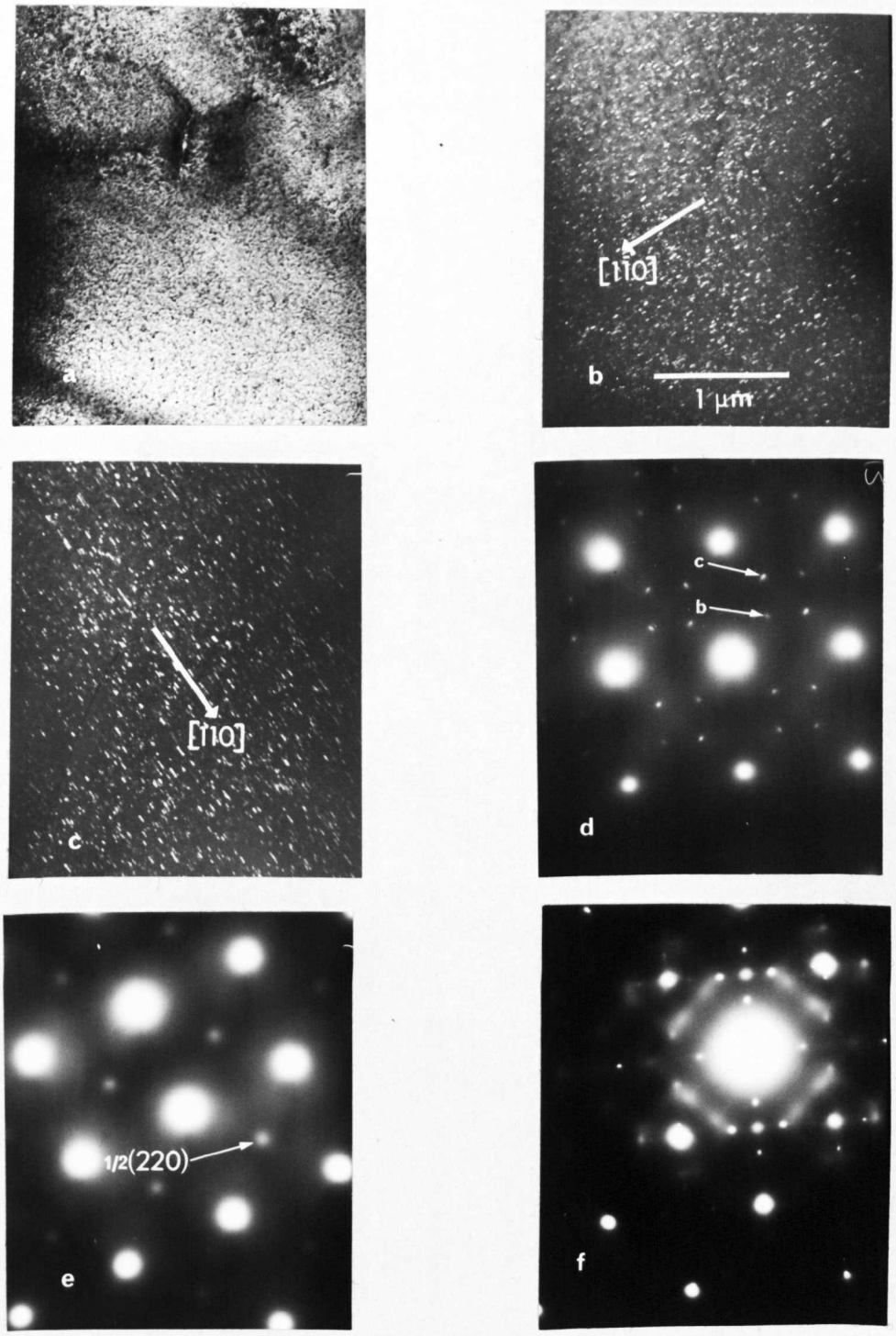

Fig. 8.5.1 Irradiation induced order in vanadium monoxide. (a) BF, (b) and (c) DF from reflections indicated in (d) (100) section, showing two orientations of small domains after irradiation at 175kev. (e) (100) section showing reflections at 1/2(220) after irradiation at 200kev. (f) (100) section showing both 1/3 and 1/2(220) reflections, in this diffraction pattern the characteristic diffuse scattering is also visible.

a diffraction pattern with 1/2(220) reflections, was subsequently irradiated at 175kev, the 1/2(220) reflections became fainter while those at 1/3(220) positions appeared. The reverse behaviour occurred for areas previously irradiated at 175kev, when followed by subsequent irradiation at 200kev. The pair of dark-field images shown in fig.8.5.1 were taken using the two different 1/3(220) reflections, and clearly show two different orientations of small domains.

(ii) A possible mechanism for radiation induced ordering in vanadium monoxide

An increased ordering rate at low temperatures as a result of irradiation is a well known phenomonen. This is attributed to the production of a large non-equilibrium concentration of vacancies and interstitials. If the temperature is sufficient for the excess defects to be mobile, an increase in the diffusion rate of several orders of magnitude is possible. Generally these defects will be mobile at temperatures well below those required for their formation in significant numbers by thermal processes. Dautreppe et al. (11) found the hitherto unknown ordered compound FeNi by means of irradiation enhanced diffusion. This compound exists in equilibrium below 320°C, too low a temperature for its formation by conventional heat-treatment. In the present case of vanadium monoxide, there already exists a high concentration of vacancies in the vanadium sublattice (>20%) and probably a not insignificant number in the oxygen sublattice. Thus the mechanism of radiation enhanced diffusion described above cannot account for the present observations. It would also appear that interstitial production under

the irradiation conditions used does not occur.
The effect could be due to a higher oxide formed on the surfaces of the foil, caused by heating from the electron beam, though the reversibility of the structure with accelerating voltage would still require explanation.

During the time required to produce the small domains shown in fig. 8.5.1 each vanadium atom has been displaced on average about 200-times by the incident electrons. For an ordered structure to form as a result of electron irradiation, it is suggested that small differences exist in the susceptibility to displacement of vanadium atoms in certain sites, and that these differences result from various types of near-neighbour coordination.
It is further suggested that other forms of long-range order, apart from the thermal equilibrium form, are energetically more favourable than the short-range order of quenched specimens. Atoms in sites which have coordination approaching a favourable long-range-ordered state should have a slightly higher threshold energy, and are thus less likely to be displaced, than atoms having unfavourable coordination. The net effect will be the displacement of atoms into favourable sites, producing small regions with some degree of long-range order.

The forces that will modify the displacement energy of an atom in a particular environment from the average displacement energy, will be similar to those leading to long-range order under thermal equilibrium (discussed in detail in Chapter 9). Since nearest-neighbour interactions exert the greatest influence, a small unit cell would be expected for an ordered structure formed

by irradiation displacement. In the present case the unit cells of the structures formed by irradiation are similar to those of the ordered modifications of titanium monoxide formed in the range $TiO_{0.7}$ to $TiO_{0.9}$ under non-equilibrium thermal conditions (see fig. 7.3.7).
The structure of these ordered titanium monoxide phases are explained in terms of vacancy segregation onto every third or second (110) plane of the cubic matrix.
For different types of atomic coordination to exert the greatest influence on the displacement threshold, the incident electron energy must be close to the mean displacement threshold. Thus for electron energies well above the mean threshold value, the differences in displacement cross-sections for various sites will be smaller than for electron energies close to this mean, although in this latter case the formation of an ordered structure would take a long time due to the low absolute values of the displacement cross-section.

The above argument can explain qualitatively the experimental observations in the following way.
At 150kev no ordered structure was formed within the given irradiation time due to the low displacement rates.
The ordered structure with a larger unit cell formed at 175kev over that at 200kev implies that longer-range interactions between atoms are exerting an effective influence on the displacement energy. This response to longer-range interactions will lead to a structure of lower energy.
At 200kev shorter-range interactions will give rise to differences in displacement rates. Possibly, irradiation at higher electron energies would produce no ordered structures. In the absence of previous experimental observations of this type of behaviour or any theoretical work, both the nature of the phenomonen and its explanation remain in doubt.

REFERENCES

1. J.D.Venables and R.G.Lye, Phil. Mag., 19, 565 (1969).
2. W.A.McKinley and H.Feshbach, Phys. Rev., 74, 1759 (1948).
3. F.Seitz and J.S.Koehler in "Solid State Physics", Vol. 2, eds. F.Seitz and D.Turnbull (Academic Press, New York, 1956).
4. W.S.Snyder and J.Neufeld, Phys. Rev., 97, 1639 (1955).
5. J.Neufeld and W.S.Snyder, Phys. Rev., 99, 1326 (1955).
6. W.Harrison and F.Seitz, Phys. Rev., 98, 1530 (1955).
7. M.J.Makin, Phil. Mag., 18, 637 (1968).
8. L.M.Howe, Phil. Mag., 22, 965 (1970).
9. A.Bourret, Phys. Stat. Sol. (a), 4, 813 (1971).
10. F.Maury, A.Lucasson and P.Lucasson, Cryst. Latt. Defects, 2, 47 (1971).
11. D.Dautreppe, J.Langler, J.Paulevé and L.Néel in "Radiation Damage in Solids", Vol. 2 (International Atomic Energy Agency, Vienna, 1962).

CHAPTER EIGHT

Addendum (following oral examination)

It should be emphasized that the ideas concerning radiation induced ordering in vanadium monoxide are speculative. There is no doubt, however, that ordering does occur. The explanation put foreward above is the only reasonable one available at the present.

CHAPTER NINE

CORRELATION AND DISCUSSION OF ORDERED VACANCY DISTRIBUTIONS

The aims of this final Chapter are to examine collectively the factors involved in the ordering of vacancies in interstitial compounds, and to then correlate these factors with the particular types of observed structure. Before proceeding to discuss these structures it will first be necessary to consider some of the general theories that have been developed to explain the phenomonen of ordering in the more familiar metal-alloy systems. Following this, the specific type of atomic interactions in interstitial compounds will be examined, with particular emphasis on how these interactions may influence the formation of ordered compounds.

9.1 Origins of the Ordering Force

One of the most important concepts used in the theory of order - disorder transformations is the central pair-wise (CPW) scheme. In this quasi-chemical model the interaction energy for a single pair of atoms can be represented by the usual potential well, with the minimum occurring at a different depth and equilibrium separation according to whether the interaction is for an A-A, B-B, or A-B pair in a simple binary alloy AB. The differences in well-depth lead to a chemical ordering force, and the different equilibrium separations to a strain ordering force.
The total configurational energy is then given by the pair Hamiltonian,

$$H = \tfrac{1}{2}\sum_i \left[V^{AA}(r_i)N^{AA}(r_i) + V^{BB}(r_i)N^{BB}(r_i) + V^{AB}(r_i)N^{AB}(r_i) \right] \qquad \ldots 1$$

where r_i is the distance between i-th neighbours in the

lattice, $N^{AA}(r_i)$ is the total number of A-A pairs in the lattice separated by that distance, and $V^{AA}(r_i)$ is the strength of the A-A interaction at that distance etc.

In practice the stability of simple superlattices based on cubic structures can usually be explained by considering the first (V_1), second (V_2), and occasionally the third (V_3), neighbour interactions (1-3). For a given compound the forces that lead to LRO will also result in SRO above T_c. Unlike a substitutional metal alloy, the interstitial location of the nonmetal atoms in the compounds studied here will result in a negligible strain ordering effect. The chemical ordering force may be broken down in several distinct types of interaction. For a metal alloy the nearest-neighbour interaction arises from the overlap of atomic orbitals, and the interaction for more distant neighbours is given by the Friedel oscillatory potential (4), which falls off as r^{-3}. Recently a long-range force that results from an electronic interaction has been characterized. It is shown later that this type of interaction may also be present in some of the interstitial compounds, and this will therefore now be examined in greater detail.

(i) Long-range electronic interaction

The stabilization of long-period superlattice structures by the reduction of conduction-electron energy has been known for some time (5). The superperiodicity imposed by regularly spaced antiphase boundaries produces a splitting of the Brillouin zones. This splitting permits the wave-vectors of a greater number of electrons to lie just below a zone boundary, where there is a depression in

the electron energy. Since long-period superlattices have large unit cells, the atomic interactions involved must also be of a long-range type. Moss (6) has shown that even above T_c this electronic ordering force still operates, and that it originates from the incomplete screening of the ion-cores by the conduction electrons. In particular, this force is associated with the flat portions of Fermi surface found below Brillouin zone boundaries. This atomic interaction depends on the quantity $Ar^{-1}\cos(2k'r)$, where A is the area, and k' the separation of the flat regions of the Fermi surface. It is the r^{-1} dependence of this force that gives the long-range interaction. There is an interesting correlation between the short-range order diffuse intensity distribution and the shape of the Fermi surface, which is based on the following arguments.

It has been shown (7) that nonspherical portions of the Fermi surface have the effect of producing minima in the function V(k), the Fourier transform of the pair interatomic potential V(r) (see eqn. 1). These minima occur at $k = 2k_F$, where k_F is the wave-vector of a nonspherical region of the Fermi surface, and are caused by the long-range electronic contribution to V(r). Clapp and Moss (8) found that a(k), the Fourier transform of a_{lmn} (see section 1.3.2) over one unit cell of reciprocal space, was related to V(k) in,

$$a(k) = \frac{C}{1 + 2m_A m_B \beta V(k)} \qquad \ldots 2$$

where C is a constant, $\beta = 1/kT$ (k = Boltzmann's constant) and m_A and m_B are the fractions of A and B atoms.

The physical interpretation of these relations is that minima in $V(k)$ at $k = 2k_F$ give maxima in $a(k)$, the diffuse scattering intensity. When the system is able to respond to the long-range electronic forces in the pair potential $V(r)$, i.e. by short-range ordering, diffuse scattering maxima in electron diffraction patterns will be observed at the positions $k = 2k_F$.

In order to determine what other types of atomic interaction are specific to interstitial compounds, an examination of the theories of atomic bonding in these compounds will be made.

9.2 Bonding Mechanisms in Interstitial Compounds

The type of atomic bonding present in most solids can be considered as belonging to one of three major types, viz. covalent (homopolar), ionic (heteropolar), and metallic. This classification is usually made on the basis of certain physical properties which are characteristic of a particular bonding mechanism. However, the refractory interstitial compounds possess a variety of physical properties which do not permit a unique classification to be made. The relevant properties are:

1. High melting point.
2. Brittle at low temperatures, ductile at high temperatures.
3. High elastic moduli and critical resolved shear stress for slip.
4. Metallic conductivity and superconducting properties.
5. Chemical and thermodynamic stability.
6. Preference for octahedral coordination

7. Extensive homogeneity ranges and high intrinsic vacancy concentrations.
8. Extensive solid solution between carbides, nitrides, and oxides of different metals.
9. Decreasing stability in higher metal Group numbers in the periodic table.

Bonding theories have been concerned with those compounds having the NaCl-type structure, since this is both simple, and representative of a large number of potentially useful and well studied carbides, nitrides, and oxides.
Different theories have emphasised the importance of strong metal-metal bonding at the expense of weak metal-nonmetal bonding and vice versa.

(i) Metal-nonmetal bonding predominant

For strong metal-nonmetal bonding to be essential to stability, the energy levels of the nonmetal 2s- and 2p-orbitals must be low. This idea was first suggested by Rundle (9), and further developed for TiC by Hume-Rothery (10), who proposed the occurrence of bonds between the sp^3-carbon and d^2sp^3-titanium hybrid orbitals. A 2/3-bond is formed, i.e. eight electrons to fill six bonding configurations. A net transfer of electrons from the metal to the nonmetal was found. The possibility of π-bonding between the metal dxy-, dxz-, and dyz-orbitals (not used for the d^2sp^3 σ-bonds) and the carbon p-orbitals giving further strength to the metal-nonmetal bonds was suggested by Krebs (11).

The first band structure calculations on this model were performed by Bilz (12) for TiC, TiN, and TiO. It was found that the density-of-states histogram was

similar for the three compounds, and the position of the Fermi level depended on the valence electron concentration (VEC), i.e. the rigid band model is applicable. The Fermi level in TiC (VEC = 8) was found to lie just below a density-of-states minimum, while for TiN (VEC = 9) it lay just above. Bilz's calculations have been criticised on two counts. Firstly, the differences in electronegativity between carbon, nitrogen, and oxygen were not taken into account, and secondly, the d-band in TiC was virtually empty, and thus increasing stability for the carbides of Groups Va and VIa would be expected as the d-band was filled.

An interesting approach to the bonding in the Group IVa nitrides has been made by Straumanis (13). Nitrogen, ammonia, and hydrogen are released when the solid nitrides are dissolved in hydrofluoric acid. From the amount of hydrogen evolved it was deduced that the metal atoms were in the 3^+ oxidation state, while from the amounts of nitrogen and ammonia, an equilibrium in the solid between atomic nitrogen and N^{3-} ions was found. The nitrogen atoms accept electrons from the metal d- and s-levels, and ionic bonding is thus inferred, which gives satisfactory agreement with the lattice energies of these nitrides (14). However, some electrons are released from the metal to form a conduction band. Further evidence for the $N + 3e \rightleftharpoons N^{3-}$ equilibrium is the evolution of nitrogen gas on heating. This is contrasted to the oxides where no gas is released, and therefore complete ionicity must exist.

The covalent (and ionic) bonding implied by the

strong metal-nonmetal bond theories is in accordance with the high stability and hardness of true covalent compounds such as diamond and silicon carbide, but it will not readily explain the metallic conductivity or extreme nonmetal deficiencies.

(ii) Metal-metal bonding predominant

The metal-metal distances found in the NaCl-type carbides, nitrides, and oxides, are similar to those of the pure metals, and thus the same type of strong metal-metal interaction would be expected. The nonmetal p-orbitals are assumed to be relatively high in energy, and electrons from these states will be transferred to fill the metallic d-bands. From examination of the relative melting points of the Group IVa and Va carbides, Dempsey (15) has shown that for TiC the bonding part of the d-band must be full, and that the higher Group carbides will be less stable than TiC due to increasing occupation of antibonding states. Comparison with the pure metals shows that there is a general increase in stability from Group IVa to VIa due to the filling of the bonding d-states. Costa and Conte (16) proposed that the metal dxy-, dxz-, and dyz-states from neighbouring metal atoms form a conduction band, and that a certain amount of interaction between the remaining metal states and nonmetal p-states gives rise to some directional bonding accounting for the stability and hardness

(iii) Recent theories of bonding

A number of more recent band structure calculations have been made mainly for titanium carbide. Lye and Logothetis (17) calculated the band structure of

TiC by the linear combination of atomic orbitals (LCAO) method similar to that used by Bilz (12), but with the band edges fitted to give agreement with optical data. They found that the Fermi level lay in a predominantly d-type band, with lower energy than in titanium metal, thus providing the extra contribution to cohesion. Electrons are transferred to the metal 3d-band from the higher energy carbon 2p-states. However there is only a small amount of ionicity, because of the enlarged radial distribution of the titanium wave functions.

Denker (18) has studied the stability of TiC, TiN, and TiO, with respect to the formation of vacancies. An LCAO method was used, and an MX_6 octahedral unit employed for the construction of the molecular orbitals. For titanium monoxide calculation showed that the observed 15% vacancies on both sublattices at the equiatomic composition gave a lowering in Fermi energy, which more than offset the energy expended in creating titanium and oxygen vacancies.

Ern and Switendick (19) calculated the band structures of TiC, TiN, and TiO, by the augmented plane wave (APW) method. This technique overcomes some of the disadvantadges of the LCAO method such as the representation of the nearly free electron waves found outside the ion-cores. The APW method assumes that the potential at each atomic site can be represented by a muffin-tin sphere. The radius of the sphere should include the maximum possible charge contributed to the crystal from the atom located on that site. The volume between spheres is represented by a plane wave expansion, and the wave functions are matched at the surface of the spheres. The advantadge

of this method is that no a priori bonding scheme is assumed. The calculations were made for 100% dense material. For TiC and TiN the density of states were found to be similar. The conduction band consists of bonding and antibonding parts mainly of (2p+3d) character, separated by a minimum in the density of states. For TiC the Fermi level lies just below this minimum, while for TiN it is just above. For TiO the Fermi level lies in a predominantly 3d-band with a small mixture of metal 4s-states. More detailed APW calculations on TiC by Conklin and Silversmith (20) were in agreement with those of (19).

Recently, Ramqvist (21-23), using the ESCA technique, and the X-ray analysis of Arbuzov and Khaenko (24), have shown that there is a considerable degree of ionic bonding in these compounds. In the ESCA technique the energies of photo and Auger electrons, emitted from the specimen during X-ray irradiation, are measured. In the carbides electron transfer between the metal and nonmetal atoms produces a shift in the carbon core-electron binding energies. This shift is then simultaneously compared with the energy spectrum from the neutral carbon atoms in residual hydrocarbons on the specimen surface. In TiC the electrostatic interaction that results from the transfer of electrons from the metal 3d- to the carbon 2p-orbitals is equal to the heat of formation of the compound, i.e. the increased stability of the carbide over the solid elements. This energy also accounts for up to one third of the total binding energy. Increasing the valence electron concentration (Group IVa $\rightarrow$ Va, or C $\rightarrow$ N $\rightarrow$ O) results in a net decrease in the ionicity. This is due to two competing processes, the greater attraction for electrons of the

more electronegative nonmetal, and the location of excess electrons, concentrated round the metal atoms in the 3d-states, in antibonding mixing with the nonmetal 2p-states.

9.3 The Origin of the Ordering Force in Interstitial Compounds

In many cases the CPW model may be confidently applied to substitutional metallic alloys. However, not only is the calculation of the interaction energy of transition metals difficult, but the occurrence of a high degree of covalent bonding will make the CPW model inapplicable, since this type of bond has strong directional properties. Two specific features of the interaction in interstitial compounds may be considered. Firstly, the free electron concentration in these compounds is probably lower than that in a metallic alloy. Thus any charges on the atoms will be poorly screened, and a long-range interaction will result. Secondly, for satisfaction of the localized covalent bonds, there must be a certain number of electrons confined to each MX_6 unit.

The tendency for ordering should then be controlled by two forces that depend directly on the type of atomic bonding, viz. a long-range electrostatic force that results from the charge on the nonmetal atoms, and a short-range, M-X, nearest-neighbour force that results from the need to maintain the maximum and minimum number of electrons in the bonding and antibonding parts of the metal d-bands.

It is unfortunate that most of the band structure calculations have been made by workers who were unaware of the significance of their results on the possible ordering of the nonmetal atoms. The one example where such a correlation has been made is the carbon-atom order in the

compound V_6C_5. Here the LCAO calculations of Lye (25) show that the bonding 3d-states are fully occupied when the vanadium to carbon-atom ratio is close to 6/5. The necessary coordination of each vanadium atom by five carbon atoms is then achieved by the formation of one of the ordered compounds with composition V_6C_5 found by Venables et al. (26) and Billingham et al. (27). The direction of electron transfer in Lye's calculations is from the carbon 2p- to the vanadium 3d-states. However, most of the theoretical calculations and experimental ESCA studies show that the electron transfer occurs in the reverse direction, to such an extent that the metal 3d-states in the carbides contain fewer electrons than in the parent metals (21).

In semi-ionic compounds Betraut (28), and van Santen (29), have suggested that electrostatic charge effects will produce specific defect rearrangements leading to a state of lower energy. Furthermore, Anderson (30) found that the difference in configurational energy between short-range and long-range ordering of ions on octahedral sites of spinels was very small, while the entropy difference was large. Thus the formation of a relatively stable short-range-ordered state will result in a depression of the critical temperature for the onset of long-range order.

9.4 Formation of the Observed Long-Range-Ordered Vacancy Distributions

(i) Carbides and nitrides with an fcc metal-atom structure

The overall similarities in the phase diagrams of the Group IVa and Va carbides and nitrides do not extend to the formation of similar superlattice structures.

The strong tendency for order in the cubic carbides is replaced by short-range order, similar to that in the carbides above T_c, in titanium nitride, while vanadium nitride shows neither long- nor short-range ordering. The reasons for these differences in ordering behaviour cannot be readily explained, even on a qualitative basis.

It is interesting to see that both the M-X nearest-neighbour interaction theory proposed by Lye(25), and the reduction in electrostatic energy by maximizing the separation of the nonmetal atoms, will result in the same type of ordered structure for the superlattices based on the composition M_6C_5. Lye's argument that the ordered arrangement of carbon atoms in V_6C_5 results from the avoidance of antibonding states, has been extended to explain the formation of similar superlattices in niobium and tantalum carbides (31). For these materials it is found that the bonding part of the d-band becomes fully occupied at higher carbon concentrations in progression from the first to the third series. Thus it is expected that the driving force for superlattice formation will be diminished for the 6/5 metal to nonmetal ratio. This idea is consistent with the observed order - disorder critical temperatures, i.e., V_6C_5, 1250°C; Nb_6C_5, 1040°C; and $TaC_{0.83}$, <1025°C (32).

Similar arguments will also account qualitatively for the ordered structure V_8C_7. In this case the number of vanadium atoms with five nearest-neighbour carbon atoms is considerably higher in the ordered structure than for a random distribution*.

* The fraction of sites p, having a coordination n (≤ 6), is found from the binomial distribution function; $p = C_n^6(r)^n(1-r)^{6-n}$, where r is the fraction of occupied nonmetal-atom sites, and C_n^6 the binomial coefficient.

However as mentioned previously, it does appear that the metal d-bands are occupied to a much smaller extent than found by Lye. If this is so, and the direction of electron transfer is from the metal to nonmetal atoms with a resulting relatively high degree of ionicity, then the second mechanism of electrostatic interaction must be the major driving force for the formation of ordered distributions of nonmetal atoms. While this mechanism will account for the structures of the superlattices V_8C_7, M_6C_5, and Ti_2C, the explanation for the different tendencies of superlattice formation is at present based on more tentative arguments.

The results of the ESCA measurements show that the degree of electron transfer to the carbon atoms is greater in TiC than VC, and thus a strong ordering tendency should be observed in the first compound. In fact, only the ordered Ti_2C-phase is found, and even the diffuse electron scattering, characteristic of short-range order, disappears at compositions above about $TiC_{0.6}$. One must surmise that in TiC the charge on the carbon atoms is very effectively screened by the radial extent of the metal 3d-orbitals. For the Group Va carbides it is found that the electrostatic energy increases slightly for the series VC → NbC → TaC, however, the reduction in ordering tendency may then again result from the screening of the nonmetal atom charges due to the increasing radial extension of the relevant d-type wave functions.

(ii) Carbides and nitrides with an hcp metal-atom structure

The largest ordering effect was seen in those compounds with hexagonal close-packed metal-atom stacking. Again this is more pronounced for the carbides, since the

high-temperature ordered modifications of V_2C and Nb_2C undergo transformations at low temperatures to structures with lower (orthorhombic) symmetry, while V_2N retains the hexagonal superlattice at low temperatures.

As for the cubic carbides, the structures of the superlattices based on hexagonal metal-atom stacking may be explained either as a repulsion between charged nonmetal atoms, or from the need to achieve the maximum average coordination of the metal atoms. For a statistical distribution of nonmetal atoms in a compound with stoichiometry M_2X, only 31% of the metal atoms have three-fold nonmetal coordination. This number can be increased to 100% by the formation of one of the ordered compounds shown in fig. 4.1.2.

Although there have been no detailed band structure calculations for these compounds, Hume-Rothery (33) has suggested that the hcp metal-atom arrangement will be stabilized when the metal d-electrons are transferred to the nonmetal atoms. Since this mechanism will depend primarily on the formation of suitable nearest-neighbour M-X hybrid bonding orbitals, equal coordination of the metal atoms would be expected.

(iii) Oxides with an fcc metal-atom structure

The ordered structures observed in the two cubic oxides (TiO, VO) showed no similarities with each other, or with the ordered structures in the carbides. Comparison of the ordered modifications of titanium monoxide (monoclinic $TiO_{1.0}$, and tetragonal $TiO_{1.25}$) shows that the type of atom distributions are in fact antithetic. Thus $TiO_{1.0}$ contains vacancies segregated onto every third (110) plane, while in $TiO_{1.25}$ the vacancies are isolated as far as possible from each other. Similarly the complex arrangement

of vacancies and vanadium atoms in $V_{244}O_{320}$, suggests that the explanation of these ordered structures in terms of the simple arguments employed for the cubic carbides are inapplicable. The ordering forces in titanium and vanadium monoxides may be conveniently discussed in more detail in the next section following the examination of short-range order in these compounds.

9.5 Short-Range Order in Transition-Metal Carbides, Nitrides, and Oxides

Before making a detailed examination of the short-range order observed in the materials presently studied, some of the relevant models for describing the short-range-ordered state will be discussed.

(i) Models of microdomain formation

While the two structural models for short-range order presented in Chapter 1 have been applied to metallic alloys, the formation of microdomains is one structural type of short-range order that has been suggested for non-stoichiometric compounds. The term 'microdomain' has often been used in rather a loose way. At present little would be gained from a more precise definition as the various interpretations will be made apparent from the more detailed descriptions given below.

One of the first models, proposed by Ariya et al. (34,35), was for titanium monoxide, where it was suggested that the structure was made up from microdomains of the lower and higher adjacent oxide phases, Ti_2O and Ti_2O_3. These microdomains which may be many unit cells in dimension, contain alternately titanium in the +1 oxidation state with oxygen vacancies (Ti_2O), and titanium in the

+3 oxidation state with titanium vacancies (Ti_2O_3). Variations in composition are achieved by changing the relative dimensions of the different types of microdomain. This type of arrangement is similar to an intergrowth structure, except that the blocks of the component phases are randomly distributed. This model has received only limited acceptance, mainly because the stability of the random microscopic dispersion over a conventional two-phase mixture could not be satisfactorily explained.

The thermodynamic stability of this type of microdomain dispersion has been theoretically examined by Anderson (36). The microdomains were considered to form a dilute solute species dissolved in a matrix with an ideal entropy of solution. It was found that the microdomain sizes were much smaller than those proposed by Ariya. The particular case studied was the transformation of a biphasic AB + AB_2 mixture into a simple nonstoichiometric phase. As the temperature was increased above T_c, the size of the microdomains rapidly decreased to atomic dimensions.

A new type of short-range-ordered configuration has been observed in several superlattice-forming metal-alloy systems quenched from above T_c, e.g. Fe-Al (37,38), Ni-Mo (39,40), Cu-Al (41,42), and Ni-Cr (43). Individual particles with an apparent high degree of order, and up to 100Å in size, are imbedded in the disordered matrix. The diffuse superlattice reflections from these specimens usually correspond to those of the final long-range-ordered state, although in one case extra reflections have been attributed to periodic antiphase boundaries within the ordered particles (44). These 'disperse two-phase systems'

can contain a particle density up to $10^{19}/cm^3$ and are stable with respect to coarsening at temperatures above T_c. This unusual behaviour has been explained by Aubauer (45) as an interplay between the decrease in surface energy and the increase in elastic strain energy during coarsening. Full coherency is maintained by a finite-sized rim zone round each particle, over which the concentrations of atomic species change from those inside the particle to those in the matrix. For sufficiently small values of the parameter $\sigma/\varepsilon D$ (where σ is the surface energy, D the rim thickness, and ε the elastic strain energy due to the difference in atomic volumes of the two phases) coarsening will be halted after the particles reach a small size. Numerical calculations based on this theory (45) give the correct order of magnitude for the particle size and density in Fe-Al alloys (i.e. outside the conventional macroscopic ordered Fe_3Al phase field), and predicts that the particle-size will be highly dependent on the relative atomic concentrations.

9.5.1 Correlation of Diffuse Scattering Observations

The most important feature found from a comparison of the diffuse electron scattering in the cubic carbides, nitrides, and oxides, is that for the first two classes of compound the diffuse scattering is similar with a particularly simple distribution. It is found that only the intensity, but not the general form of the scattering is composition dependent. For the oxides, the distributions are complex and composition dependent. The principle feature in common shown by specimens giving diffuse electron scattering is the black and white dot contrast which

increases in intensity for the sequence, nitrides→carbides →vanadium monoxide→titanium monoxide. It is difficult to specify exactly the origin of this contrast, although it would seem reasonable to suggest that it arises from variations in interatomic spacing that result from differences in either the distribution or concentration of vacancies in adjacent regions.

The diffuse scattering intensity and associated contrast were not affected by heat-treatment above the respective T_c's. In vanadium monoxide, niobium carbide (also vanadium carbide), and titanium monoxide ($TiO_{1.0}$ to $TiO_{1.25}$), the equilibrium long-range-ordered domains formed by nucleation and growth, and the untransformed matrix showed the same diffuse intensity found above T_c.

Two examples were found where the initiation of long-range order was associated with changes in the diffuse scattering. In titanium carbide, the formation of the equilibrium cubic superlattice Ti_2C was accompanied by the gradual peaking of the diffuse scattering into sharp superlattice reflections. For titanium oxide, in the composition range $TiO_{0.7}$ to $TiO_{0.9}$, dark-field images showed the diffuse scattering was associated with small metastable ordered domains. In this latter case it is not thought that this microstructure was an extension of the diffuse scattering and dot contrast found in specimens with higher compositions (above $TiO_{1.0}$).

9.5.2 Interpretation of Diffuse Scattering Distributions

(i) Titanium and vanadium monoxides

One example of a detailed investigation of diffuse scattering has been for titanium monoxide by Castles et al. (46). In this work a correlation was made, based

on the type of electronic interaction discussed in 9.1, between the band structure calculations of Ern and Switendick (19) and the distribution of diffuse scattering in the composition range $TiO_{0.9}$ to $TiO_{1.25}$.

Ern and Switendick's calculation of the band structure of fully dense TiO showed flat regions on three of the four bands that intersect the Fermi surface. In the fully dense condition the system would not be able to respond to the long-range electronic interaction. However as there is a high concentration of vacancies in titanium monoxide, it was shown that the diffuse electron scattering resulted directly from the shape of the Fermi surface, although it was not possible to determine the nature of the short-range-ordered distribution giving rise to the diffuse scattering.

The explanation of the diffuse scattering in vanadium monoxide in terms of a similar long-range electronic interaction is strongly favoured on the basis of the following arguments. It is significant that the change in sign of the Hall and Seebeck coefficients (47-49) on passing through the stoichiometric composition are accompanied by a change in the diffuse scattering distribution. This suggests that in the vicinity of the stoichiometric composition, small compositional variations give rise to important changes in the shape of the Fermi surface. The only band structure calculations for vanadium monoxide, made by Norwood and Fry (50), support this idea. The calculations assume a fully dense stoichiometric material. Although the shape of the Fermi surface is not given, the energy band diagram shows that several of the bands cross the Fermi level a number of times, and that some of the bands are close and parallel to the Fermi level.

This is in contrast to titanium monoxide where the energy of those bands near the Fermi level changes rapidly across the reciprocal lattice unit cell directions. As a consequence of the band structure of vanadium monoxide, small changes in composition will result in large changes in the occupancy of the bands close to the Fermi level, and thence in the shape of the Fermi surface. This in turn will lead to a rapid change in the type of diffuse scattering pattern.

From the relative sharpness of the features in electron diffraction patterns and the dot contrast in micrographs from vanadium and titanium monoxides, it is clear that the short-range ordering correlation extends over much larger distances (about 100Å) than found in metal alloys.

If the long-range ordered structures in vanadium and titanium monoxides also result primarily from electron energy interaction, the superlattice reflections would be expected at the positions of the diffuse intensity maxima, or at least close to the most important minima in $V(\mathbf{k})$. However, while the a_{lmn}'s of the short-range-ordered distributions closely follow the strengths of the interatomic pair potentials (V_1, V_2, etc.), the long-range-ordered superlattice must fulfil the requirements of a periodic structure, and thus the number of possible atomic distributions will be limited. A reasonably small-sized unit cell must therefore be expected.

The two apparently unrelated superlattices in titanium monoxide may result from attempts to follow the minima in $V(k)$. Similarly for vanadium monoxide, the large unit cell of the $V_{244}O_{320}$ superlattice indicates

that ordering occurs under the influence of extremely long-range atomic interactions. The strengths of the ordering forces can be gauged from the absence of growth faults associated with the $V_{52}O_{64}$ 'subcell', and their scarcity with respect to the placing of the vacancy spirals. The constancy of the short-range-ordered microstructures of titanium and vanadium monoxides with heat-treatment above T_c is not satisfactorily explained by the models of microdomain formation developed from thermodynamic arguments discussed in section 9.5(i). In view of the strong ordering forces that would be expected for these two oxides, it is at first sight surprising that the ratios of the critical temperature for the onset of LRO to the melting point of these compounds (T_c/T_m) are considerably lower than the ratios found for most metal-alloy superlattices. One possible explanation for the low values of T_c/T_m is that a large fraction of the reduction in configurational energy in the long-range-ordered structure is included in the short-range-ordered structure. While at the same time it is necessary to postulate a configurational entropy for the short-range-ordered structure comparable to that of a statistical arrangement of vacancies.

Nonstoichiometric ferrous oxide, $Fe_{1-x}O$ (NaCl-type), is one example where the arrangement of atoms in the short-range-ordered structure is well understood. In a detailed X-ray investigation by Koch and Cohen (51), following the initial electron microscope observations of Manenc et al. (52) and Herai et al. (53), a specific type of defect cluster was identified. Each defect cluster actually consists of several smaller clusters, these latter

comprising an iron atom in a tetrahedral site in the NaCl-type lattice, surrounded by four vacant octahedral iron sites. At low temperatures the larger clusters are arranged periodically, while at high temperatures they have a random distribution. These defects in ferrous oxide show a close similarity with the tetrahedral vanadium atom - vanadium vacancy clusters found in $V_{244}O_{320}$. If the formation of these defect clusters in vanadium monoxide accounts for a considerable proportion of the reduction in configuratioal energy, then the short-range-ordered structure may well contain a random arrangement of these clusters. This type of short-range order is quite unlike that in those metal alloy systems where the short-range order can be described in terms of statistical occupation probabilities. This type of defect arrangement could then account for the stabilization of the short-range-ordered state against the long-range-ordered structure at relatively low temperatures.

(ii) Cubic carbides and nitrides

The observation of the same type of diffuse scattering distribution for a number of compounds (TiC, TiN, VC, NbC, TaC) implies that the driving force for the short-range-ordered distribution of nonmetal atoms is unlikely to arise from the type of electronic interaction proposed for titanium and vanadium monoxides. This appears reasonable since the shape of the Fermi surfaces of the respective compounds vary considerably. In view of the possible ionic contribution to the atomic bonding, a more feasible mechanism would be one which involves the electrostatic repulsion between nonmetal atoms, similar

to that proposed to explain the long-range-ordered structures in these conpounds. For this model a similar charge distribution around each nonmetal atom is expected, and only the strength of the interaction, and hence intensity of the diffuse scattering, will be altered by variations in the charge transfer to the nonmetal atoms and the charge screening by the metal d-orbitals. Thus in the ordered superlattices based on the Ti_2C and M_6C_5 structures the nonmetal atoms have maximum spatial separation, and the positions of the respective superlattice reflections are on the bands of diffuse intensity*.

An interesting example of short-range order in the ionic compound a-$LiFeO_2$ has been found by Allpress (55). This material is based on the NaCl-type structure, and the Li^+ and Fe^{3+} ions share the cation positions in the lattice. Only a (100) section diffraction pattern is reproduced in this reference, but contains an identical diffuse scattering distribution as shown in fig. 3.2.2 (for niobium carbide). In this compound the driving force for the short-range order is thought to arise from repulsion between the Fe^{3+} ions, i.e. by analogy with the carbides and nitrides the Fe^{3+} ions behave as nonmetal atoms, and the Li^+ ions as vacancies.

* Using the diffuse scattering patterns from these compounds, recent numerical calculations of the short-range-ordered nonmetal-atom distributions, made by Parthé and Sauvage (54), have confirmed this type of mechanism. It should be noted that a long-range periodic structure will give rise to some superlattice reflections that do not occur at diffuse intensity maxima.

REFERENCES

1. P.C.Clapp and S.C.Moss, Phys. Rev., 171, 754 (1968).
2. S.C.Moss and P.C.Clapp, Phys. Rev., 171, 764 (1968).
3. M.J.Richards and J.W.Cahn, Acta Met., 19, 1263 (1971).
4. J.Friedel, Phil. Mag., 43, 153 (1952).
5. H.Sato and R.S.Toth, Phys. Rev., 124, 1833 (1961); 127, 469 (1962).
6. S.C.Moss, Phys. Rev. Letts., 22, 1108 (1969).
7. L.M.Roth, A.J.Zieger and T.A.Kaplan, Phys. Rev., 149, 519 (1966).
8. P.C.Clapp and S.C.Moss, Phys. Rev., 142, 418 (1966).
9. R.E.Rundle, Acta Cryst., 1, 180 (1948).
10. W.Hume-Rothery, Phil. Mag., 44, 1154 (1953).
11. H.Krebs, Acta Cryst., 9, 95 (1956).
12. H.Bilz, Z. Physik., 153, 338 (1958).
13. M.E.Straumanis in "Anisotropy in Single-Crystal Refractory Compounds", Vol. 1, eds. F.W.Valdiek and S.A.Mersol (Plenum Press, New York, 1968).
14. E.D.Baughan, Trans. Farad. Soc., 55, 736 (1959).
15. E.Dempsey, Phil. Mag., 8, 285 (1963).
16. P.Costa and R.R.Conte, Nuclear Metallurgy Symp., Met. Soc. AIME, Vol. 10 (1964).
17. R.G.Lye and E.M.Logothetis, Phys. Rev., 147, 622 (1966).
18. S.P.Denker, J. Phys. Chem. Solids, 24, 1397 (1964).
19. V.Ern and A.C.Switendick, Phys. Rev., 137, 1927 (1965).
20. J.B.Conklin and D.J.Silversmith, Int. J. Quantum Chem., Symp. No. 2, 243 (1968).
21. L.Ramqvist, K.Hamrin, G.Johansson, A.Fahlman and C.Nordling, J. Phys. Chem. Solids, 30, 1835 (1969).

22. L.Ramqvist, B.Ekstig, E.Källne, E.Noreland and R.Manne, J. Phys. Chem. Solids, 30, 1849 (1969).
23. L.Ramqvist, J. Appl. Phys., 42, 2113 (1971).
24. M.P.Arbuzov and B.V.Kaenko, Uk. Fiz. Zh., 16, 1420 (1971).
25. R.G.Lye, Private Communication, quoted in J.D.Venables, PhD thesis, University of Warwick (1970).
26. J.D.Venables, D.Kahn and R.G.Lye, Phil. Mag., 18, 177 (1968).
27. J.Billingham, P.S.Bell and M.H.Lewis, Phil. Mag., 25, 661 (1972).
28. E.F.Betraut, Acta Cryst., 6, 557 (1953).
29. J.H. van Santen, Philips Res. Repts., 5, 282 (1950).
30. P.W.Anderson, Phys. Rev., 102, 1008 (1956).
31. R.G.Lye, RIAS Tech. Rept., 71-21c (Oct. 1971).
32. J.D.Venables and M.H.Meyerhoff, RIAS Tech. Rept., 71-20c (Oct. 1971).
33. W.Hume-Rothery, Phil. Mag., 7, 1955 (1962).
34. S.M.Ariya and M.P.Morozova, Russ. J. Gen. Chem., 28, 2647 (1958).
35. S.M.Ariya and Y.G.Popov, Russ. J. Gen. Chem., 32, 2077 (1962).
36. J.S.Anderson in "Problems of Nonstoichiometry", ed. A.Rabenau (North-Holland, Amsterdam, 1970).
37. H.Warlimont and G.Thomas, Met. Sci. J., 4, 47 (1970).
38. D.Watanabe, H.Morita, H.Saito and S.Ogawa, J. Phys. Soc. Japan, 29, 722 (1970).
39. E.Ruedl, P.Delavignette and S.Amelinckx, Phys. Stat. Sol., 28, 305 (1968).
40. B.Chakravarti, E.A.Starke and B.G.Lefvre, J. Mat. Sci., 5, 394 (1968).

41. W.Gaudig and H.Warlimont, Z. Metallk., 60, 488 (1969).
42. M.Hida and T.Imura, J. Phys. Soc. Japan, 29, 242 (1970).
43. M.Hirabayashi, M.Koiwa, K.Tanaka, T.Tadaki, T.Saburi, S.Nenno and H.Nishiyama, Trans. Jap. Inst. Metals, 10, 365 (1969).
44. P.R.Okamoto and G.Thomas, Acta Met., 19, 825 (1971).
45. H.-P.Aubauer, Acta Met., 20, 165 (1972); 20, 173 (1972).
46. J.R.Castles, J.M.Cowley and A.E.C.Spargo, Acta Cryst., A27, 376 (1971).
47. S.P.Denker, USAEC Ann. Prog. Rept., No. CU-3553-6 (Jan. 1967).
48. R.Steinitz, GT&E Tech. Rept., No. TR67-186.2 (Aug. 1967).
49. M.D.Banus and T.B.Reed in "The Chemistry of Extended Defects in Non-Metallic Solids", eds. L.Eyring and M.O'Keeffe (North-Holland, Amsterdam 1970).
50. T.E.Norwood and J.L.Fry, Phys. Rev., B2, 472 (1970).
51. F.Koch and J.B.Cohen, Acta Cryst., B25, 275 (1969).
52. J.Manenc, J.Bourgeot and J.Bénard, Compt. Rend. Acad. Sci. Paris, 256, 931 (1963).
53. T.Herai, B.Thomas, J.Manenc and J.Bénard, Compt. Rend. Acad. Sci. Paris, 258, 4528 (1964).
54. E.Parthé and M.Sauvage, Private Communication.
55. J.G.Allpress, J. Mat. Sci., 6, 313 (1971).